THÈSE DE DOCTORAT

PRÉSENTÉE PAR

Hao HU

POUR L'OBTENTION DU TITRE DE

DOCTEUR DE L'UNIVERSITÉ DE LILLE

Ecole Doctorale: Sciences de la Matière, du Rayonnement et de l'Environnement

Spécialité : Chimie théorique, physique, analytique

Étude Théorique de la Revolatilisation d'Iodures Métalliques et d'Oxydes de Ruthénium lors d'Accident Nucléaire

Soutenue le 28 mai 2019 devant le jury composé de :

Dr. David LOFFREDA	ENS Lyon	Président, Rapporteur
Pr. Frederik TIELENS	Vrije Universiteit Brussel	Rapporteur
Dr. Hadrien PERRON	EDF-RD	Examinateur
Dr. Murielle RIVENET	ENSCL	Examinateur
Pr. Jean-François PAUL	Université de Lille	Directeur de thèse
Dr. Laurent CANTREL	IRSN	Co-directeur

THÈSE DE DOCTORAT

PRÉSENTÉE PAR

Hao HU

POUR L'OBTENTION DU TITRE DE

DOCTEUR DE L'UNIVERSITÉ DE LILLE

Ecole Doctorale: Sciences de la Matière, du Rayonnement et de l'Environnement

Spécialité : Chimie théorique, physique, analytique

Theoretical Study of the Revolatilization of Control Rod Metal Iodides and Ruthenium Oxides Species in Nuclear Accident

Soutenue le 28 mai 2019 devant le jury composé de :

Dr. David LOFFREDA	ENS Lyon	Président, Rapporteur
Pr. Frederik TIELENS	Vrije Universiteit Brussel	Rapporteur
Dr. Hadrien PERRON	EDF-RD	Examinateur
Dr. Murielle RIVENET	ENSCL	Examinateur
Pr. Jean-François PAUL	Université de Lille	Directeur de thèse
Dr. Laurent CANTREL	IRSN	Co-directeur

I know that I know nothing.

-Socrates

ACKNOWLEDGEMENTS

ABSTRACT

In 2011, the nuclear accident in Fukushima reminded an absolute requirement to assure a high level of safety in nuclear installations. In fact, a severe nuclear accident could lead to significant radiological consequences due to the releases of radio toxic compounds. These fission products will be liberated from degraded fuel, transported in the primary circuit. They may reach to the containment and therefore could be released into the environment. Depending on their half-lifetimes and their chemical evolution, some isotopes, such as: ^{131}I, ^{103}Ru and ^{106}Ru, are particularly dangerous due to their high volatility and significant radiological consequences. In the primary circuit aerosols formed at high temperatures will partially condense and nucleate on the walls of the primary circuit. In this work, the adsorption of some fission products (control rod metal iodides and ruthenium oxides) on the surface of the primary circuit will be studied as well as the mechanisms leading to the re-volatilization of these deposits. Since the surface of the primary circuit, constituted by 304L stainless steel, is mainly composed by iron and chromium oxides, we studied theoretically (by DFT periodic calculations) the adsorption mechanisms of control rod metal iodides and ruthenium oxides on iron oxide and chromium oxide model surfaces. These surfaces are modified to take into account the experimental conditions. We investigated in this thesis the formation of gaseous components ($I_{2(g)}$, $RuO_{3(g)}$ or $RuO_{4(g)}$) from these adsorbed species as well as the oxidation of RuO_2 surface. Our results show that it is possible to form $I_{2(g)}$, $RuO_{3(g)}$ or $RuO_{4(g)}$. However, $I_{2(g)}$ only possible forms on oxidized chromium oxide surface. On the other surfaces, the co-adsorption of an oxidant ($OH^\bullet$) is needed to form $I_{2(g)}$. On the same surfaces, the formation of $RuO_{3(g)}$ or $RuO_{4(g)}$ is possible with or without the presence of $O_{2(g)}$. We have found that the stainless steel surface plays an important role in the decomposition of RuO_4 and can also catalyse the reaction.

Keywords: *DFT, Reaction mechanism, Activation energy, Nuclear accident, Silver iodide, Cadmium iodide, Ruthenium oxides.*

RESUME

En 2011, l'accident nucléaire de Fukushima a rappelé la nécessité absolue d'assurer un haut niveau de sureté des installations nucléaires. Les conséquences de ces accidents sont liées principalement aux rejets de composés radiotoxiques produits par la fission de l'uranium. Ces composés peuvent être transportés dans le circuit de refroidissement primaire et atteindre l'enceinte de confinement. En cas de fuite de cette enceinte, ils sont, in fine, dispersés dans l'environnement. En fonction de la période radioactive ou de leur évolution chimique, certains isotopes, par exemple : ^{131}I, ^{103}Ru, ^{106}Ru, sont particulièrement nocifs, en raison de leur grande volatilité et de leurs radiotoxicités importantes. Dans le circuit primaire, en raison d'un fort gradient thermique, les aérosols formés à haute température, près du cœur du réacteur, vont se condenser sur les parois du circuit primaire. Dans ce travail, nous avons étudié l'adsorption de ces produits de fissions (iodures métalliques et ruthénium oxydes) sur la surface du circuit primaire ainsi que les mécanismes conduisant à la revolatilisation de ces dépôts. La surface du circuit primaire, en inox 304L, est constituée majoritairement d'oxydes de fer ou de chrome. Nous avons étudié par voie théorique (calculs périodiques par DFT) les mécanismes d'adsorption d'iodures métalliques et d'oxydes de ruthénium sur des modèles de surfaces d'oxyde de fer, d'oxyde de Chrome modifiées pour tenir compte des conditions expérimentales. Nous avons étudié la formation des composés gazeux ($I_{2(g)}$, $RuO_{3(g)}$ ou $RuO_{4(g)}$) à partir de ces molécules adsorbées et à partie de surface de RuO_2. Nos résultats ont montré qu'il est possible de former $I_{2(g)}$, $RuO_{3(g)}$ ou $RuO_{4(g)}$ à partir des molécules adsorbées. Cependant, seule la surface d'oxyde de chrome suroxydée permet de former I_2 spontanément à haute température. Dans les autres cas, la coadsorption d'un oxydant ($OH^{\bullet}$) est indispensable pour former $I_{2(g)}$. Par contre, la formation de $RuO_{3(g)}$ ou $RuO_{4(g)}$ est possible avec ou sans présence de l'$O_2(g)$. Nous avons démontré que la surface d'inox joue un rôle important dans la décomposition de RuO_4 qui peut aussi accélérer la réaction.

Mots-clés: *DFT, Mécanisme réactionnel, Énergie d'activation, Accident nucléaire, Iodure d'argent, Iodure de cadmium, Oxyde de ruthénium.*

TABLE OF CONTENTS

TABLE OF FIGURES

TABLE OF TABLES

CHAPTER 1   INTRODUCTION

The global warming is clearly observed since the beginning of the 20th century, origin is the industrial revolution, though the increase of earth, water and air temperature. This temperature increase will have important consequences: increase of extreme weather events, rise of ocean levels (disappearance of coasts and island), glacier ablation, changes on ecology system which also may have an influence on biodiversity. In Fifth Assessment Report of the Intergovernmental Panel on Climate Change (IPCC), it was concluded that "It is extremely likely that human influence has been the dominant cause of the observed warming since the mid-20th century."[1]

Greenhouse gas effect is one of the initial main causes of global warming. Carbon dioxide, nitrous oxide and fluorinated gases (such as: hydrofluorocarbons, perfluoro-carbons, sulfur hexafluoride and nitrogen trifluoride) are all greenhouse gases. One of the most important causes of carbon dioxide emission is through electricity production. Therefore, an energy source with small CO_2 emission and a low cost should be chosen for ecological and economic reasons. A Nuclear Power Plant (NPP) seems to be a good example for producing a worthy energy as it releases less CO_2 at cheaper cost than fossil fuel based energy plants.[2] However, there is important disadvantages for Nuclear Power Plant (NPP). In the worst situation, a severe nuclear accident can lead to significant radiological consequences. These consequences are due to radiotoxic compounds, in particular fission products (FPs), which may be released in the atmosphere. They will be released from degraded fuels, and then be transported in the primary circuit, to finally reach the containment building. FPs releases in the environment result from natural leakages and from the venting procedure if it is operated.[3] Depending on their half-life and their chemical evolution, some isotopes, such as ^{131}I, ^{103}Ru and ^{106}Ru are especially dangerous due to their high volatility and important radiological consequences.[4]

1.1 PRESENTED NUCLEAR POWER PLANT (NPP)

A Nuclear Power Plant (NPP) is a thermal power station where the fissile fuel is used as a heat source. The heat is produced by the fission reaction of nuclei ^{235}U and ^{239}Pu

and is used to generate the steam. Most NPP in the world are Light-Water Reactor (LWR). They can be separated in two categories: one generate directly steam in the reactor (Boiling Water Reactor/ BWR) and the other one generate the steam in a secondary loop whose water is heated by the primary system via a heat exchanger called "steam generator" (Pressurized Water Reactor/ PWR). All the reactor in France are PWRs.[5]
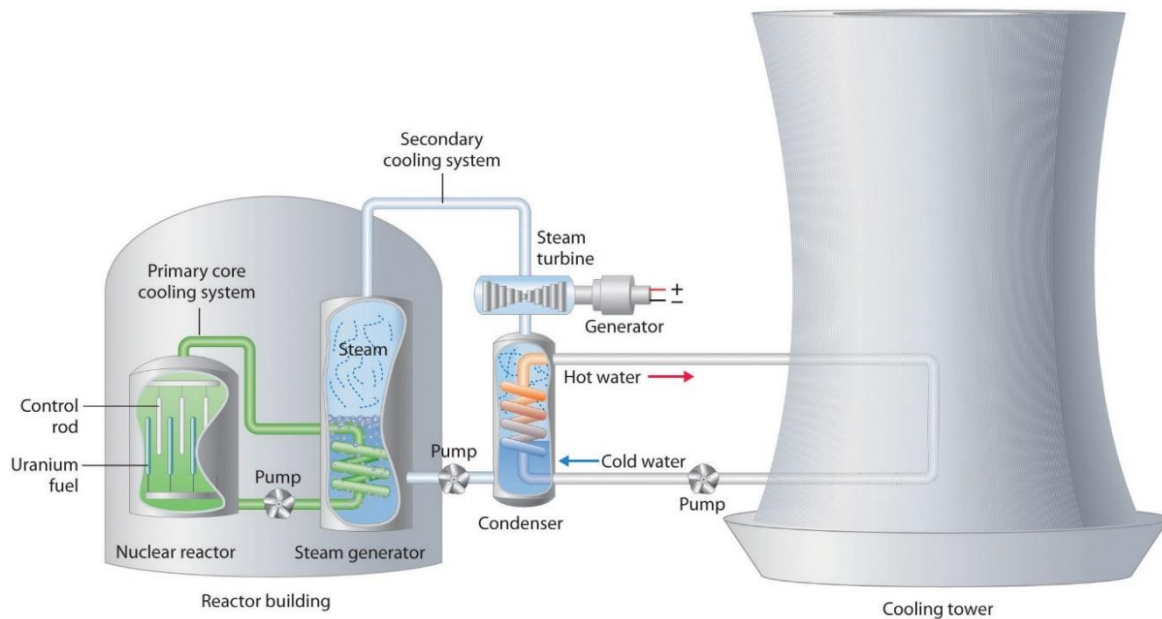
Figure 1.1. Schematic presentation of Pressurized Water Reactor (PWR).[6]

More in details, a Pressurized Water Reactor (PWR) is represented in **Figure 1.1**. The fuel rods are made by a corrosion-resistant alloy where the fission reactions of ^{235}U or ^{239}Pu occur and produce heat. Fission reactions of ^{235}U and ^{239}Pu give new fragments that contain at least one radioactive daughter nuclei. These new fragments and their daughters are called fission products (FPs) and they continue to disintegrate until stable nuclei are formed. Water in the primary core cooling system [also called primary circuit, or reactor cooling system (RCS)] extracts the heat generated by the nuclear core (around 300°C) to the secondary cooling system. In the secondary cooling system, steam will be produced through a heat exchanger (exchange heat from the primary circuit with the secondary circuit), then the steam will drive the turbine and produce electricity. In the end, the steam in the second cooling system will be condensed by cold water from the cooling tower and then reutilized for the generation of electric power.

As the fission products are highly radioactive, three barriers present inside a NPP in order to avoid the leaks of FPs to environment. The first barrier is constituted by sheaths made by Zircaloy that contains the fuel pellets. However, there is still some defects who can allow very small amount of the FPs entry into the primary circuit. The second barrier is the closed primary circuit that allows the exchange of heat between the nuclear core and the secondary circuit. The third barrier is the nuclear containment building that contains both the nuclear core and the primary circuit. This building, made by concrete, can resist to high internal pressure and should confine FPs in case of a break occurring to the primary circuit.

1.2 SEVERE NUCLEAR ACCIDENT

A severe nuclear accident can lead to significant consequences to the population and the environment. According to their severity and impact on environment and human being, nuclear incidents and accidents are classified into seven levels (International Nuclear Events Scale/ INES; **Figure 1.2**) by International Atomic Energy Agency (IAEA).
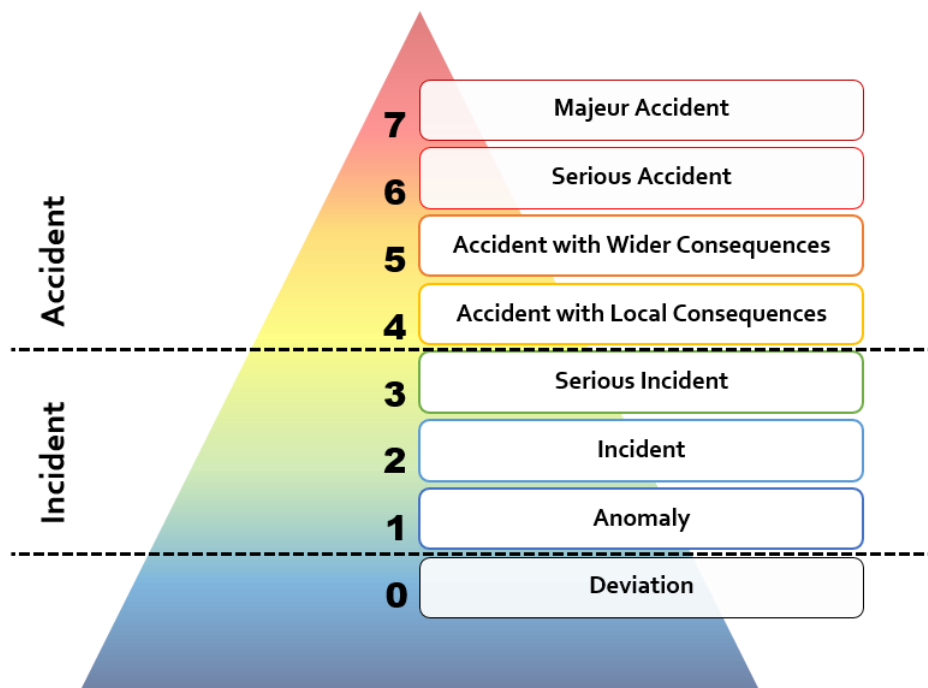
Figure 1.2. International Nuclear Events Scale (INES)

Nowadays, three serious accidents have been occurred by Light-Water Reactors (LWR).

- 1979: Three Mile Island accident (USA) Level 5 (PWR)
- 1986: Chernobyl accident (ex-USSR) Level 7 (RBMK reactor design, sort of specific BWR)
- 2011: Fukushima accident (Japan) Level 7 (BWR)

In a severe accident, the fuel is not enough cooled down and can melt with emission of large amounts of fission products (FPs) and leading to significant amounts of radioactive FPs released to environment [called "Source Term" (ST)]. **Table 1.1** gives part the radioactivity released into the atmosphere during the two major accidents. It can be noticed that a large activity due to Cs and I isotopes is liberated. Furthermore, ruthenium isotopes were also detected. In Chernobyl accident, Ru isotopes and ^{131}I and ^{137}I are responsible for similar radioactive activity in air and on the ground.[7,8] ^{106}Ru is also observed in the Fukushima accident, with a ^{106}Ru/^{137}Cs activity ratio around 0.07-0.2 in water.[9]

Table 1.1. Isotopes released during Nuclear Accidents in Pbq.[10] (PBq=10^{15}Bq)

Nuclide	Half life	Chernobyl	Fukushima	Factor difference
^{134}Cs	2.0 y	85	12	× 7
^{137}Cs	30 y	85	12	× 7
^{129}I	1.6×10^7 y	45×10^{-6}	5.7×10^{-6}	× 8
^{131}I	8 d	1 760	150	× 12
^{133}I	21 h	910	146	× 6
^{132}Te	3.2 d	~ 1 150	~ 180	× 6
^{129}Te	34 d	240	15	× 16

Source terms during an accident can be dispersed widely. For the accident of Chernobyl, during the 10-day period of maximum release (between April 26 and May 6, 1986), volatile radionuclides were broadly dispersed over Europe and the all northern hemisphere.[7,11,12] At 8 000 km from Chernobyl (Hiroshima, Japan), a relatively important quantity of nuclides was detected.[13] According to the type of accident and location, radionuclides can be transported by sea and by air[14] over large areas. During this accident, more than 80% of FPs are solubilized into the ocean.[15] ^{35}S radioactivity has even been measured in California and has been supposed to come from Fukushima Nuclear Plant.[16]

1.3 RADIOLOGICAL CONSEQUENCES OF FISSION PRODUCTS

The releases of fission products to the environment can lead to important radiological consequences. Radionuclides disintegrate more or less rapidly according to their stability. During disintegration, ionizing radiation and energy are emitted and can damage biological tissues. However, the radiotoxicity depends on the type of isotopes, their activity, the type of radiation and energy released. The physical and toxicological characteristic of fission products, that will be studied, are listed in **Table 1.2**. The possible pathway for human being contamination following a release of radionuclides to environment is shown in **Figure 1.3**.

Table 1.2. Physical and toxicological characteristics of certain fission products.[17]

Radionuclide	Emission	Half-life (d)	Mass Activity (Bq/g)	DPUI* public inhalation (Sv/Bq) (Target organ)
^{131}I	β^-, γ	8.04	4.6×10^{15}	2.92×10^{-7} (Thyroid)
^{103}Ru	β^-	39.3	1.19×10^{15}	7.3×10^{-10} (Colon)
^{106}Ru	β	368.2	1.24×10^{14}	7.0×10^{-9} (Colon)

*DPUI: dose per unit intake.
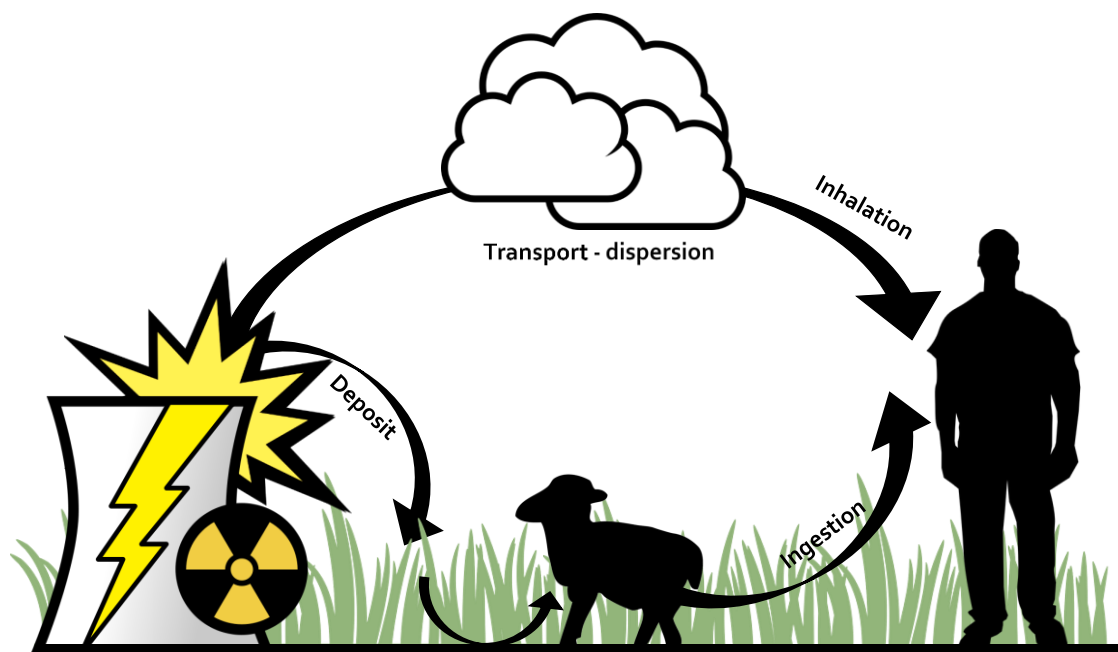
Figure 1.3. Scheme of human being contamination following a release of radionuclides to environment.

In **Table 1.3**, fission products, in which we are interested, and their possible chemical states are sorted depending on the effect on human beings and environment. Iodine will be either released as metallic iodide aerosols (for example: AgI, CsI, CdI_2 etc.) or, as gaseous iodine ($I_{2\,(g)}$ and $CH_3I_{\,(g)}$).[18,19] [131]I is the radionuclides that have the most significant impact on the exposed population at short term.[20] It can be easily deposited into humans' thyroid. From a radiological point of view, [103]Ru belongs to the medium toxicity group while [106]Ru has high toxicity.[17] The metallic Ru behaves in the human body in a similar way as the other platinum group metals meanwhile volatile ruthenium ($RuO_{4\,(g)}$) can be deposited into the lungs or throat after inhalation.[21]

In Chernobyl case, volatile iodine and ruthenium aerosols of microscopic size have been produced. They had high mobility and travel up to 1400-1800 km[22] from the nuclear plant. Iodine may have severe impact on environment especially as it may react with the atmospheric species[23] to form numerous volatile species or fine particles after nucleation processes. The main toxicity of ruthenium is due to the deposition of fission products on skin.[24]

Table 1.3. Fission-product classification and possible chemical states in irradiated UO_2 fuel rods[25]

Class	Fission Products	Chemical State*
1	Xe, Kr	Xe, Kr
2	I, Br	Single phase halide solution CsI, I, I_2
3	Cs, Rb	Cs, CsI, $Cs_2UO_{3.56}$, Cs_2UO_4, Cs_2Te, Cs_2MoO_4
4	Te, Sb	Single phase chalcogenide solution Cs_2Te
5	Ba, Sr	Oxides which can dissolve to some extent in the fuel and form separate phases BaO, $Ba_2(Zr–U-Pu)O_3$
6	Mo	Single phase metallic alloy, MoO_2, Cs_2MoO_4
7	Tc, Ru, Rh, Pd	Single phase metallic alloy
8	La, Y, Zr, Nb, lanthanides, actinides	Oxides which dissolve in fuel
9	Ag, Cd, In, Sn, Sb	Not determine really

* Principle element used as surrogate for other members of the group of fission products

1.4 RELEASE AND TRANSPORT OF FISSION PRODUCTS

As mentioned in paragraph *1.1* (p.1), the fission products are generated by fission reactions of [235]U and [239]Pu inside the nuclear reactor. It has been shown in **Table 1.3**

that fission products can be presented in different chemical states after fission reaction. According to different research programs[26–29], fission products can be classed into four categories:

- Fission gas and volatile fission products (Kr, Xe, I, Cs, Br, Rb, also Te, Sb, Ag).
- Semi-volatile fission products (Mo, Ba, Y, Rh, Pd, Tc).
- Fission products with low volatility (Sr, Nb, Ru, La, Ce, Eu, Np).
- Non-volatile fission products (Zr, Nd).
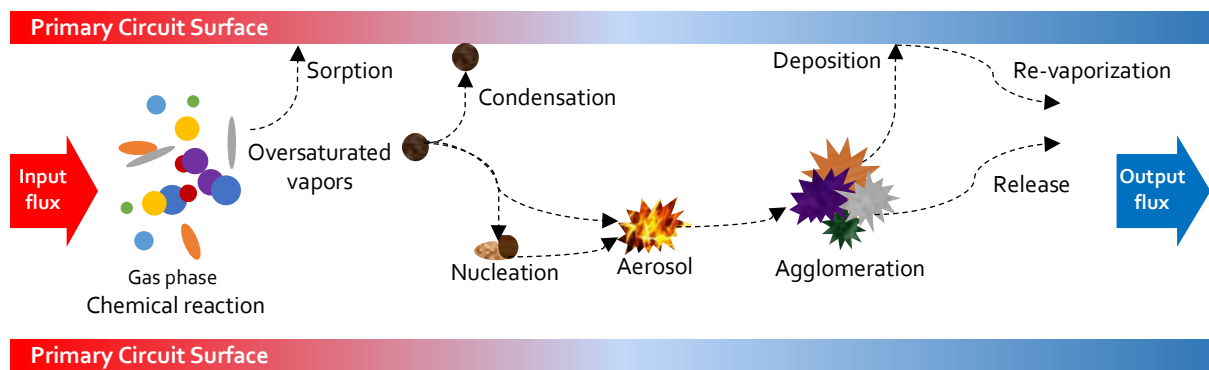
Figure 1.4. Physical-chemical phenomena occurring in the primary circuit in a severe accident

In a nuclear accident, FPs will be, in a first step, released to the primary circuit and transported by it. Depending on the nature of the accident, the FPs can be transported to other parts of NPP (until nuclear containment building) or even environment. The comportment of fission products in the primary circuit is quite complex. The temperature inside the primary circuit varies a lot according to the location. At the beginning of the primary circuit (close to the nuclear reactor), the temperature may be as high as 1500 °C. For a break in the cold leg, the temperature near the break is down to 200°C. The physical-chemical phenomena occurring in the primary circuit in a serious accident are presented in **Figure 1.4**.[30] First of all, fission gases and vapours of fission products can react with other gases/vapour, aerosols and surfaces. It is noticing that structural and control rod materials may be involved the FPs chemical reactivity. Then, the fission products vapour condenses together and form aerosols by homogeneous or heterogeneous nucleation or condenses directly on the surface of the primary circuit. Thereafter, aerosols can be deposited to the surface by Brownian diffusion; thermophoresis; diffusiophoresis, electrophoresis, sedimentation, flow-geometry changes, turbulence and pool scrubbing. The deposits formed in the RCS can potentially be remobilized due to chemical reaction with the surfaces or with a

change in the carrier gas with potential formation of higher volatile species or mechanical resuspension due to gas flow acceleration. Consequently, it is important to understand the phenomena occurring on the surface of the primary circuit to evaluate this remobilisation phenomena.

1.5 OBJECTIVE OF WORK

As we mentioned before, in a severe nuclear accident, fission products will be released from the nuclear reactor and parts of them will be deposited on the surface of the primary circuit. In our work, we will study the chemical reactions occurring on the surface of the primary circuit in case of severe accident (adsorption of fission products, re-vaporization of volatile species, etc.). The nature of the RCS surfaces will be discussed in the introduction. The chemical behaviour of iodine and ruthenium species will be presented in the introduction of chapter three and four respectively.

1.5.1 NATURE OF THE SUBSTRATE

Adsorption and reactions will occur on the surface of the primary circuit. To model these surfaces, it is mandatory to define the nature of the materials in contact with the gas flow. The RCS surface is made in 304L stainless steel that has good resistance to corrosion thanks to its high concentration of chromium. This alloy is mainly constituted by iron and chromium ($18.17_{wt.}$ %) and a little quantity of other metals (ex: Mn $1.74_{wt.}$ % etc.). [31]

This surface can be exposed to a mixture of air and steam or steam. Consequently oxidation of the surface may occur. Hence many studies have been realized at different temperatures, for different duration, on the oxidation of 304L stainless steel by air and steam.

N, Zacchetti *et al.*[32] have used SEM (Scanning Electron Microscope) and GDOES (Glow Discharge Optical Emission Spectroscopy) techniques to understand the early stage oxidation on 304L stainless steel surface under air at different temperatures. At 1200 °C, they found that, in the first few seconds, oxidation of chromium occurred and a fine-grained oxide layer of Cr_2O_3 is formed on the surface. When all the chromium on the surface has been totally oxidized, chromium will diffuse from the steel and the oxidation of iron will begin. These iron oxides will be grown outside the initial chromium oxides layer and these two oxide layers will cover the steel (**Figure 1.5**). After 20s of

oxidation, a 7.5 mm thick duplex scale is formed which is unchanged even after 200s. After 1200s, its thickness growth up to 9.5 mm. They also study the oxidation under air at lower temperature (≤1000°C). The formation rate for oxide film is quite low. However, formation of a thin chromium rich oxide layer can always be observed which is much thinner than at 1200°C.
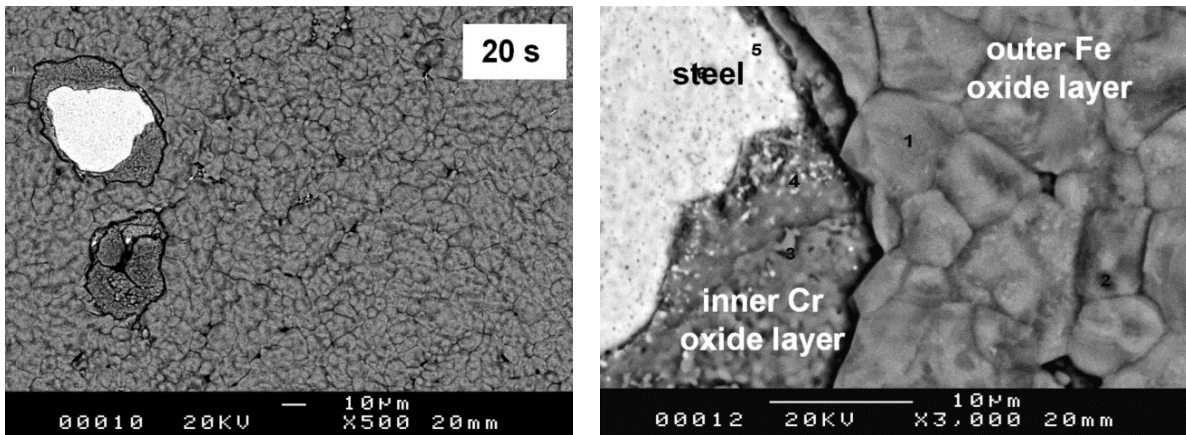
Figure 1.5. SEM surface micrographs in backscattered electrons at two different magnification (×500 and × 3000) of oxidized specimens at 1200°C in air for 20 seconds.[32]

Using the combination of TOF-SIMS (Time of Flight-Secondary Ion Mass Spectrometry), XPS (X-ray Photoelectron Spectroscopy) and LEIS (Low Energy Ion Scattering), A.-S. Mamede *et al.*[33] have studied the influence of temperature on the oxidation of 304L stainless steel surface under air and steam for long timescale. They found that the global surface composition does depend neither on oxidation temperature nor an oxidation time. However, the exact nature of the crystallites formed may change. For oxidation under air, at 750°C (**Figure 1.7** left top and middle), a mixture of manganese chromite (small particles, representing very small part of the surface, large crystals present in point 1 in **Figure 1.6**), iron chromite and separated chromium and iron oxides are presented on the surface.
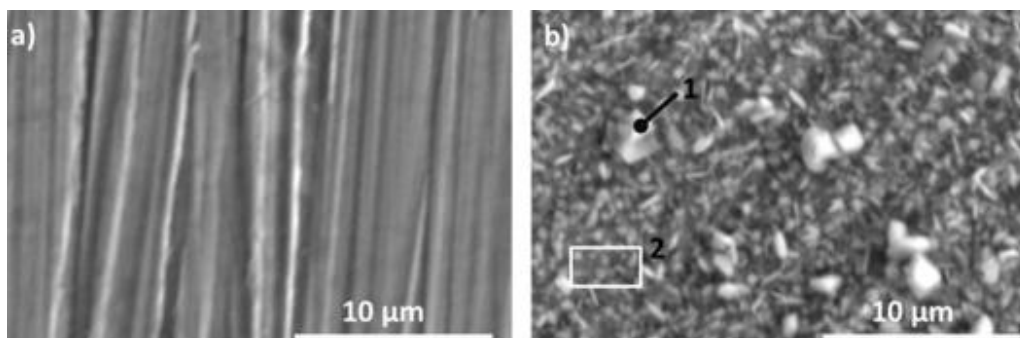
Figure 1.6. SEM images of 304L (a) before oxidation and after oxidation in air at (b) 750°C 24 h.

With LEIS analyses, it has been evidenced that iron is not present on the first atomic layer, but it is detected on the second atomic layer in a close contact with chromium. However, it is hard to distinguish between the mixed oxides and the pure oxide phases. When the temperature rises to 950°C (**Figure 1.7** left down), the surface becomes more homogeneous with a mixture of Cr_2O_3 and $MnCr_2O_4$, iron oxide being detected in a second oxide layer. For the oxidation under steam (**Figure 1.7** right), the nature of the surface is different. At 750 °C, the first atomic layer is almost MnO, while, at 950 °C, a mixture of manganese and iron can be found on the surface.
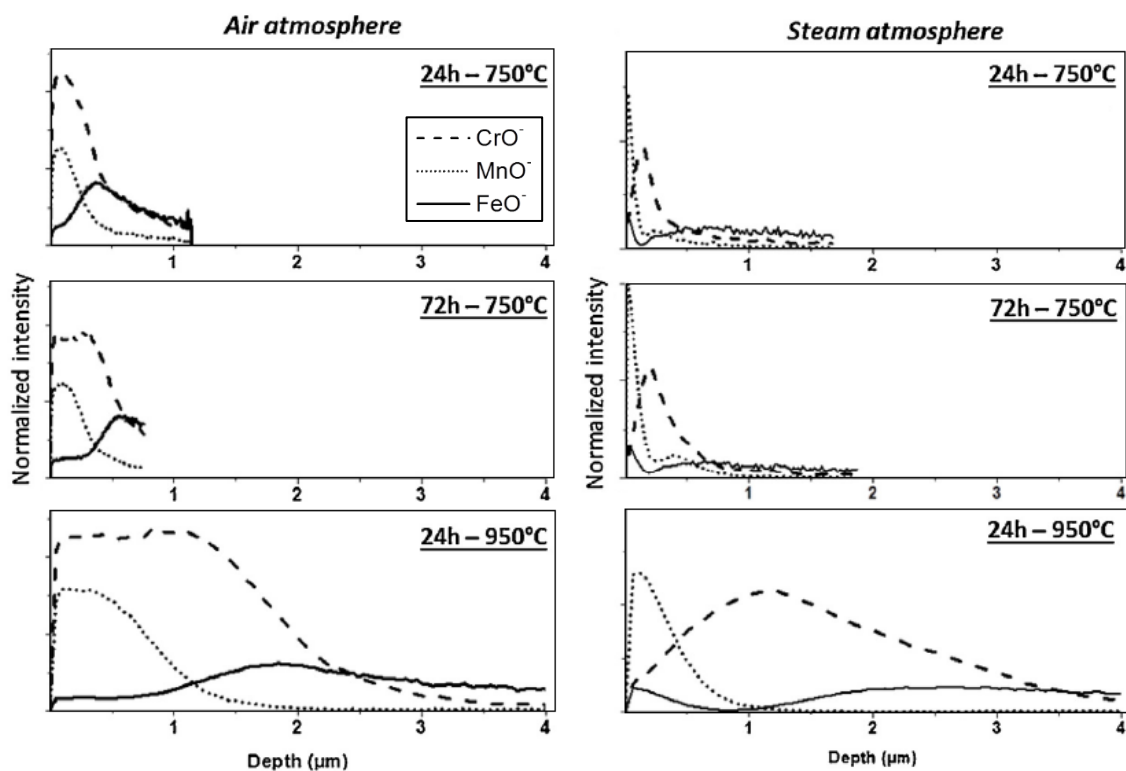
Figure 1.7. ToF-SIMS depth profiling on specimens after oxidation in air and steam atmospheres. short line: CrO⁻; point: MnO⁻; line: FeO⁻ [33]

1.5.2 STRUCTURAL MODEL

In our work, we will model the reactions, on the surface of the primary circuit (made by 304L stainless steel). Consequently, the theoretical models of the surfaces should be chosen. As mentioned in the previous paragraph, the global composition of the surface does not change for oxidation under air. However, the nature of the surface is quite complex depending on the temperature and exposition time. Overall, manganese oxide (MnO), manganese chromite ($MnCr_2O_4$), chromium oxide (Cr_2O_3), iron oxides (Fe_2O_3),

mixture of manganese and iron oxides and mixture of chromium and iron oxides might be present on the surface.

The theoretical study on magnetic orderings in $MnO_{(s)}$ have been performed recentely.[34] It was found that magnetic coupling constants s is well described by hybrid-DFT, but not at the GGA level. However, hybrid-DFT calculations are much more time consuming than GGA one. Consequently, it will not be possible to study the reactivity on surfaces at this level. For manganese chromite ($MnCr_2O_4$), only few theoretical studies have been published. D. Das $et\ al.$[35] have run the first systematic study on the bulk chromite series (including $MnCr_2O_4$) comparing their structural and magnetic properties by using DFT+U method. They found that in order to obtain the correct structure for the ground state, it is necessary to include the electron-electron correlation. In the bulk, $MnCr_2O_4$ is different from the ideal spinel structure with significant local structural distortions. However, no theoretical study has been performance on manganese oxide (MnO) and manganese chromite ($MnCr_2O_4$) for their stability under different conditions.

S. Souvi $et\ al.$ [36,37] have realized a theoretical study on chromium oxide and iron oxide surface in order to determine the most stable structure under different atmospheres (O_2, H_2 and H_2O) and temperature. For a chromium oxide surface, the most stable structure is terminated with 1 Cr and 3 O atoms. It will be named as **Cr_2O_3Cr** (***Figure 1.8 a***). At ambient temperature, the dissociative adsorption of O_2 stabilizes the surface. In this case, one oxygen atom is adsorbed on top of the chromium atom of the surface (Cr_2O_3Cr) and this oxidized surface will be called **Chromyl** (***Figure 1.8 b***). At 600K, 900K and 1200K, this structure is always the most stable one above 10^{-8}, 10^{-1} and 300 bars. Cr_2O_3Cr surface is the most stable one even under oxygen. At ambiance temperature, under steam, the surface with 1.5 water molecules adsorbed on each site is the most stable one for pressures lower than 3 bars. This hydrated surface is named **$Cr_2O_3Cr_2(OH)_3$** (***Figure 1.8 c***). Above 3 bars, totally saturated surface becomes the most stable one with 3 water molecules adsorbed per site. At 600K, $Cr_2O_3Cr_2(OH)_3$ is stable above 3.10^{-3} bar of water. Below these pressures, Cr_2O_3Cr surface is still the more stable one. For the iron oxide, in conditions relevant to severe accident the most stable surface is similar to the chromium one. This surface is called **Fe_2O_3Fe** (***Figure 1.8 d***).
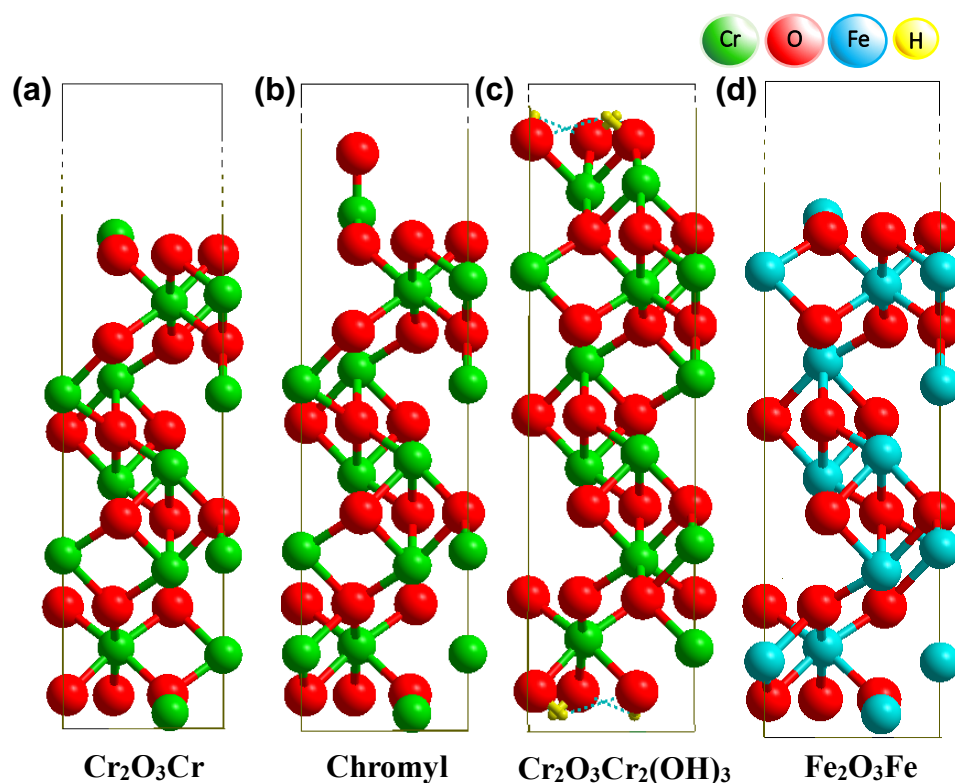
Figure 1.8. Theoretical models for the different chromium oxide and iron oxide surfaces under different pressures, temperatures and atmospheres. [36,37] (a) **Cr₂O₃Cr** (neutral chromium oxide surface), (b) **Chromyl** (oxidized chromium oxide surface), (c) **Cr₂O₃Cr₂(OH)₃** (hydrated chromium oxide surface), (d) **Fe₂O₃Fe** (neutral iron oxide surface). Chromium: green. Iron: blue. Oxygen: red. Hydrogen: yellow.

1.5.3 CONCLUSION

There are many possibilities of oxide formation on the 304L stainless steel surface in case of severe nuclear accident: manganese oxide (MnO), manganese chromite (MnCr$_2$O$_4$), chromium oxide (Cr$_2$O$_3$), iron oxides (Fe$_2$O$_3$), as well as mixture of manganese and iron oxide and mixture of chromium and iron oxides. Calculations surfaces of all these magnetic oxides will be challenging and time consuming. Since chromium oxide and iron oxide surfaces have already been investigated and since they have similar structures, this work will focus only on these two systems. The calculations on other surfaces should be performed in the future.

 The goal of this work is to investigate the vaporization of iodine and ruthenium species coming from the aerosol deposited on the RCS surfaces or vapours condensed on the RCS surfaces. For iodine, it is supposed that the aerosols are formed for metallic iodide such as CsI, AgI and CdI$_2$.[38–40] The iodide formation form CsI has been studied in a

previous work, we will focus on AgI and CdI_2. At high temperature, the volatile species of ruthenium are ruthenium oxides such as RuO_2, RuO_3 and RuO_4. We will investigate theoretically, at the GGA-DFT level, their interactions with chromium and iron oxides.

In the following chapters, firstly, calculation methods will be presented. Then the adsorption of metal iodides (AgI and CdI_2) on chromium and iron oxides surface and the possible formation volatile species ($I_{2\,(g)}$) will be discussed. In the following chapter, the adsorption of ruthenium oxides on these two surfaces will be presented. Additionally, the formation of volatile ruthenium oxide ($RuO_{4\,(g)}$) from these surfaces and from ruthenium dioxide surfaces ($RuO_{2\,(s)}$) will be presented.

REFERENCE

(1)   Stocker; T.F., D. Qin, G.-K. Plattner, M. Tignor, S.K. Allen, J. Boschung, A. Nauels, Y. Xia, V. B. and P. M. M. (eds. Summary for Policymakers. In: Climate Change 2013: The Physical Science Basis. Contribution of Working Group I to the Fifth Assessment Report of the Intergovernmental Panel on Climate Change. *CEUR Workshop Proc.* **2015**, *1542*, 33–36.

(2)   *Nuclear Power and Sustainable Development*; Non-serial Publications; INTERNATIONAL ATOMIC ENERGY AGENCY: Vienna, 2016.

(3)   Ducros, G.; Malgouyres, P. P.; Kissane, M.; Boulaud, D.; Durin, M. Fission Product Release under Severe Accidental Conditions: General Presentation of the Program and Synthesis of VERCORS 1-6 Results. *Nucl. Eng. Des.* **2001**, *208* (2), 191–203.

(4)   Preedy, V.; Burrow, G.; Watson, R. *Comprehensive Handbook of Iodine*; Elsevier, 2009.

(5)   International Atomic Energy Agency. Nuclear Power Reactors in the World. **2017**, No. 2, 88.

(6)   Gordon, E. A Light-Water Nuclear Fission Reactor for the Production of Electric Power https://chem.libretexts.org/LibreTexts/Furman_University/CHMA_Chemistry_and_Global_Awareness_(Gordon)/A_Nuclear_Energy/A_Nuclear_Reactor_Components (accessed Nov 29, 2017).

(7)   Fry, F. A.; Clarke, R. H.; O'Riordan, M. C. Early Estimates of UK Radiation Doses from the Chernobyl Reactor. *Nature* **1986**, *321* (6067), 193–195.

(8)   DENSCHLAG, H. O.; DIEL, A.; GLÄSEL, K.-H.; HEIMANN, R.; KAFFRELL, N.; KNITZ, U.; MENKE, H.; TRAUTMANN, N.; WEBER, M.; HERRMANN, G. Fallout in the Mainz Area from the Chernobyl Reactor Accident. *Radiochim. Acta* **1987**, *41* (4).

(9)   Schwantes, J. M.; Orton, C. R.; Clark, R. A. Analysis of a Nuclear Accident: Fission and Activation Product Releases from the Fukushima Daiichi Nuclear Facility as Remote Indicators of Source Identification, Extent of Release, and State of Damaged Spent Nuclear Fuel. *Environ. Sci. Technol.* **2012**, *46* (16),

8621–8627.

(10)   Fairlie, I. TORCH-2016 of the Chernobyl Nuclear Disaster. **2016**, 1–93.

(11)   Fairlie, I.; Sumner, D. The Other Report on Chernobyl (TORCH). *Greens EFA Eur. Parliam.* **2006**, *20* (April), 1–91.

(12)   SMITH, F. B.; CLARK, M. J. Radionuclide Deposition from the Chernobyl Cloud. *Nature* **1986**, *322* (6081), 690–691.

(13)   Shizuma, K.; Iwatani, K.; Hasai, H.; Nishiyama, F.; Kiso, Y.; Hoshi, M.; Sawada, S.; Inoue, H.; Suzuki, A.; Hoshita, N.; et al. Observation of Fallout in Hiroshima Caused by the Reactor Accident at Chernobyl. *Int. J. Radiat. Biol. Relat. Stud. Physics, Chem. Med.* **1987**, *51* (2), 201–207.

(14)   Yoshida, N.; Kanda, J. Tracking the Fukushima Radionuclides. *Science (80-.).* **2012**, *336* (6085), 1115–1116.

(15)   Buesseler, K.; Dai, M.; Aoyama, M.; Benitez-Nelson, C.; Charmasson, S.; Higley, K.; Maderich, V.; Masqué, P.; Morris, P. J.; Oughton, D.; et al. Fukushima Daiichi–Derived Radionuclides in the Ocean: Transport, Fate, and Impacts. *Ann. Rev. Mar. Sci.* **2017**, *9* (1), 173–203.

(16)   Priyadarshi, A.; Dominguez, G.; Thiemens, M. H. Evidence of Neutron Leakage at the Fukushima Nuclear Plant from Measurements of Radioactive 35S in California. *Proc. Natl. Acad. Sci.* **2011**, *108* (35), 14422–14425.

(17)   Caractéristiques Physiques et Toxicologiques de Radionucléides Significatifs. *clefs CEa* **2003**, *48*, 109–110.

(18)   Clement, B.; Cantrel, L.; Ducros, G.; Funke, F.; Herranz, L.; Rydl, A.; Weber, G.; Wren, C. State of the Art Report on Iodine Chemistry. 2007.

(19)   Nuclear Energy Agency/Committee on the Safety of Nuclear Installations. *Insights into the Control of the Release of Iodine, Cesium, Strontium and Other Fission Products in the Containment by Severe Accident Management*; 2000.

(20)   Saenko, V.; Ivanov, V.; Tsyb, A.; Bogdanova, T.; Tronko, M.; Demidchik, Y. U.; Yamashita, S. The Chernobyl Accident and Its Consequences. *Clin. Oncol.* **2011**, *23* (4), 234–243.

(21)   Miradji, F. Quantum Modelling of Ruthenium Chemistry in the Field of Nuclear

Power Plant Safety,Thesis, Université Lille 1, 2016.

(22) Pöllänen, R.; Valkama, I.; Toivonen, H. Transport of Radioactive Particles from the Chernobyl Accident. *Atmos. Environ.* **1997**, *31* (21), 3575–3590.

(23) Trincal, J. Modélisation Du Comportement de l'iode Dans l'atmosphère, Université de Lille 1, 2015.

(24) Pöllänen, R. Highly Radioactive Ruthenium Particles Released from the Chernobyl Accident: Particle Characteristics and Radiological Hazard. *Radiat. Prot. Dosimetry* **1997**, *71* (1), 23–32.

(25) Bowsher, B. R. Fission-Product Chemistry and Aerosol Behaviour in the Primary Circuit of a Pressurized Water Reactor under Severe Accident Conditions. *Prog. Nucl. Energy* **1987**, *20* (3), 199–233.

(26) Pontillon, Y.; Ducros, G.; Malgouyres, P. P. Behaviour of Fission Products under Severe PWR Accident Conditions VERCORS Experimental Programme - Part 1: General Description of the Programme. *Nucl. Eng. Des.* **2010**, *240* (7), 1843–1852.

(27) Pontillon, Y.; Ducros, G. Behaviour of Fission Products under Severe PWR Accident Conditions: The VERCORS Experimental Programme—Part 2: Release and Transport of Fission Gases and Volatile Fission Products. *Nucl. Eng. Des.* **2010**, *240* (7), 1853–1866.

(28) Pontillon, Y.; Ducros, G. Behaviour of Fission Products under Severe PWR Accident Conditions. The VERCORS Experimental Programme—Part 3: Release of Low-Volatile Fission Products and Actinides. *Nucl. Eng. Des.* **2010**, *240* (7), 1867–1881.

(29) Pontillon, Y.; Geiger, E.; Le Gall, C.; Bernard, S.; Gallais-During, A.; Malgouyres, P. P.; Hanus, E.; Ducros, G. Fission Products and Nuclear Fuel Behaviour under Severe Accident Conditions Part 1: Main Lessons Learnt from the First VERDON Test. *J. Nucl. Mater.* **2017**, *495*, 363–384.

(30) *Nuclear Safety in Light Water Reactors: Severe Accident Phenomenology*, 1st ed.; Sehgal, B. R., Ed.; Academic Press: Oxford UK, 2012.

(31) Nordmann, F.; Legry, P. Chimie de l'eau et Corrosion Dans Les REP. *Tech. l'Ingenieur*.

(32) Zacchetti, N.; Bellini, S.; Adrover, A.; Giona, M. Early Stage Oxidation of AISI 304 Stainless Steel: Role of Temperature and Oxygen Pressure. *Mater. High Temp.* **2009**, *26* (1), 31–38.

(33) Mamede, A.; Nuns, N.; Cristol, A.; Cantrel, L.; Souvi, S.; Cristol, S. Applied Surface Science Multitechnique Characterisation of 304L Surface States Oxidised at High Temperature in Steam and Air Atmospheres. *Appl. Surf. Sci.* **2016**, *369*, 510–519.

(34) Logsdail, A. J.; Downing, C. A.; Catlow, C. R. A.; Sokol, A. A. Magnetic Coupling Constants for MnO as Calculated Using Hybrid Density Functional Theory. *Chem. Phys. Lett.* **2017**, *690*, 47–53.

(35) Das, D.; Ghosh, S. Density Functional Theory Based Comparative Study of Electronic Structures and Magnetic Properties of Spinel ACr 2 O 4 (A = Mn, Fe, Co, Ni) Compounds. *J. Phys. D. Appl. Phys.* **2015**, *48* (42), 425001.

(36) Souvi, S. M. O.; Badawi, M.; Paul, J.-F.; Cristol, S.; Cantrel, L. A DFT Study of the Hematite Surface State in the Presence of H2, H2O and O2. *Surf. Sci.* **2013**, *610*, 7–15.

(37) Souvi, S. M. O.; Badawi, M.; Virot, F.; Cristol, S.; Cantrel, L.; Paul, J.-F. Influence of Water, Dihydrogen and Dioxygen on the Stability of the Cr 2 O 3 Surface: A First-Principles Investigation. *Surf. Sci.* **2017**, *666*, 44–52.

(38) Weber, C. F.; Beahm, E. C.; Kress, T. S. *Models of Iodine Behavior in Reactor Containments*; Oak Ridge, TN, 1992.

(39) Girault, N.; Bosland, L.; Dienstbier, J.; Dubourg, R.; Fiche, C. LWR Severe Accident Simulation: Fission Product Behavior in FPT2 Experiment. *Nucl. Technol.* **2010**, *169* (3), 218–238.

(40) Gouëllo, M.; Kalilainen, J.; Rantanen, P.; Kärkelä, T.; Auvinen, A. Experimental Study of the Cadmium Effects on Iodine Transport in the Primary Circuit During Severe Nuclear Accident. In *Volume 3: Next Generation Reactors and Advanced Reactors; Nuclear Safety and Security*; ASME, 2014.

CHAPTER 2   METHODOLOGY

T he chemical properties of reactions in our studies, such as structures of transition states and the activation energy for the reaction, are computed by *ab initio* calculations. In order to find electronic structure of a system, the Schrödinger equation should be solved. However, the determination of such an exact solution for this equation is not possible for many body systems. Therefore, numerous approximations can be utilized in order to obtain a reliable solution keeping reasonable calculation times. Density Functional Theory (DFT) will be utilized in our work as it has proven to achieve good precision in relatively short calculation time.[1] In this chapter the approximations and methods that will be used in this thesis will be presented.

2.1   THEORETICAL CONTEXT

2.1.1 SCHRÖDINGER EQUATION

Schrödinger equation is the fundamental equation in quantum physics that can describe the quantum state of a physical system in function of time. In quantum chemistry, Schrödinger equation is used to predict physical properties of a chemical system. It can be applied to a molecule, a surface or a solid in order to determine its energy and other properties. In quantum chemistry, the state n of a system can be described by a time-dependent wave function $\Psi_n(r_1, r_2, \ldots, t)$ with r_n are the coordinates of particles n and t corresponds to time. Only stationary states will be studied in our work, the wave function can be written without time: $\psi_n(r_1, r_2, \ldots)$. By solving time-independent Schrödinger equation (*Equation 2.1*), the wave function ψ_n of a particle and its associate energy can be found.[2]

$$\widehat{\mathcal{H}} \, \psi_n = E \, \psi_n \qquad\qquad \textit{Equation 2.1}$$

- $\mathcal{H}$:   Hamiltonian of the system
- ψ_n :   Wave function of system
- E :   Energy associated to the wave function

The Hamiltonian of the system $\hat{\mathcal{H}}$ contains the energy operators (*Equation 2.2*): operator for the electrons kinetic energy $\hat{T}_e$, the operator for kinetic energy of nuclei $\hat{T}_n$, operator for electrostatic interaction between electrons $\hat{V}_{ee}$, operator for electrostatic interaction between nuclei $\hat{V}_{nn}$ and operator for electrostatic interaction between nuclei and electrons $\hat{V}_{ne}$.

$$\hat{\mathcal{H}} = \hat{T}_e + \hat{T}_n + \hat{V}_{ee} + \hat{V}_{nn} + \hat{V}_{ne}$$

Equation 2.2

Where

$$\hat{T}_e = -\frac{1}{2} \sum_{i=1}^{N} \nabla_i^2$$

$$\hat{T}_n = -\sum_{A=1}^{M} \frac{\nabla_A^2}{2M_A}$$

$$\hat{V}_{ee} = \sum_{i=1}^{N} \sum_{i>j}^{N} \frac{1}{|r_i - r_j|}$$

$$\hat{V}_{nn} = \sum_{A=1}^{M} \sum_{B>A}^{M} \frac{Z_A Z_B}{|R_A - R_B|}$$

$$\hat{V}_{ne} = -\sum_{i=1}^{N} \sum_{A=1}^{M} \frac{Z_A}{|r_i - R_A|}$$

All the equations above are in atomic unit and with M_A and Z_A equal to mass and charge of the atom A. The equation is not soluble directly, and some approximation will be applied.

2.1.2 BORN-OPPENHEIMER APPROXIMATION

The Born-Oppenheimer approximation is one of the classical approximations. It is used when the motion of nuclei and the motion of electrons can be separated. The wave functions of a molecule could be diverse into two parts (electronic and nuclear components) in a mathematical way.

$$\psi_{total} = \psi_e \cdot \psi_n$$

Equation 2.3

As the nucleus is heavier than electrons (more than 2000 times), the nuclei move much more slowly than electrons. Consequently, electrons can relax for each nucleus motion and reach the fundamental state instantly. Thus the kinetic energy and electrostatic repulsion term of nuclei in the Hamiltonian can be considered as a constant. As a result, the total Hamiltonian can be simplified (*Equation 2.4*).

$$\hat{\mathcal{H}} = \hat{T}_e + \hat{V}_{ee} + \hat{V}_{ne}$$
Equation 2.4

However, it is still impossible to solve this equation exactly for a system bigger than one hydrogen atom. Thus several approximations should be used to find an approximated wave function. For example, we can mention: Hartree-Fock Method, Post-Hartree-Fock Method and **D**ensity **F**unctional **T**heory (DFT) method. In our study, all the calculations were performed by using DFT method.

2.2 DENSITY FUNCTIONAL THEORY

2.2.1 HOHENBERG-KOHN THEOREM

Density Functional Theory based 3 theorems: the first, Hohenberg and Kohn theorem which demonstrates that the electronic density $\rho(r)$ of the ground state of the system is unique for the extern potential $V(r)$ (interaction between electron and nucleus). Furthermore, the kinetic energy and the potential for interaction between electrons can be written also in function of the electronic density. Thus, the properties of the studied system can be determined by using only the electronic density, for example: the Hamiltonian, the wave function, total energy, and all the properties of the ground state. The second theorem of Hohenberg and Kohn states that there exists a universal functional for the electronic density $\rho(r)$ to compute the energy of the system. This functional does not depend on the external potential. Moreover, the exact electronic density is minimized the energy at the ground state of the system.

So for a given potential $V(r)$, the energy of the ground state of the system can be described as a function of $\rho(r)$ (*Equation 2.5*):

$$E[\rho(r)] = \int V(r)\rho(r)dr + F[\rho]$$
Equation 2.5

- $V(r)$: Coulombian attraction between electrons and nuclei

- $F[\rho]$: Universal functional, sum of kinetic energy, interaction between electron and electron, exchange-correlation.

The minimization of the total energy of a system, depending on the electronic density will give both the exact energy and the exact electronic density.

2.2.2 KOHN-SHAM METHOD

Kohn-Sham Method is used to find energy of the ground state. Orbitals (Kohn-Sham Orbitals) are introduced in order to obtain a better description for the kinetic energy of the system.[3] A Slater determinant is used to describe the wave function. Thus the following terms can be described:

- Total wave function:
$$\psi_s = \frac{1}{\sqrt{N!}}|\phi_1 \ldots \phi_N|$$
Equation 2.6

- Electronic density:
$$\rho(r) = \sum_i^N |\phi_i(r)|^2$$
Equation 2.7

- Kinetic energy of non-interacting particles:
$$T_0 = \sum_i^N \left\langle \phi_i \left| -\frac{1}{2}\nabla^2 \right| \phi_i \right\rangle$$
Equation 2.8

Thus the energy of the ground state (*Equation 2.5*) can be written as below:

$$E[\rho(r)] = \sum_i^N \left\langle \phi_i \left| -\frac{1}{2}\nabla^2 \right| \phi_i \right\rangle + \int V(r)\rho(r)dr + J[\rho] + E_{xc}[\rho]$$
Equation 2.9

- $J[\rho]$: Classic interaction between electron and electron (repulsion Colombian)
- $E_{xc}[\rho]$: Exchange-correlation energy (contains all the non-classic electron-electron interaction terms)

Then the Kohn-Sham equations can be solved:

$$\left(-\frac{1}{2}\nabla^2 + V_{eff}\right)\phi_i = \varepsilon_i\phi_i$$
Equation 2.10

With
$$V_{eff} = V(r) + V_H(r) + V_{xc}(r)$$
Equation 2.11

- $V(r)$:Extern potential nuclei apply to electrons cloud
- $V_H(r)$:Potential associate to classic part of electron-electron interaction
- $V_{xc}(r)$:Exchange-correlation potential

The resolution of the Kohn-Sham equation is performed by an iterative method who is called a SCF (self-consistent field) process (**Figure 2.1**).
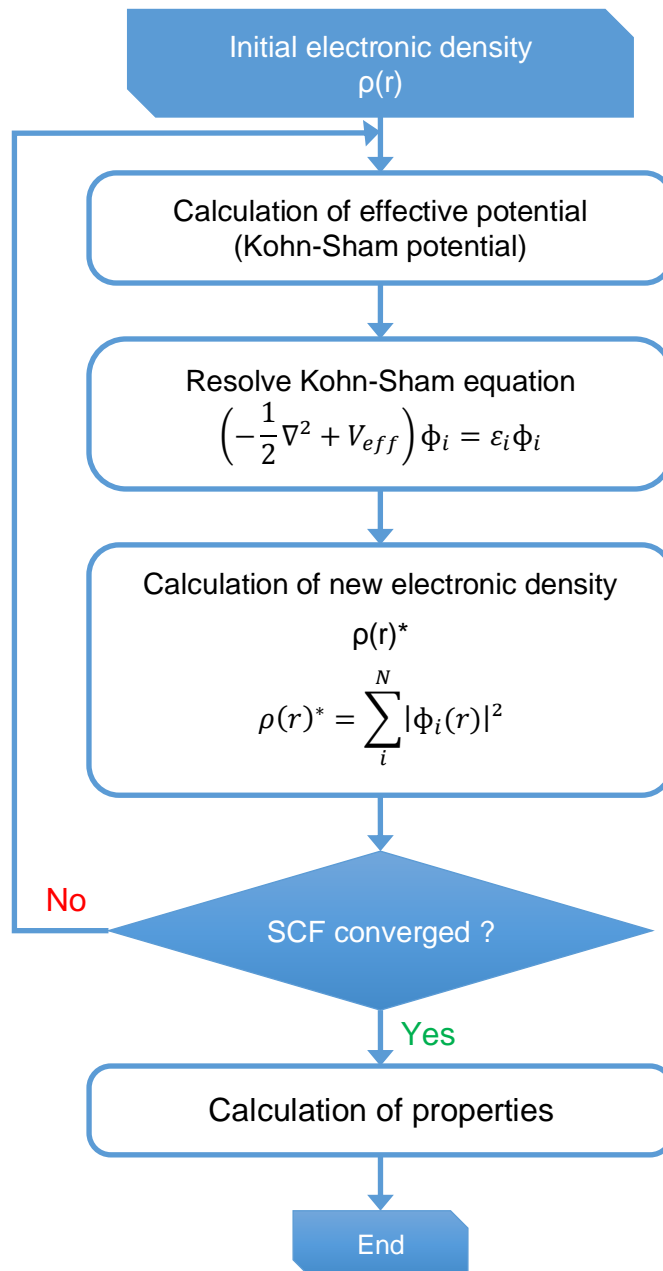
Figure 2.1. Self-consistent Field (SCF) process

2.2.3 APPROXIMATIONS TO EXCHANGE CORRELATION FUNCTIONAL

The main difficulty to solve Kohn-Sham equation is the calculation of exchange-correlation part E_{xc} that can be decomposed in two parts: exchange part and correlation part (*Equation 2.12*).

$$E_{xc}[\rho] = E_x[\rho] + E_c[\rho]$$
Equation 2.12

where
$$E_x[\rho] = \int \rho(r)\epsilon_x[\rho(r)]dr$$

$$E_c[\rho] = \int \rho(r)\epsilon_c[\rho(r)]dr$$

Equation 2.13

2.2.3.1 LOCAL DENSITY APPROXIMATION (LDA)

The first approximation of the exchange-correlation energy is called the Local Density Approximation (LDA) that considers the energy as a local functional of the electronic density.[3] This approximation can be used in systems with slow electronic density variation that can be treated as a Uniform Electron Gas (UEG) system.

$$E_{xc}^{LDA}[\rho] = \int \rho(r)\epsilon_{xc}^{UEG}[\rho(r)]dr \qquad \textit{Equation 2.14}$$

- ϵ_{xc}^{UEG}: exchange correlation energy density of a UEG of density ρ

This exchange correlation energy can also be separated in two parts: exchange energy and correlation energy (*Equation 2.15*), as is discussed higher (see *Equation 2.13*).

$$\epsilon_{xc}^{UEG} = \epsilon_x^{UEG} + \epsilon_c^{UEG} \qquad \textit{Equation 2.15}$$

- The exchange energy has been determined by Slater[4] and Dirac[5].

$$\epsilon_x^{UEG}[\rho(r)] = -\frac{3}{4}\left(\frac{3\rho(r)}{\pi}\right)^{\frac{1}{3}} \qquad \textit{Equation 2.16}$$

- The correlation energy has no exact expression yet. Meanwhile, ϵ_c^{UEG} can be described by an analytical expression obtained by fitting quantum Monte-Carlo calculations[6].

However, this method is not fully appropriate for chemical systems that could not be treated as a uniform electron gas (UEG). For example, in molecules and oxides, there is an important variation in the electronic density. In this case, electronic correlations will be overestimated while the electronic exchanges are underestimated. Therefore, better approximations that consider inhomogeneity of the electronic density in the calculation of exchange and correlation energy should be used to improve the accuracy of the calculation of the chemical system.

2.2.3.2 *THE GENERALIZED GRADIENT APPROXIMATION (GGA)*

Generalized gradient approximation (GGA) is an improved version of LDA to describe a complex chemical system (solid or molecule). By using a Taylor type development, the evaluation of the energy will take into account "a non-local correction" including the gradient of ρ to the exchange-correlation energy (*Equation 2.17*).[7]

$$E_{xc}^{GGA}[\rho] = \int \rho(r)\epsilon_{xc}^{GGA}[\rho(r), |\nabla\rho(r)|]dr \qquad \text{\textit{Equation 2.17}}$$

As we mentioned before, the exchange correlation energy can be separated in two parts (*Equation 2.18*).

$$E_{xc}^{GGA} = E_x^{GGA} + E_c^{GGA} \qquad \text{\textit{Equation 2.18}}$$

The exchange term can be written as below:

$$E_x^{GGA} = \int \rho(r)\epsilon_x^{UEG}[\rho(r)]f(\zeta)dr \qquad \text{\textit{Equation 2.19}}$$

- f : Enhancement factor
- ζ : Dimensionless variable

with
$$\zeta = \frac{|\Delta\rho|^2}{(2(3\pi^2)^{\frac{1}{3}})^2\rho^{\frac{8}{3}}} \qquad \text{\textit{Equation 2.20}}$$

The exchange functional can be described by two famous "families": empirical functionals (suggested Becke[8]) or rational functionals (suggested by Perdew[7]). In our work, the exchange energy was calculated by the latter approximation.

2.2.3.3 *PSEUDOPOTENTIAL*

In a periodic solid, the electronic wave functions can be described by a basis set of plane waves. Very large number of plane waves is needed to describe the oscillations of wave functions of the valence electrons in the core region as it varies very rapidly. In order to decrease the computational time, a pseudo-potential approximation should be used. As the chemical bonds are formed by the external valence electrons, and that the electrons located in the core do not participate in the chemical bonds, the oscillations of wave functions of core electrons can be removed to simplify the calculation. These

oscillations of wave functions of core electrons can be replaced by a smoother pseudopotential that acts on a set of pseudo wave functions illustrated schematically in **Figure 2.2**. The all-electron valence wave function (solid line) oscillated very rapidly in the core region. The pseudo wave function (Ψ_{pseudo}) generated by a pseudopotential V_{pseudo} (dashed line) is identical to coulomb potential (Z/r) (solid line) after a certain radius r_c (cutoff radius). After this approximation, the profile of wave function is much smoother near the core, hence it requires less plane waves to describe it.
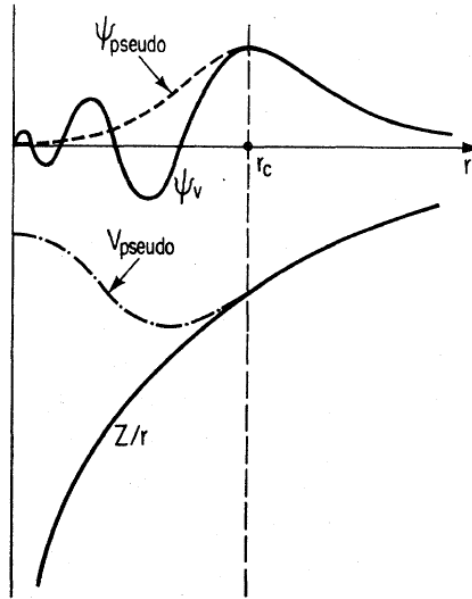
Figure 2.2. Schematic illustration of all-electron (solid lines) and pseudo-electron (dashed lines) potentials and their corresponding wave functions. The radius at which all-electron and pseudo-electron value match is designated r_c.[9]

In our work, a Projector Augmented Waves (PAW) approach[10,11] will be utilized to describe the electron–ion interactions. In this method, the pseudo wave function can be expanded into pseudo partial waves:

$$|\Psi^{PS}\rangle = \sum_i |\phi_i^{PS}\rangle c_i$$

Equation 2.21

The transformation of true all-electron wave function with pseudo wave function can be written as:

$$|\Psi^{AE}\rangle = \mathcal{T}|\Psi^{PS}\rangle = \sum_i |\phi_i^{AE}\rangle c_i$$

Equation 2.22

with identical coefficients c_i in both expressions. Hence the all-electron wave function can be described by *Equation 2.23*

$$|\Psi^{AE}\rangle = |\Psi^{PS}\rangle - \sum_i |\phi_i^{PS}\rangle c_i + \sum_i |\phi_i^{AE}\rangle c_i$$

Equation 2.23

In this equation, only expansion coefficients for the partial wave expansions are still unknown. As the transformation $\mathcal{T}$ is required to be linear, the coefficients are scalar products of the pseudo wave function with some fixed functions $\langle p_i^{PS}|$ called projector functions. Hence, the coefficients could be the linear function of the pseudo wave function.

$$c_i = \langle p_i^{PS}|\Psi^{PS}\rangle$$

Equation 2.24

Therefore, the all-electron wave function can be found from the pseudo wave function by using *Equation 2.25*.

$$|\Psi^{AE}\rangle = |\Psi^{PS}\rangle + \sum_i \left(|\phi_i^{AE}\rangle - |\phi_i^{PS}\rangle\right)\langle p_i^{PS}|\Psi^{PS}\rangle$$

Equation 2.25

This equation can be illustrated schematically by **Figure 2.3**.

Plan wave part   "True" spherical part   Pseudo spherical part
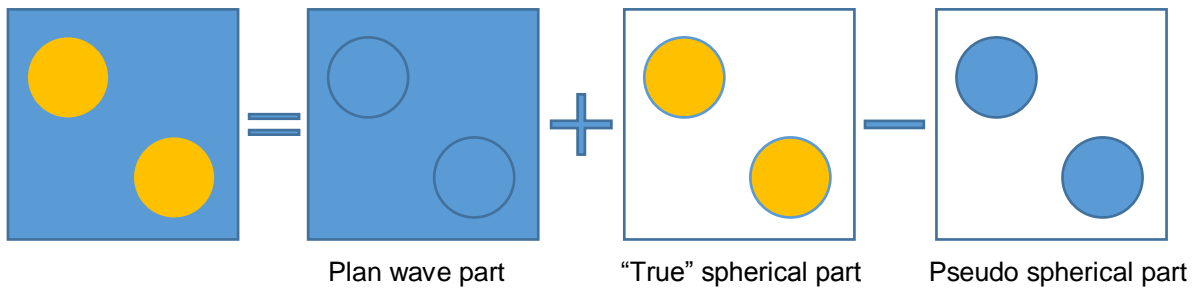
Figure 2.3. Schematic illustration of equation of all-electron wave function.

2.2.3.4 DFT+U METHOD

Highly correlated systems cannot be described correctly by LDA or GGA since DFT over delocalize electron. Therefore, an additional Hubbard term (denoted "U") that describes Coulomb interaction should be added in the calculation. The Coulomb interactions are particularly important for localized d and f orbital, but can be also important for p orbital. The interactions can be described by two parameters: U

(Coulomb interaction) and J (exchange interaction). These parameters U and J can be deduced from *ab initio* calculations or in a semi-empirically way.

In first principle calculations, the DFT+U corrections can be introduced in two main different ways: the first is introduced by Liechtenstein *et al.*[12] and the second is proposed by Dudarev *et al.*[13] In our work, the first method will be utilized, and the total energy of the system will be calculated with the following equation (*Equation 2.26*).

$$E_{tot} = E_{DFT} + E_{HF} - E_{dc}$$

Equation 2.26

- E_{tot} : Total energy of the system with correction term
- E_{DFT}: Energy obtain by DFT calculation
- E_{HF} : Correction term that considers the correlation
- E_{dc} : Double-counting term that contains the part of the correlation for localized electrons already taken into account in the DFT

2.3 TRANSITION STATE THEORY

Studying the reactivity of a system requires discovering the minima on the free energy surface and also the Transition State (TS) of the possible reactions. As far back as 1935, Eyring, Polanyi and Evans proposed the Transition State theory.[14] In this concept, a chemical reaction can be represented as nuclei moving from one minimum to another. The origin of Transition State theory is the path of minimum energy that connects the reactants to the products. This reaction path can be described by **Figure 2.4**. At the maximum energy of the reaction path, the geometrical configuration of a system is called the Transition Structure. The activation Gibbs free energy ($\Delta G^{\neq}$) corresponds to the energy difference between the Gibbs free energies of the Transition State and the reactant (*Equation 2.27*).

$$\Delta G^{\neq} = G_{TS} - G_{reactant}$$

Equation 2.27

The macroscopic reaction rate constant can be defined by *Equation 2.28*:

$$k_{rate} = \frac{k_B T}{h} e^{-\frac{\Delta G^{\neq}}{RT}}$$

Equation 2.28
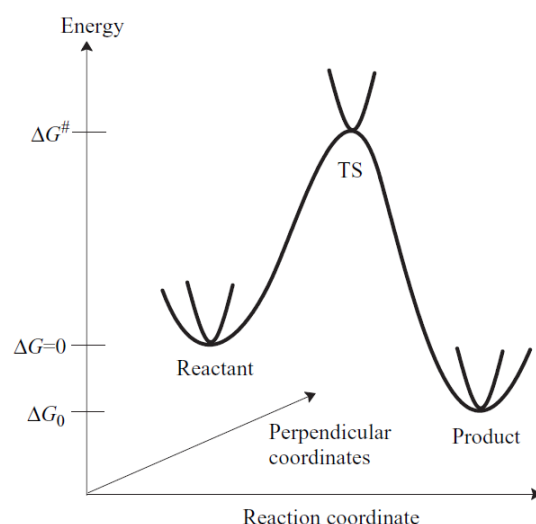
Figure 2.4. Schematic illustration of a reaction path[15]

2.3.1 NUDGED ELASTIC BAND METHOD (NEB)

In order to find the geometry of the Transition State, the Minimum Energy Path (MEP) should be found first. Nudged elastic band method (NEB)[16–20] is the most utilized method for determining the MEP between two local minima (reactants and products). This method is quite operative to find the Transition State of various types of chemical reactions[21], or the diffusions of molecule or atom on a surface[22].
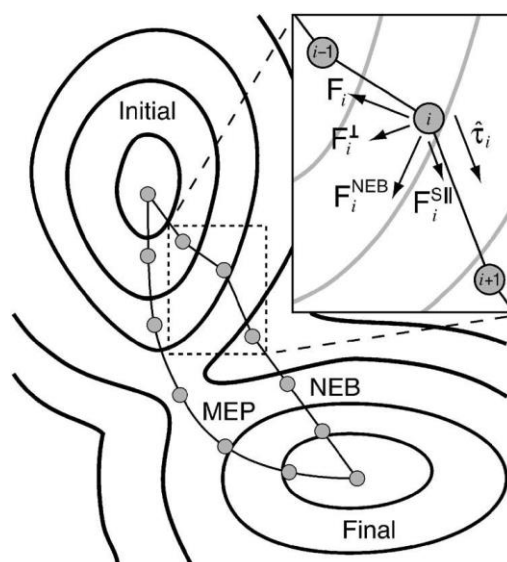
Figure 2.5. The nudge-elastic band (NEB) method for locating transition states.[16]

The principle of NEB is shown in **Figure 2.5**. It is necessary to create intermediate geometries between the initial state and the final state. These intermediate geometries can be considered as an elastic band of N+1 images (labelled $R_0, R_1, R_2, ..., R_N,$

where R_0 and R_N should be fixed as they correspond to initial and final states). During the global geometric optimization of the band, a set of forces is determined from the position of the previous and following images and applied to the intermediate image in order to avoid the relaxation of all the geometry towards the initial or final states. The corrected energy on each point of NEB is calculated according to the equation below.

$$F(R_1, \dots, R_N) = \sum_{i=1}^{N-1} E(R_1) + \sum_{i=1}^{N} \frac{k}{2}(R_i - R_{i-1})^2 \qquad \textit{Equation 2.29}$$

The NEB force acting on each image i can be considered as a perpendicular force and a parallel force (cf. **Figure 2.5**)[16]:

$$\boldsymbol{F}_{NEB} = \boldsymbol{F}_i^{S\parallel} + \boldsymbol{F}_i^{\perp} \qquad \textit{Equation 2.30}$$

- $\boldsymbol{F}_i^{\perp}$: Perpendicular force due to the external potential

$$\boldsymbol{F}_i^{\perp} = -\nabla E(R_i) + \nabla E(R_i).\,\hat{\boldsymbol{\tau}}_i\,\hat{\boldsymbol{\tau}}_i \qquad \textit{Equation 2.31}$$

- $\boldsymbol{F}_i^{S\parallel}$: Spring force

$$\boldsymbol{F}_i^{S\parallel} = k[(R_{i+1} - R_i) - (R_i - R_{i-1})].\,\hat{\boldsymbol{\tau}}_i \qquad \textit{Equation 2.32}$$

- $\hat{\boldsymbol{\tau}}_i$: Tangent at image i

$$\hat{\boldsymbol{\tau}}_i = \frac{R_{i+1} - R_{i-1}}{|R_{i+1} - R_{i-1}|} \qquad \textit{Equation 2.33}$$

The weakness of this method is that it could not reach the transition state directly but only an approximate geometry. Therefore, it is possible to use the "climbing image" NEB method[17]. In this method, the force on the image with highest energy is no longer present in *Equation 2.30* but as equation below:

$$\begin{aligned} \boldsymbol{F}_{i_{max}} &= -\nabla E(R_{i_{max}}) + 2\nabla E^{\parallel}(R_{i_{max}}) \\ &= -\nabla E(R_{i_{max}}) + \nabla E(R_{i_{max}}).\,\hat{\boldsymbol{\tau}}_{i_{max}}\,\hat{\boldsymbol{\tau}}_{i_{max}} \end{aligned} \qquad \textit{Equation 2.34}$$

It can be noticed that, this image is not submitted to spring forces. The climbing image moves up or down the potential energy surface along or perpendicular to the elastic

bond. Meanwhile the other images converge to the MEP with a good approximation to the reaction coordinate around the saddle point. When the CI-NEB converge, the climbing image will converge to the saddle point, consequently the Transition State will be found.

2.4 MOLECULAR DYNAMICS

Molecular dynamics (MD) is an efficient method for modelling systems at atomic level. Many effects that will modify the properties of modelled system can be included, for example solvent and physical parameter effects (ex: temperature). In order to define the temporal evolution of the atomic positions, a classical Newton's equation of motion is integrated depending on the forces acting on the atoms. These forces can be computed either at the classical or quantum level. Therefore, both equilibrium thermodynamic and dynamic properties of a system at finite temperature can be computed.

2.4.1 BORN-OPPENHEIMER MOLECULAR DYNAMICS

In order to combine electronic structure calculation with Molecular Dynamics, several approaches can be utilized: Ehrenfest[23], Born-Oppenheimer[24] and Car-Parrinello[25] molecular dynamics. In our work, Born-Oppenheimer approximation will be used. This approximation is based on classical molecular dynamics. In this method, each molecular dynamic step is considered as a static electronic structure problem. Hence at each time a set of fixed nuclear positions can be found. In this context, the electronic structure can be obtained by resolving the time-independent Schrödinger equation. For the electronic ground state, the Born–Oppenheimer molecular dynamics method is defined by the following equations.

$$M_I \ddot{\boldsymbol{R}}_I(t) = -\nabla_I \min_{\psi_0}\{\langle\psi_0|\mathcal{H}_e|\psi_0\rangle\}$$

Equation 2.35

$$\mathcal{H}_e\psi_0 = E_0\psi_0$$

Equation 2.36

- $\boldsymbol{R}_I$: Nuclear coordinates
- ψ_0 : Fundamental state
- $\mathcal{H}_e$: Electronic Hamiltonian

The Born-Oppenheimer Molecular Dynamics is a good approximation as equations of motion can be integrated on the time scale of nuclear motion. However, electronic structure problems have to be solved self-consistently at each molecular step. The bottle neck of the simulation is the time needed to solve the Schrödinger equation and to compute the forces acting on the atoms. However, this method is needed when the chemical bonds are formed or broken. A classical calculation, using empirical force fields is not adapted to the evolution of the chemical products.

2.4.2 VERLET ALGORITHM

The Verlet algorithm is commonly used to calculate the particles trajectories in molecular dynamics simulations. In this method, Newton's equations of motion will be integrated. Firstly, two third-order Taylor expansions for the positions $r(t)$ will be written, one forward and one backward in time.

$$r(t + \Delta t) = r(t) + v(t)\Delta t + \frac{a(t)}{2}\Delta t^2 + \frac{1}{3!}\frac{d^3 r}{dt^3}\Delta t^3 + \mathcal{O}(\Delta t^4) \qquad \text{Equation 2.37}$$

$$r(t - \Delta t) = r(t) - v(t)\Delta t + \frac{a(t)}{2}\Delta t^2 - \frac{1}{3!}\frac{d^3 r}{dt^3}\Delta t^3 + \mathcal{O}(\Delta t^4) \qquad \text{Equation 2.38}$$

Add *Equation 2.37* with *Equation 2.38* get the basic form of the Verlet algorithm.

$$r(t + \Delta t) + r(t - \Delta t) = 2r(t) + a(t)\Delta t^2 + \mathcal{O}(\Delta t^4) \qquad \text{Equation 2.39}$$

As here we integrate the Newton's equations of motion, so the acceleration $a(t)$ can be written by *Equation 2.40*.

$$a(t) = \frac{f}{m} \qquad \text{Equation 2.40}$$

Where the force is a function of the position $r(t)$.

$$a(t) = -\frac{\nabla V(r(t))}{m} \qquad \text{Equation 2.41}$$

It can be noticed that the velocity $v(t)$ is not shown in the basic form of Verlet algorithm (*Equation 2.39*). In fact, the velocity can be found derived from the trajectory:

$$v(t) = \frac{r(t + \Delta t) - r(t - \Delta t)}{2\Delta t} + \mathcal{O}(\Delta t^2) \qquad \text{Equation 2.42}$$

2.4.3 ENSEMBLE AND THERMOSTAT

In molecular dynamic simulation, three main canonical ensembles are defined:

- Micro-canonical ensemble: NVE in which E is constant.
- Canonical ensemble: NVT in which T is constant.
- Isothermal-isobaric ensemble: NPT in which P and T are constant.

In our Molecular dynamic calculation, canonical ensemble is used, hence thermostat is operated in order to maintain constant temperature in our system. The temperature of a molecular system can be defined by instantaneous kinetic energy. The temperature can be carried out by following expression.

$$T = \frac{\sum_{i=1}^{N} m_i v_i^2}{3NK_B}$$ *Equation 2.43*

- m_i: Masse of particle i
- v_i: Velocity of particle i

The Nosé-Hoover thermostat[26–28] is a good thermostat for canonical ensemble. The equation of motion can be represented in following form:

$$\frac{d\vec{r}_i}{dt} = \frac{\vec{p}_i}{m_i}$$ *Equation 2.44*

$$\frac{d\vec{p}_i}{dt} = \vec{F}_i - \varepsilon * \vec{p}_i$$ *Equation 2.45*

$$\dot{\varepsilon} = \frac{1}{Q}\left[\sum_{i=1}^{N} \frac{p_i^2}{m_i} - D_f k_B T_0\right]$$ *Equation 2.46*

- $\vec{p}_i$: Momentum of the atom i
- D_f: Number of degrees of freedom
- T_0: Temperature of the thermostat
- Q: Adjustable parameter called virtual mass

ε is identical for all the particles in the system. ε increase when the temperature of the system is higher than the thermostat (T_0), on the other hand, it will decrease when the instantaneous temperature of the system is lower than T_0. Q is the parameter who will fix the oscillation frequency of the temperature.

2.5   APPLICATION IN OUR WORK

2.5.1 GEOMETRY OPTIMIZATION

All calculations are performed within the Density Functional Theory (DFT) framework using the Generalized Gradient Approximation (GGA) of Perdew, Burke and Ernzerhof (PBE) [7]. The Vienna Ab-initio Simulation Package (VASP)[29,30] was used to solve the Kohn-Sham equations[3]. The electron wave functions were expanded on a plane-wave basis set with an energy cut-off of 600 eV. The electron–ion interactions were described within the Projector Augmented Waves (PAW) approach[10]. For the calculation of a small cell (a ≈ 5 Å; b ≈ 5 Å; c = 35 Å), a (5 5 1) k-points mesh was used. And for a bigger cell (a ≈ 10 Å; b ≈ 10 Å; c = 35 Å), a (3 3 1) k-points mesh was used. For a transition metal, the Coulomb repulsion for electrons located in a 3d orbital is not correctly described in a spin polarized treatment of DFT, therefore a DFT+U approach will be used to solve the problem.[31,32] The Value of U is equal to 4 eV for Fe and Cr with J equal to 1 eV in both cases. The Kohn-Sham equations were solved self-consistently until energy difference between cycles become lower than 10^{-4} eV. The atomic positions have been fully optimized until all forces applying on the atoms were smaller than 0.03 eV/ Å per atom.

For molecular dynamic simulations, Born–Oppenheimer molecular dynamic simulations were carried out in the canonical NVT ensemble, the temperature was controlled by a Nosé–Hoover thermostat[26,27] around 450K. A time step of 1 fs was utilized for motion equation.

2.5.2 ENERGY AND THERMODYNAMIC CALCULATION

For the adsorbed molecules, various optimized structures were compared and their adsorption energies compared. The adsorption energy per molecule is calculated by the equation below (*Equation 2.47*). Furthermore, a negative adsorption energy corresponds to an exothermic adsorption.

$$E_{ads} = \frac{E_{total} - E_{surface} - (E_{adsorbate} \times n_{adsorbate})}{n_{adsorbate}} \qquad \textit{Equation 2.47}$$

The Gibbs energy is defined in terms of a system's enthalpy and entropy as below:

$$G = H - TS$$

Equation 2.48

At constant temperature and pressure, the energy change (ΔG) may be written as following:

$$\Delta G = \Delta H - T\Delta S$$

Equation 2.49

It can be noticed that it varies with temperature. For a given temperature, the Gibbs energy for an equation can be described by following expression.

$$\Delta G(T) = \sum_i v_i \Delta G(i, T)$$

Equation 2.50

- v_i: the stoichiometric coefficients of the species i of the reaction

For a reaction taking place at 0 K the enthalpy change is simply the electronic energy change at 0 K[33]:

$$\Delta H(0K) \approx \Delta E_{total}^{0K}$$

Equation 2.51

Our calculation are running at 0 K, hence the Gibbs energy can be presented as below:

$$\Delta G(0K) = \Delta E_{total}^{0K}$$

Equation 2.52

Combining *Equation 2.50* and *Equation 2.52*:

$$\Delta G(T) = \Delta E_{total}^{0K} + \sum_i v_i G_{corr}(i, T)$$

Equation 2.53

Our study mainly focusses on interactions between a solid surface and molecules in the gas phase. For a solid, its Gibbs energy will not change, as its volume is fixed for different temperatures under different pressures. Only the thermodynamic corrections of the Gibbs energy for adsorbed molecules will be calculated using the Gaussian[34] program which is based on statistical thermodynamic for a perfect gas. The correction to the internal thermal energy and thermal correction to enthalpy and Gibbs energy are calculated by following enquations.[35]

$$\varepsilon_{tot} = \varepsilon_t + \varepsilon_r + \varepsilon_v + \varepsilon_e$$

Equation 2.54

furthermore

$$H_{corr} = \varepsilon_{tot} + k_B T$$

Equation 2.55

and

$$G_{corr} = H_{corr} - T S_{tot}$$

Equation 2.56

where

$$S_{tot} = S_t + S_r + S_v + S_e$$

Equation 2.57

REFERENCES

(1) Koch, W.; Holthausen, M. C. *A Chemist's Guide to Density Functional Theory*, 2nd ed.; Wiley-VCH, 2001.

(2) *Methods of Electronic Structure Theory*; Schaefer, H. F., Ed.; Springer US: Boston, MA, 1977.

(3) Kohn, W.; Sham, L. J. Self-Consistent Equations Including Exchange and Correlation Effects. *Phys. Rev.* **1965**, *140* (4A), A1133–A1138.

(4) Slater, J. C. A Simplification of the Hartree-Fock Method. *Phys. Rev.* **1951**, *81* (3), 385–390.

(5) Dirac, P. A. M. Note on Exchange Phenomena in the Thomas Atom. *Math. Proc. Cambridge Philos. Soc.* **1930**, *26* (03), 376.

(6) Ceperley, D. M.; Alder, B. J. Ground State of the Electron Gas by a Stochastic Method. *Phys. Rev. Lett.* **1980**, *45* (7), 566–569.

(7) Perdew, J. P.; Burke, K.; Ernzerhof, M. Generalized Gradient Approximation Made Simple. *Phys. Rev. Lett.* **1996**, *77* (18), 3865–3868.

(8) Becke, A. D. Density-Functional Exchange-Energy Approximation with Correct Asymptotic Behavior. *Phys. Rev. A* **1988**, *38* (6), 3098–3100.

(9) Payne, M. C.; Teter, M. P.; Allan, D. C.; Arias, T. A.; Joannopoulos, J. D. Iterative Minimization Techniques for Ab Initio Total-Energy Calculations: Molecular Dynamics and Conjugate Gradients. *Rev. Mod. Phys.* **1992**, *64* (4), 1045–1097.

(10) Kresse, G.; Joubert, D. From Ultrasoft Pseudopotentials to the Projector Augmented-Wave Method. *Phys. Rev. B* **1999**, *59* (3), 1758–1775.

(11) Blöchl, P. E. Projector Augmented-Wave Method. *Phys. Rev. B* **1994**, *50* (24), 17953–17979.

(12) Liechtenstein, A. I.; Anisimov, V. I.; Zaanen, J. Density-Functional Theory and Strong Interactions: Orbital Ordering in Mott-Hubbard Insulators. *Phys. Rev. B* **1995**, *52* (8), R5467–R5470.

(13) Dudarev, S. L.; Botton, G. A.; Savrasov, S. Y.; Humphreys, C. J.; Sutton, A. P. Electron-Energy-Loss Spectra and the Structural Stability of Nickel Oxide: An LSDA+U Study. *Phys. Rev. B* **1998**, *57* (3), 1505–1509.

(14)   Eyring, H. The Activated Complex in Chemical Reactions. *J. Chem. Phys.* **1935**, *3* (2), 107–115.

(15)   Jensen, F. *Introduction to Computational Chemistry*; John Wiley & Sons, Ltd.: USA, 2007.

(16)   Sheppard, D.; Terrell, R.; Henkelman, G. Optimization Methods for Finding Minimum Energy Paths. *J. Chem. Phys.* **2008**, *128* (13).

(17)   Henkelman, G.; Uberuaga, B. P.; Jónsson, H. Climbing Image Nudged Elastic Band Method for Finding Saddle Points and Minimum Energy Paths. *J. Chem. Phys.* **2000**, *113* (22), 9901–9904.

(18)   Henkelman, G.; Jónsson, H. Improved Tangent Estimate in the Nudged Elastic Band Method for Finding Minimum Energy Paths and Saddle Points. *J. Chem. Phys.* **2000**, *113* (22), 9978–9985.

(19)   Villarba, M.; Jónsson, H. Diffusion Mechanisms Relevant to Metal Crystal Growth: Pt/Pt(111). *Surf. Sci.* **1994**, *317* (1–2), 15–36.

(20)   Villarba, M.; Jónsson, H. Atomic Exchange Processes in Sputter Deposition of Pt on Pt(111). *Surf. Sci.* **1995**, *324* (1), 35–46.

(21)   Maeda, S.; Morokuma, K. Finding Reaction Pathways of Type A + B → X: Toward Systematic Prediction of Reaction Mechanisms. *J. Chem. Theory Comput.* **2011**, *7* (8), 2335–2345.

(22)   Keith, J. A.; Jerkiewicz, G.; Jacob, T. Theoretical Investigations of the Oxygen Reduction Reaction on Pt(111). *ChemPhysChem* **2010**, *11* (13), 2779–2794.

(23)   Ehrenfest, P. Bemerkung Über Die Angenäherte Gültigkeit Der Klassischen Mechanik Innerhalb Der Quantenmechanik. *Zeitschrift für Phys.* **1927**, *45* (7–8), 455–457.

(24)   Born, M.; Oppenheimer, R. Zur Quantentheorie Der Molekeln. *Ann. Phys.* **1927**, *389* (20), 457–484.

(25)   Car, R.; Parrinello, M. Unified Approach for Molecular Dynamics and Density-Functional Theory. *Phys. Rev. Lett.* **1985**, *55* (22), 2471–2474.

(26)   Nosé, S. A Unified Formulation of the Constant Temperature Molecular Dynamics Methods. *J. Chem. Phys.* **1984**, *81* (1), 511–519.

(27) Hoover, W. G. Canonical Dynamics: Equilibrium Phase-Space Distributions. *Phys. Rev. A* **1985**, *31* (3), 1695–1697.

(28) Evans, D. J.; Holian, B. L. The Nose–Hoover Thermostat. *J. Chem. Phys.* **1985**, *83* (8), 4069–4074.

(29) Kresse, G.; Furthmüller, J. Efficiency of Ab-Initio Total Energy Calculations for Metals and Semiconductors Using a Plane-Wave Basis Set. *Comput. Mater. Sci.* **1996**, *6* (1), 15–50.

(30) Kresse, G.; Hafner, J. *Ab Initio* Molecular-Dynamics Simulation of the Liquid-Metal–amorphous-Semiconductor Transition in Germanium. *Phys. Rev. B* **1994**, *49* (20), 14251–14269.

(31) Rollmann, G.; Rohrbach, A.; Entel, P.; Hafner, J. First-Principles Calculation of the Structure and Magnetic Phases of Hematite. **2004**, 1–12.

(32) Rohrbach, A.; Hafner, J.; Kresse, G. Ab Initio Study of the (0001) Surfaces of Hematite and Chromia : Influence of Strong Electronic Correlations. **2004**, *125426* (0001), 1–17.

(33) Lewars, E. G. *Computational Chemistry*; Springer Netherlands: Dordrecht, 2011; Vol. 116.

(34) Frisch, M. J.; Trucks, G. W.; Schlegel, H. B.; Scuseria, G. E.; Robb, M. A.; Cheeseman, J. R.; Scalmani, G.; Barone, V.; Petersson, G. A.; Nakatsuji, H.; et al. Gaussian16 Revision B.01. 2016.

(35) Ochterski, J. W.; Ph, D. Thermochemistry in Gaussian. **2000**, 1–19.

CHAPTER 3   REACTIVITY OF IODINE ON SURFACE NUCLEAR REACTOR COOLANT SYSTEM

U nder severe accident conditions, part of the iodine presented in the RCS is under metal iodide aerosols (e.g. AgI, CdI_2, etc.) or under of gaseous iodine ($I_{2(g)}$).[1] Iodinated aerosols or condensed vapours are deposited on the RCS surface consisted of 304L stainless steel tubes.[2] In this chapter, the adsorption of control rods metal iodide (AgI and CdI_2) on chromium and iron oxide surface will be detailed. Additionally, the formation of volatile species ($I_{2(g)}$) from adsorbed surfaces will be discussed.

3.1 LITERATURE REVIEW ON IODINE

As mentioned in Chapter I section 1.3, ^{131}I is one of the most important radionuclides regarding the radiation dose received by the exposed population.[3] It could be easily concentrated into humans' thyroid. Iodine can be found under different forms in the reactor: metal iodide (for example: AgI and CdI_2) or volatile Iodine ($I_{2(g)}$).

3.1.1 PHYSICAL PROPERTIES OF IODINE AND METAL IODIDE

The silver–indium–cadmium control rod alloy is used in PWRs, and contains ~80%$_{wt}$ of silver, 15%$_{wt}$ of indium and 5%$_{wt}$ of cadmium.[4] These elements can be released in case of failure of the control rod and in a lesser extent as fission products. They are important as they can react with fission products such as iodine. First of all, the physics properties of metal iodide (AgI and CdI_2) and molecular iodine ($I_{2(g)}$) that will be studied in our work, will be introduced. Several isotopes exist for iodine. Only one isotope (^{127}I) is stable in nature. Other artificial isotopes have mass numbers ranging from 108 to 141. The commonly used radioactive tracer elements are: ^{123}I ($t_{1/2}$ = 13.27 h, electron capture decay), ^{125}I ($t_{1/2}$ = 59.408 d, electron capture decay), ^{129}I ($t_{1/2}$ = 1.57×10^{7}y, β decay), ^{131}I ($t_{1/2}$ = 8.02070 d, β$^-$ decay).[5]

3.1.1.1   PHYSICAL PROPERTIES OF IODINE

At room temperature, iodine (I_2) is a bluish-black and lustrous solid[6] with an irritating odour[5]. Its melting point is equal to 113.7 °C and its boiling point is equal to 184.4 °C. Its vapour is violet with a density equal to 6.75 g/L at 101.3 MPa. Iodine is not very soluble in pure water (with 0.03 g per 100 g water at 20 °C)[6], however, its solubility in organic solution is fairly high (for example at 25°C: in CCl_4 19.2 g/kg, in ether 337.3 g/kg, in ethanol 27.1 g/kg, in benzene 164.0 g/kg and in toluene 182.5 g/kg).[7] Models of Iodine (I_2) under different forms are shown in **Figure 3.1**. The solid iodine is in an orthorhombic structure (C_{mca}). The volatile iodine is in a diatomic form with a distance between two iodine atoms equal to 2.66 Å.
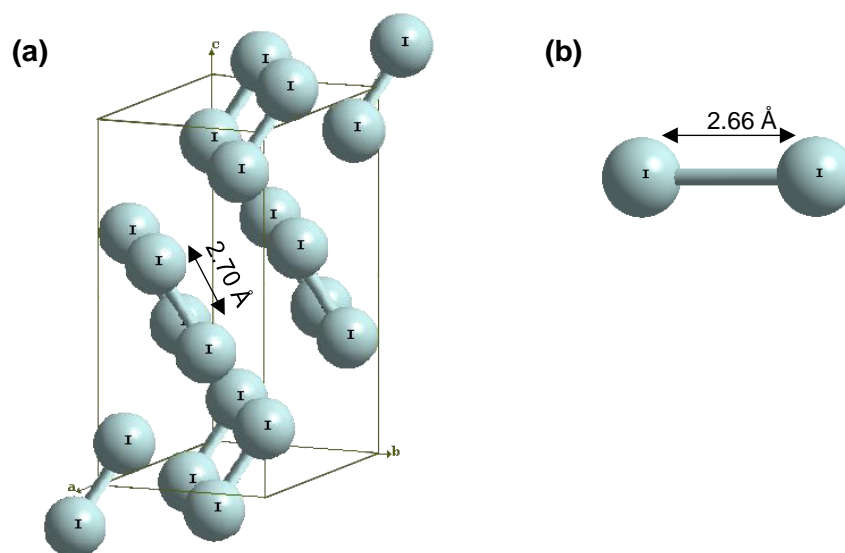
Figure 3.1. Iodine molecule (I_2) in (a) solid form and (b) gas form.

3.1.1.2   PHYSICAL PROPERTIES OF SILVER IODIDE

Silver iodide (AgI) is a yellow solid with a density equal to 5.68 g.cm^{-3} and its melting point is equal to 558 °C meanwhile its boiling point is equal to 1506 °C.[6] It is not soluble in water (28×10^{-7} g/L at 25°C; 25×10^{-6} g/L at 60°C) and most acids.[8] At ambient temperature, silver iodide crystallize in its β-phase with a hexagonal Wurtzite structure (**Figure 3.2** (a) and (b)) in which AgI form six member rings. Above 420 K (147 °C), its α-phase becomes more stable with a body-centred cubic structure (zinc blende) and has the silver centre cations are distributed randomly.[9] The gas form of AgI is represented in **Figure 3.2** (c). The distance between Ag and I atom is equal to 3.39 Å.
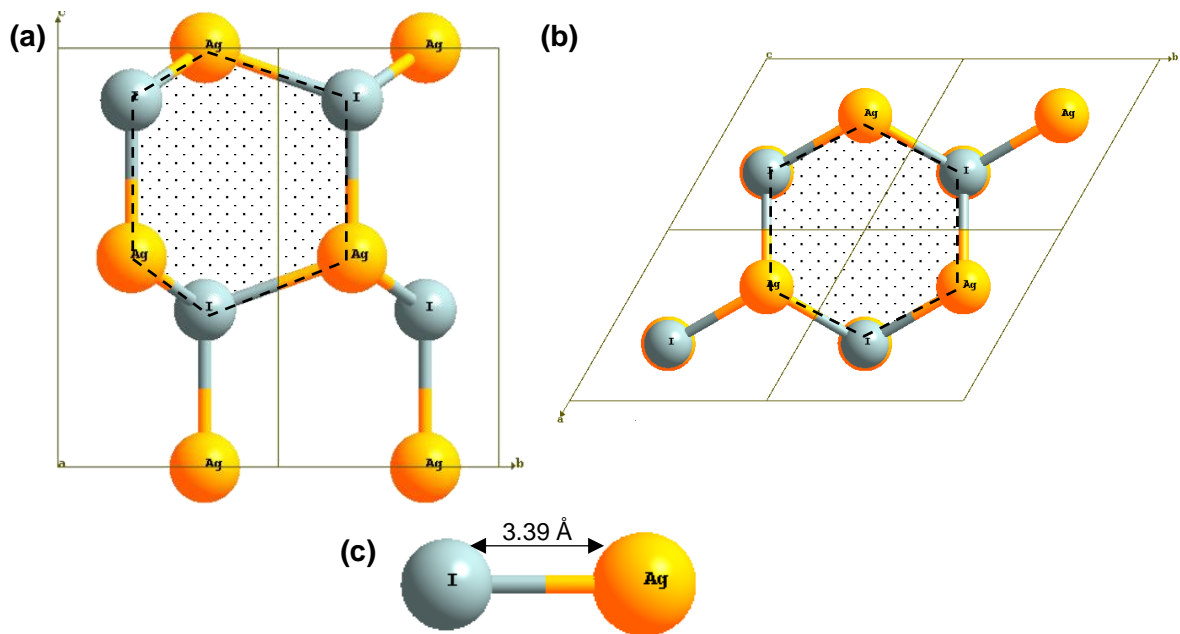
Figure 3.2. Silver iodide (AgI): (a) β-phase solid form (side view) (b) β-phase solid form (top view); (c) gas form.

3.1.1.3   PHYSICAL PROPERTIES OF CADMIUM IODIDE
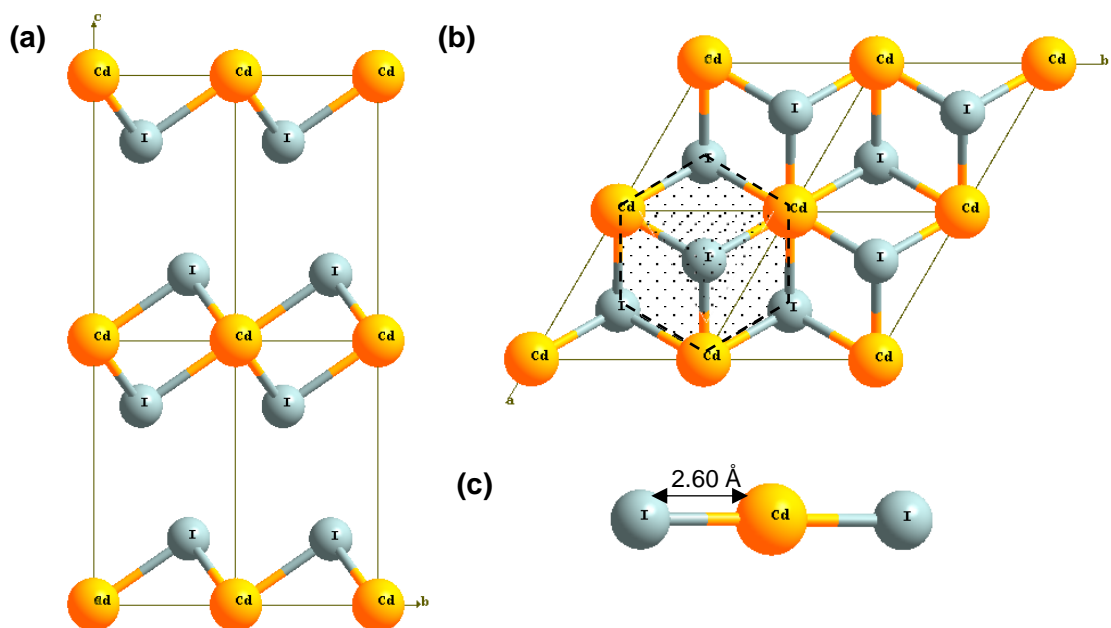
Figure 3.3. Cadmium iodide (CdI_2) molecule: (a) solid form (side view) (b) solid form (top view); (c) gas form.

Cadmium iodide is a stable pearly white or bright white solid which is often found under hexagonal pads form.[10] Its density is equal to 5.64 g.cm^{-3} and its melting point is equal to 387 °C, meanwhile its boiling point is equal to 742 °C.[6] Cadmium iodide is very

I,

soluble in the water (86.2 g at 25 °C and 125 g at 100 °C for 100 g of water) and its solubility in alcohol is even higher (110.5 g at 20 °C for 100 g ethanol and 206.7 g at 25 °C for 100 g methanol).[6,11] Models for cadmium iodide (CdI_2) are shown in **Figure 3.3**. Layers of CdI_2 are represented in the solid form (**Figure 3.3** (a)) with a ring structure (**Figure 3.3** (b)). The Cd-I bonds are mainly ionic with a character partially covalent. The distance between Cd and I atoms is equal to 2.60 Å for CdI_2 gas.[12]

3.1.1.4   OVERVIEW

In conclusion, control rods metal iodide (AgI or CdI_2) can form 6 member rings structures in their solid states. The three compounds which will be studied in this chapter (AgI, CdI_2 and I_2) are in gas form at high temperature (above 1500 °C). Pressure evolution of saturation vapour for different compounds that contain iodine is presented in **Figure 3.4**.[13] It is shown that silver iodide (AgI) is the most condensable iodine species among considered compounds.
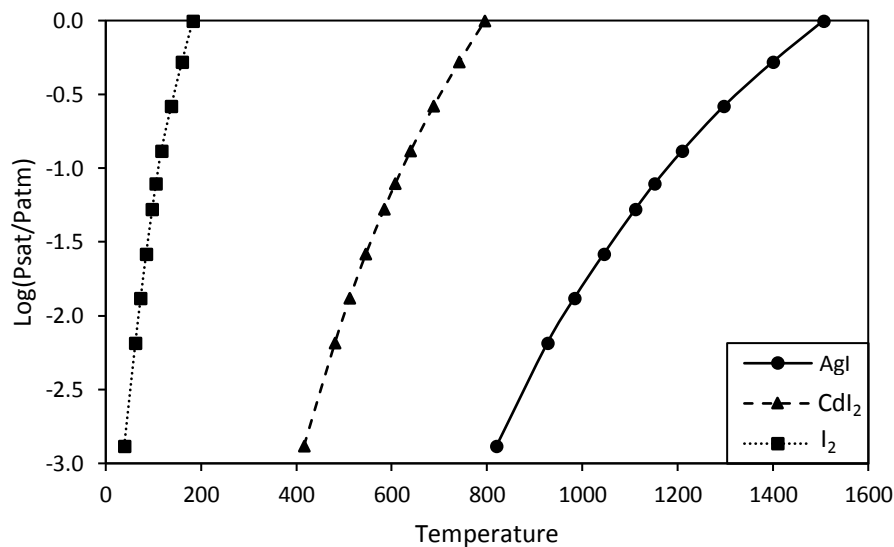
Figure 3.4. Pressure evolution of the saturation vapour of AgI (line, circle) CdI_2 (short line, triangle) and I_2 (point, square).[13]

3.1.2 BEHAVIOUR OF IODINE AND METAL IODIDE IN SEVERE ACCIDENT CONDITIONS

Behaviours of molecular iodine and metal iodides in severe accident conditions have been discussed for a long time. They have been studied firstly by US Nuclear Regulatory Commission[14]. Their behaviours will depend on the accidental conditions: temperatures, pressures, flows and reactions with various materials.[2] For example,

molecular iodine can form organic and inorganic species during a severe accident. These compounds can be released directly in gas form. Or else, some of them can interact with the surface of the coolant system and be deposited on it. Aerosols that reach the nuclear containment settle in the liquid phase to form iodide (I^-) which can be oxidized into molecular iodine ($I_{2(g)}$). In this section, literature on chemical behaviours of iodine and metal iodides will be reviewed into two parts: liquid phase behaviours and gas phase behaviours.

3.1.2.1   LIQUID PHASE BEHAVIOURS

In case of a nuclear accident, a large amount of iodine and metal iodides may be released into liquid phase. Even though, iodine is not very soluble in water (Chapter III, Section 3.1.1.1), some metal iodides are soluble in water (ex: CdI_2). So understanding of chemical behaviours of iodine and metal iodides in the liquid phase is important.

3.1.2.1.1   Chemistry of Iodine under Radiation

In 1980, Lin firstly studied the chemistry of iodine ions in aqueous solution under high intensity gamma-rays at ambient temperature.[15] He found that iodide ions can be easily oxidized to I_2 at higher concentration of I^- and low pH. He proposed the following reaction schemes:

$$I^- + OH \rightarrow I + OH^-$$
$$I + OH \rightarrow HIO$$
$$I + I \rightarrow I_2$$
$$I^- + HIO + H^+ \rightarrow I_2 + H_2O$$
$$I_2 + H_2O \rightarrow H^+ + I^- + HIO$$
$$HIO + n\ OH(\text{successive oxidation}) \ \rightarrow\ IO_3{}^-$$
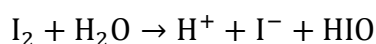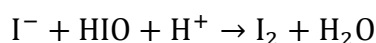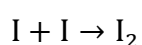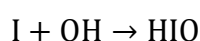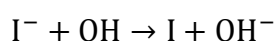
J-W. Yeon *et al.*[16] have concluded that the iodine formation from I^- ion started by its oxidation to $I_{2(g)}$ by $HO^\bullet$ formed by gamma radiation and is followed by its release in air (**Figure 3.5**). They studied the temperature effect on these steps. They found that, with the augmentation of temperature, the rate of first step (gamma oxidation) decrease while the rate for the second step (evaporation of I_2) increase.
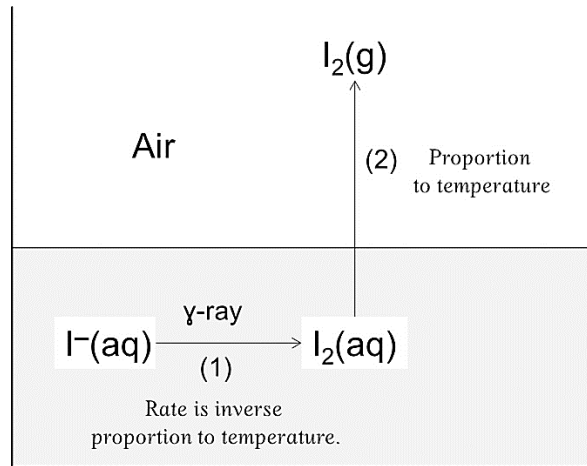
Figure 3.5. Paths of iodine from I^- ion dissolved in solution to $I_{2(g)}$ in the air.[16]

3.1.2.1.2 *Iodine reactions with silver*

Iodine in cooling systems may react with silver. A mechanism of this reaction has been proposed by Furrer *et al.*[17]:

$$I_2 + 2\,Ag \rightleftharpoons 2\,AgI \qquad\qquad \textit{Equation 3.1}$$
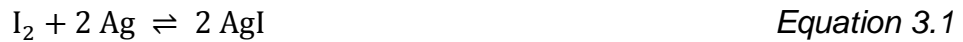
They calculated the forward and reverse rate constant for this reaction ($k_{forward}$ =1 mol^{-1}.L^{-1}.s^{-1} and $k_{reverse}$ =10^{-10} mol^{-1}.L^{-1}.s^{-1})[17]. Hence the formation of I_2 from AgI in the liquid phase is not kinetically favourable.

3.1.2.2 GAS PHASE BEHAVIOURS

In accidental conditions, temperature can be very high in the reactor (up to 2000°C), therefore, iodine behaviour in gas phase is of great importance. Iodine and metal iodides can be released from the primary system or from molten core debris. They can remain airborne or can deposit on surfaces, dissolve in sprays or be otherwise transferred to liquid.[2] Inside the reactor coolant system (RCS), gas phase reactivity is of prime importance or with RCS surface (stainless steel).

3.1.2.2.1 *Effect of Cadmium in Transport of Iodine*

Cadmium is released primarily in case of failure of the control rod.[18] In the reactor coolant system (RCS), cadmium can be expected as: metal (Cd), oxide (CdO), hydroxide (Cd(OH)$_2$) or even may form cadmium iodide (CdI$_2$) in case of reaction with iodine compounds.[19,20] Experimentally, M. Gouëllo *et al.*[20] found that cadmium may play an important role in transport of iodine in RCS. They heat metallic cadmium and

caesium iodide in a crucible under three different atmospheres (different percentages of argon, steam and hydrogen gases) at a temperature lower than 400 °C. By adding caesium iodide and cadmium at the same time, they observed that iodine was retained in the crucible by possible formation of a Cd-I compound when there is no hydrogen or only a very small amount of hydrogen gas. L. Bosland and L. Cantrel[21] have simulated the Cd-Cs-I-Mo-H$_2$O gaseous system in order to understand the iodine transport through the RCS in presence of control rod metals. Under oxidant and reducing conditions, the formation of CdI$_2$ is limited. The system does not reach thermodynamic equilibrium. Kinetic limitations will determine the exact composition of the gaseous phase. Hence, it is interesting to understand the reaction pathway of CdI$_2$ formation.

3.1.2.2.2   *Gas Phase Deposition onto Aerosols*

Aerosols are very small solid particles or liquid droplets suspended in a gas phase. The particles size ranges between 0.01-20 μm.[22] Many reactions may occur on their surfaces. H.J Allelein *et al.*[22] have reviewed aerosol physics processes. In severe nuclear accident, the aerosol formation is the main mechanism by which fission products would be transported inside the reactor coolant system (RCS). They are formed by the material volatilized in the core. Then, they are carried out to lower temperature regions and grow up by vapour condensation and agglomeration. Many experimental experiences and theoretical studies have been performed on this process.[23–27] H. Hijazi[28] has performed theoretical study on the adsorption of water on AgI aerosols and on the formation of I$_{2(g)}$ and IOH(g) with and without radical (OH$^\bullet$) in the gaseous phase. The interaction between AgI surfaces and water is very week which is coherent with the low solubility of AgI in water. The direct formation of volatile iodine species from AgI (110) surface is not possible. Moreover, the dissociation of water molecules on the surface is endothermic, consequently formation of HI is not favourable. However the formation of iodine species becomes favourable with the participation of oxidative species such as OH$^\bullet$ radical. The activation energy of the process is equal to 1.00 eV for the formation of I$_{2(g)}$ and 0.65 eV for the formation of IOH. The reaction pathway for the IOH formation in gas form is shown in **Figure 3.6**. Firstly, the surface is oxidized by two radical (OH$^\bullet$) (A→B). Then one iodine moves towards OH group and forms IOH on the top of the Ag atom (B→C). Afterwards, IOH on the surface is desorbed by breaking bond with iodine on the surface (C→D). In the

end, there is a displacement of OH group in order to fill the vacancy created by the missing iodine (D→E).
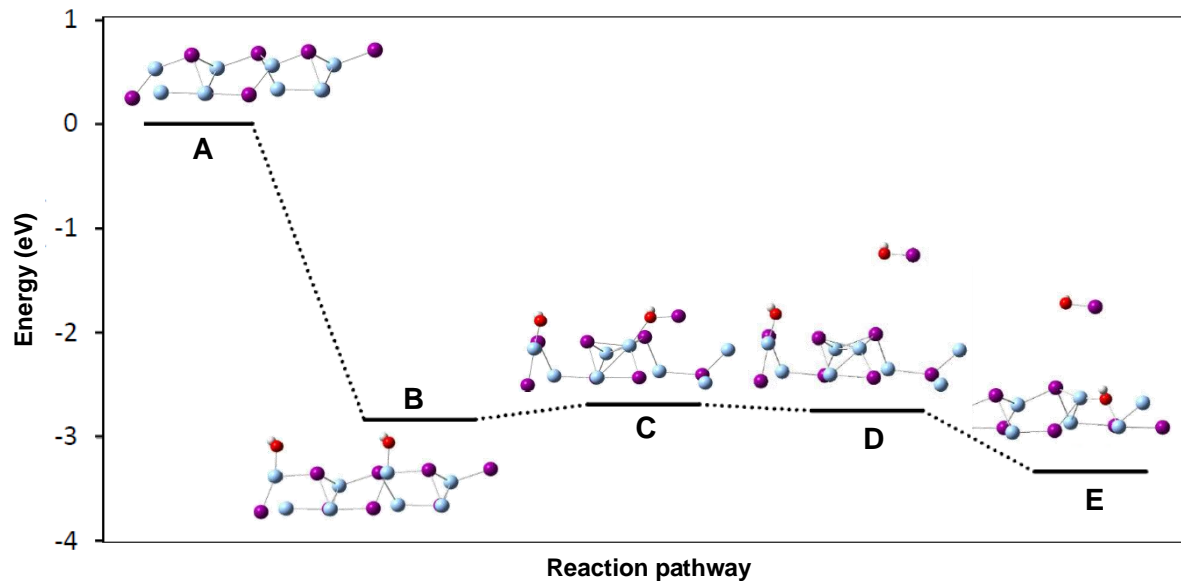
Figure 3.6. Reaction pathway leading to the formation of IOH including the oxidizing the surface twice with two OH• (Ag, I, H and O are respectively coloured in bright blue, purple, red and white).[28]

3.1.2.2.3   *Gas Phase Deposition onto RCS Surface*

An NEA Group of Experts[29] has defined the remobilization phenomena of fission products which can happen on the primary circuit surface and inside the containment building. They describe four steps: re-suspension, re-entrainment, re-vaporization and re-volatilization (**Figure 3.7**). The three former phenomena may occur on the reactor coolant system (RCS) surface. Resuspension means that aerosol or condensed materials that are deposited on the structure surface can be carried as fine fragments due to drag force generated by fluid flow. Re-vaporization of a compound may occur, at high temperature, when vapour pressure on the surface (equal to the saturation pressure) is larger than its partial pressure of surrounding gas. Re-entrainment describes the entrainment of dissolved or deposited chemical compounds as droplets by the boiling of liquid or by steam flashing.
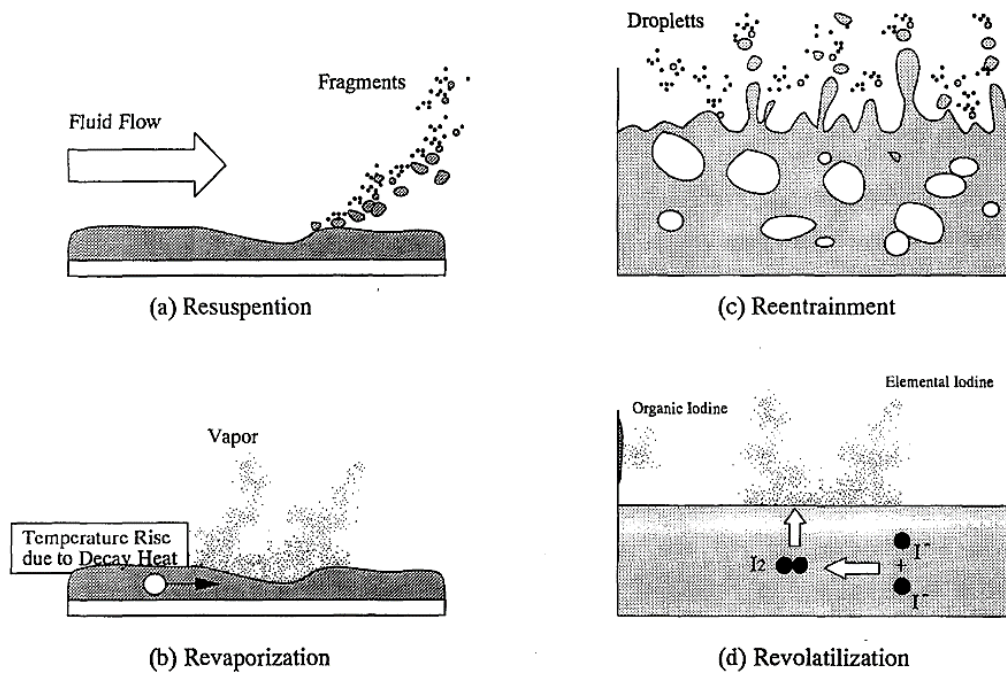
Figure 3.7. Transport behaviour by (a) Resuspension (b) Re-entrainment (c) Re-vaporization (d) Re-volatilization.[29]

The re-vaporization and resuspension of deposited fission product particles on the primary circuit surface have been considered as the main source term in late phase of fuel degradation in a severe nuclear accident.[30] Some studies have been done on this topic.[30–34] P.D.W. Bottomley *et al.*[30] have studied the re-vaporization of fission product deposits (Cs and I) in the primary circuit. By combining experimental and theoretical modelling studies, the detailed surface interaction and the reactivity of the deposited fission product can be better understood. They detailed re-vaporization of Cs and I on the stainless steel 304L surfaces.

D. Obada *et al.*[32,35] have studied the re-vaporization of CsI and AgI aerosols deposited on stainless steel, by combing ToF-SIMS and XPS, in order to simulate reactions that occur on the surface of RCS in severe accident condition. For the re-vaporization of CsI deposits, between 400 °C and 550 °C, the release of molecular iodine is very slow. At higher temperature (>550°C), the release of iodine is faster. So they supposed that CsI revolatilize from the surface as CsI species and then react with gas-phase molecules to form $I_{2(g)}$. The re-vaporization of AgI deposits was studied at a temperature lower or equal to 750°C under three conditions: synthetic air, argon/steam (%$_{vol.}$ 70/30) and air/steam (%$_{vol.}$ 20/80). The elementary composition of the remaining compounds on the surfaces, determined by XPS, after re-vaporization of AgI, are

displayed in **Table 3.1**. It depends on the gas composition. Under air, the atomic ratio Ag/I equal to 2.25 which means that there is a preferential re-vaporization of iodine as $I_{2(g)}$. Under argon/steam ($\%_{vol.}$ 70/30) condition, the presence of AgI on the surface after re-vaporization is very low (Ag 0.7 $\%_{at.}$ and I 0.3$\%_{at.}$) with an atomic ratio Ag/I equal to 2.3. Consequently, under this condition, even though only very few AgI remains on the surface after re-vaporization, the re-vaporization of $I_{2(g)}$ is expected. Under the third condition (air/steam $\%_{vol.}$ 20/80), an important re-vaporization of $I_{2(g)}$ can be noticed. Indeed, the surface is composed of 2.1 $\%_{at.}$ of Ag while only traces of iodine can be found ($\ll$0.01 $\%_{at}$). The shape of the TPD analysis depends on atmosphere composition: only one release pic for re-vaporization under synthetic air and two release pics under air/steam condition.

Table 3.1. Residual quantities of I, Ag, Mn, Cr and Fe after re-vaporization of AgI deposition in different atmospheric conditions (XPS quantitative analysis, %at.) after treatment at 750°C[35]

	Re-vaporization atmosphere		
	Synthetic air	Argon / steam (%vol. 70/30)	Air / steam (%vol. 20/80)
Iodine	1.6	0.3	$\ll$0.01
Silver	3.6	0.7	2.1
Manganese	2.7	17.4	9.6
Chrome	4.6	3.1	13.5
Iron	25.9	1.5	6.1

The ToF-SIMS profiles of Ag-containing ionic fragments for a re-vaporized cutting under three conditions at 750 °C are shown in **Figure 3.8**. Normally, this technique is very sensitive to isotopic element composition analysis. Conversely, from **Figure 3.8**, it can be noticed that there is some incoherent in this case with this technique which up to now have not been determined. For example, for argon/steam $\%_{vol.}$ 70/30 (**Figure 3.8** middle**)**, isotropies AgO$^+$ and ^{109}AgO$^+$ show in totally different evolution shape. However, the presence of AgI$^+$ and Ag^{109}AgO$^+$ on the surface under synthetic air can be observed. Therefore, theoretical study on these processes will be very useful in order to understand the chemistry of AgI on primary circuit surface.
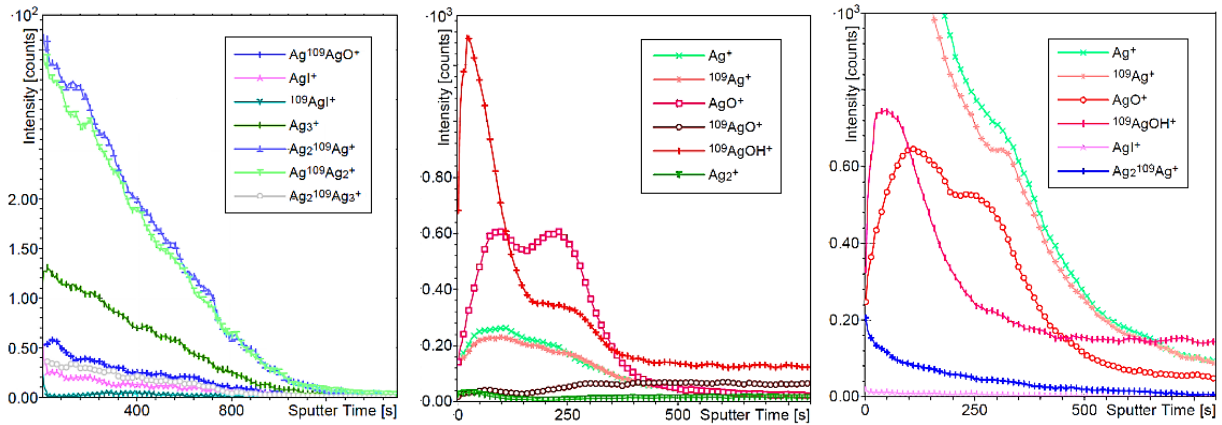
Figure 3.8. ToF-SIMS profiles of Ag-containing ionic fragments for a re-vaporized cutting under (left) synthetic air (middle) argon/steam (%vol. 70/30) (right) air/steam (%vol 20/80) at 750 °C.[35]

3.2 ADSORPTION OF AgI ON CHROMIUM AND IRON OXIDE SURFACES

In this chapter, theoretical study for the adsorption of control rods metals iodides (AgI and CdI$_2$) on the surface of the primary circuit and the mechanisms leading to the re-vaporization of these iodine deposits will be investigated in order to understand the influence of Ag and Cd onto the transport of iodine. First of all, the adsorption of AgI on the surface of the reactor coolant system (RCS) will be discussed. The section is divided into two parts: thermodynamic and reactivity.

3.2.1 THERMODYNAMIC STUDY

Firstly, AgI molecules were adsorbed on five different surfaces mentioned before (Chapter I section 1.5.2) in order to understand the adsorption of silver iodides on stainless steel surface and the formation of molecular iodine from these adsorbed surfaces: **Cr$_2$O$_3$Cr** (neutral chromium oxide surface), **Chromyl** (oxidized chromium oxide surface), **Cr$_2$O$_3$Cr$_2$(OH)$_3$** (hydrated chromium oxide surface), **Fe$_2$O$_3$Fe** (neutral iron oxide surface) and **Fe$_2$O$_3$HFe** (reduced iron oxide surface)[36,37]. The adsorption simulations are run under different coverages which can be described by equation below:

$$r = \frac{n_{AgI\ adsobed}}{n_{adsorbed\ sites}}$$

- ▪ $n_{AgI\ adsobed}$: Number of adsorbed AgI molecules.
- ▪ $n_{adsorbed\ sites}$: Number of Cr or Fe sites available for AgI adsorption.

The most stable structures of adsorbed AgI molecules on these five surfaces are classed by coverage (**Table 3.2**). It can be noticed that almost all stable structures are non-dissociative adsorptions, except the adsorption of AgI below 25% coverage on the chromyl surface. Hence, it can be concluded that the associative adsorption of AgI over these five oxide surfaces are more favourable than dissociative ones.

Table 3.2. Adsorption of AgI on chromium and iron oxide surfaces in function of its coverage. Chromium: green. Iron: blue. Oxygen: red. Hydrogen: light yellow. Silver: yellow. Iodine: grey.

	Model	AgI Coverage (%)		
		25	50	100
Cr	Cr$_2$O$_3$Cr			
	Chromyl			
	Cr$_2$O$_3$Cr$_2$(OH)$_3$			
Fe	Fe$_2$O$_3$Fe			
	Fe$_2$O$_3$HFe			

Furthermore, in order to compare the adsorption of AgI on different surfaces, the adsorption energy per AgI molecule adsorbed was summarized in **Table 3.3**. This

energy is calculated according to the equation mentioned in Chapter II Section 2.5.2 which can be written as below for adsorption of AgI:

$$E_{ads} = \frac{E_{total} - E_{surface} - (E_{AgI} \times n_{AgI})}{n_{AgI}}$$

with $E_{ads} < 0$, corresponding to an exothermic reaction.

Table 3.3. Adsorption energy per AgI, for different coverages, on chromium and iron oxide surfaces.

| | Model | AgI Coverage (%) | | |
		25	50	100
	Cr₂O₃Cr	-1.51 eV	-1.82 eV*	-1.81 eV*
Cr	**Chromyl**	-1.41 eV	-1.42 eV*	-1.63 eV*
	Cr₂O₃Cr₂(OH)₃	-1.21 eV	-1.51 eV*	-1.47 eV*
Fe	**Fe₂O₃Fe**	-1.93 eV	-2.15 eV*	-2.23 eV*
	Fe₂O₃HFe	-1.89 eV**	-1.62 eV**	-1.66 eV**

* AgI form a chain/a cycle, so the energy includes energy of formation of a chain/ a cycle and the interaction energy between the chain and the surface.
** Spin problem, these energies cannot be compared with the other adsorbed surfaces.
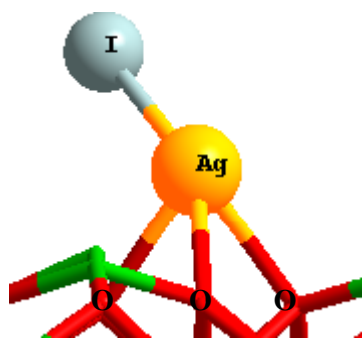
Figure 3.9. Tripod structure of AgI on the surface. Cr: green. O: red. Ag: yellow. I: grey.

For adsorption of AgI on **Cr₂O₃Cr** (neutral chromium oxide surface), the most stable structure of AgI on this surface is in tripod form (Ag-OOO, **Figure 3.9**) where silver atom is situated on the hollow site of the surface. At 25% coverage, AgI stays isolated on the surface with an adsorption energy equal to -1.51 eV. When the coverage increases (50% and 100%), AgI form a chain structure with a slight increase of adsorption energy due to the formation of the chain (-1.81 eV, with E adsorption AgI chain = -0.70 eV per adsorbed AgI).

On the **Chromyl** surface (oxidized chromium oxide surface), adsorption mode of AgI changes compared to the other surfaces. At 25% coverage, AgI is dissociated on the surface. The silver atom is situated between two terminal oxygen atoms and iodine atom is in bridging position between terminal oxygen atoms of surface (**Figure 3.10**). Its adsorption energy is weaker than the one for neutral surface (-1.41 eV).
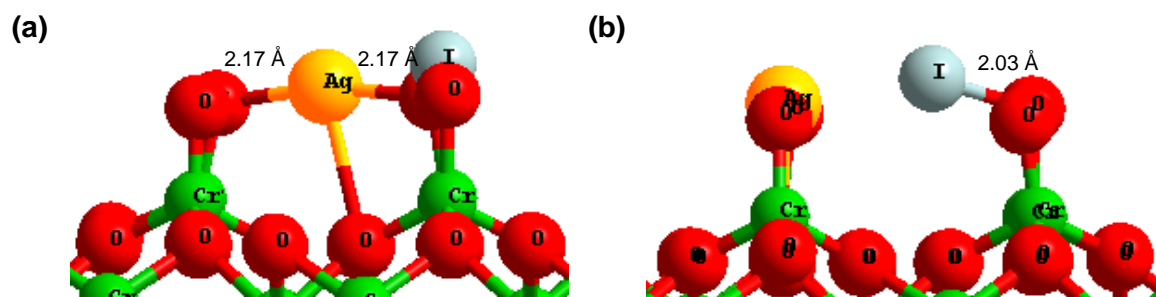
Figure 3.10. Side view adsorption of AgI on the Chromyl surface at 25% coverage (a) side $\overrightarrow{bc}$ (b) side $\overrightarrow{ac}$. Chromium: green. Oxygen: red. Silver: yellow. Iodine: grey.

When the coverage reaches to 50%, AgI forms a chain with a slight augmentation of adsorption energy (-1.42 eV, **Figure 3.11** a) which is probably due to the formation of Ag-I bond in the chain that compensates the reduction of the interaction with the surface (E $_{adsorption\ AgI\ chain}$ = - 0.30 eV per AgI adsorbed). When AgI coverage is equal to 100% on the Chromyl surface, AgI molecules form a cycle that is in epitaxy with the surface (**Figure 3.11** b), due to the formation of bonds between silver atoms and terminal oxygen atoms . Its adsorption energy is increased due to the formation of the cycle (-1.63 eV with E $_{adsorption\ AgI\ cycle}$ = - 0.19 eV per AgI adsorbed). This type of cycle structure has already observed in the solid structure of silver iodide (Chapter III, Section 3.1.1.2).
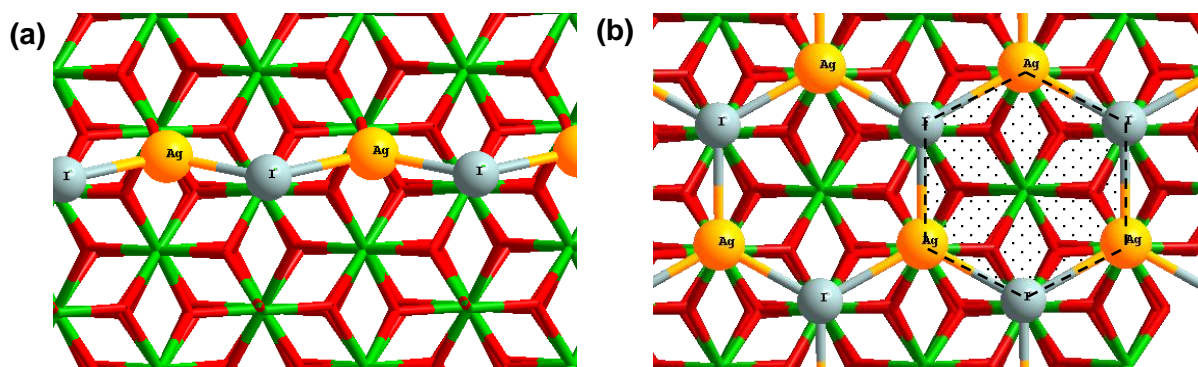
Figure 3.11. Top view for adsorption of AgI at (a) 50% (b) 100% coverage on the Chromyl surface. Chromium: green. Oxygen: red. Silver: yellow. Iodine: grey.

One the **Cr$_2$O$_3$Cr$_2$(OH)$_3$** surface (hydrated chromium oxide surface), at 25% coverage, AgI molecule is isolated on the surface with Ag atom present on hollow position (tripod structure (Ag-OOO)). Compared to other chromium oxide surfaces, its adsorption energy is less favourable (-1.21 eV). When the coverage increases to 50%, AgI molecules form a chain (**Figure 3.12** a). The distance between the chain and the

surface is about 2.5 to 3.5 Å. The adsorption energy no longer totally corresponds on adsorption of AgI, but also on the formation of AgI chain (-1.51 eV, E $_{adsorption\ AgI\ chain}$ = - 0.40 eV per AgI adsorbed). Half of Ag atoms still stay on the hollow position on the surface, meanwhile the others moved away from the hollow position and they do not form any bond with the surface. When coverage reaches 100%, AgI forms a ring structure (**Figure 3.12** b) with a formation energy equal to -1.47 eV (where E $_{adsorption}$ $_{AgI\ cycle}$ = - 0.04 eV per AgI adsorbed). In this case, no more Ag atom is staying on hollow position and no bond is formed with the surface. Comparing adsorption energy per AgI adsorbed on this surface with the other ones, it is fair to say that hydrated surface is less favourable for adsorption of AgI.
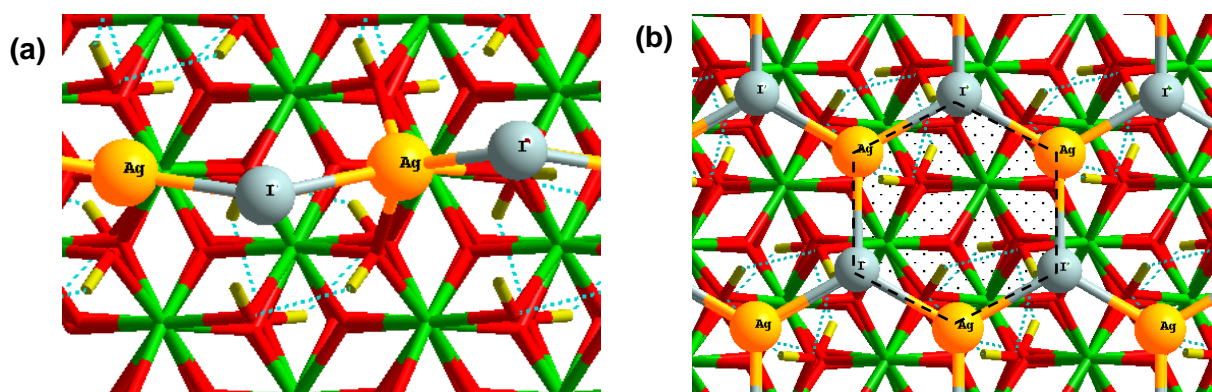
Figure 3.12. Top view for adsorption of AgI with (a) 50% (b) 100% coverage on the Cr$_2$O$_3$Cr$_2$(OH)$_3$ surface. Chromium: green. Oxygen: red. Silver: yellow. Iodine: grey. Hydrogen: light yellow.

Another hydrated surface with H$_2$O atoms adsorbed directly on chromium oxide was studied (**Figure 3.13** a). H$_2$O molecules are adsorbed on chromium oxide surface until a totally saturated surface is obtained where six water molecules are adsorbed. Thermodynamic stability of this surface has been discussed in recent study[36]. This surface (named Cr-O$_3$-H-Cr-OH-(H$_2$O)$_2$ in article[36]) is stable at ambient temperature with water partial pressure above 3 bars. The presence of water molecules on the surface does not prevent AgI to adsorb on the surface. In this case, the Ag atom is still present with a tripod structure on the surface (Ag-OOO, **Figure 3.13** b). The adsorption energy for 25% coverage of AgI on this surface is even slightly more favourable (-1.61 eV) compared to surface without presence of water (-1.51 eV on Cr$_2$O$_3$Cr surface). However, when coverage of AgI rises to 75% or 100%, this advantage does not exist anymore as water molecules adsorbed on the surface block the formation of bonds between some of AgI molecules and the surface (**Appendix** Figure A.1).

(a)

(b)
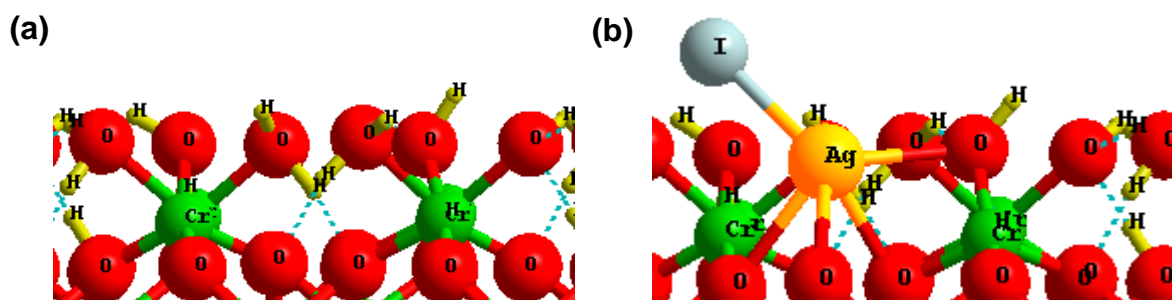
Figure 3.13. a) Totally saturated hydrate chromium oxide surface (with six water molecules). b) AgI adsorbed on totally saturated hydrate chromium oxide surface. Chromium: green. Oxygen: red. Silver: yellow. Iodine: grey. Hydrogen: light yellow.
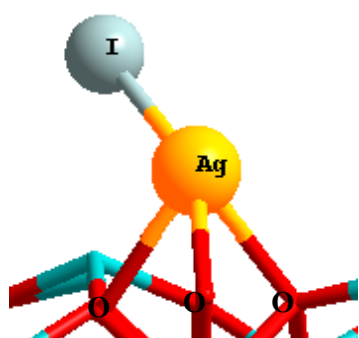
Figure 3.14. Tripod structure of AgI on the surface. Fe: Blue. O: red. Ag: yellow. I: grey.

On the **Fe_2O_3Fe** surface (neutral iron oxide surface), the AgI adsorbed in a geometry similar to the one on neutral chromium oxide surface (Cr_2O_3Cr). Silver atom is located in hollow position of the surface with a tripod structure (Ag-OOO, **Figure 3.14**) and remains isolated on the surface at 25% coverage. Furthermore, adsorbed AgI also forms a chain with higher coverage (50% and 100% with $E_{adsorption\ AgI\ chain}$ = -1.03 eV and -1.10 eV per AgI adsorbed). Overall, the adsorption energy is slightly higher than for neutral chromium oxide (Cr_2O_3Cr, -1.51 eV to -1.80 eV depending on the coverage) and range from -1.93 eV to -2.23 eV in function of number of AgI adsorbed.

On the **Fe_2O_3HFe** surface (reduced iron oxide surface) with coverage equal to 25%, the tripod structure of AgI (Ag-OOO) is still present on the surface. At higher coverage (50% and 100%), the presence of H atom on the surface avoids the formation of Ag-O bond with the surface. Therefore, a bipod structure (Ag-OO) presents on the surface with the formation of a chain (**Figure 3.15**). A spin problem has been encountered during the calculation, so it is not possible to compare its absorption energy directly with the one for other surfaces. This issue may be associated with the low probability of existence of this surface. **Therefore, we will not study this surface in following works.**

Figure 3.15. Bipod and chain structure of AgI on the surface. Fe: Blue. O: red. Ag: yellow. I: grey. H: light yellow.

In conclusion, at high coverage, AgI tends to form a chain or ring structure rather than isolated moieties on the surface. AgI adsorbs in same way on the neutral chromium oxide surfaces (Cr_2O_3Cr) and neutral iron oxide surface (Fe_2O_3Fe) with similar adsorption energy. From an energetic point of view, adsorption on neutral surfaces are more stable than adsorption on modified surfaces (oxidized or hydrated). It can also be noticed that the adsorption energy on iron oxide surface is more favourable than on chromium oxide surface. It may be noticed that the surface of oxidized chromium oxide (Chromyl), will favour the oxidation of I^- into I_2. The chemistry of this surface will be studied in the next part.

A *bader*[38] analysis of the electronic density has been performed in order to get a better understanding of the AgI interaction with the surface. For most of our models (**except** Chromyl surface), silver and iodine atoms stay in ionic state (Ag^+ and I^-), and the electron distribution on the surfaces is almost unchanged compared to bare surfaces (spin differences below to 0.1). For **Chromyl** surface, with indirect connection between chromium atoms of the surface and adsorbed AgI molecules by terminal oxygen atoms, there is an exchange of electrons between surface and adsorbed species. Chromium atoms on the top of the surface show an important variation of spin (0.5 - 0.9) according to the number of AgI adsorbed on the surface. As the surface has been peroxided, AgI molecules can make exchange of electrons with the surface much easier.

3.2.2 REACTIVITY STUDY

As mentioned in previous chapter, during a nuclear accident, iodine could be liberated as gaseous iodine $I_{2(g)}$ and it may impact the iodine source term, hence, the formation of $I_{2(g)}$ and **$AgI_{(g)}$** from adsorbed surface will be studied in this section. Furthermore, the formation of **$Ag_{(s/g)}$** on adsorbed surface has also been discussed, in order to compare its formation with the iodine one. In **Table 3.4**, formation energies for $I_{2(g)}$ and **$Ag_{(s/g)}$** and sublimation energy of **$AgI_{(g)}$** on the three most interesting surface models are reported. All the calculations are based on most stable structures with different AgI coverages.

Table 3.4. Formation energy of $I_{2(g)}$ and Ag $_{(s/g)}$ and sublimation energy of AgI(g) from different surface models with AgI adsorbed.

	N°	Reaction	Surface Model	ΔE (eV)
Formation $I_{2(g)}$	1	Surface-AgI ➔ Surface-Ag + ½ I_2(g)	Cr_2O_3Cr	2.36
			Chromyl	0.20
			Fe_2O_3Fe	2.13
	2	Surface-2AgI ➔ Surface-2Ag + I_2(g)	Cr_2O_3Cr	5.41
			Chromyl	0.71
			Fe_2O_3Fe	4.67
	3	Surface-4AgI ➔ Surface-4Ag + 2 I_2(g)	Cr_2O_3Cr	10.63
			Chromyl	3.09
			Fe_2O_3Fe	9.06
Formation Ag $_{(s/g)}$	4	Surface-2AgI ➔ Surface-2I + 2 Ag(s)	Cr_2O_3Cr	0.04
			Chromyl	1.25
			Fe_2O_3Fe	1.33
	5	Surface-2AgI ➔ Surface-2I + 2 Ag(g)	Cr_2O_3Cr	3.26
			Chromyl	4.47
			Fe_2O_3Fe	4.56
Sublimation AgI(g)	6	Surface-AgI ➔ Surface + AgI(g)	Cr_2O_3Cr	1.51
			Chromyl	1.29
			Fe_2O_3Fe	1.93
	7	Surface-2AgI ➔ Surface +2 AgI(g)	Cr_2O_3Cr	3.65
			Chromyl	2.84
			Fe_2O_3Fe	4.31
	8	Surface-4AgI ➔ Surface +4 AgI(g)	Cr_2O_3Cr	7.26
			Chromyl	6.50
			Fe_2O_3Fe	8.87

By comparing formation energy on three different surfaces, it can be noticed that formation of **Ag$_{(s)}$** on **Cr$_2$O$_3$Cr** surface seems to be the most favourable reaction compared to other reactions (ΔE = 0.04 eV). However this advantage in energy between *Reaction 3* and *Reaction 4* (**Table 3.4**) comes from sublimation of **Ag$_{(s)}$**. The silver fusion temperature is around 960°C. If the temperature in the RCS is higher,

silver is expected to become liquid, but its partial pressure will remain low. The second favourable reaction is the formation of **I$_{2(g)}$** on **Chromyl** surface (oxidized chromium oxide surface). For a coverage of 25% (Reaction 1, **Table 3.4**), formation of I$_{2(g)}$ is slightly endothermic ($\Delta E = 0.20$ eV). On the opposite, the formation of I$_{2(g)}$ from a chromyl surface with a coverage of 50% is more endothermic ($\Delta E = 0.71$ eV). In order to describe the conditions of the reactor, thermodynamic correction taking into account the temperature and pressure are needed. Furthermore, the thermodynamic correction term of **I$_{2(g)}$** and **AgI$_{(g)}$** are important at high temperature as silver and iodine atoms are heavy. Consequently, there may be a competition between formation of I$_{2(g)}$ and sublimation of AgI$_{(g)}$ at high temperature.

3.2.2.1   *FORMATION OF I$_{2(g)}$ ON OXIDES SURFACES WITH AgI ADSORBED*
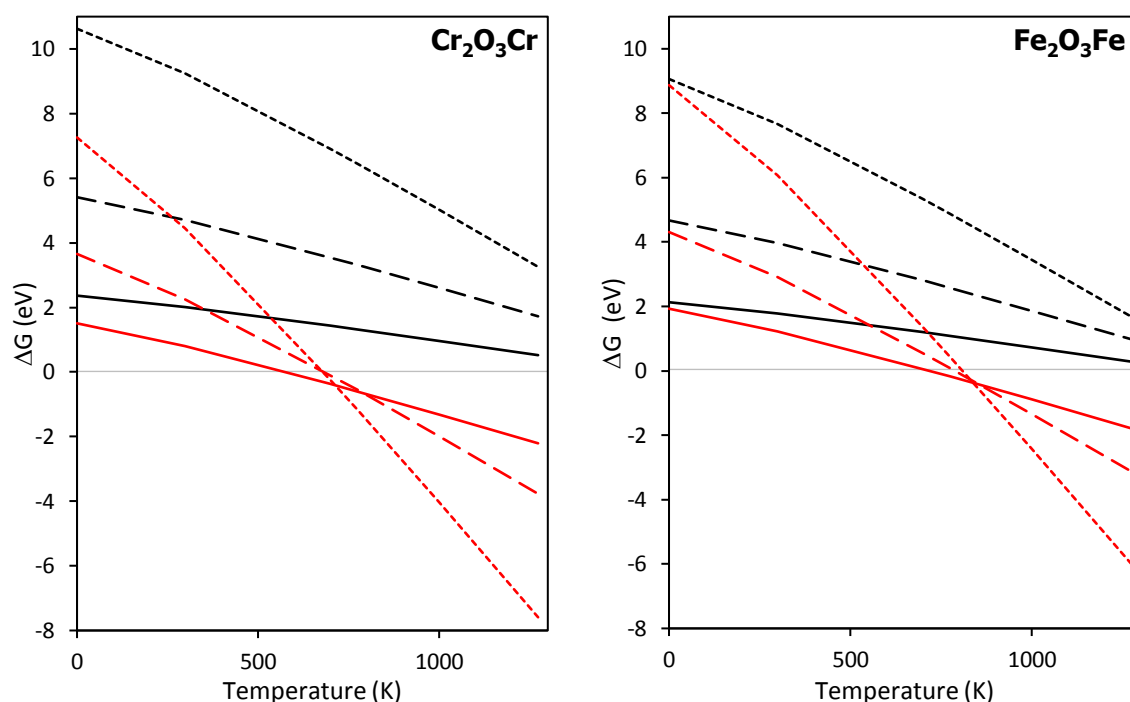
Figure 3.16. Gibbs free energy for (black) formation of I$_{2(g)}$ and (red) sublimation of AgI(g) on surfaces Cr$_2$O$_3$Cr and Fe$_2$O$_3$Fe with AgI coverage equal to (line) 25%, (short line) 50% and (point) 100% from 0 K to 1300 K.

By adding thermodynamic correction terms of **I$_{2(g)}$** and **AgI$_{(g)}$**, Gibbs free energy for formation of I$_{2(g)}$ and sublimation of AgI$_{(g)}$ on three most interested surfaces are calculated and shown on **Figure 3.16** and **Figure 3.17.** It can be noticed that the formation of I$_{2(g)}$ is not possible on Cr$_2$O$_3$Cr and Fe$_2$O$_3$Fe surfaces as the sublimation of AgI(g) (red) is more favorable than the formation of I$_{2(g)}$ (black) (**Figure 3.16**).

Furthermore the sublimation of $AgI_{(g)}$ will be favoured thermodynamically only when $\Delta G < 0$. Consequently, for Cr_2O_3Cr surface, the sublimation of $AgI_{(g)}$ occurs at about 556 K for a coverage equal to 25% and about 655 K for coverages equal to 50 % and 100%. Besides, for Fe_2O_3Fe surface, the sublimation temperatures for $AgI_{(g)}$ on an adsorbed surface with coverages equal to 25%, 50% and 100% are 702 K, 766 K and 794 K.

On Chromyl surface with adsorbed AgI (**Figure 3.17**), it can be noticed that the formation of $I_{2(g)}$ (black) is always more favourable than the sublimation of $AgI_{(g)}$ (red) at low temperature. $I_{2(g)}$ (black, line) can be formed almost spontaneously (at 75 K) with a 25% coverage while the $AgI_{(g)}$ sublimation is thermodynamically possible above 550 K and even more favourable than the $I_{2(g)}$ formation above 930 K. When the coverage increases to 50%, the formation of $I_{2(g)}$ (black, short line) can occur between 305 K and 780 K. Over this temperature, the sublimation of $AgI_{(g)}$ (red, short line) would happen. For a surface totally covered by AgI (100%), the temperature ranges for the formation of $I_{2(g)}$ (black, point) is very small (from 593 K to 637 K). For higher temperature, AgI adsorbed on surface will be sublimated (red, point).
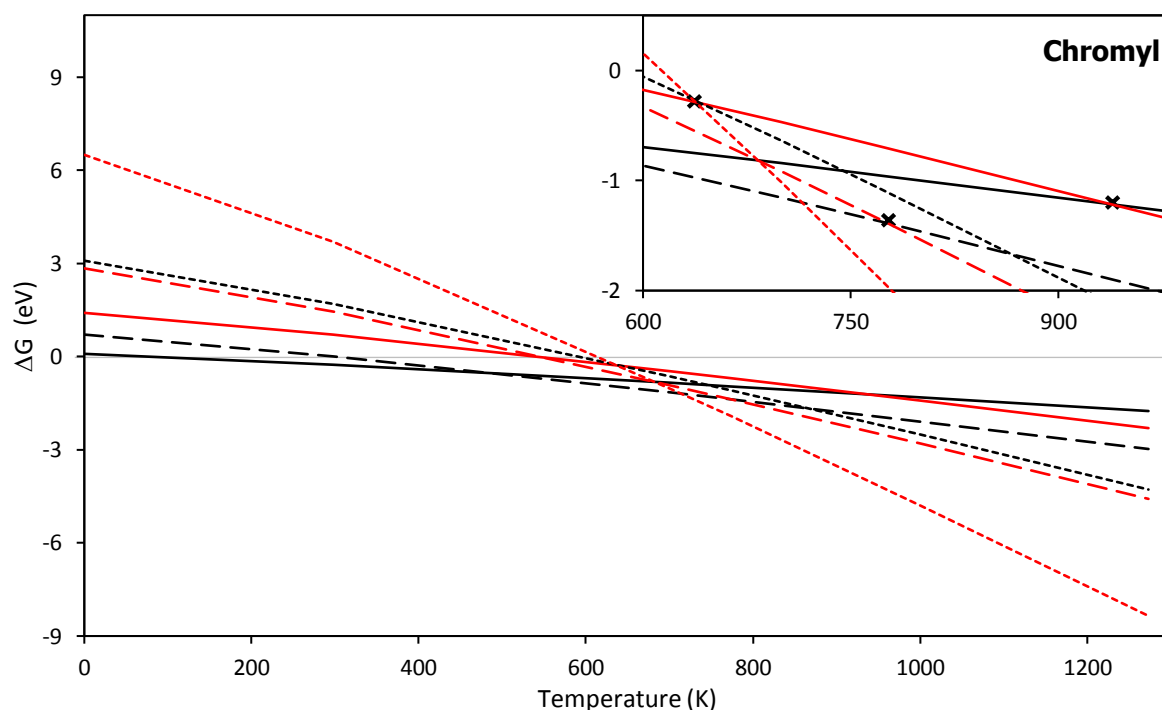
Figure 3.17. Gibbs free energy for (black) formation of $I_{2(g)}$ and (red) sublimation of $AgI_{(g)}$ on surfaces Chromyl with AgI coverage equal to (line) 25%, (short line) 50% and (point) 100% from 0 K to 1300 K.

As the formation of $I_{2(g)}$ on adsorbed chromyl surface is possible, the reaction pathway for this formation will be discussed. At 25% coverage, the most stable form of AgI on Chromyl surface is a dissociated one (**Table 3.2**) then the reaction pathway to form $I_{2(g)}$ will be simple as shown in **Figure 3.18**. Firstly, AgI adsorbed on the surface, with one bond created between Ag atom and terminal oxygen on the surface (**A→B**). Then AgI can be dissociated on the surface with a negative dissociation energy (-1.41 eV; **B→D**) with Ag adsorbed between two terminal oxygen atoms of the surface and I atom adsorbed on one of the two rest of terminal oxygen atoms of Chromyl surface (**Figure 3.10**). This step goes through an un-dissociated AgI intermediate (**C**) adsorbed between the two terminal oxygen atoms of the surface. Afterwards, it is possible to form $I_{2(g)}$ with I^- that come from the dissociation of two different AgI molecules (**D→E**).
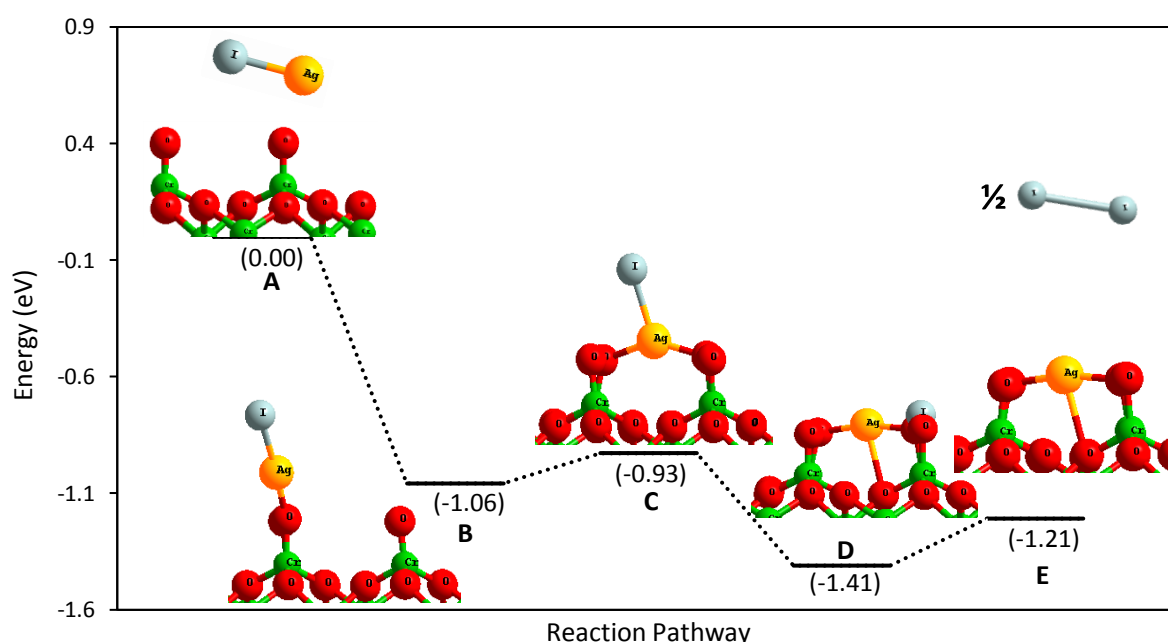
Figure 3.18. Energy diagram for formation of $I_{2(g)}$ on Chromyl surface adsorbed by AgI at 25% coverage. Chromium: green. Oxygen: red. Silver: yellow. Iodine: grey.

Then transition states between different stable states are calculated by *Nudged elastic band method (NEB)* method[39–41] (Chapter II Section 2.3.1). Between state **B** and **C** no transition state can be found and the energy gap between two states are quite small (0.13 eV). The transition state between C and D is shown in **Figure 3.19** (top) with an activation energy equal to 0.77 eV. During this step the distance between Ag and I atoms increases (**C**: d_{Ag-I}= 2.62 Å; **TS$_1$**: d_{Ag-I}= 3.97 Å and **D**: d_{Ag-I}= 4.55 Å) and iodine atom moves from the top position on the Ag atom towards one of the terminal oxygen atoms of Chromyl surface. In order to calculate the transition state between state **D**

and **E** (liberation of $I_{2(g)}$), a larger surface (double size) is used aiming to contain two iodine atoms. The transition state between these two new states are shown in **Figure 3.19** (down). It can be seen that the activation for this step is equal to 0.64 eV. However, energy difference between state D and E for a double size cell is slightly lower than that in a single one (0.14 eV instead of 0.20 eV) which is due to the change of cell size. The distance between two iodine atoms decrease from state **D** to **E**. One iodine atom that is still located on the top of one terminal oxygen atom of the surface while the second iodide move from the top position to form the I-I bond. The $I_{2(g)}$ molecule is formed and can be released from the surface. Hence, with several steps slightly endothermic ($\Delta E_{activation} < 0.80$ eV), this reaction can occur rapidly inside reactor coolant system when the temperature is high. In conclusion, $I_{2(g)}$ could be liberated in presence of air when coverage of AgI lower or equal to 25% on Chromyl surface.
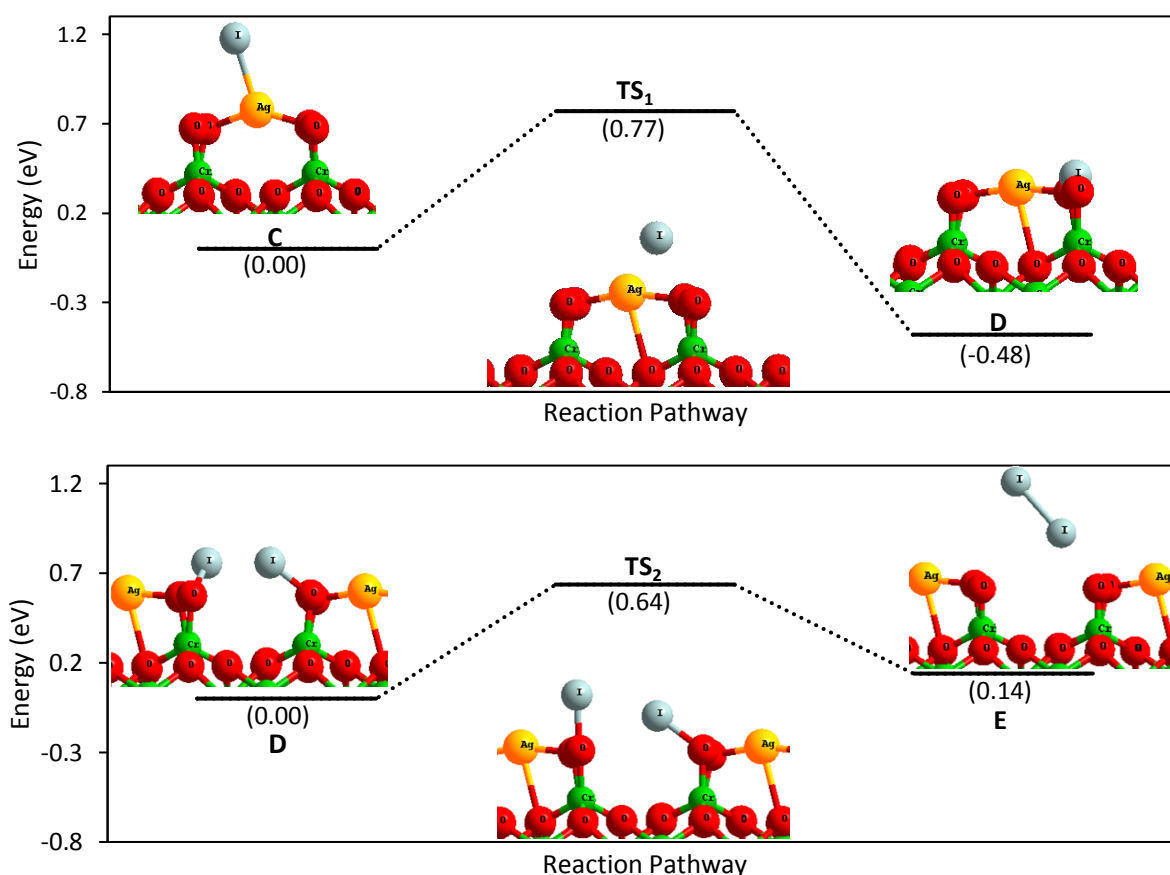
Figure 3.19. Energy diagram of transition states for formation of $I_{2(g)}$ on Chromyl surface with AgI adsorbed with a coverage equal to 25%. (top) transition state from state C to D (down) transition state from state D to E. Chromium: green. Oxygen: red. Silver: yellow. Iodine: grey.

As shown in **Figure 3.17**, with AgI coverage equal to 50%, the formation of $I_{2(g)}$ is also possible. The reaction pathway for the formation of $I_{2(g)}$ is shown in **Figure 3.20**. When

the coverage reaches 50%, AgI forms a chain structure on the surface (**B**) which is very stable (ΔE = -2.84 eV). After compression and distortion of this chain (**C**), two AgI molecules are separated and move into the spaces between two terminal oxygen atoms of Chromyl surface (**D**). In the end, the distance between two iodine atoms decreases until forming I_2 and be released from the surface (**E**).
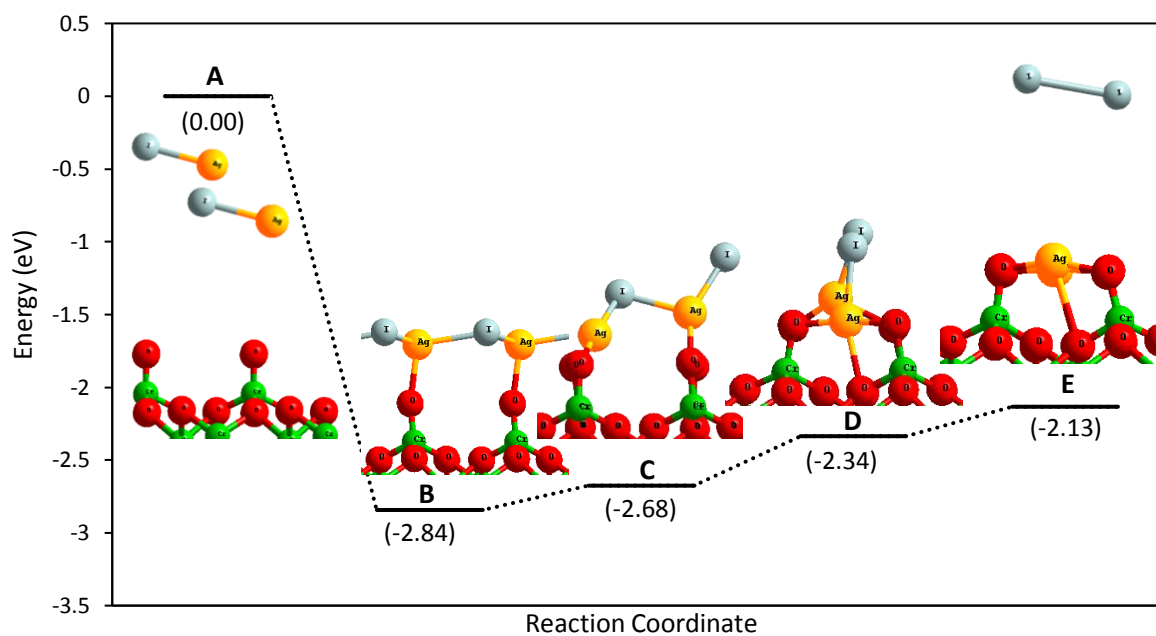
Figure 3.20. Energy diagram for formation of $I_{2(g)}$ on Chromyl surface adsorbed by AgI with coverage equal to 50%. Chromium: green. Oxygen: red. Silver: yellow. Iodine: grey.

All previous steps are endothermic and the transition states between different stable states will be looking for also by using *Nudged elastic band method (NEB)* method[39–41] (Chapter II Section 2.3.1). From state **B** to **C** (**Figure 3.21**, top), the chain structure of AgI distorts, and forms small segment of AgI which contains two AgI molecules (**TS₁** and **C**). The transition state was found with an activation energy equal to 0.52 eV. From state **C** to **D** (**Figure 3.21**, middle), the bond between two AgI molecules is broken and each molecule moves towards the space between two terminal oxygen atoms of chromyl surface. For this step the activation energy is higher than the first step (0.83 eV). For the last step where $I_{2(g)}$ is formed (**Figure 3.21**, down), the distance between two iodine atoms decreases (**D**: 3.25 Å; **TS₃**: 3.08 Å and **E**: 2.66 Å). The activation energy for this step is even higher than for the previous ones (1.14 eV). Compared with the reaction with an AgI coverage equal to 25%, the activation energy for the 50% coverage is higher, so the reaction with this coverage is slower.
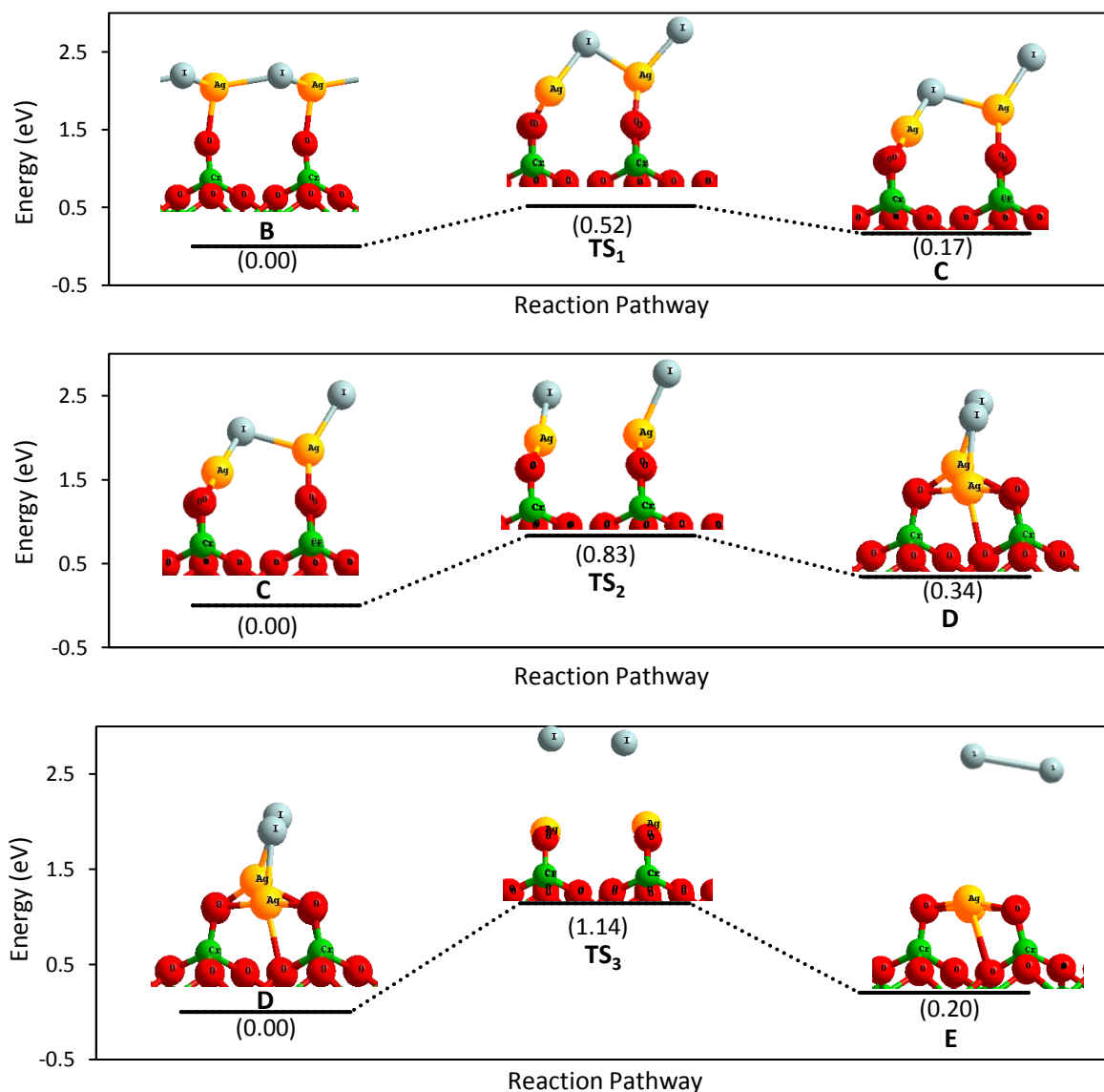
Figure 3.21. Energy diagram of transition states for formation of $I_{2(g)}$ on Chromyl surface with AgI adsorbed with a coverage equal to 50%. (top) transition state from state B to C (middle) transition state from state C to D (down) transition state from state D to E. Chromium: green. Oxygen: red. Silver: yellow. Iodine: grey.

When chromyl surface is totally covered by AgI atoms, the formation of $I_{2(g)}$ is almost not probable. It occurs only in a very small temperature range (from 569 K to 613 K). Since chains and rings are formed on the surfaces at this coverage, we can expect that the activation energy will be equivalent to the 50% ones. As many possible reaction pathways may occur, formation of I_2 and/or AgI (at the same time), and as the thermodynamic calculations indicated that the desorption is less probable on the fully covered surfaces, we did not study these mechanisms.

3.2.2.2 *FORMATION OF $I_{2(g)}$ ON OXIDE SURFACES WITH AN OXIDANT.*

From **Figure 3.16**, it can be noticed that the formation of $I_{2(g)}$ on Cr_2O_3Cr and Fe_2O_3Fe is not possible. As a result, the formation of $I_{2(g)}$ on these two surfaces could occur only by adding an oxidant. In nuclear studies, $OH^\bullet$ is often used as an oxidant as it can be generated by water radiolysis. The energies of these reactions are grouped in **Table 3.5**. It can be observed that, with the participation of oxidants ($OH^\bullet$), the formation of $I_{2(g)}$ will be observed spontaneously (reaction exothermic).

Table 3.5. Formation energy of $I_{2(g)}$ on chromium and iron oxide surface with AgI adsorbed in presence of oxidants ($OH^\bullet$).

Reaction	Model	Δ Energy (eV)
Surface-2AgI + 2OH$^\bullet$ → Surface-2AgI-2OH → Surface-2Ag-2OH + I$_{2(g)}$	Cr_2O_3Cr	-2.84
	Fe_2O_3Fe	-3.29

3.2.3 CONCLUSION

In conclusion, the formation of $I_{2(g)}$ not possible on Cr_2O_3Cr and Fe_2O_3Fe surfaces by thermal effect. Sublimation of $AgI_{(g)}$ on these two surfaces is more favourable. From a thermodynamic point of view, the formation of $I_{2(g)}$ should be occurred on Chromyl surface with AgI adsorbed in some temperature ranges. By transition state calculation, it can be noticed that the formation of $I_{2(g)}$ over a chromyl surface covered by 25% of AgI is faster than 50%. Furthermore, with participation of an oxidant in the reaction, the formation of $I_{2(g)}$ on neutral surfaces (Cr_2O_3Cr and Fe_2O_3Fe) become possible.

3.3 ADSORPTION OF CdI₂ ON CHROMIUM AND IRON OXIDE SURFACES.

Secondly, adsorption of cadmium iodide (CdI_2), with Cd coming from rod degradation on the surface of the reactor coolant system (RCS) will be studied. Mechanisms for re-vaporization of iodine species will also be discussed. It will also be presented into two parts: thermodynamic study and reactivity study.

3.3.1 THERMODYNAMIC STUDY

Firstly, CdI_2 molecules were adsorbed on four different surfaces mentioned before (Chapter I section 1.5.2) in order to understand the adsorption of cadmium iodide on

stainless steel surface and the potential formation of molecular iodine from these surfaces: **Cr₂O₃Cr** (neutral chromium oxide surface), **Chromyl** (oxidized chromium oxide surface), **Cr₂O₃Cr₂(OH)₃** (hydrated chromium oxide surface) and **Fe₂O₃Fe** (neutral iron oxide surface)[36,37]. **Fe₂O₃HFe** (reduced iron oxide surface) surface would not be discussed in this section as a reduced surface will not favour the oxidation of an adsorbed species.

Table 3.6. Adsorption of CdI₂ on chromium and iron oxide surfaces in function of its coverage. Chromium: green. Iron: blue. Oxygen: red. Cadmium: yellow. Iodine: grey.
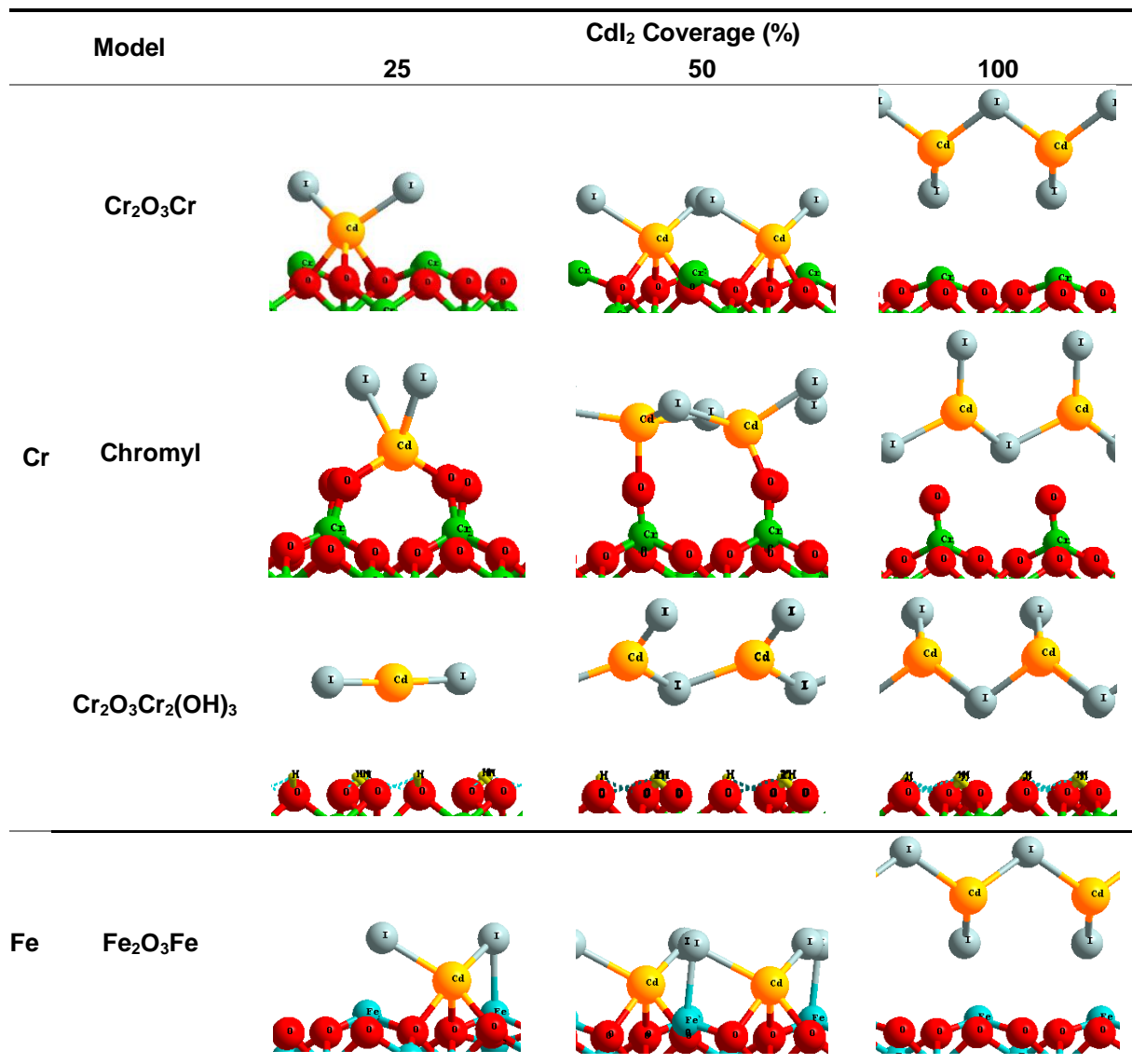
The adsorption simulations are run under different coverages which can be described by equation below:

$$r = \frac{n_{CdI_2\ adsobed}}{n_{adsorbed\ sites}}$$

- $n_{CdI_2\ adsobed}$: Number of adsorbed CdI₂ molecules.

- $n_{adsorbed\ sites}$: Number of Cr or Fe sites available for CdI₂ adsorption.

The most stable structures for adsorption on these four surfaces are classed by coverage in **Table 3.6**. It can be noticed that almost all stable structures represent an associative adsorption. Hence, it can be concluded that the associative adsorption of CdI₂ on these four oxide surfaces are more favourable than dissociative adsorption. The adsorption energy per CdI₂ molecule adsorbed was summarized in **Table 3.7**.This energy is calculated by equation mentioned in Chapter II Section 2.5.2 which can be written as below for a surface adsorbed by CdI₂:

$$E_{ads} = \frac{E_{total} - E_{surface} - \left(E_{CdI_2} \times n_{CdI_2}\right)}{n_{CdI_2}}$$

with $E_{ads} < 0$, corresponding to an exothermic reaction.

Table 3.7. Adsorption energy per CdI₂ adsorbed for different CdI₂ coverage on chromium and iron oxide surfaces.

	Model	CdI₂ Coverage (%)		
		25	50	100
	Cr₂O₃Cr	-1.40 eV	-1.40 eV	-0.52 eV*
Cr	**Chromyl**	-0.36 eV	-0.80 eV	-0.56 eV*
	Cr₂O₃Cr₂(OH)₃	-0.04 eV	-0.22 eV*	-0.42 eV*
Fe	**Fe₂O₃Fe**	-2.50 eV	-2.35 eV	-0.64 eV*

* CdI₂ form a chain/ a cycle, so the energy corresponds part or a big part to energy of formation of a chain/ a cycle.

For **Cr₂O₃Cr** surface (neutral chromium oxide surface), CdI₂ is also stable in a tripod structure (Cd-OOO, **Figure 3.22** a). At 25% and 50% coverage, CdI₂ is isolated on the surface with an adsorption energy equals to -1.40 eV per adsorbed CdI₂. When coverage reaches 100%, CdI₂ forms a cycle that has no contact with surface (**Figure 3.22** b). The adsorption energy here corresponds to formation energy of a cycle or to the condensation energy of CdI₂ (- 0.52 eV where E adsorption CdI2 cycle = - 0.10 eV).
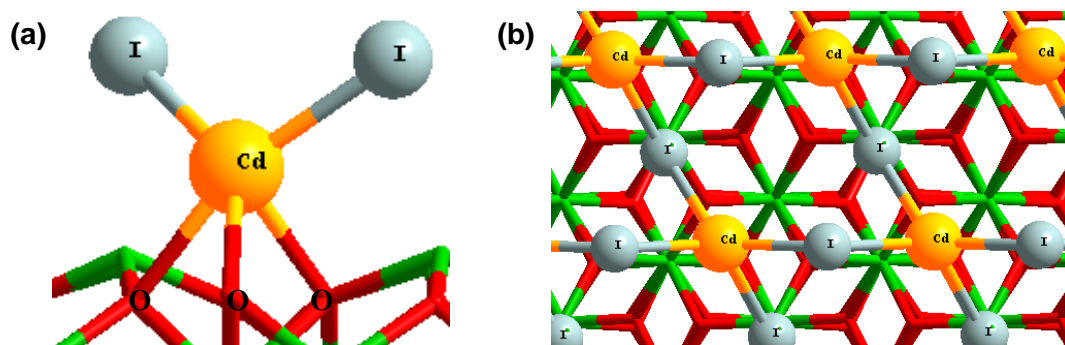
Figure 3.22. (a) Tripod structure of CdI_2 on the surface. (b)Top view for adsorption of CdI_2 with 100% coverage on the Cr_2O_3Cr surface. Chromium: green. Oxygen: red. Cadmium: yellow. Iodine: grey.

On **Chromyl** surface (oxidized chromium oxide surface), as AgI, CdI_2 adsorbed in different ways compared to adsorption on other surfaces. At 25% coverage, Cd is situated between two terminal oxygen atoms of the surface with an adsorption energy lower than on other surfaces (-0.36 eV). The cadmium is located in the center of a tetrahedral-like structure that is formed by two terminal oxygen atoms of the surface and two iodine atoms. When the coverage reaches 50%, CdI_2 group adsorbed on the top position on terminal oxygen of surface and form a dimer (**Figure 3.23** a) with an adsorption energy equal to -0.80 eV per CdI_2. For a Chromyl surface totally covered by CdI_2 (100%, **Figure 3.23** b), CdI_2 forms a chain which has no contact with the surface. The formation energy of this chain equal to -0.56 eV per CdI_2 (where E $_{adsorption}$ $_{CdI2\ chain}$ = -0.36 eV per CdI_2 adsorbed).
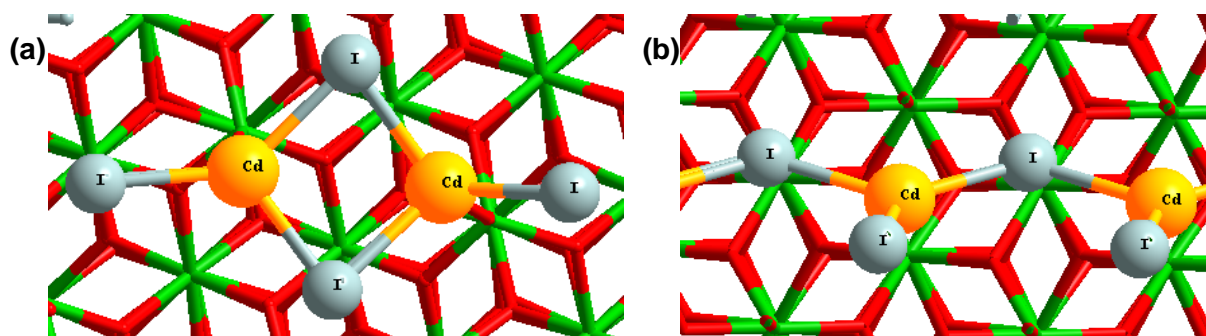
Figure 3.23. Top view for adsorption of CdI_2 with (a) 50% (b) 100% coverage on the Chromyl surface. Chromium: green. Oxygen: red. Cadmium: yellow. Iodine: grey.

For **$Cr_2O_3Cr_2(OH)_3$** surface (hydrated chromium oxide surface): at 25% coverage, CdI_2 has no contact with the surface, hence its adsorption energy is almost zero (-0.04 eV). When coverage rises to 50%, CdI_2 forms a chain but still have almost no contact with the surface (**Figure 3.24** a) with a formation energy equal to -0.22 eV (E $_{adsorption}$ $_{CdI2}$

chain = -0.04 eV). When coverage reaches 100%, CdI_2 forms a ring structure that still has no contact with the surface (**Figure 3.24** b). The cycle formation energy is equal to -0.39 eV (E adsorption CdI2 cycle = 0.00 eV). Consequently, it can be concluded that hydrated surface is not favourable for adsorption of CdI_2.
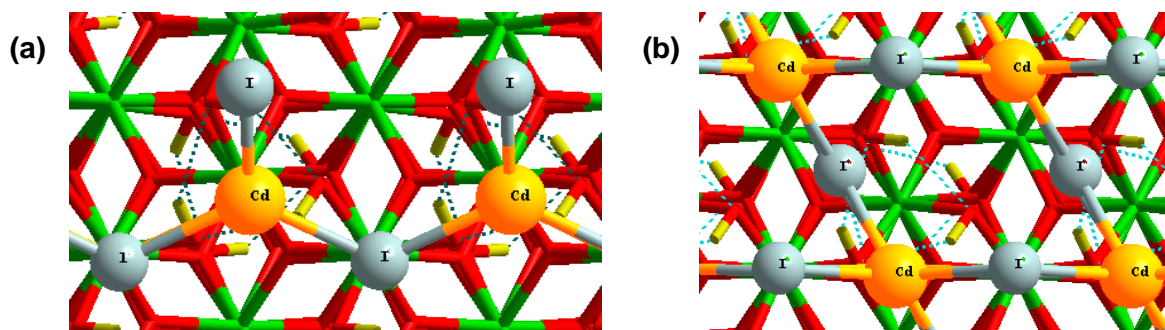
Figure 3.24. Top view for adsorption of CdI_2 with (a) 50% (b) 100% coverage on the $Cr_2O_3Cr_2(OH)_3$ surface. Chromium: green. Oxygen: red. Cadmium: yellow. Iodine: grey. Hydrogen: light yellow.

As for AgI, we considered another totally saturated hydrated surface with six water atoms adsorbed directly on chromium oxide surface (**Figure 3.25** a) that is stable above 3 bars of pressure at ambient temperature[36]. The adsorption of CdI_2 molecule is not avoided by the presence of water. Cadmium atom is still present in a tripod structure on this surface (Cd-OOO, **Figure 3.25** b). The adsorption energy for 25% CdI_2 coverage, on this highly hydrated surface, is less exothermic (ΔE = -1.00 eV) than on adsorption on a dry surface (ΔE = -1.40 eV on Cr_2O_3Cr surface). However, the adsorption on this surface is already more favourable than on the $Cr_2O_3Cr_2(OH)_3$ surface (ΔE = -0.04 eV for 25% CdI_2 coverage on $Cr_2O_3Cr_2(OH)_3$ surface). On the hydrated surface, bond is formed between adsorbed molecule and surface. However, with more CdI_2 adsorbed on surface, the adsorption becomes less favourable and CdI_2 begins to "float" on the surface as of presence of water molecules inhibits the formation of bonds between the surface and the CdI_2 (**Appendix** Figure A.2). It can be observed that there is always one CdI_2 in a tripod structure (Cd-OOO) while the excess CdI_2 molecules polymerize and "float" on the surface. Hence, with low coverage (≤ 50%), CdI_2 can be adsorbed on totally hydrated chromium oxide surface which is stable at high pressure (above 3 bars) under ambient temperature.

(a)
(b)
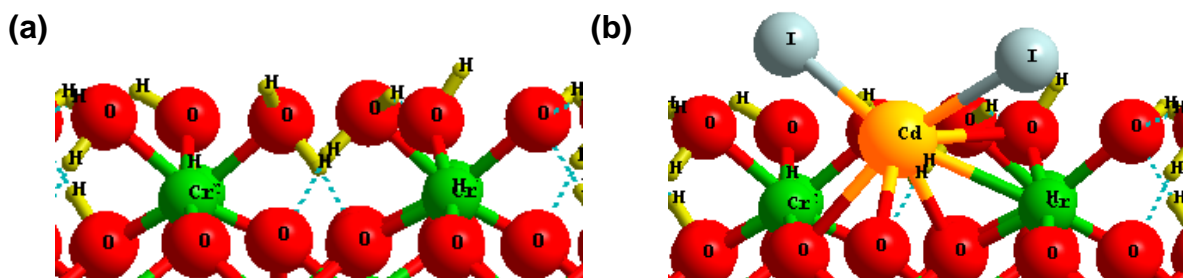
Figure 3.25. a) Totally saturated hydrate chromium oxide surface (with six water molecules). b) CdI$_2$ adsorbed on totally saturated hydrate chromium oxide surface. Chromium: green. Oxygen: red. Cadmium: yellow. Iodine: grey. Hydrogen: light yellow.

For **Fe$_2$O$_3$Fe** surface (neutral iron oxide surface), adsorbed CdI$_2$ reacts in the same way as on the neutral chromium oxide surface and forms a tripod structure (Cd-OOO, **Figure 3.26** a). CdI$_2$ stays also isolated on the surface for coverage equal to 25% and 50% and their adsorption energy (-2.50 eV and -2.35 eV) is significantly higher than on Cr$_2$O$_3$Cr (-1.40 eV). CdI$_2$ also forms a cycle that has no contact with the surface at 100% coverage (**Figure 3.26** b). The cycle formation energy is slightly higher than on Cr$_2$O$_3$Cr surface (-0.64 eV with E $_{adsorption\ CdI2\ cycle}$ = -0.22 eV)

In conclusion, when CdI$_2$ totally covers the surface, CdI$_2$ has no contact with surfaces and forms cycles. In fact, with the increase of the number of adsorbed CdI$_2$ atoms on the surface, CdI$_2$ polymerizes and forms network that are in weak interactions with the surface. On iron oxide surface, adsorption of CdI$_2$ on this surface is slightly more favourable than on chromium oxide surface. The adsorptions energy on a neutral surface is much more important than adsorption energy on modified surfaces (oxidized or hydrated). The only possible way to adsorb CdI$_2$ on a hydrated surface is on a totally saturated surface which only exists under high pressure at ambient temperature.

(a)
(b)
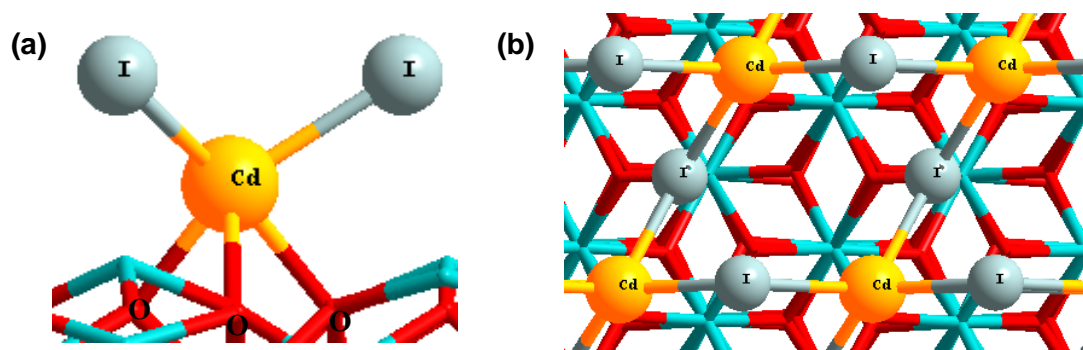
Figure 3.26. (a) Tripod structure of CdI$_2$ on the surface. (b)Top view for adsorption of CdI$_2$ with 100% coverage on Fe$_2$O$_3$Fe surface. Iron: blue. Oxygen: red. Cadmium: yellow. Iodine: grey.

Additionally, a *bader*[38] analysis has also been performed. For the adsorption of CdI_2 on these surfaces, on most of the surfaces (**except** Chromyl surface), cadmium (Cd^{2+}) and iodide I^- ions do not exchange electrons with the surface. The repartition of the electrons on the surface is almost unchanged (difference of spin population below 0.07). For **Chromyl** surface, as adsorption of AgI, CdI_2 molecules being adsorbed on terminal oxygen atoms, there is an exchange of electron between surface and adsorbed species. Chromium atoms on the top of the surface show an important variation of spin (0.9) for 25% and 50% coverage of CdI_2. As the surface has been pre-oxidised, the exchange of electron between CdI_2 molecules and surface is much easier.

3.3.2 REACTIVITY STUDY

As silver iodide, during a nuclear accident, adsorbed cadmium iodide adsorbed on reactor coolant surface may also release gaseous iodine ($I_{2(g)}$, $CdI_{2(g)}$). Therefore, the formation of $I_{2(g)}$ and $CdI_{2(g)}$ from adsorbed surface will be investigated in this section. Additionally, as a reference, the formation of $Cd_{(s/g)}$ on adsorbed surface has also been discussed in order to compare with the formation of iodine species. In **Table 3.8**, formation energies for $I_{2(g)}$ and $Cd_{(s/g)}$ and sublimation energy of $CdI_{2(g)}$ on the three most representative surface models is simulated. All the calculations are based on most stable structures with different coverage in CdI_2.

By comparing formation energy on three different surfaces, it can be noticed that the formation of $I_{2(g)}$ can occur spontaneously on **Chromyl** surface with 25% coverage (**Table 3.8**, *Reaction 9*, ΔE = -0.08 eV). With augmentation of the coverage, the formation energy of $I_{2(g)}$ on chromyl surface increase (ΔE = 1.35 eV for 50% coverage and ΔE = 4.04 eV for 100%) and become impossible from a thermodynamic point of view. At the same time, the sublimation of $CdI_{2(g)}$ on these coverages seem more favourable (ΔE = 1.61 eV for 50% coverage and ΔE = 1.36 eV for 100% coverage). As mentioned in previous section, our theoretical calculations are performed 0 K while the temperature inside the reactor coolant system (RCS) may vary from room temperature to over 1800 K. Moreover, thermodynamic correction term of $I_{2(g)}$ and $CdI_{2(g)}$ are important as cadmium atom and iodine atom are heavy.

Table 3.8. Formation energy of $I_{2(g)}$ and $Cd_{(s/g)}$ and sublimation energy of $CdI_{2(g)}$ from different surface models with CdI_2 adsorbed.

		Reaction	Model	Δ Energy (eV)
Formation $I_{2(g)}$	9	Surface-CdI$_2$ ➔ Surface-Cd + I$_2$(g)	Cr$_2$O$_3$Cr	3.38
			Chromyl	-0.08
			Fe$_2$O$_3$Fe	4.28
	10	Surface-2CdI$_2$ ➔ Surface-2Cd + 2 I$_2$(g)	Cr$_2$O$_3$Cr	6.77
			Chromyl	1.35
			Fe$_2$O$_3$Fe	8.27
	11	Surface-4CdI$_2$ ➔ Surface-4Cd + 4 I$_2$(g)	Cr$_2$O$_3$Cr	10.47
			Chromyl	4.35
			Fe$_2$O$_3$Fe	8.79
Formation $Cd_{(s/g)}$	12	Surface-CdI$_2$ ➔ Surface-2I + Cd(s)	Cr$_2$O$_3$Cr	0.19
			Chromyl	1.17
			Fe$_2$O$_3$Fe	1.88
	13	Surface-CdI$_2$ ➔ Surface-2I + Cd(g)	Cr$_2$O$_3$Cr	1.84
			Chromyl	2.81
			Fe$_2$O$_3$Fe	3.53
Sublimation $CdI_{2(g)}$	14	Surface-CdI$_2$ ➔ Surface + CdI$_2$(g)	Cr$_2$O$_3$Cr	1.40
			Chromyl	0.36
			Fe$_2$O$_3$Fe	2.50
	15	Surface-2CdI$_2$ ➔ Surface + 2 CdI$_2$(g)	Cr$_2$O$_3$Cr	2.81
			Chromyl	1.61
			Fe$_2$O$_3$Fe	4.70
	16	Surface-4CdI$_2$ ➔ Surface + 4 CdI$_2$(g)	Cr$_2$O$_3$Cr	2.09
			Chromyl	2.25
			Fe$_2$O$_3$Fe	2.61

Consequently, as the energy for the formation of $I_{2(g)}$ and sublimation of $CdI_{2(g)}$ are close, a competition can exist and they may become exergonic at high temperature. Hence, calculation on thermodynamic correction terms of **$I_{2(g)}$** and **$CdI_{2(g)}$** have to be performed in order to know which would be the favourable product. Additionally, it should be mentioned here that, as CdI_2 molecules form a ring structure that has no

contact with surface, the sublimation of $CdI_{2(g)}$ at 100% coverage is much more favourable than at lower coverages. Hence the release of CdI_2 in gas form on this coverage should be easy. The formation of $Cd_{(s)}$ on **Cr₂O₃Cr** surface seems also to be a favourable reaction (ΔE = 0.19 eV). Same as in previous section (formation of gaseous species form surface with AgI adsorbed), the formation of $I_{2(g)}$ (ΔE = 1.35 eV) and sublimation of $CdI_{2(g)}$ (ΔE = 1.61 eV) with same coverage (50%) are not thermodynamically favoured.

3.3.2.1 FORMATION OF $I_{2(g)}$ ON OXIDE SURFACES WITH CdI_2 ADSORBED.

By adding thermodynamic correction terms to **I₂₍g₎** and **CdI₂₍g₎** at different temperatures, we can calculate the Gibbs free energy for $I_{2(g)}$ formation and $CdI_{2(g)}$ sublimation on the three most interested surfaces (Cr₂O₃Cr, Chromyl and Fe₂O₃Fe) in function of temperature. The results are displayed in **Figure 3.27** and **Figure 3.28**.
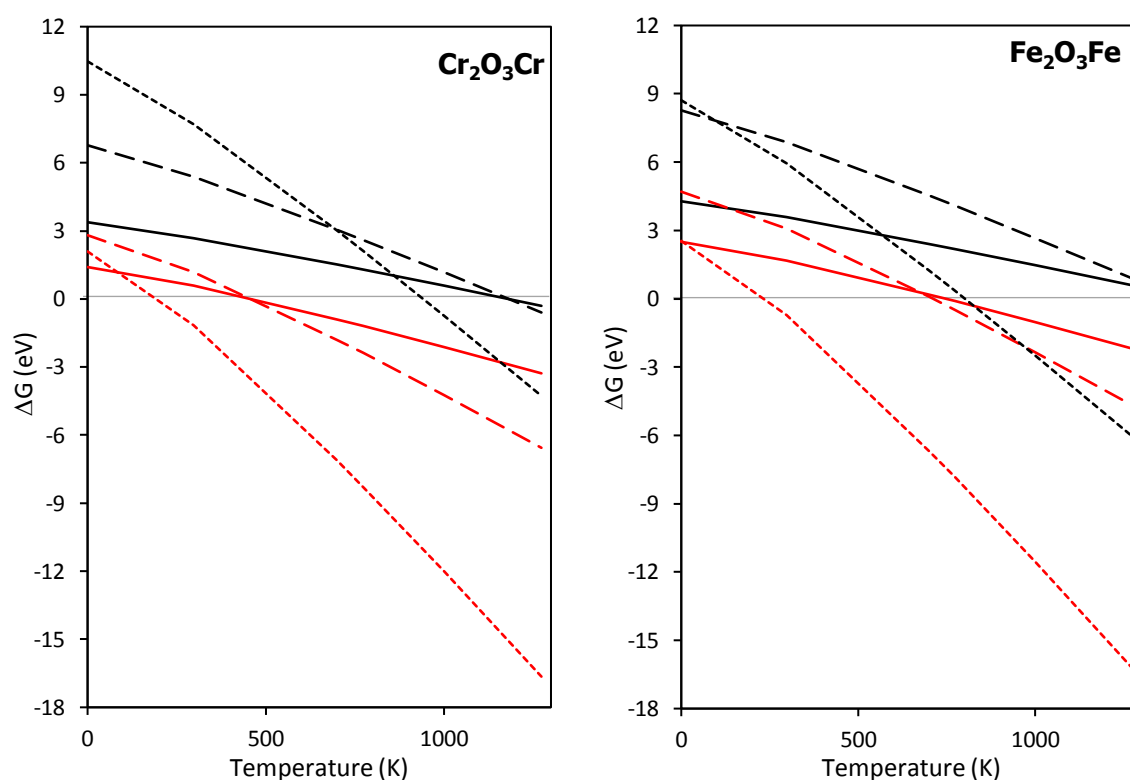
Figure 3.27. Gibbs free energy for (black) formation of $I_{2(g)}$ and (red) sublimation of $CdI_{2(g)}$ on surfaces Cr₂O₃Cr and Fe₂O₃Fe with CdI₂ coverage equal to (line) 25%, (short line) 50% and (point) 100% from 0 K to 1300 K.

It can be noticed that the formation of $I_{2(g)}$ (black) is not possible on Cr₂O₃Cr and Fe₂O₃Fe surface as the sublimation of $CdI_{2(g)}$ (red) occurs before (**Figure 3.27**). The

minimal temperature required for sublimation of $CdI_{2(g)}$ ($\Delta G < 0$) at coverages equal to 25% and 50% on Cr_2O_3Cr surface is almost the same, about 458 K. On the Fe_2O_3Fe surface, this temperature is higher but still quite close for 25% and the one for 50% coverages (757 K for 25% and 707 K for 50%). As CdI_2 molecules form ring structure when the surface is totally covered, there is no contact with the surface, its desorption could occur at very low temperature (192 K for Cr_2O_3Cr surface and 233 K for Fe_2O_3Fe surface).
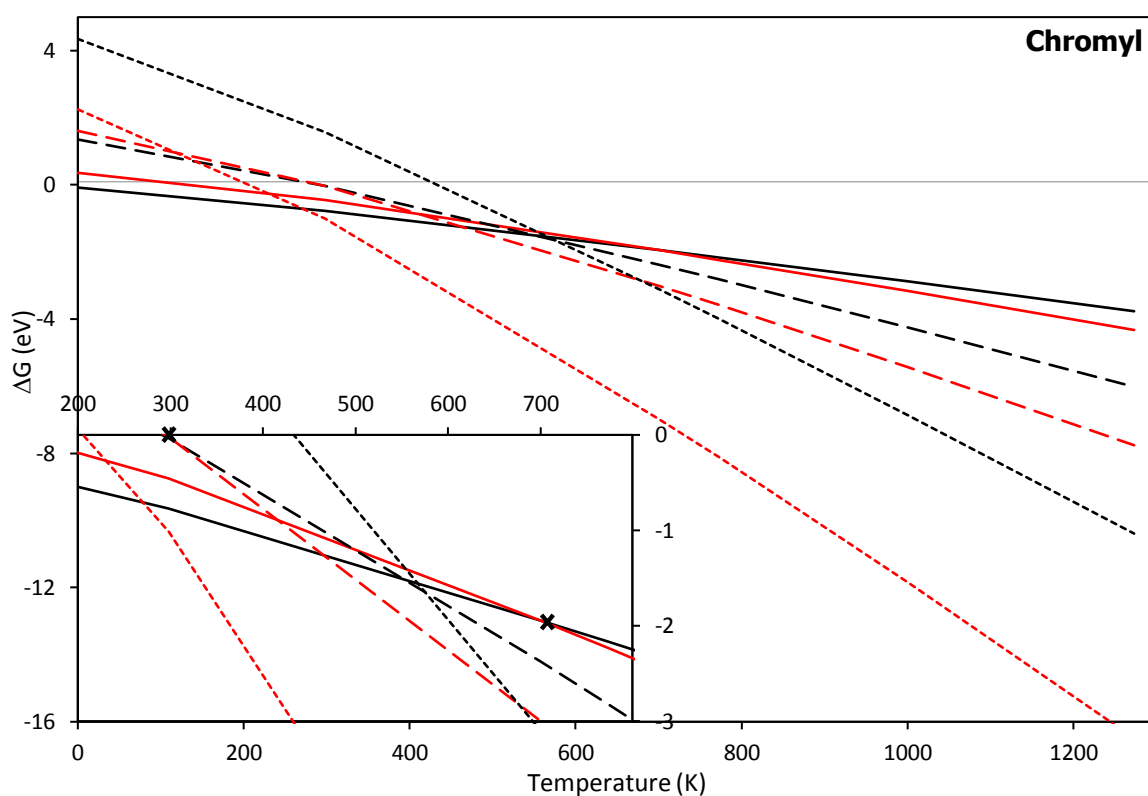
Figure 3.28. Gibbs free energy for (black) formation of $I_{2(g)}$ and (red) sublimation of $CdI_{2(g)}$ on surfaces Chromyl with coverage of CdI_2 equal to (line) 25%, (short line) 50% and (point) 100% from 0 K to 1300 K.

The comparison of Gibbs free energy for formation of $I_{2(g)}$ (black) and sublimation of $CdI_{2(g)}$ (red) on Chromyl surface is shown in **Figure 3.28**. The formation of $I_{2(g)}$ with coverage equal to 25% occurs spontaneously (black, line). Then at about 700 K, the sublimation of $CdI_{2(g)}$ (red, line) become more favourable for this coverage. For coverage equal to 50%, the formation of $I_{2(g)}$ (black short line) is more favourable at low temperature than the CdI_2 sublimation, but its Gibbs free energy is positive, the partial pressure of the gas will remain low. Around 293 K, the Gibbs free energy becomes negative and at this moment the sublimation of $CdI_{2(g)}$ (red short line) is more

favourable than the formation of $I_{2(g)}$. For a surface totally covered by CdI_2, the sublimation of $CdI_{2(g)}$ (red point) is always favourable and at 206 K the reaction becomes possible.
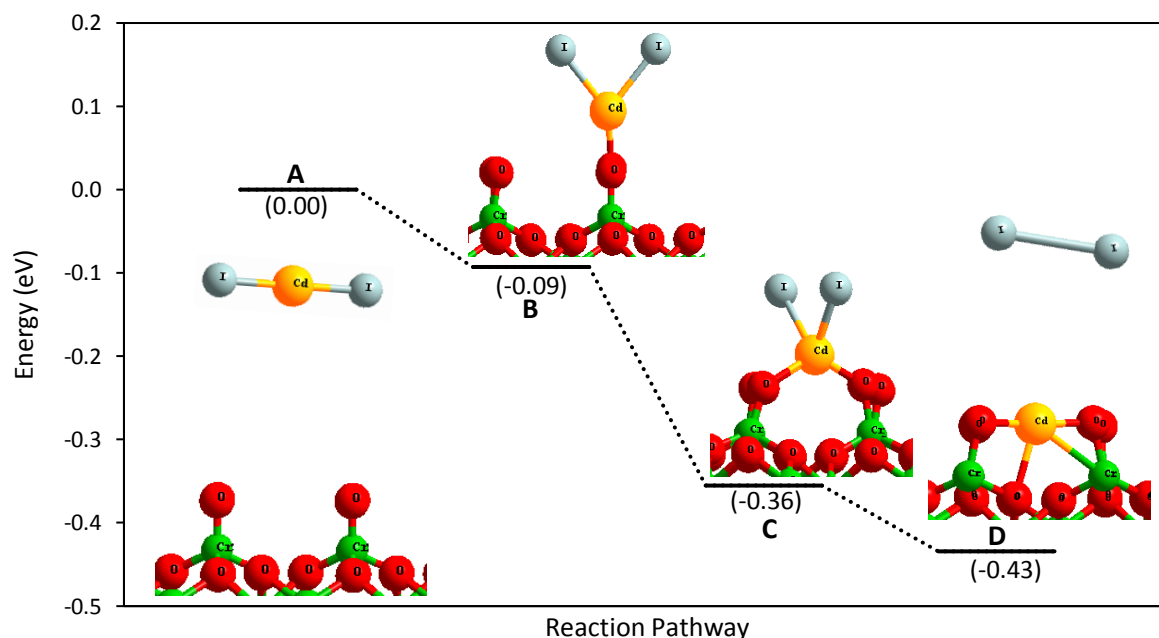
Figure 3.29. Energy diagram for formation of $I_{2(g)}$ on Chromyl surface adsorbed by CdI_2 with coverage equal to 25%. Chromium: green. Oxygen: red. Cadmium: yellow. Iodine: grey.

As the formation of $I_{2(g)}$ on adsorbed chromyl surface is possible, the reaction pathway will be discussed. First of all, CdI_2 adsorbed on Chromyl surface with only one bond created between cadmium atom and terminal oxygen atom of surface (**Figure 3.29**, **A→B**, ΔE = -0.09 eV). Afterwards, CdI_2 moves between two terminal oxygen atoms of surface and form two Cd-O bonds (**B→C**). In the last step, the distance between two iodine atoms decreases until the theoretical distance in iodine gas ($I_{2(g)}$, $d_{I-I, th}$ = 2.66 Å, **C→D**) and then can be released from the surface. It can be observed that every step is exothermic. So theoretically, the only limitations will be kinetic ones.

The transition states between different stable states will still be calculated by using *Nudged elastic band method (NEB)* method[39–41] (Chapter II Section 2.3.1).From geometry B to C (**Figure 3.30**, top), CdI_2 molecule which makes a bond with one of the terminal oxygen atoms of the surface and moves towards the space between two terminal oxygen atoms (**B→ TS₁**). It forms a tetrahedral-like structure with cadmium atom in the centre of two iodine atoms and two terminal oxygen ones (**C**). The activation energy for this step is quite small (0.06 eV), hence equilibrium between B and C will be reached at all temperature. From C to D (**Figure 3.30**, down), the distance

between two iodine atoms decreases close to the distance in $I_{2(g)}$ molecule (**C**: 3.369 Å; **TS$_2$**: 2.969 Å and **D**: 2.66 Å). The activation energy for this step is slightly higher than for the previous step (0.17 eV). We can conclude that the decomposition of CdI$_2$ on an oxidized surface will be very fast and will prevent the formation of important coverage. CdI$_2$ is a very probable source of gaseous iodine.
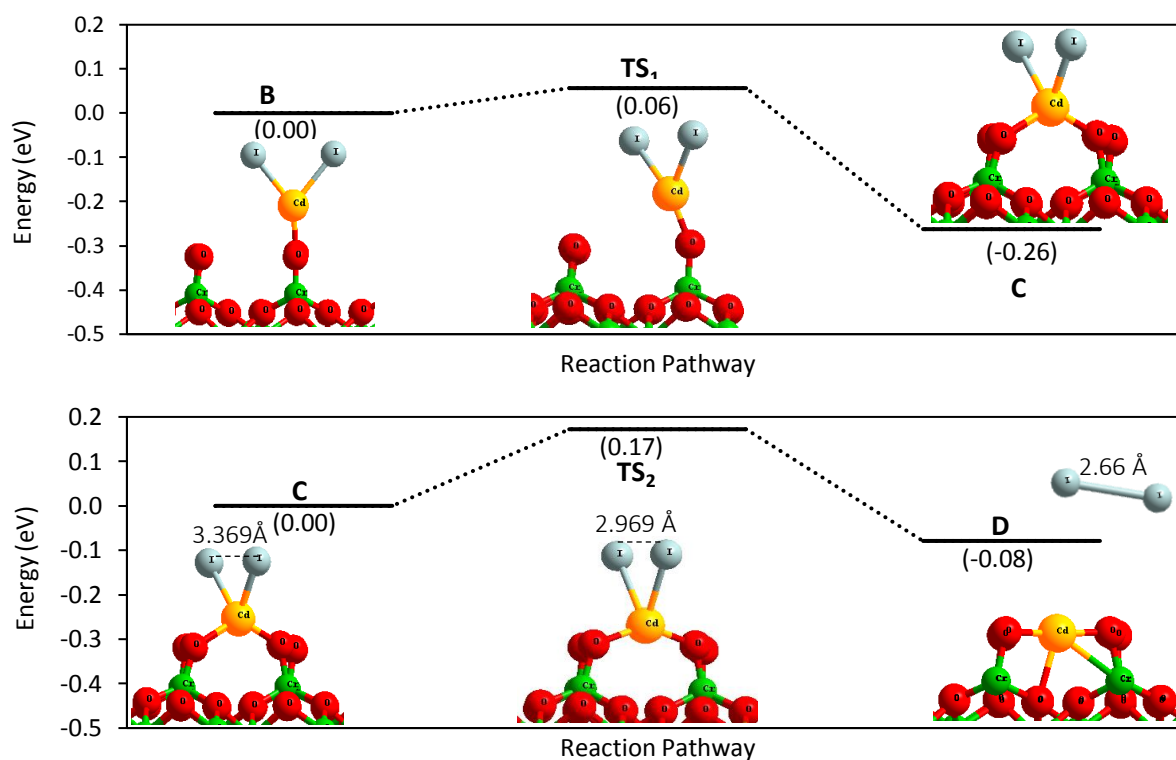
Figure 3.30. Energy diagram of transition states for formation of $I_{2(g)}$ on Chromyl surface with CdI$_2$ adsorbed with coverage equal to 25%. (top) transition state from state B to C (down) transition state from state C to D. Chromium: green. Oxygen: red. Cadmium: yellow. Iodine: grey.

3.3.2.2   *FORMATION OF $I_{2(g)}$ ON OXIDES SURFACES WITH AN OXIDANT.*

From **Figure 3.27**, it can be noticed that the formation of $I_{2(g)}$ on Cr$_2$O$_3$Cr and Fe$_2$O$_3$Fe is not possible. As a result, the formation of $I_{2(g)}$ on these two surfaces occurs only by adding an oxidant. In nuclear studies, OH$^\bullet$ is often used as an oxidant formed by water radiolysis. The energies of these reactions are grouped in **Table 3.9**. It can be observed that, once the oxidant is added, the formation of $I_{2(g)}$ will be spontaneous (reaction exothermic).

Table 3.9. Formation energy of $I_{2(g)}$ on oxide chromium and oxide iron surface with CdI_2 adsorbed in presence of oxidants ($OH^\bullet$).

Reaction	Model	Δ Energy (eV)
Surface-CdI_2 + 2$OH^\bullet$ → Surface-CdI_2-2OH →	Cr_2O_3Cr	-3.40
Surface-Cd-2OH + $I_{2(g)}$	Fe_2O_3Fe	-3.24

3.3.3 CONCLUSION

In conclusion, the formation of $I_{2(g)}$ is not possible on Cr_2O_3Cr and Fe_2O_3Fe surfaces with CdI_2 by pure thermal effect without any oxidant. The sublimation of CdI_2 is advantageous on these two surfaces. This result is similar to the conclusion drawn on AgI adsorption studies. The formation of $I_{2(g)}$ can only occur with 25% of CdI_2 adsorbed on Chromyl surface at temperature lower than 700 K. When a strong oxidant such as $OH^\bullet$ is present, the formation of $I_{2(g)}$ on neutral surfaces (Cr_2O_3Cr and Fe_2O_3Fe) become possible.

3.4 GENERAL CONCLUSION

In our study, the adsorption of control rod metal iodides on the oxide surfaces (chromium and iron oxides) representative of the RCS surfaces. Overall, the associative adsorption is more favourable than dissociative adsorption on almost all these surfaces (except AgI on Chromyl surface with a coverage lower than 25%).

When AgI adsorbs onto these surfaces, it tends to form a chain or ring structures on the surface forming bonds between silver atoms and oxygen atoms from the surface. The silver atom stays in a tripod structure (Ag-OOO, hollow site) on most of the surfaces except the chromyl one (oxidized chromium oxide surface). On the opposite, when CdI_2 is adsorbed on these surfaces, Cd only forms bonds with oxygen atoms of the surface when coverage is low (coverage ≤ 50%, except hydrated chromium oxide surface). Cd also stays in a tripod structure (Ag-OOO) on most of the surfaces except chromyl surface (oxidized chromium oxide surface). At high coverage, it will form a cycle that has no direct interaction with the surface. The adsorption of these two iodide molecules is always more favourable on a neutral surface than on a modified surface (oxidized or hydrated).The adsorptions on chromium oxide surface are always less favourable than on iron oxide surface.

H. Hijazi[28] has found that the formation of $I_{2(g)}$ from AgI aerosols without an oxidant is not possible for moderate temperature (~100°C). However, in our case, it is possible to form $I_{2(g)}$ from AgI adsorbed on an oxidized chromium oxide surface (Chromyl). However, the temperature needed to form $I_{2(g)}$ depends on the AgI coverage. At 25%, the formation is easier than over other coverage, due to formation of strong bonds between AgI moieties. Besides, for a surface totally covered by AgI, the range for the formation of $I_{2(g)}$ is quite small. This conclusion can explain the partial re-vaporization of $I_{2(g)}$ on stainless steel surface observed by D. Obada *et al.*[35]

The formation of $I_{2(g)}$ form CdI_2 adsorbed on the RCS surfaces shows similar trends. The formation of $I_{2(g)}$ will occur rapidly on the oxidized surface when the coverage is low ($CdI_2 \leq 25\%$. For both systems, the formation of $I_{2(g)}$ is unfavourable on a neutral surfaces (Cr_2O_3Cr and Fe_2O_3Fe) without the action of an oxidant ($OH^\bullet$).

REFERENCE

(1)   Nuclear Energy Agency/ Committee on the Safety of Nuclear installations. Insights into the Control of the Release of Iodine, Cesium, Strontium and Other Fission Products in the Containment by Severe Accident Management. 2000.

(2)   Weber, C. F.; Beahm, E. C.; Kress, T. S. *Models of Iodine Behavior in Reactor Containments*; Oak Ridge, TN, 1992.

(3)   Saenko, V.; Ivanov, V.; Tsyb, A.; Bogdanova, T.; Tronko, M.; Demidchik, Y. U.; Yamashita, S. The Chernobyl Accident and Its Consequences. *Clin. Oncol.* **2011**, *23* (4), 234–243.

(4)   Petti, D. A. Silver-Indium-Cadmium Control Rod Behavior in Severe Reactor Accidents. *Nucl. Technol.* **1989**, *84* (2), 128–151.

(5)   *The Merck Index: An Encyclopedia of Chemicals, Drugs, and Biologicals*, 14th ed.; O'Neil, M. J., Ed.; Merck and Co., Inc., 2006.

(6)   Williams, M. L. CRC Handbook of Chemistry and Physics, 76th Edition. *Occup. Environ. Med.* **1996**, *53* (7), 504–504.

(7)   Laird, T. Ullmann's Encyclopedia of Industrial Chemistry, 5th Edition VCH: Weinheim, Germany. 1996/1997. Section A, 28 Vols. Section B, 8 Vols. DM 19 400. *Org. Process Res. Dev.* **1997**, *1* (5), 391–392.

(8)   *Patty's Industrial Hygiene and Toxicology: Volume 2A, 2B, 2C*, 3rd ed.; Clayton, G. D., Clayton, F. E., Eds.; John Wiley Sons: New York, 1981.

(9)   Hull, S. Superionics: Crystal Structures and Conduction Processes. *Reports Prog. Phys.* **2004**, *67* (7), 1233–1314.

(10)   Verlag, T.; März, S. Cadmiumiodid. In: Römpp Chemie-Lexikon. **2002**.

(11)   Bernard, M.; Busnot, F. *Usuel de Chimie Générale et Minérale*; 2e cycle universitaire/écoles d'ingénieurs; Dunod, 1996.

(12)   Zinc, Cadmium and Mercury. In *Chemistry of the Elements*; Elsevier, 1997; pp 1201–1226.

(13)   Stull, D. R. Inorganic Compounds. *Ind. Eng. Chem.* **1947**, *39* (4), 540–550.

(14)   Nuclear Regulatory Commission. *Reactor Safety Study. An Assessment of*

Accident Risks in US Commercial Nuclear Power Plants. Executive Summary: Main Report; Nuclear Regulatory Commission, 1975.

(15) Lin, C.-C. Chemical Effects of Gamma Radiation on Iodine in Aqueous Solutions. *J. Inorg. Nucl. Chem.* **1980**, *42* (8), 1101–1107.

(16) Yeon, J. W.; Jung, S. H. Effects of Temperature and Solution Composition on Evaporation of Iodine as a Part of Estimating Volatility of Iodine under Gamma Irradiation. *Nucl. Eng. Technol.* **2017**, *49* (8), 1689–1695.

(17) Furrer, M.; Cripps, R. C.; Frick, E. Iodine Severe Accident Behaviour Code IMPAIR 2. 1989.

(18) Grégoire, A.-C.; Haste, T. Material Release from the Bundle in Phébus FP. *Ann. Nucl. Energy* **2013**, *61*, 63–74.

(19) Girault, N.; Bosland, L.; Dienstbier, J.; Dubourg, R.; Fiche, C. LWR Severe Accident Simulation: Fission Product Behavior in FPT2 Experiment. *Nucl. Technol.* **2010**, *169* (3), 218–238.

(20) Gouëllo, M.; Kalilainen, J.; Rantanen, P.; Kärkelä, T.; Auvinen, A. Experimental Study of the Cadmium Effects on Iodine Transport in the Primary Circuit During Severe Nuclear Accident. In *Volume 3: Next Generation Reactors and Advanced Reactors; Nuclear Safety and Security*; ASME, 2014.

(21) Bosland, L.; Cantrel, L. Iodine Behaviour in the Circuit and Containment: Modeling Improvements in the Last Decade and Remaining Uncertainties. In *Proceedings of the International OECD-NEA/NUGENIA-SARNET*; Marseille, France, 2015.

(22) Allelein, H. J.; Auvinen, A.; Ball, J.; Guentay, S.; Herranz, L. E.; Hidaka, A.; Jones, A.; Kissane, M.; Powers, D.; Weber, G. *State of the Art Report on Nuclear Aerosols*; 2009.

(23) Grégoire, A. C.; Haste, T. Material Release from the Bundle in Phébus FP. *Ann. Nucl. Energy* **2013**, *61*, 63–74.

(24) Cantrel, L.; Louis, F. Gas-Phase Reactivity of Cesium-Containing Species by Quantum Chemistry. **2015**.

(25) Grégoire, A. C.; Délicat, Y.; Tornabene, C.; Cousin, F.; Gasnot, L.; Lamoureux,

N.; Cantrel, L. Study of the Iodine Kinetics in Thermal Conditions of a RCS in Nuclear Severe Accident. *Ann. Nucl. Energy* **2017**, *101*, 69–82.

(26) Clement, B.; Cantrel, L.; Ducros, G.; Funke, F.; Herranz, L.; Rydl, A.; Weber, G.; Wren, C. State of the Art Report on Iodine Chemistry. 2007.

(27) Grégoire, A.-C.; Kalilainen, J.; Cousin, F.; Mutelle, H.; Cantrel, L.; Auvinen, A.; Haste, T.; Sobanska, S. Studies on the Role of Molybdenum on Iodine Transport in the RCS in Nuclear Severe Accident Conditions. *Ann. Nucl. Energy* **2015**, *78*, 117–129.

(28) Hijazi, H. Réactivité Chimique Des Aérosols d'iode En Conditions Accidentelles Dans Un Réacteur Nucléaire, Thesis, Université de Lille 1, 2017.

(29) Sugimoto, J.; Kajimoto, M.; Hashimoto, K.; Soda, K. Short Overview on the Definitions and Significance of the Late Phase Fission Product Aerosol/Vapour Source. 1994.

(30) Bottomley, P. D. W.; Knebel, K.; Van Winckel, S.; Haste, T.; Souvi, S. M. O.; Auvinen, A.; Kalilainen, J.; Kärkelä, T. Revaporisation of Fission Product Deposits in the Primary Circuit and Its Impact on Accident Source Term. *Ann. Nucl. Energy* **2014**, *74*, 208–223.

(31) Kalilainen, J.; Kärkelä, T.; Zilliacus, R.; Tapper, U.; Auvinen, A.; Jokiniemi, J. Chemical Reactions of Fission Product Deposits and Iodine Transport in Primary Circuit Conditions. *Nucl. Eng. Des.* **2014**, *267*, 140–147.

(32) Obada, D.; Mamede, A. S.; Nuns, N.; Grégoire, A. C.; Gasnot, L. Combined ToF-SIMS and XPS Characterization of 304L Surface after Interaction with Caesium Iodide under PWR Severe Accident Conditions. *Appl. Surf. Sci.* **2018**, *459* (May), 23–31.

(33) Haste, T.; Payot, F.; Bottomley, P. D. W. Transport and Deposition in the Phébus FP Circuit. *Ann. Nucl. Energy* **2013**, *61*, 102–121.

(34) Kress, T. S.; Beahm, E. C.; Weber, C. F.; Parker, G. W. Fission Product Transport Behavior. *Nucl. Technol.* **1993**, *101* (3), 262–269.

(35) Obada, D. Evaluation de Rejets Moyen-Terme En Situation Accidentelle Grave d'un Réacteur à Eau Pressurisée : Étude Expérimentale de La Re-Vaporisation de Dépôts de Produits de Fission (Cs, I),Thesis, Université de Lille 1, 2017.

(36) Souvi, S. M. O.; Badawi, M.; Virot, F.; Cristol, S.; Cantrel, L.; Paul, J.-F. Influence of Water, Dihydrogen and Dioxygen on the Stability of the Cr_2O_3 Surface: A First-Principles Investigation. *Surf. Sci.* **2017**, *666*, 44–52.

(37) Souvi, S. M. O.; Badawi, M.; Paul, J.-F.; Cristol, S.; Cantrel, L. A DFT Study of the Hematite Surface State in the Presence of H_2, H_2O and O_2. *Surf. Sci.* **2013**, *610*, 7–15.

(38) Bader, R. F. W. A Quantum Theory of Molecular Structure and Its Applications. *Chem. Rev.* **1991**, *91* (5), 893–928.

(39) Sheppard, D.; Terrell, R.; Henkelman, G. Optimization Methods for Finding Minimum Energy Paths. *J. Chem. Phys.* **2008**, *128* (13).

(40) Henkelman, G.; Uberuaga, B. P.; Jónsson, H. Climbing Image Nudged Elastic Band Method for Finding Saddle Points and Minimum Energy Paths. *J. Chem. Phys.* **2000**, *113* (22), 9901–9904.

(41) Henkelman, G.; Jónsson, H. Improved Tangent Estimate in the Nudged Elastic Band Method for Finding Minimum Energy Paths and Saddle Points. *J. Chem. Phys.* **2000**, *113* (22), 9978–9985.

CHAPTER 4   REACTIVITY OF RUTHENIUM IN SEVERE ACCIDENT CONDITIONS

Early October 2017, a mysterious presence of ^{106}Ru has been detected in almost all European countries with activities ranging from a few µBq/m^3 to about 150 mBq/m^3.[1] This type of ruthenium isotope could not be observed in normal condition in the atmospheres. Until now, the cause and exact location of this release have not been confirmed. However, it should be recognized that during a nuclear accident, ruthenium radionuclide (including ^{106}Ru) can be released outside from the reactor containment as gaseous ruthenium tetroxide and aerosol of ruthenium dioxide. A great part of ruthenium released is deposited on the reactor coolant system (RCS) surface.[2,3] In this chapter, the adsorption of ruthenium oxide on the surface of the reactor coolant system (chromium and iron oxide surfaces) will be presented. Furthermore, the possible formation of volatile ruthenium oxide ($RuO_{4(g)}$) from these adsorbed surfaces and the ruthenium dioxide aerosols ($RuO_{2(s)}$) will be studied.

4.1 LITERATURE REVIEW ON RUTHENIUM

Ruthenium is one of the fission products that can be formed by fission of uranium. C. Mun *et al.*[4] made a review of ruthenium behaviour and have presented three reasons why ruthenium is important in nuclear safety study. Firstly, the amount of ruthenium rises with fuel burn up and increases with fuel enrichment in ^{235}U for identical burn up. Furthermore, it becomes even greater in a mixed-oxide fuel (Pu/U). Hence, the quantity of ruthenium formed during fuel life will continuously rise in the future. Secondly, ruthenium is a high-specific-activity fission product. Thirdly, not only for their chemical toxicity, from a radiological point of view, ^{103}Ru and ^{106}Ru are also two isotopes who have medium and high toxicity.[5] As a consequence, ruthenium is radiologically important in both short-term and middle-term.

4.1.1 PHYSICAL PROPERTIES OF RUTHENIUM AND RUTHENIUM OXIDES

Ruthenium has 34 known isotopes, with a mass number varying between 87 and 120. Among them, 7 isotopes are stable (^{96}Ru, ^{98}Ru, ^{99}Ru, ^{100}Ru, ^{101}Ru, ^{102}Ru and ^{104}Ru) and 27 radioisotopes are radioactive with various half-lives. The most stable radioisotopes are the following: ^{106}Ru ($t_{1/2}$ = 373.59 d, β^- decay), ^{103}Ru ($t_{1/2}$ = 39.26 d, β^- and γ decay), ^{97}Ru ($t_{1/2}$ = 2.9 d, β^+ and γ decay).[6] Ruthenium can be found under metallic and oxides. Ru can exist in several oxidation states, from 0 to +8. In our works, only most stable ruthenium oxides will be studied with oxidation states equal to +2, +4, +6 and +8 (RuO, RuO_2, RuO_3 and RuO_4)[3].
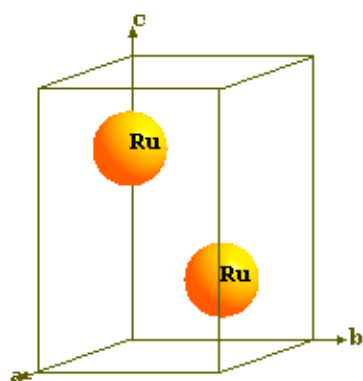
Figure 4.1. Crystal model for metallic ruthenium.

4.1.1.1 PHYSICAL PROPERTIES OF RUTHENIUM

Ruthenium is a rare transition metal belonging to the platinum group and it presents as a lustrous metal[6]. Its melting point is equal to 2607 K and its boiling point is equal to 4423 K. Its density near room temperature is equal to 12.1 g/cm^3.[7] The solid ruthenium has four allotropic structures. It appears in hexagonal close-packed (hcp) (P6$_3$/mmc, **Figure 4.1**) below 1273.15 K.[7,8]

4.1.1.2 PHYSICAL PROPERTIES OF RUTHENIUM OXIDES.

Ruthenium monoxide (RuO) has been found only in the gaseous phase at high temperature (> 1600 K, **Figure 4.2** (a)) and no solid form has been identified.[3] Ruthenium dioxide (RuO_2) is the most stable and most common form of ruthenium oxides. It is a grey-black solid with density equal to 7.05 g.cm^{-3} meanwhile its boiling point is equal to 1470 K and it is not soluble in water or in acid.[7] As lots of dioxide species, solid ruthenium dioxide shows a rutile structure (TiO_2 type, **Figure 4.2** (b)). The gas form of RuO_2 is represented in **Figure 4.2** (c) and it can be noticed that the distance between Ru and O atom in solid from (1.94 - 1.98 Å) is higher than in gas form (1.68 Å). Furthermore, according to F. Garisto[9], the ruthenium dioxide can exist in gas form only at very high temperature (> 2000 K). The existence of RuO_3 has been proved experimentally by H. Schäfer[10] and W. E. Bell[11]. However, until now, it can only be found in gas form and its geometry is shown in **Figure 4.2** (d). It can be noticed that all four atoms (1 Ru and 3 O) are in the same plan[12] and the distance between Ru

atom and O atoms increases slightly compared to the one for RuO_2(g) (from 1.68 Å to 1.69 Å). Ruthenium tetroxide is the most oxidised and was probably the main form released in early October 2017[1]. Ruthenium tetroxide appears in a prism with a yellow colour in solid form.[7] Its density equal to 3.29 g.cm^{-3} and its melting point is equal to 25.4 °C.[7] RuO_4 is highly volatile and its vapour is very toxic with a pungent odour like ozone.[6,13] It can enter in the humans' body mainly by the respiratory system[14]. The decomposition of RuO_4 begins at 40 °C[7] and a complete decomposition is observed at about 108°C[15]. Its decomposition is limited by kinetic factors as, at room temperature, the partial pressure in equilibrium with $RuO_{2(s)}$ is equal to 10^{-20} bar. Ruthenium tetroxide is soluble in water (20.3 g/L at 20 °C and 22.4 g/L at 74 °C) and also in acids, alkalis, ethanol and especially carbon tetrachloride (freely soluble)[16]. The model for RuO_4 is shown in **Figure 4.2** (e). It can be noticed that RuO_4 stays in a tetrahedral structure with distance between Ru atom and O atoms equal to 1.70 Å.
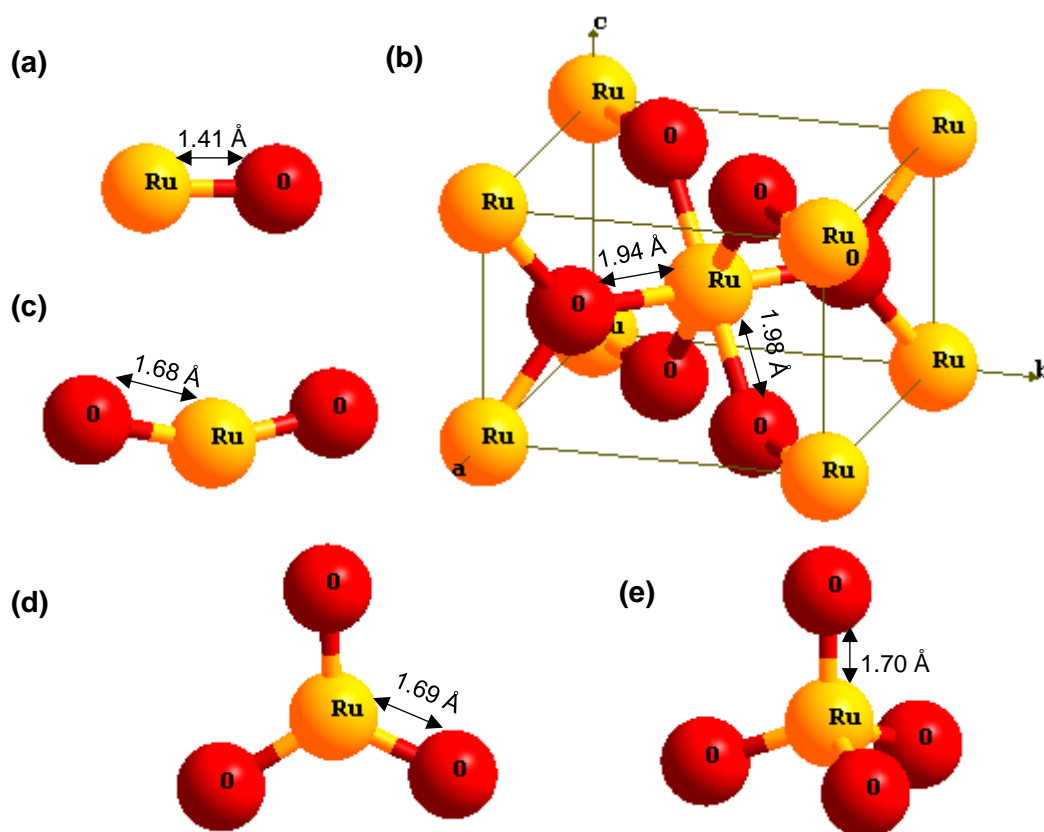
Figure 4.2. Theoretical models for ruthenium oxides molecules: (a) ruthenium monoxide (gas) (b) ruthenium dioxide (solid) (c) ruthenium dioxide (gas) (d) ruthenium trioxide (gas) (e) ruthenium tetroxide (gas). Ruthenium: yellow; Oxygen: red.

4.1.2 RUTHENIUM OXIDES BEHAVIOUR IN SEVERE ACCIDENT CONDITIONS

During a severe nuclear accident of a pressurized water reactor (PWR), the fission products (FPs) can be released from the nuclear fuel. Then it could be transported in the reactor coolant system (RCS) and may reach the reactor containment. In the end, they may be released to environment. Among all the possible fission products, ruthenium oxides are particularly important due to their high reactivity, high volatility and toxicity. The non-volatile forms are mainly deposited on the reactor cooling system surfaces and also on the containment surfaces. In this section, firstly literature on chemical relativity of ruthenium oxides will be presented including their thermodynamic proprieties and on the behaviour in severe accident conditions. In the end, literature on interactions between ruthenium oxides and reactor coolant system and containment surfaces will be described.

4.1.2.1 CHEMICAL REACTIVITY OF RUTHENIUM OXIDES.

The chemical reactivity of ruthenium oxides is complex. At high temperature, all the studied oxide species (RuO, RuO_2, RuO_3 and RuO_4) are in gas form.

4.1.2.1.1 Experimental and Theoretical Studies on Different Ruthenium Oxides

Using mass spectrometry, J. H. Norman et al.[17] have detected the formation of RuO, RuO_2, RuO_3, and RuO_4 vapour over $Ru_{(s)}$ surface under O_2 atmosphere for a temperature over 1000 K. Furthermore, H. Schäfer et al.[10] found that at 1273.15 K, RuO_4, RuO_3 and RuO_2 can be decomposed into RuO. On the other hand, experimentally, B. Eichler et al.[3] observed the existence of RuO above 1900 K. RuO_2 is not quite stable under gas form. By exposing to oxygen, it can form RuO_3 and RuO_4, and then, as RuO_3 and RuO_4 are thermodynamically unstable, decomposition of these two oxide compounds should be attended when temperature decreases. This process can be explained with following reaction[3,18]:

$$RuO_2 + \frac{1}{2}O_2 \rightleftharpoons RuO_3 \qquad \qquad \textit{Equation 4.1}$$

$$RuO_2 + O_2 \rightleftharpoons RuO_4 \qquad \qquad \textit{Equation 4.2}$$

C. Mun et al.[4] have calculated the equilibrium constant for direct sense of *Equation 4.2*, it is equal to 5×10⁻¹⁷ at 373 K. For oxygen partial pressure of ~0.2 bar, only ~3×10⁻

[19] mol/L of ruthenium tetroxide will be formed. Hence, the formation of ruthenium tetroxide from ruthenium dioxide in presence of dioxygen is weak. Furthermore, A. Leudet[19] calculated the equilibrium constant for the reverse reaction as follows:

$$ln \, K = \frac{14880}{T} - 11.53 + 1.135 \, ln \, T \quad \text{(T in K)}$$ *Equation 4.3*

The equilibrium constant calculated decreases with increase of temperature (for example: at 293 K, $K=7\times10^{19}$; at 373 K, $K=2\times10^{15}$). Hence, if equilibrium is reached, the decomposition is almost complete, RuO_4 decomposes to RuO_2. C. Mun et al.[20] have proposed different decomposition mechanisms for $RuO_{4(g)}$ both in dry and humid air atmospheres (**Table 4.1**).

Table 4.1. Chemical steps leading to $RuO_{4(g)}$ decomposition, with or without steam.[20]

N°	Reactions	Steps	
Eq. 4.4	$RuO_4(g) \rightarrow RuO_3\,(g) + \frac{1}{2}O_2$	Initiation processes	Low
Eq. 4.5	$RuO_4(g) + H_2O(g) \rightarrow H_2RuO_5$		Fast
Eq. 4.6	$RuO_3(g) \rightarrow \frac{1}{2}Ru_2O_5 + \frac{1}{4}O_2$	First $+VI \rightarrow +V$	Low
Eq. 4.7	$H_2RuO_5 \rightarrow \frac{1}{2}Ru_2O_5 \cdot 2H_2O + \frac{3}{4}O_2$	Reduction $+VIII \rightarrow +V$	Intermediate
Eq. 4.8	$RuO_3(g) + RuO_2(s) \rightarrow Ru_2O_5(s)$	Catalytic effect of RuO_2	Fast
Eq. 4.9	$Ru_2O_5(s) \rightarrow 2RuO_2(s) + \frac{1}{2}O_2$	Final $+V \rightarrow +IV$	?
Eq. 4.10	$\frac{1}{2}Ru_2O_5 \cdot 2H_2O + 2H_2O \rightarrow 2(RuO_2 \cdot 2H_2O) + \frac{1}{2}O_2$	Reduction $+V \rightarrow +IV$	?

In a dry environment, RuO_4 decomposes firstly to $RuO_{3(g)}$ in the gas phase (*Eq. 4.4*). Then $RuO_{3(g)}$ reduces to $Ru_2O_{5\,(s)}$ directly (*Eq. 4.6*) or by another reaction path that is supposed to be much faster with RuO_2 as catalyse (*Eq. 4.8*). In a second step, the decomposition of $Ru_2O_{5\,(s)}$ to $RuO_{2\,(s)}$ will take place (*Eq. 4.9*). It should be noticed that, once RuO_2 is formed, the formation of Ru_2O_5 by catalytic way (*Eq. 4.8*) will be much more rapid than the direct formation (*Eq. 4.6*). In a humid environment, $RuO_4(g)$ can be dissolved in water and formed hyper-ruthenic acid (*Eq. 4.5*). And then, hyper-

ruthenic acid is reduced in two steps to the hydrated form of RuO_2 (*Eq. 4.7* and *Eq. 4.10*).

4.1.2.1.2 *Thermodynamic Properties of Ruthenium Species in Gas From.*

In order to predict ruthenium behaviour in severe accident conditions, the thermodynamic properties of ruthenium species in gas from have been studied by experimental and theoretical approaches.[9,21–24] Parts of results for the standard enthalpies of formation ($\Delta_f H°$) of ruthenium and ruthenium oxides were classed in **Table 4.2**.

Table 4.2. Standard enthalpies of formation $\Delta_f H°_{(298\ K)}$ of ruthenium and ruthenium oxides in kJ/mol

Species	Cordfunke and Konings[21,25]	Garisto[9]	Zimmerman *et al.*[23]	Miradji *et al.*[24]
$Ru_{(g)}$	649.0 ± 3.0	649.6 ± 13.0 [26]	640 ± 4	638.4 ± 2.1
$RuO_{(g)}$	376 ± 25	372.0 ± 42.0 [27]	376 ± 4	420.4 ± 1.6
$RuO_{2(g)}$	136 ± 10	133.7 ± 15.0	140 ± 4	140.3 ± 1.0
$RuO_{3(g)}$	-64.1 ± 2.5	-48.4 ± 12.7	-58 ± 4	-50.7 ± 0.5
$RuO_{4(g)}$	-188.0 ± 0.4	-187.1 ± 8.4	-188 ± 4	-

E. Cordfunke and R. Konings[21,28] determined the Gibbs energy of formation for different compounds with experimental data (E.M.F[29], electron diffraction[30] or mass spectrometry[17,31,32]). F. Garisto[9] used average enthalpies of formation for $Ru_{(g)}$ which is calculated by J. Rard[26] using several experimental and theoretical works[17,31–34]. For standard enthalpy of formation of $RuO_{(g)}$, it is extrapolated from the value proposed by J. Pedley[27] which is based on the experimental measurement using mass spectrometric performed by J. Norman *et al.*[17]. The standard enthalpies of formation of $RuO_{2(g)}$, $RuO_{3(g)}$ and $RuO_{4(g)}$ have been determined by using a second or third law of thermodynamic from high temperature vapour pressure data[10,11,17,26,35]. G. Zimmerman *et al.*[23] have estimated enthalpies of formation mainly based on some mass spectrometric data[17] and some additional knowledges of structures and vibrational frequencies obtained from low-temperature matrix studies[12,36]. Theoretically, F. Miradji *et al.*[24] use TPSSh-5% HF for geometry optimization followed

by CCSD(T) (single and double coupled cluster theory with inclusion of a perturbative estimation for triple excitation using MOLPRO40[37] software package) with complete basis set (CBS) extrapolations for the calculation of the total electronic energies of ruthenium species. They used experimental standard enthalpy of formation of RuO_4 and have derived the $\Delta_fH°_{(298\,K)}$ value from four reactions for each ruthenium oxide and they calculated the average $\Delta_fH°_{(298\,K)}$ value for each oxide. As a result, the energetic uncertainties obtained are quite small.

4.1.2.1.3   Overview

The thermodynamic instability of RuO_4 has been evidenced many times by experimental and theoretical works. Moreover, standard enthalpies of formation have been measured and calculated in literatures. Furthermore, in the same project as our work (MiRE project (Mitigation of outside releases in case of nuclear accident) of IRSN), P. Nérisson et al.[38] studied the filtration on RuO_4 by a sand filter and a metallic filter. They found these filters employed in French PWRs have no practically retention for $RuO_{4(g)}$ but thermal decomposition can promote the trapping. However, a remarkable decrease of quantity of RuO_4 could be noticed, due to the reduction of $RuO_{4(g)}$ to $RuO_{2(s)}$ which occurs for a temperature between 100 °C and 120 °C. This result is coherent with literature[15] where RuO_4 reaches a complete decomposition at 108 °C.

Knowing the boiling point of all our mainly chemical forms of ruthenium, it can be noticed that they all tendency to be present in gas form at high temperature (except $Ru_{(s)}$). Ruthenium species at thermodynamic equilibrium at 1 bar pressure and in $50_{wt}\%$ air-steam mixture are shown in **Figure 4.3**. This chemical speciation is calculated by U. Backman et al.[39]. It can be noticed that ruthenium metal solid exist only at very high temperature (over 1450 °C) and in gas forms, there are two dominant gaseous vapour species (RuO_3 and RuO_4). As we mentioned before (Chapter IV section 4.1.1.2), RuO only exist above 1350 °C (1633 K) in gas form. Furthermore, above 1300 °C, a great amount of $RuO_{2(g)}$ could be formed, exactly as in nuclear reactor core accident conditions. Hence, in severe nuclear accident, RuO, RuO_2, RuO_3 and RuO_4 may all be present in gas form. Furthermore, two thermodynamic equilibrium calculations have similar profiles, the only important difference is the formation of $RuO_3OH_{(g)}$ under $50_{wt}\%$ air-steam mixture but the thermodynamic data of this species has been reviewed recently and with these new data, it is no longer a stable form[40].
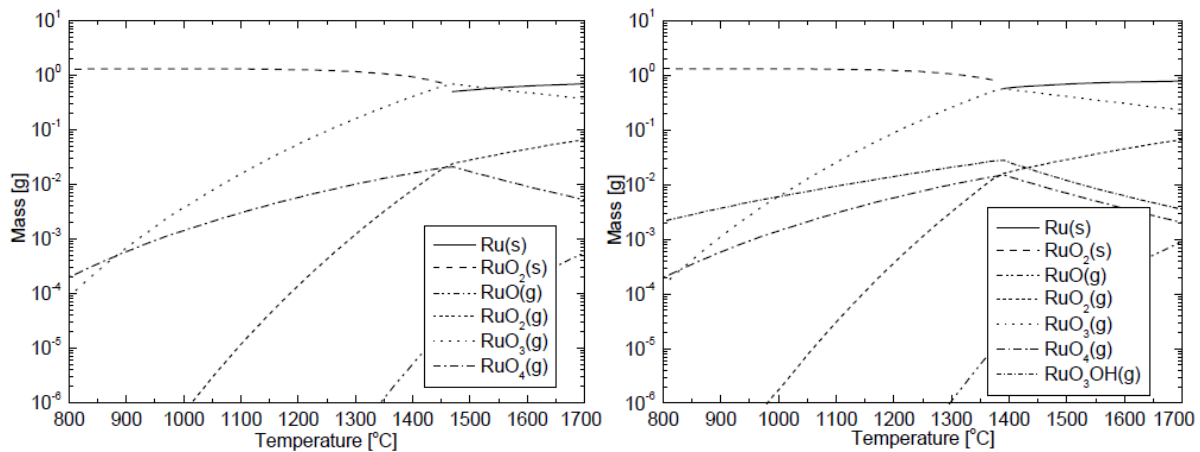
Figure 4.3. (Left) Ruthenium species at thermodynamic equilibrium in air at 1 bar pressure. (Right) Ruthenium species at thermodynamic equilibrium in 50_{wt}% air-steam mixture.[39]

4.1.2.2 BEHAVIOUR OF RUTHENIUM RELEASE FROM DEGRADED FUEL AND TRANSPORT IN THE REACTOR COOLANT SYSTEM.

P. Froment *et al.*[41] investigated the behaviour of ruthenium under severe accident conditions. They overheated U and Ru oxide mixtures in order to study released particles (including ruthenium oxides) which depends on many conditions (for example: the fuel matrix, the temperature, the oxygen potential of the atmosphere in contact with the fuel). When RuO_2 is heated in argon, dismutation of oxide leads to the emission of volatile RuO_3-RuO_4 following the equation below with an activation energy equal to 172 kJ/mol.

$$RuO_2(s) \rightarrow Ru_m(s) + RuO_{3,4}(g) \qquad \text{Equation 4.11}$$
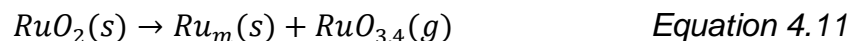
When mixtures of U and Ru oxides heated under air, higher oxidation state species are emitted firstly which may pre-exist in the starting pellet materials and then lower oxidation ruthenium species are released after 40s. However, they did not identify the released species.

VTT Technical Research Centre of Finland (U. Backman *et al.*[39,42] and T. Kärkelä *et al.*[43,44]) have run several experiments in order to study ruthenium transport and deposition in reactor coolant system (RCS) in case of serve accident condition. They found that the ruthenium can be transported under several oxidation state. $RuO_{4(g)}$ has been detected in trapping bottle in different percentages depending on the experimental condition. This trapping of RuO_4 will be discussed in the next section (Chapter IV section 4.1.2.3). In addition, depending on the experimental conditions,

12–35 $_{wt}$% of the released ruthenium was trapped in the outlet filter as RuO_2 particles. The ratio of RuO_2 particles could be improved by seed particles and sharper temperature gradient. Depending on the reactor temperature, the composition of gaseous ruthenium is different. At 1300 K, ruthenium was transported in gaseous form ($RuO_{4(g)}$) and the increase of steam partial pressure increases the fraction of gaseous ruthenium. Above 1500 K, ruthenium species are transported almost totally as aerosol particles ($RuO_{2(s)}$) and the gaseous ruthenium seemed to react on the surface of the stainless steel tube where RuO_2 particles had been deposited.

As RuO_2 can also be used in catalytic reaction, numerous theoretical studies[45–49] have been performed on this system. The most stable surface for RuO_2 is (1 1 0) surface[47–49] (**Figure 4.4**) which has also been confirmed by our calculations.
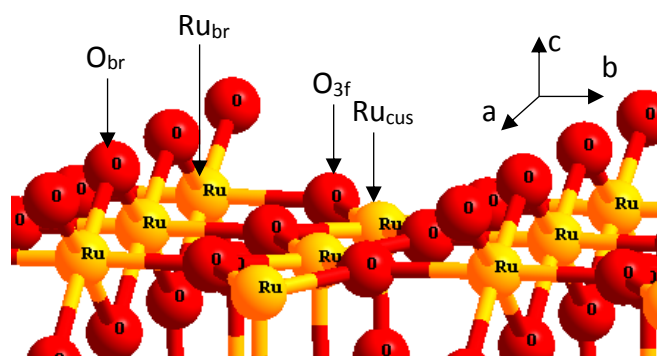
Figure 4.4. Theoretical model for RuO_2 (1 1 0) surface. Respectively, the directions a, b, and c are [0 0 1], [-1 1 0] and [1 1 0]. The definitions for different special sites (Ru_{br}, Ru_{cus}, O_{br} and O_{3f}) are indicated in the figure. Ruthenium: yellow. Oxygen: red.

H. Wang *et al.*[49] has studied the O_2 dissociation on the RuO_2 (1 1 0) surface. They found that O_2 adsorbed in bridging position between two adjacent Ru_{cus} atoms (low coordination Ru atoms) is the most stable geometry for a molecular adsorption. However, the dissociative adsorption of O_2 on the same position (*cus-cus*) is about 0.6 eV more favourable. When all Ru_{cus} sites are occupied in a 7-fold coordinated structure, the adsorption energy per O_2 adsorbed is about 1.0 eV less favourable than the one for lower coverage. They also calculated the transition states between different adsorption modes. They found that, diffusion of O atoms on the surface along *cus* row has activation energy about 1.3 eV.

4.1.2.3 INTERACTIONS BETWEEN RUTHENIUM OXIDES REACTOR COOLANT SYSTEM AND CONTAINMENT SURFACES.

Current studies generally believe that $RuO_{(g)}$, $RuO_{2(g)}$ and $RuO_{3(g)}$ could not reach the containment as they are thermodynamically unstable below 1000 °C, as a result, only $RuO_{4(g)}$ might be present in containment.[4]

P. Cains and S. Barnes[50] deposited volatile ruthenium on steel surfaces and found that above 150 °C the deposition could happen and deposits are under crystalline $RuO_{2\,(s)}$ without bonding with steel surfaces. The decomposition of $RuO_{4(g)}$ on the surface has been observed by previous mentioned experiments and other experiments[51,52] according to the reaction described by *Equation 4.12*.

$$RuO_4(g) \rightarrow RuO_2(s) + O_2(g)$$
Equation 4.12
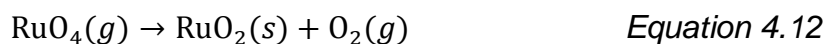
Only few experimental studies have observed the presence of RuO_3. B. Eichler *et al.*[3] studied the volatilization and deposition of ruthenium oxides in a thermal gradient tube. They detected Ru, RuO_2, RuO_3 and RuO_4 according to different conditions in the tube. Furthermore, G. Zimmermann *et al.*[23] studied the photochemical decomposition of RuO_4, they found that Ru, RuO, RuO_2 and RuO_3 have been observed during the photochemical decomposition.

T. Sakuria *et al.*[53] have adsorbed $RuO_{4(g)}$ on stainless steel, Ni, Cu, and Au metals and have tried to identify the products by X-ray analysis and XPS. They did not observe any liberation of $O_{2(g)}$ and, by XPS analysis, they concluded that no ruthenium oxide nor metal oxides were formed. Hence, they supposed that adsorbed RuO_4 stays in a peroxide state on the metals with Ru-O-O-Ru bonds linked between two RuO_4 molecules. However, the results have never been reproduced. J. Holm *et al.*[2] have studied the deposition of ruthenium tetroxide on various surfaces (aluminium, copper and zinc who represent in reactor containment) using X-ray photoelectron spectroscopy (XPS), scanning electron microscopy (SEM), X-ray diffraction (XRD) and inductivity coupled plasma-mass spectrometry (ICP-MS). Anhydrous ruthenium dioxide, hydrous ruthenium dioxide and copper-hydro-oxo-oxoruthenate are identified in ruthenium deposits. Over 300 °C, according to XPS analysis, anhydrous ruthenium dioxide could be found on the surface. SEM and ICP-MS results show that there is more ruthenium deposit on copper and zinc surfaces than on aluminium surface.

Hence, they conclude that $RuO_{4(g)}$ reacts fast and extensively on metal surfaces in severe accident condition.
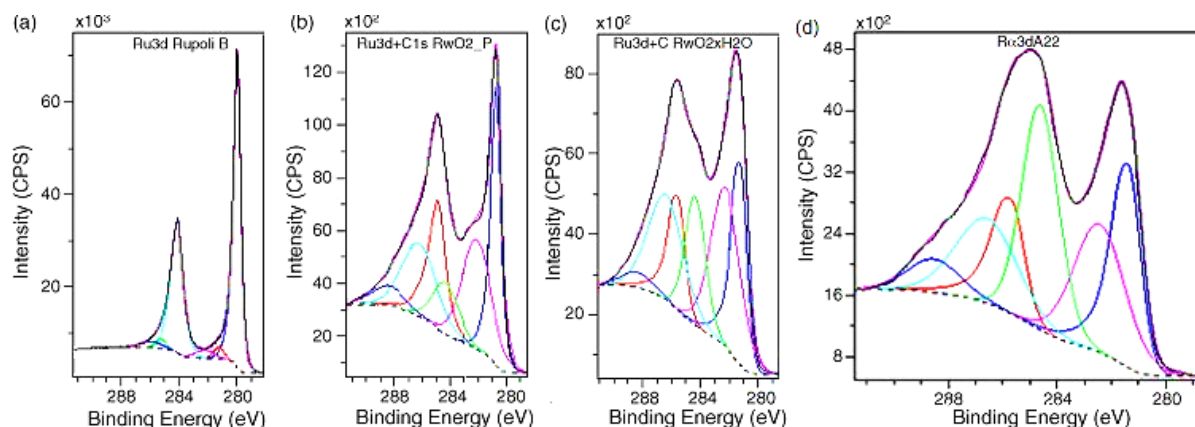
Figure 4.5. XPS spectra of Ru 3d core level lines: (a) on a clean metallic sample, (b) of anhydrous RuO_2, (c) of hydrated $RuO_2 \cdot xH_2O$, (d) of a ruthenium layer deposited on a piece of stainless steel.[54]

C. Mun *et al.*[54] have studied ruthenium deposition on the inner surface of nuclear reactor containment buildings by XPS. They compare the XPS spectra of a ruthenium layer deposited on a piece of stainless steel (**Figure 4.5** d) with reference spectra (metallic ruthenium, anhydrous ruthenium dioxide and hydrated ruthenium dioxide, **Figure 4.5** a, b, c). The shape of the Ru 3d for stainless steel samples is similar to the one for hydrated $RuO_2 \cdot xH_2O$ (**Figure 4.5** c). Therefore, ruthenium species deposited on the surface show in an IV oxidation state. Furthermore, it was observed that the ruthenium species form on the stainless steel surface is in the same state as the one formed on a painted stainless steel surface. As mentioned in the previous section, VTT Technical Research Centre of Finland (U. Backman *et al.*[39,42] and T. Kärkelä *et al.*[43,44]) have run several experiments in order to study ruthenium transport and deposition in reactor coolant system (RCS) in case of serve accident condition. With a stainless steel tube in a dry atmosphere, they found that only very small part of the released ruthenium (0.1%–0.2%) can reach the trapping bottle. As they did not observe same results with an alumina tube, they think that the stainless steel surface may play an important role in the decomposition of RuO_4 to RuO_2. And they found that the re-vaporization of the deposited RuO_2 particles is a very significant source of gaseous ruthenium oxides. However, in an atmosphere completely saturated with water vapour at ambient temperature, 5% of the released ruthenium was detected in trapping bottle (50 times more than the previous case in dry condition). It seems that no decomposition of RuO_4

has took place, hence they suspected that water vapour passivated the stainless steel surface. Besides, they supposed that RuO_2 deposits are mainly deposited by decomposition of RuO_3 to the stainless steel surface. Furthermore, they found that, above 1500 K, the gaseous ruthenium reacts on the surface of the stainless steel tube where RuO_2 is deposited. In additional, the re-vaporization of ruthenium leads to a percentage of Ru transported in gaseous form that reaches up to 65%. They think that this indicates that the surfaces of RCS may act as a source of volatile ruthenium species even in the late phase of an accident. The nature of the stainless steel (oxidised or neutral) plays an important role for retention of gaseous RuO_4. At high temperature, RuO_4 can be trapped by oxidized stainless steel surface efficiently and the presence of RuO_2 on the surface can improve the retention and catalysed the decomposition of RuO_4. Additionally, at about 100-150 °C, the surface is more efficient for RuO_4 trapping. Intensive works were also performed by IRSN concerning the transport of ruthenium inside the RCS and it was evidenced potential revaporisation of Ru deposits at high temperature (T > 800°C) for oxidised stainless steel tube.[55]

Besides, it can be noticed that, all previous literature is based on experimental studies. No theoretical study has been performed on this kind of situation.

4.1.3 CONCLUSION

It can be concluded that, at high temperature, all our interested oxide species (RuO, RuO_2, RuO_3 and RuO_4) are in gas form. RuO_3 and RuO_4 are not very stable and can be decomposed into RuO_2. RuO_2 may even have a catalytic effect on the decomposition process. Moreover, in severe accident conditions, ruthenium can be partially transported inside the reactor coolant system and containment in gaseous form ($RuO_{4(g)}$ and $RuO_{3(g)}$) or aerosol form ($RuO_{2(s)}$). Hence, it is important to understand the reaction occurring on the reactor cooling system surfaces and the $RuO_{2(s)}$ aerosol surface. Furthermore, RuO_2 can be deposited on the stainless steel surface directly or by decomposition of RuO_3 and RuO_4. Besides, at high temperature, RuO_4 can be trapped by oxidized stainless steel surface efficiently and the presence of RuO_2 on the surface can improve the retention and catalyses the decomposition of RuO_4. Moreover, the presence of steam may restrict the decomposition of RuO_4 on the stainless steel surface. Therefore, the objective is to study the ruthenium behaviour on these surfaces (RCS and RuO_2 aerosol) in a theoretical way in order to complement

experimental observations and better understand how the ruthenium oxides are adsorbed on the surface (deposition and decomposition) and how the mechanism of re-vaporization for volatile ruthenium oxide species occurs.

Consequently, in the following sections, different ruthenium oxides will be adsorbed on the stainless steel surfaces in order to understand all the processes that can occur on these surfaces (deposition, decomposition and re-vaporization). Then, the reaction which can be performed on the surface of $RuO_{2(s)}$ aerosol will be discussed. In the end, the formation of $RuO_{4(g)}$ from adsorbed RuO_2 surface will be investigated using *ab initio* molecular dynamics.

4.2 Adsorption of Ruthenium Oxides on Chromium and Iron Oxide Surfaces.

As mentioned in a previous section (Chapter IV section 4.1.2), in most of the experimental studies concerning the deposition of $RuO_{4(g)}$ on stainless steel surfaces, the ruthenium deposits appear as $RuO_{2(s)}$. However, there are still some misunderstanding on the formation of these species. For example, in some of the experimental studies RuO_3 and RuO_4 are observed on the surface[3,23,53]. Consequently, in this section, first of all, a theoretical study on the adsorption of ruthenium dioxide, ruthenium trioxide and ruthenium tetroxide on the stainless steel surface and the mechanisms leading to the re-vaporization ruthenium oxide deposits will be performed. The objective is to understand the competition between stability of RuO_2, RuO_3 and RuO_4 on the surface and how RuO_3 or RuO_4 can be transformed into RuO_2 on the surface. This section includes a thermodynamic and a kinetic study.

4.2.1 Thermodynamic Study

The thermodynamic study on the surface of stainless steel will be presented into three parts: the adsorption of RuO_2, RuO_3 and RuO_4.

4.2.1.1 Adsorption of RuO_2 on Chromium and iron oxide Surfaces

Firstly, RuO_2 molecules are adsorbed on the four different surfaces mentioned before (Chapter I section 1.5.2) in order to understand the adsorption of ruthenium dioxide on stainless steel surface: **Cr₂O₃Cr** (neutral chromium oxide surface), **Chromyl** (oxidized
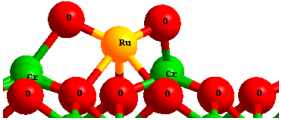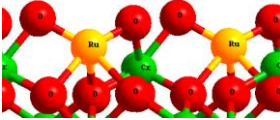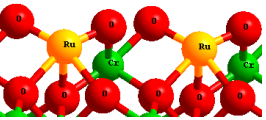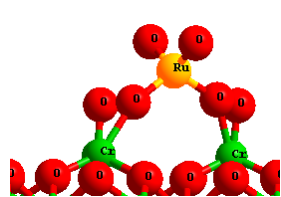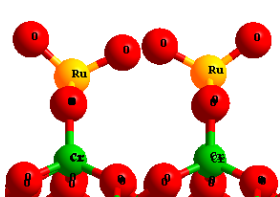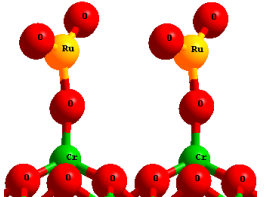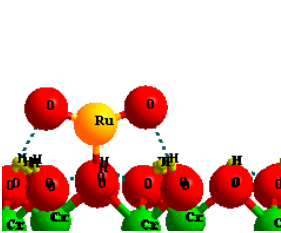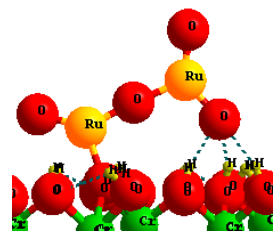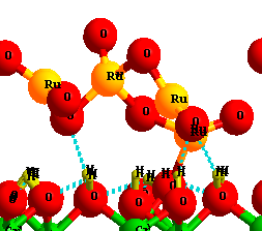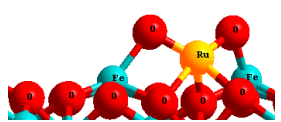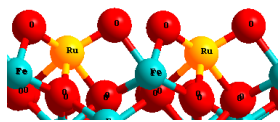
chromium oxide surface), **$Cr_2O_3Cr_2(OH)_3$** (hydrated chromium oxide surface) and **Fe_2O_3Fe** (neutral iron oxide surface)[56,57]. The adsorption simulations are run under different coverages which can be described by equation below:

$$r = \frac{n_{RuO_2 \ adsobed}}{n_{adsorbed \ sites}}$$

- ▪ $n_{RuO_2 \ adsobed}$: Number of adsorbed RuO_2 molecules.
- ▪ $n_{adsorbed \ sites}$: Number of Cr or Fe sites available for RuO_2 adsorption.

The most stable structures for adsorption geometry of RuO_2 molecules on these four surfaces are presented for different coverages in **Table 4.3**. It can be noticed that all the most stable structures are molecular adsorption. Hence, it can be concluded that RuO_2 will not dissociate on these surfaces.

Table 4.3. Adsorption of RuO_2 on chromium and iron oxide surfaces in function of coverage. Chromium: green. Iron: blue. Oxygen: red. Hydrogen: light yellow. Ruthenium: yellow.

| | Model | Coverage of RuO_2 (%) | | |
		25	50	100
Cr	Cr_2O_3Cr			
	Chromyl			
	$Cr_2O_3Cr_2(OH)_3$			
Fe	Fe_2O_3Fe			

Furthermore, in order to compare the adsorption of RuO_2 on different surfaces, the adsorption energies per RuO_2 molecule are computed and summarized in **Table 4.4.** This energy is calculated according to equation mentioned in Chapter II Section 2.5.2 which can be written as below for adsorption of RuO_2:

$$E_{ads} = \frac{E_{total} - E_{surface} - \left(E_{RuO_2} \times n_{RuO_2}\right)}{n_{RuO_2}}$$

with $E_{ads} < 0$, corresponding to an exothermic reaction.

Table 4.4. Adsorption energy per RuO_2 adsorbed for different coverages on chromium and iron oxide surfaces.

	Model	Coverage of RuO_2 (%)		
		25	50	100
	Cr_2O_3Cr	-3.26 eV	-3.25 eV	-3.03 eV
Cr	Chromyl	-3.50 eV	-3.30 eV	-2.64 eV
	$Cr_2O_3Cr_2(OH)_3$	-1.59 eV	-1.83 eV	-2.25 eV
Fe	Fe_2O_3Fe	-3.80 eV	-3.71 eV	-2.78 eV
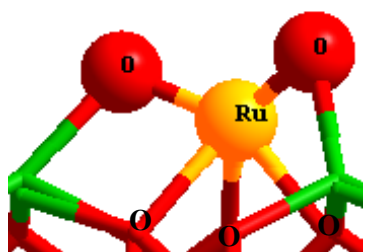
Figure 4.6. Tripod structure of RuO_2 on the surface. Cr: green. O: red. Ru: yellow.

For the adsorption of RuO_2 on **Cr_2O_3Cr** (neutral chromium oxide surface), the most stable structure of RuO_2 on this surface is in tripod (Ru-OOO, **Figure 4.6**) where ruthenium atom is placed in an hollow site of the surface. For the other coverages, RuO_2 does not polymerize on the surface. The adsorption energy for 25% and 50% coverages is equal to -3.25 eV per adsorbed molecule. For a surface totally covered by RuO_2 the adsorption energy is slightly lower (-3.03 eV per molecule adsorbed).

On the **Chromyl** surface (oxidized chromium oxide surface), adsorption geometry of RuO_2 on this surface is different from the others. At 25% coverage, ruthenium atom is situated between two terminal oxygen atoms of the surface and forms a tetrahedral-like structure, the adsorption energy is equal to -3.50 eV. When the coverage reaches 50%, the adsorption geometry is similar to 25% one. The adsorption energy is equal to -3.30 eV. When coverage increases to 100%, RuO_2 molecules form planar triangle

species with terminal oxygen atoms (**Figure 4.7** b) with a smaller adsorption energy (-2.64 eV for 100% coverage). It should be noticed that RuO_2 are isolated on this surface.
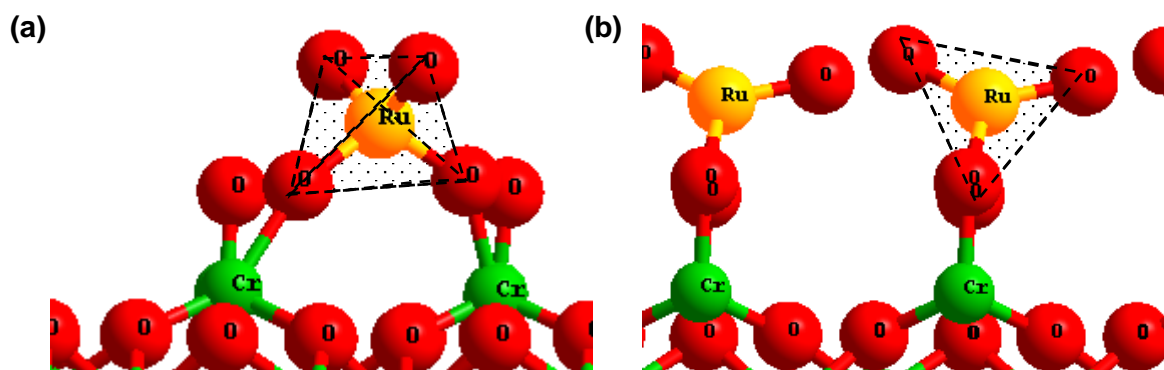
Figure 4.7. Side view for adsorption direct of RuO_2 with (a) 25 % and (b) 100 % coverage on the Chromyl surface. Chromium: green. Oxygen: red. Ruthenium: yellow.

On the **$Cr_2O_3Cr_2(OH)_3$** surface (hydrated chromium oxide surface), at 25% coverage, RuO_2 molecule is isolated on the surface and ruthenium atom from a bond with one oxygen atom of the surface and this oxygen atom and three atoms from RuO_2 are located in the same plan (same geometry as RuO_3). Compared to other chromium oxide surfaces, its adsorption energy is less favourable (-1.59 eV). When coverage increases to 50%, in the most stable structure, RuO_2 molecules form a dimer. The adsorption energy is a little more favourable than for the lower coverages (-1.83 eV) due to the formation of dimer. When coverage reaches 100%, RuO_2 molecules polymerize on the surface with an adsorption energy being equal to -2.25 eV. The adsorption on the hydrated surface may be a source for the aerosol formation. As for the adsorption of iodine species, we study the adsorption on RuO_2 on the totally saturated hydrate surface (with 6 H_2O) (**Figure 4.8** a). Thermodynamic stability of this surface has been discussed in recent study (named $Cr-O_3-H-Cr-OH-(H_2O)_2$ in the article)[57] and it is stable at ambient temperature with pressure above 3 bars. The presence of water molecules on the surface does not prevent RuO_2 adsorption on the surface. The ruthenium atom still presents in a tripod structure on the surface (Ru-OOO,**Figure 4.8** b). The adsorption energy, for 25% coverage of RuO_2 on this surface, is slightly more favourable (-3.35 eV) than on the surface without water (-3.26 eV on Cr_2O_3Cr surface). The adsorption of the second RuO_2 molecule is more favourable (-3.42 eV). The Ru is still located in a threefold hollow site (**Appendix** Figure A.3 b). When more RuO_2 molecules are adsorbed on the surface, the adsorption energy decreases as water molecules present on the surface inhibit adsorption of RuO_2. RuO_2

molecule begins to "float" on the surface where it can only form hydrogen bonds with the water molecules (**Appendix** Figure A.3 c and d).

(a)

(b)
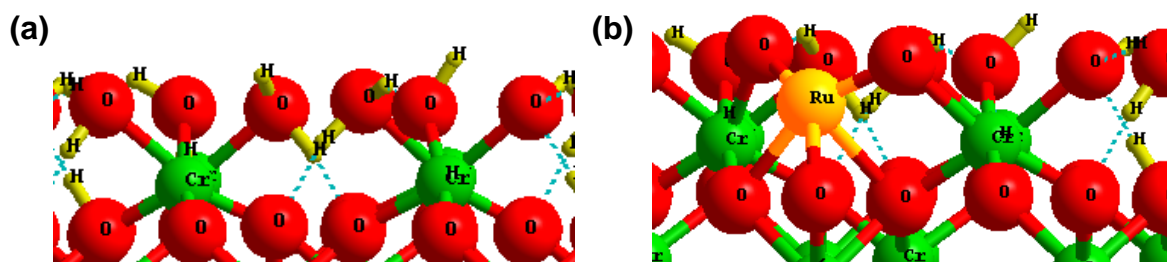
Figure 4.8. a) Totally saturated hydrate chromium oxide surface (with six water molecules). b) RuO$_2$ adsorbed on totally saturated hydrate chromium oxide surface. Chromium: green. Oxygen: red. Ruthenium: yellow. Hydrogen: light yellow.
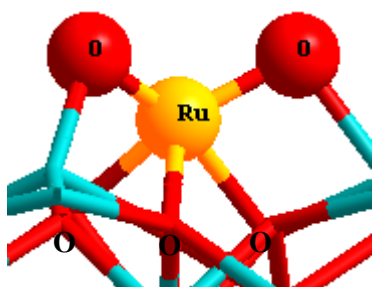
Figure 4.9. Tripod structure of RuO$_2$ on the surface. Fe: Blue. O: red. Ru: yellow.

On **Fe$_2$O$_3$Fe** surface (neutral iron oxide surface), RuO$_2$ adsorbed on this surface in a geometry similar to the neutral chromium oxide surface (Cr$_2$O$_3$Cr). Ruthenium atom is located in hollow position of the surface with a tripod structure (Ru-OOO, **Figure 4.9**). For larger coverage, RuO$_2$ always stay isolated on the surface. However the adsorption energy decreases with augmentation of coverage. For 25%, 50% and 100% coverages, their adsorption energies are respectively equal to -3.80 eV, -3.71 eV and -2.78 eV. It can be noticed that the adsorption of RuO$_2$ on this surface (neutral iron oxide surface) is slightly more favourable for lower coverage (≤ 50%) than on neutral chromium oxide surface.

4.2.1.2 ADSORPTION OF RuO$_3$ ON CHROMIUM AND IRON OXIDE SURFACES

Secondly, RuO$_3$ molecules are adsorbed on four different surfaces mentioned before (Chapter I section 1.5.2) in order to understand the adsorption of ruthenium trioxide on stainless steel surface: **Cr$_2$O$_3$Cr** (neutral chromium oxide surface), **Chromyl** (oxidized chromium oxide surface), **Cr$_2$O$_3$Cr$_2$(OH)$_3$** (hydrated chromium oxide surface) and **Fe$_2$O$_3$Fe** (neutral iron oxide surface)[56,57]. The adsorption simulations are run for different coverages which can be described by equation below:
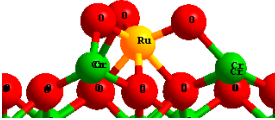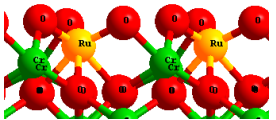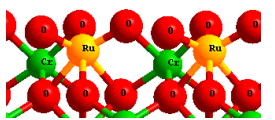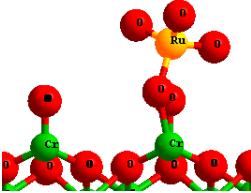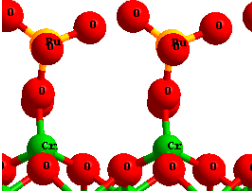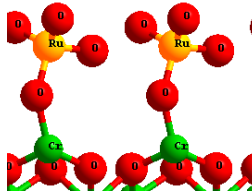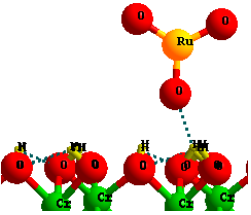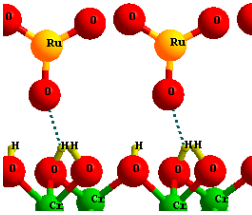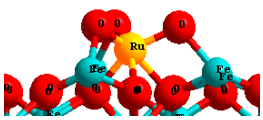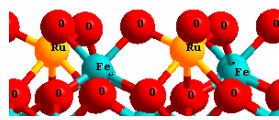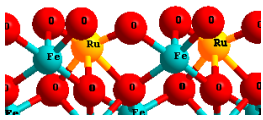
$$r = \frac{n_{RuO_3\ adsobed}}{n_{adsorbed\ sites}}$$

- $n_{RuO_3\ adsobed}$: Number of adsorbed RuO$_3$ molecules.

- $n_{adsorbed\ sites}$: Number of Cr or Fe sites available for RuO_3 adsorption.

The geometry of the most stable structures for adsorption of RuO_3 molecules on these surfaces are presented in **Table 4.5**. It can be noticed that all most stable structures are molecular ones.

Table 4.5. Adsorption of RuO_3 on chromium and iron oxide surfaces in function of coverage. Chromium: green. Iron: blue. Oxygen: red. Hydrogen: light yellow. Ruthenium: yellow.

Model	Coverage of RuO_3 (%)		
	25	50	100
Cr	Cr_2O_3Cr		
	Chromyl		
	$Cr_2O_3Cr_2(OH)_3$		
Fe	Fe_2O_3Fe		

Furthermore, in order to compare the adsorption of RuO_3 on different surfaces, the adsorption energies per RuO_3 molecule adsorbed are calculated and summarized in **Table 4.6**. This energy is calculated by equation mentioned in Chapter II Section 2.5.2 which can be written as below for adsorption of RuO_3:

$$E_{ads} = \frac{E_{total} - E_{surface} - \left(E_{RuO_3} \times n_{RuO_3}\right)}{n_{RuO_3}}$$

with $E_{ads} < 0$, corresponding to an exothermic reaction.

Table 4.6. Adsorption energy per RuO_3 adsorbed for different coverages of RuO_3 on chromium and iron oxide surfaces.

Model		Coverage of RuO_3 (%)		
		25	50	100
Cr	Cr_2O_3Cr	-3.14 eV	-3.08 eV	-2.83 eV
	Chromyl	-1.68 eV	-1.65 eV	-1.62 eV
	$Cr_2O_3Cr_2(OH)_3$	-0.16 eV	-0.15 eV	-0.13 eV
Fe	Fe_2O_3Fe	-3.51 eV	-2.95 eV	-2.17 eV
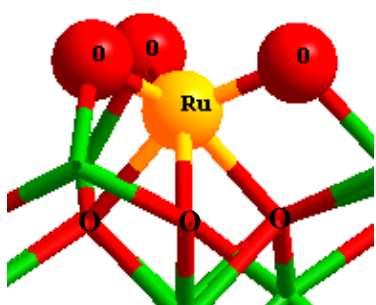
Figure 4.10. Tripod structure of RuO_3 on the surface. Cr: green. O: red. Ru: yellow.

For adsorption of RuO_3 on **Cr_2O_3Cr** (neutral chromium oxide surface), as adsorption of RuO_2 on this surface, the most stable structure of RuO_3 on this surface is also in a hollow site (Ru-OOO, **Figure 4.10**). For different coverages, RuO_3 is always isolated on the surface. The adsorption energy per molecule adsorbed decreases with increasing of coverage. For 25% coverage, the adsorption energy is equal to -3.14 eV. For 50% RuO_3 covered the surface, adsorption energy reduces (-2.08 eV) and the adsorption position of RuO_3 does no change. For a surface totally covered by RuO_3, its adsorption energy is equal to -2.83 eV. Furthermore, it should also be noticed that for coverages higher than 50%, the configuration of RuO_3 shows a perfect epitaxy with the surface (**Figure 4.11**). The Ru atoms continue the Cr_2O_3 structure **Figure 4.11** (c).
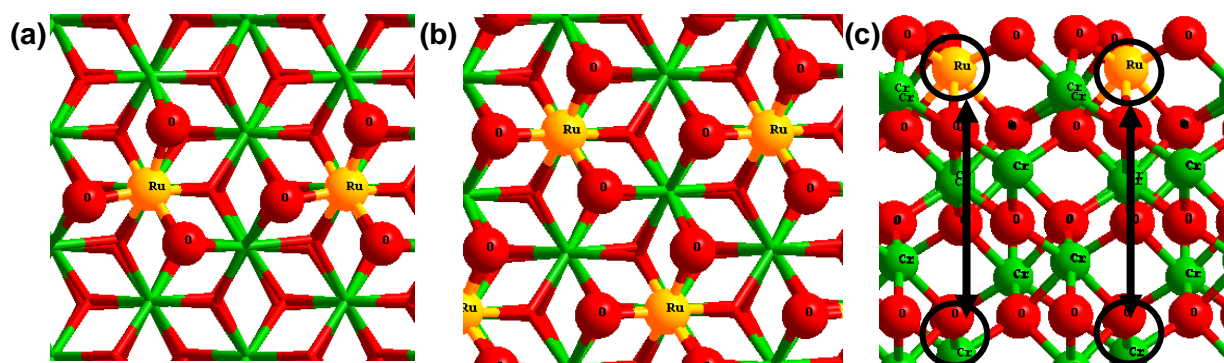
Figure 4.11. Top view for adsorption of RuO_3 with (a) 50% (b) 100% coverage and (c) side view for adsorption of RuO_3 with 100% coverage on the Cr_2O_3Cr surface. Chromium: green. Oxygen: red. Ruthenium: yellow.

On the **Chromyl** surface (oxidized chromium oxide surface), the RuO_3 molecules adsorbed on this surface do not polymerize. Ruthenium atom is in the centre of a tetrahedral configuration formed by three oxygens from RuO_3 and one oxygen atom from the surface (terminal oxygen atom). When RuO_3 is adsorbed on one terminal oxygen atom, the Cr-O bond of this oxygen atom is slightly tilted (the charge of ruthenium atoms will be discussed in the following part as its nature seems to have changed). The adsorption energy per molecule adsorbed is very close and reduces slightly with increasing of coverage (25%: -1.68 eV; 50%: -1.65 eV; 100%: -1.62 eV).

On the **$Cr_2O_3Cr_2(OH)_3$** surface (hydrated chromium oxide surface), RuO_3 molecules only create hydrogen bonds with the surface. The adsorption energy is very low (-0.15 eV per RuO_3 adsorbed). Comparing adsorption energy per RuO_3 adsorbed on this surface with the others, it can be concluded that hydrated surface does not favour RuO_3 adsorption. As for RuO_2, we study the totally saturated hydrated surface (**Figure 4.8** a). The conclusions are similar to the RuO_2 ones. The presence of water molecules on the surface does not prevent the absorption of the first two RuO_3 molecules on the surface (**Figure 4.12**). In this case, ruthenium atom is still in a hollow site (Ru-OOO, **Figure 4.10**). The adsorption energy for 25% and 50% coverage of RuO_3 on this surface is slightly more favourable than on the other surfaces (25%: -3.24 eV and 50%: -3.19 eV; 25%: -3.14 eV and 50%: -3.08 eV on Cr_2O_3Cr surface). However, with more RuO_3 molecules adsorbed on the surface, the adsorption energy is reduced to -2.41 eV for 75% coverage and -1.93 eV for 100% coverage. RuO_3 cannot form bonds with oxygen atoms of the surface (**Appendix** Figure A.4 c and d).
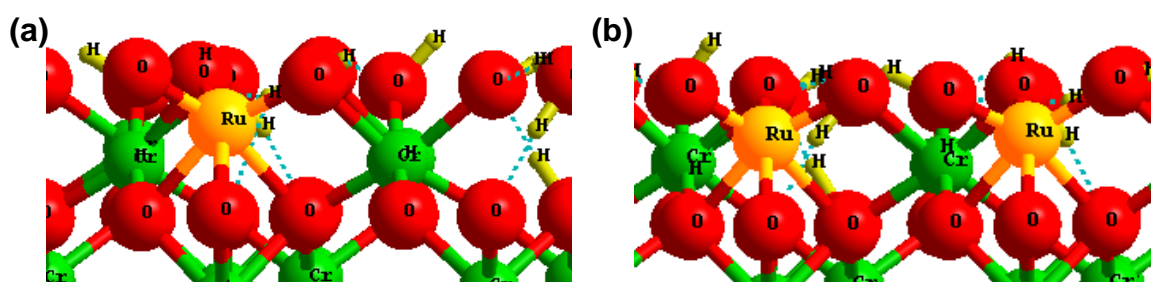
Figure 4.12. RuO_3 adsorbed on totally saturated hydrate chromium oxide surface with (a) 25% and (b) 50% coverage. Chromium: green. Oxygen: red. Silver: yellow. Iodine: grey. Hydrogen: light yellow.

For **Fe_2O_3Fe** surface (neutral iron oxide surface), the geometry in which RuO_3 is adsorbed on this surface is similar to the one on neutral chromium oxide surface
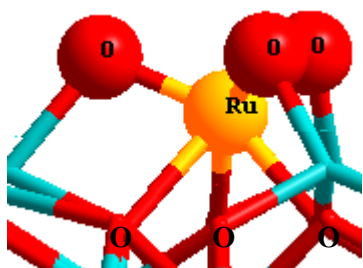
Figure 4.13 Tripod structure of RuO_3 on the surface. Fe: Blue. O: red. Ru: yellow.

(Cr_2O_3Cr). Ruthenium atom is located in hollow position (Fe-OOO, **Figure 4.13**). For different coverages, RuO_3 always stays alone on the surface. There is a significant decrease of adsorption energy when coverage increases (25%: -3.51 eV; 50%: -2.95 eV; 100%: -2.17 eV). For coverage equal to 50%, as for the adsorption on Cr_2O_3Cr surface, adsorption position of RuO_3 has no influence on adsorption energy. For coverage higher than 50%, the configuration of RuO_3 is in perfect epitaxy with the surface (**Figure 4.14**). The Ru atoms continue the Fe_2O_3 structure **Figure 4.14** (c).
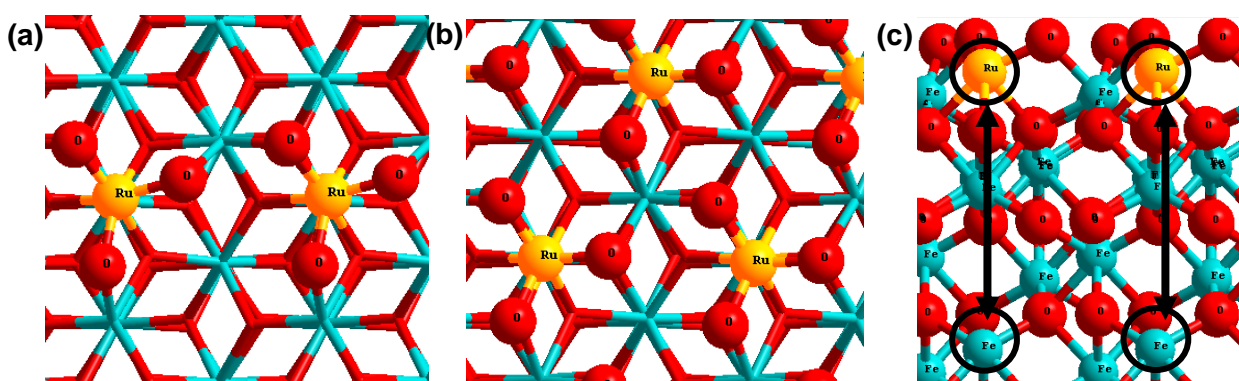
Figure 4.14. Top view for adsorption of RuO_3 with (a) 50% (b) 100% coverage and (c) side view for adsorption of RuO_3 with 100% coverage on the Fe_2O_3Fe surface. Iron: Blue. Oxygen: red. Ruthenium: yellow.

4.2.1.3 ADSORPTION OF RuO_4 ON CHROMIUM AND IRON OXIDE SURFACES

RuO_4 molecules were adsorbed on four different surfaces mentioned before (Chapter I section 1.5.2) in order to understand the adsorption of ruthenium tetroxide on stainless steel surface: **Cr_2O_3Cr** (neutral chromium oxide surface), **Chromyl** (oxidized chromium oxide surface), **$Cr_2O_3Cr_2(OH)_3$** (hydrated chromium oxide surface) and **Fe_2O_3Fe** (neutral iron oxide surface)[56,57].

The adsorption simulations are run under different coverages which can be described by equation below:

$$r = \frac{n_{RuO_4\ adsobed}}{n_{adsorbed\ sites}}$$

- $n_{RuO_4\ adsobed}$: Number of adsorbed RuO_4 molecules.

- $n_{adsorbed\ sites}$: Number of Cr or Fe sites available for RuO_4 adsorption.

Table 4.7. Adsorption of RuO₄ on chromium and iron oxide surfaces in function of coverage. Chromium: green. Iron: blue. Oxygen: red. Hydrogen: light yellow. Ruthenium: yellow.

	Model	Coverage of RuO₄ (%)		
		25	50	100
	Cr₂O₃Cr			
Cr	Chromyl			
	Cr₂O₃Cr₂(OH)₃			
Fe	Fe₂O₃Fe			
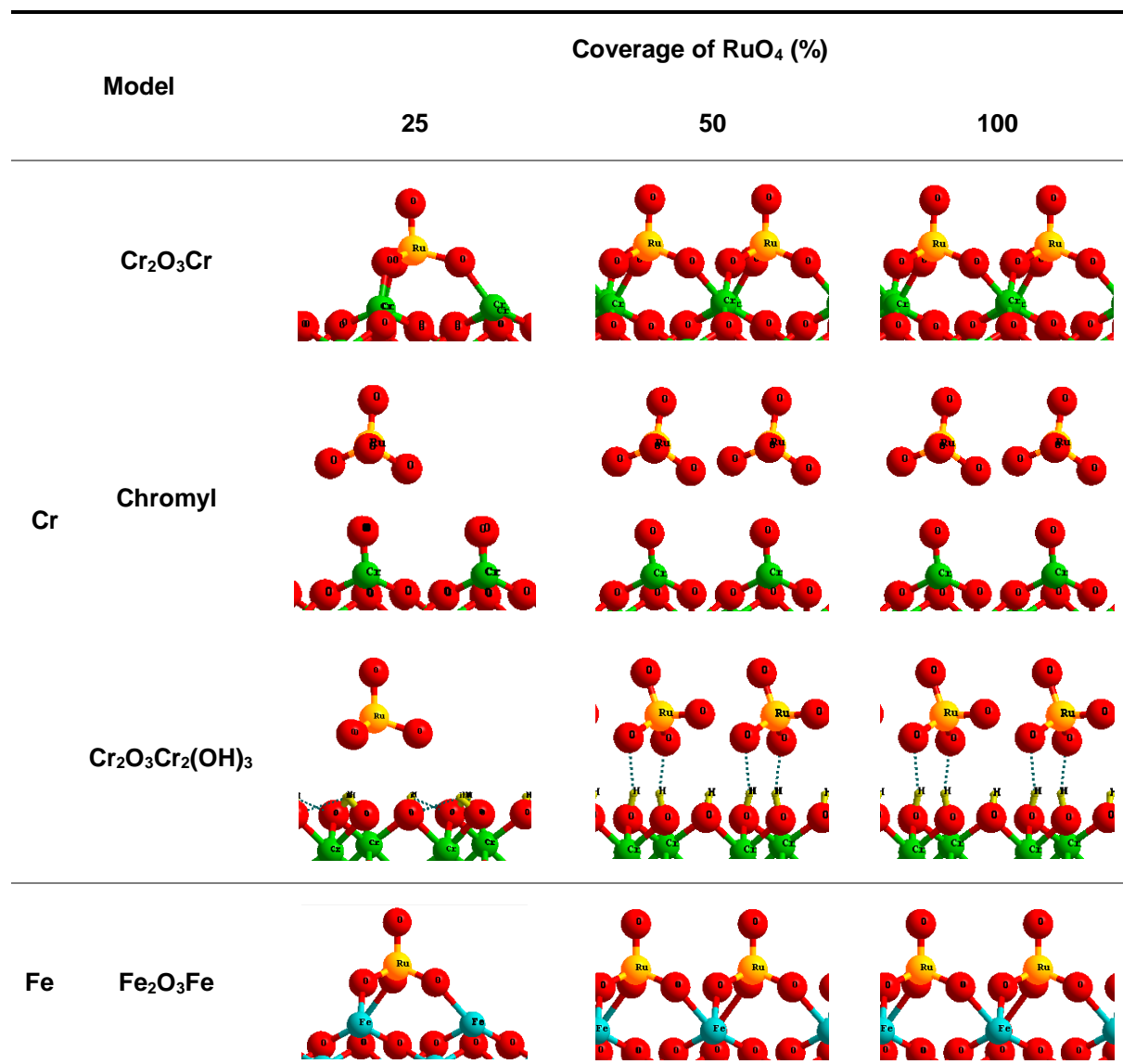
The most stable structures for RuO₄ adsorption on these four surfaces are presented in **Table 4.7**. It can be noticed that all most stable structures are molecular ones. The adsorption energies are presented in **Table 4.8.** They are computed according to the following equation:

$$E_{ads} = \frac{E_{total} - E_{surface} - \left(E_{RuO_4} \times n_{RuO_4}\right)}{n_{RuO_4}}$$

with $E_{ads} < 0$, corresponding to an exothermic reaction.

Table 4.8. Adsorption energy per RuO_4 adsorbed for different coverages of RuO_4 on chromium and iron oxide surfaces.

	Model	Coverage of RuO_4 (%)		
		25	50	100
Cr	Cr_2O_3Cr	-1.89 eV	-1.30 eV	-1.10 eV
	Chromyl	-0.10 eV	-0.08 eV	-0.05 eV
	$Cr_2O_3Cr_2(OH)_3$	-0.12 eV	-0.00 eV	-0.01 eV
Fe	Fe_2O_3Fe	-1.86 eV	-1.21 eV	-0.72 eV
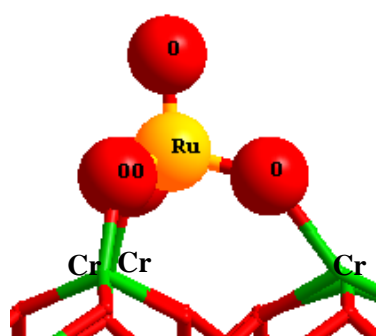
Figure 4.15. Configuration of RuO_4 on the surface. Cr: green. O: red. Ru: yellow.

The RuO_4 adsorption on **Cr_2O_3Cr** (neutral chromium oxide surface), differs from the adsorption of the other ruthenium oxide species. The most stable structure of RuO_4 on this surface presents no bond between ruthenium atom and oxygen atoms of the surface. However, the oxygen atoms of RuO_4 form bonds with chromium atoms of the surface (**Figure 4.15**) and RuO_4 is still tetrahedral. For all the coverage, RuO_4 is isolated on the surface. The interaction energy per molecule adsorbed becomes less favourable with augmentation of the coverage. For 25% coverage, the adsorption energy equal to -1.89 eV, for 50%, it reduces to -1.30 eV. It should be noted that the relative adsorption positions of RuO_4 have no influence on adsorption energy which means that all the sites on the surface are identical (**Figure 4.16**). For a surface totally covered by RuO_4, its adsorption energy is equal to -1.10 eV per RuO_4 adsorbed.
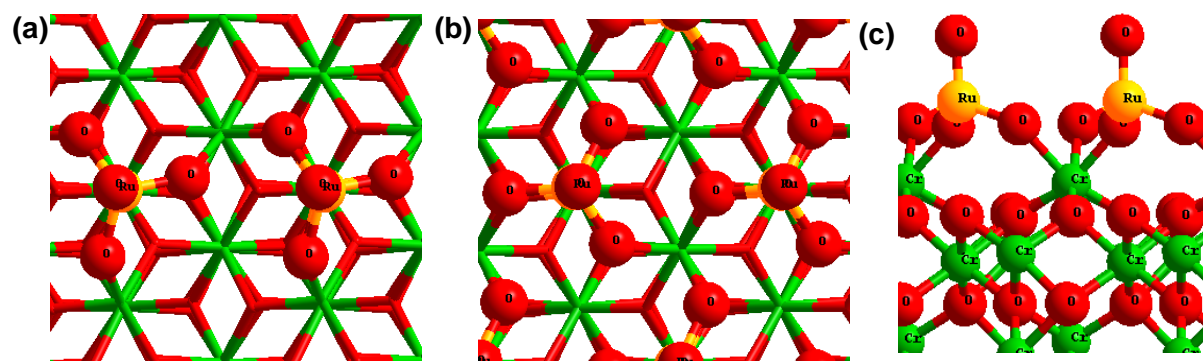
Figure 4.16. Top view for adsorption of RuO_4 with (a) 50% (b) 100% coverage and (c) side view for adsorption of RuO_4 with 50% and 100% coverage on the Cr_2O_3Cr surface. Chromium: green. Oxygen: red. Ruthenium: yellow.

For the adsorption on **Chromyl** surface (oxidized chromium oxide surface) and **Cr₂O₃Cr₂(OH)₃** surface (hydrated chromium oxide surface), RuO_4 molecule is isolated above the surface. The adsorbed RuO_4 creates no real bond with the surface. On the hydrated surface, hydrogen bonds are created between oxygen atoms of ruthenium tetroxide and the hydrogen atoms of the surface. The adsorption energies per molecule adsorbed are all close to zero, even for the most favourable one, the adsorption energy is equal to only -0.12 eV. Hence, it can be concluded that Chromyl surface and $Cr_2O_3Cr_2(OH)_3$ surfaces are not favourable for adsorption of RuO_4. This effect may cause by the tetrahedral geometry of RuO_4 which makes it a nonpolar molecule and almost non-polarizable (as ClO_4^-). Consequently, this molecule has only small Van der Waals interactions with surfaces that do not present Levis site. As other ruthenium oxide species, the adsorption on the totally hydrated surface (**Figure 4.8** a) was tested. The presence of water molecules on the surface does not prevent first RuO_4 to adsorb on the surface. The water molecules are displaced to allow the formation of bond between the RuO_4 oxygen atoms and the chromium of the surface (25% coverage, **Figure 4.17** a). The adsorption for 25% coverage of RuO_4 on this surface is less favourable (E_{ads} = -1.37 eV) compared to surface without water (-1.89 eV on Cr_2O_3Cr surface). However, with more RuO_4 molecules adsorbed on the surface, RuO_4 molecules began to "float" on the surface without creating any kind of bonds, however, the first adsorbed RuO_4 molecule is always adsorbed on the surface (**Figure 4.17** b and **Appendix** Figure A.5) and their adsorption energies per RuO_4 adsorbed decrease (50%: -0.94 eV; 75%: -0.64 eV and 100%: -0.51 eV) which indicates that the interaction of the last three RuO_4 molecules with the surface is almost null.

(a)   (b)
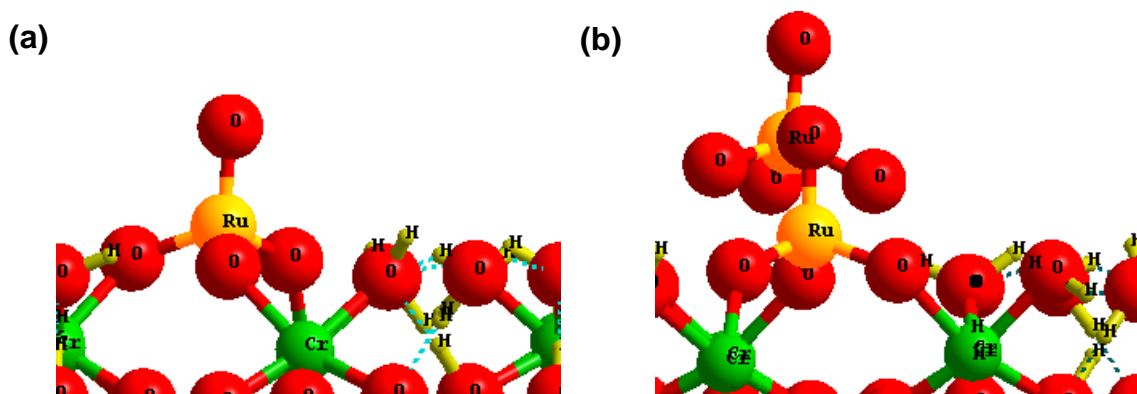
Figure 4.17. RuO_4 adsorbed on totally saturated hydrate chromium oxide surface for (a) 25% and (b) 50% coverage. Chromium: green. Oxygen: red. Ruthenium: yellow. Hydrogen: light yellow.
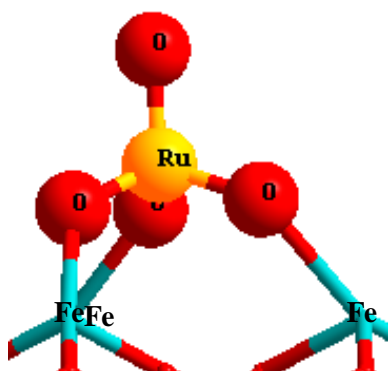
Figure 4.18. Configuration of RuO_4 on the surface. Fe: blue. O: red. Ru: yellow.

For **Fe₂O₃Fe** surface (neutral iron oxide surface), RuO_4 is adsorbed on this surface in a geometry similar to the one on the neutral chromium oxide surface (Cr_2O_3Cr). (**Figure 4.18**). For all the coverage, RuO_4 is isolated on the surface. For 25% coverage, the adsorption energy is equal to -1.86 eV and -1.21 eV for a 50% coverage. For a surface totally covered by RuO_4, its adsorption energy decreases to -0.72 eV. (**Figure 4.19**)
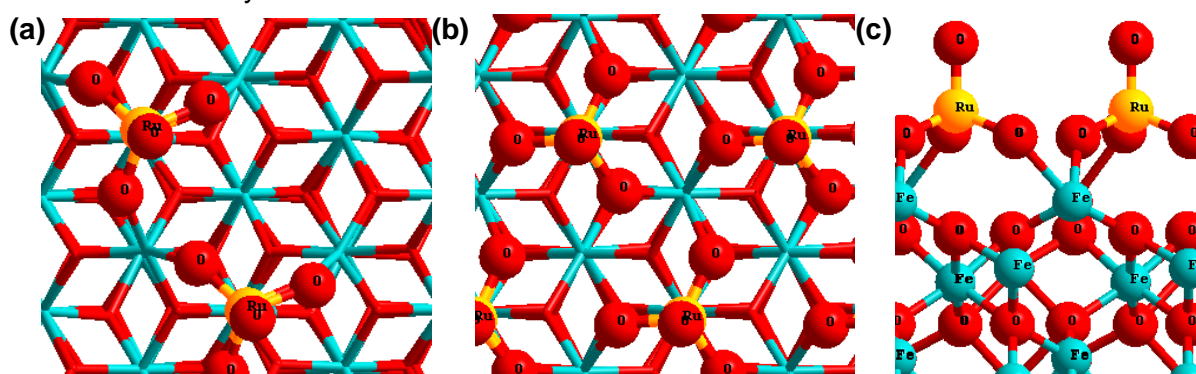
Figure 4.19. Top view for adsorption of RuO_4 with (a) 50% (b) 100% coverage and (c) side view for adsorption of RuO_4 with 50% and 100% coverage on the Fe_2O_3Fe surface. Iron: Blue. Oxygen: red. Ruthenium: yellow.

4.2.1.4 OXIDE STATE DETERMINATION FOR ADSORBED RUTHENIUM SPECIES

For adsorption of RuO_2 and RuO_3 on chromyl surface, the adsorption is favourable but it is difficult to evaluate the electron transfers between the oxidized surface and the adsorbate. In order to determinate their oxidation state, the DOS (density of state) of adsorbed ruthenium atom has been traced for the most interesting configurations (RuO_2 and RuO_3 adsorbed on Chromyl surface with 25% coverage). By tracing DOS, normally by identifying the peak position, the oxidation state of interested species could be determined. The reference DOS for *d* orbitals of ruthenium atoms in RuO_2, RuO_3 and RuO_4 were drawn in **Appendix** Figure A.6. It can be observed that, for RuO_4, a small peak and an intense peak at -24.79 eV and -13.05 eV. For RuO_3, the small peak is located at -24.57 eV and two identical intense peaks are at -12.51 eV and -11.57 eV. For RuO_2, the small peak is positioned at -24.18 eV and two peaks with different intensities are sited at -11.17 eV and -10.56 eV. The DOS for *d* orbital of Ru atoms in most stable structure of RuO_2 adsorbed on Chromyl surface and RuO_3 adsorbed on

Chromyl surface with 25% coverage are shown in **Appendix** Figure A.7 and 8. It is hard to identify the oxidation state of Ru from peaks around -13 eV to -10 eV as no peaks can be directly compared to references. However, the position of the small peaks around -25 eV can provide some information. The adsorbed Ru atom in RuO_2 adsorbed on Chromyl surface with 25% coverage (α: -24.96 eV; β: -24.78 eV) and RuO_3 adsorbed on Chromyl surface with 25% coverage (α: -24.84 eV; β: -24.66 eV) have similar positions as in RuO_4 (-24.79 eV). However, the differences with the RuO_3 peak is small (-24.57 eV). So supplementary charge calculations should be performed in order to identify the oxidation state of adsorbed ruthenium oxides.

An additional *bader*[58] analysis was performed for the same configurations (RuO_2 and RuO_3 adsorbed on Chromyl surface with 25% coverage) and reference molecules (RuO_2, RuO_3 and RuO_4) in order to compare electron charge on ruthenium atoms. The electron charge on ruthenium atoms for some interested configurations and reference species are presented in **Table 4.9**.

Table 4.9. Electron charge on ruthenium atom for some interested configurations and reference species.

Model	RuO_2	RuO_3	RuO_4	25% RuO_2 on Chromyl surface	25% RuO_3 on Chromyl surface
Electron charge	12.73	12.17	11.98	11.81	11.75

It can be easily noticed the adsorbed RuO_2 and RuO_3 on Chromyl surface (25% coverage) are oxidized, the charge on the ruthenium atom being similar to the RuO_4 molecule. So we can suppose that these ruthenium species might be released from the surface as RuO_4. This point will be discussed in the next section.

4.2.1.5 CONCLUSION

Most of the ruthenium oxide species are adsorbed molecularly and are isolated on the surface. On the opposite, for $Cr_2O_3Cr_2(OH)_3$ surface, at high coverage, RuO_2 molecules polymerize on the surface. However, the adsorption on $Cr_2O_3Cr_2(OH)_3$ surface is not favourable and no covalent bond is formed between the surface and the adsorbate. The comparison of the molecules studied shows that the adsorption of RuO_2 is the most favourable and the adsorption of RuO_3 is slightly less favourable. For adsorption of RuO_2 and RuO_3 on neutral surfaces (Cr_2O_3Cr and Fe_2O_3Fe), ruthenium atom is located in threefold hollow site of the surface. For adsorption of RuO_2 and RuO_3

on chromyl surface, the adsorption is still favourable by forming RuO_4 like species. The adsorption of RuO_4 is not favourable on Chromyl surface and $Cr_2O_3Cr_2(OH)_3$ surface. On the opposite, the adsorption on the neutral chromium oxide surfaces (Cr_2O_3Cr) and neutral iron oxide surface (Fe_2O_3Fe) is always favourable with the formation of three oxygen-metal bonds between surface and RuO_4 molecule.

4.2.2 REACTIVITY STUDY

As mentioned in a previous section (Chapter IV section 4.1.2.1.2), many reactions can occur on the stainless steel surface: decomposition of RuO_3, decomposition of RuO_4 and re-vaporization of RuO_2. Therefore, in this section, these possible reactions will be examined in order to determine the reaction that will occur depending on the experimental conditions and the possible reaction pathways.

4.2.2.1 DECOMPOSITION OF RuO₃

U. Backman *et al.*[59] have found that, due to the decomposition of RuO_3, a major part of ruthenium released, can be deposited on stainless steel surface and formed RuO_2 on the surface. So it is interesting to understand the decomposition of RuO_3 on the stainless steel surface. Hence, the decomposition of RuO_3 over adsorbed surface will be studied in this section. Moreover, the sublimation of $RuO_{3(g)}$ from surface has also been discussed, in order to compare it with the decomposition processes. The reaction energies for above-mentioned reactions are presented in **Table 4.10**. All calculations are based on most stable structures with different coverages in RuO_3 and RuO_2.

By comparing formation energies on the three different surfaces, it can be noticed that decomposition of RuO_3 on **Chromyl** surface with 25% coverage (Reaction 1, **Table 4.10**) seems to be the most favourable reaction ($\Delta E = 0.60$ eV). On the other hand, the sublimation of $RuO_{3(g)}$ form this chromyl surface with 25% coverage is very endothermic ($\Delta E = 1.68$ eV). However, our theoretical calculations are performed at 0 K. Therefore, by introducing thermodynamic corrections, these reactions may become exergonic at high temperature. Besides, the thermodynamic corrections term of **$RuO_{3(g)}$** may become more important than the one for **$O_{2(g)}$** at high temperature as ruthenium atom is heavy. Consequently, there may be a competition between decomposition of RuO_3 and sublimation of $RuO_{3(g)}$ at high temperature.

Table 4.10. Energy for decomposition and sublimation of RuO_3 on different surfaces.

	N°	Reaction	Surface Model	ΔE (eV)
Decomposition of RuO₃	1	Surface-RuO₃ ➜ Surface-RuO₂ + ½O₂(g)	Cr₂O₃Cr	2.30
			Chromyl	0.60
			Fe₂O₃Fe	2.14
	2	Surface-2RuO₃ ➜ Surface-2RuO₂ + O₂(g)	Cr₂O₃Cr	5.40
			Chromyl	1.54
			Fe₂O₃Fe	3.44
	3	Surface-4RuO₃ ➜ Surface-4RuO₂ + 2O₂(g)	Cr₂O₃Cr	8.77
			Chromyl	5.69
			Fe₂O₃Fe	7.22
Sublimation of RuO₃	4	Surface-RuO₃ ➜ Surface+ RuO₃(g)	Cr₂O₃Cr	3.15
			Chromyl	1.68
			Fe₂O₃Fe	3.52
	5	Surface-2RuO₃ ➜ Surface+ 2RuO₃(g)	Cr₂O₃Cr	6.17
			Chromyl	3.30
			Fe₂O₃Fe	5.91
	6	Surface-4RuO₃ ➜ Surface+ 4RuO₃(g)	Cr₂O₃Cr	11.35
			Chromyl	6.50
			Fe₂O₃Fe	8.64

By adding thermodynamic correction terms of **O$_{2(g)}$** and **RuO$_{3(g)}$**, Gibbs free energies for decomposition of RuO_3 and sublimation of RuO_3(g) on three most interested surfaces can be calculated and drawn in **Figure 4.20** and **Figure 4.21.** It can be noticed that the decomposition of RuO_3 is not possible at high temperature on Cr_2O_3Cr and Fe_2O_3Fe surface as the sublimation of $RuO_{3(g)}$ (red) occurs before the decomposition of RuO_3 (black) (**Figure 4.20**). Moreover, the sublimation of $RuO_{3(g)}$ could not happen directly, it could occur only when $\Delta G < 0$. Consequently, for Cr_2O_3Cr surface, the sublimation of $RuO_{3(g)}$ occurs at about 1036 K for 25% coverage, about 1008 K for 50% coverage and about 951 K for 100% coverage. Besides, for Fe_2O_3Fe surface, the sublimation temperatures for $RuO_{3(g)}$ on an adsorbed surface with coverages equal to 25 %, 50% and 100% are 1131 K, 975 K and 779 K respectively. In addition, no decomposition of RuO_3 can follow. As the sublimation temperature decreases with

augmentation of coverage, it can be concluded that more RuO_3 molecules adsorbed on the surface, the more easily they could be sublimated. This effect will limit the RuO_3 coverage at high temperature.
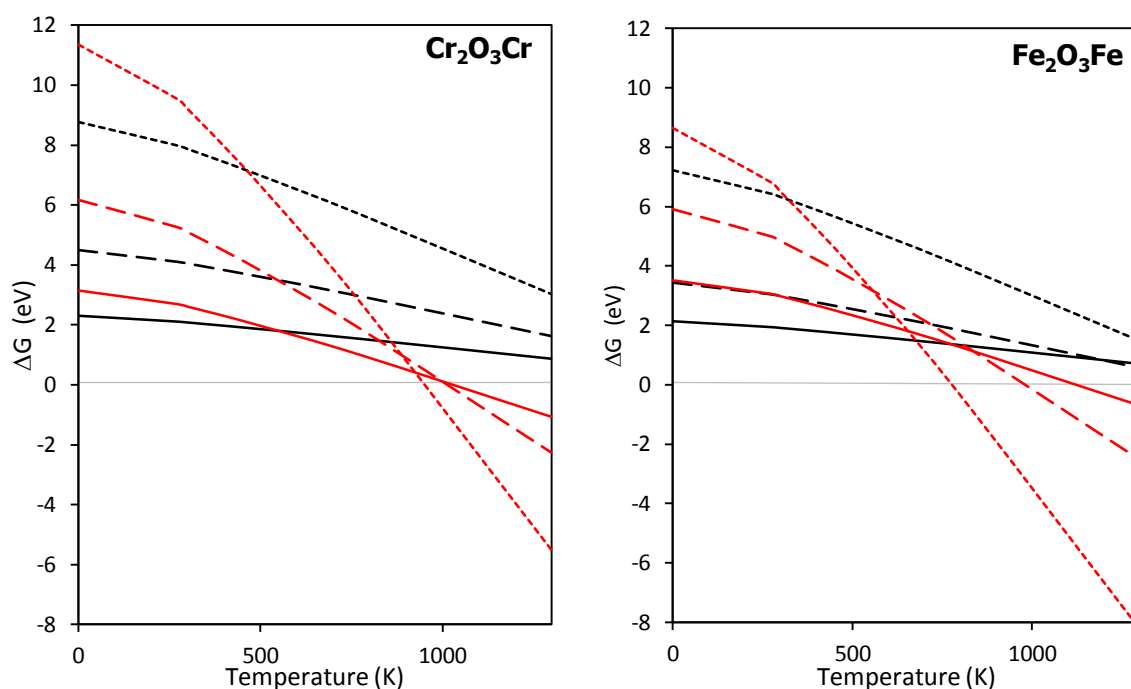
Figure 4.20. Gibbs free energy for (black) decomposition of RuO_3 and (red) sublimation of $RuO_{3(g)}$ on surfaces Cr_2O_3Cr and Fe_2O_3Fe with a coverage of RuO_3 equal to (line) 25%, (short line) 50% and (point) 100% from 0 K to 1300 K.

On Chromyl surface with RuO_3 adsorbed (**Figure 4.21**), it can be noticed that, at low temperature, the decomposition of RuO_3 on the surface (black) is always more favourable than sublimation of $RuO_{3(g)}$ (red). However their Gibbs free energy (ΔG) is always positive except for the surface with 25% RuO_3 coverage. For a very tiny range of temperature (630 K to 666 K), the decomposition of RuO_3 on this surface (black, line) is more favourable than sublimation of $RuO_{3(g)}$ (red, line). For other surfaces, the sublimation of $RuO_{3(g)}$ (red, short line or point) is more favourable. For Chromyl surface, the sublimation of $RuO_{3(g)}$ occurs at about 633 K for 50% coverage and about 625 K for 100% coverage. So it can be concluded that the sublimation of RuO_3 occurs at almost the same temperature range for different coverages on chromyl surface. Furthermore, as the temperature range that will favour the decomposition of RuO_3 on chromyl surface with 25% coverage is very small, the existence of this reaction is very improbable. Hence, its reaction path and the corresponding transition states will not discuss in our work.
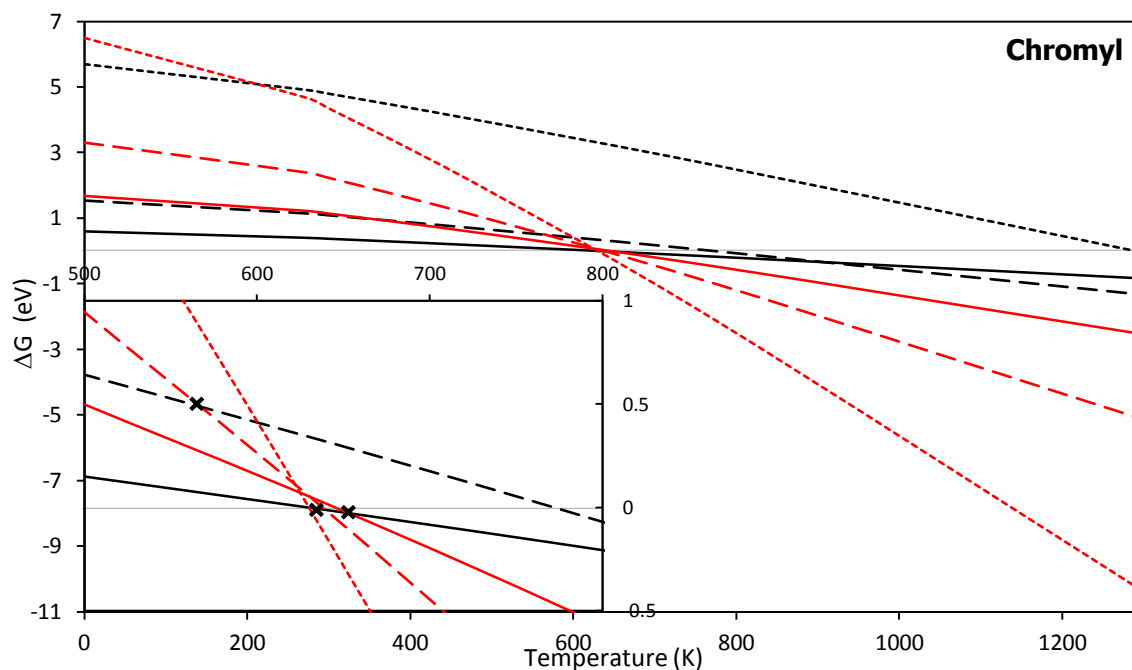
Figure 4.21. Gibbs free energy for (black) decomposition of RuO_3 and (red) sublimation of $RuO_{3(g)}$ on Chromyl surfaces with a coverage of RuO_3 equal to (line) 25%, (short line) 50% and (point) 100% from 0 K to 1300 K.

In conclusion, the sublimation of $RuO_{3(g)}$ is more favourable than the decomposition of RuO_3 on these adsorbed surfaces. The only possibility for the decomposition of RuO_3 is on a Chromyl surface with 25% coverage between 630K and 666K. But, this range is very limited, the reaction is not probable.

However, experimental studies suggested that major part of released ruthenium can be deposited on to stainless steel surface and formed RuO_2 on the surface are due to the decomposition of RuO_3.[59] Hence, we think that most of decomposition of RuO_3 does not occur on the surface of stainless steel surface, but in the gas phase. This process will occur with the following equation:

$$RuO_3(g) \rightarrow RuO_2(g) + \frac{1}{2}O_2(g) \rightarrow RuO_2(s) + \frac{1}{2}O_2(g) \qquad \textit{Equation 4.13}$$
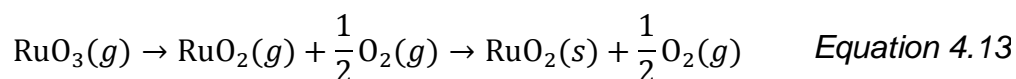
4.2.2.2 DECOMPOSITION OF RUO4

As mentioned in a previous section (Chapter IV section 4.1.2.1.2), U. Backman *et al.*[39,42] think that the stainless steel surface may play an important role for the decomposition of RuO_4 to RuO_2. They also found that in an environment totally

saturated by water, no RuO_4 decomposition can take place. P. Cains and S. Barnes[50] have deposited volatile ruthenium on steel surfaces and found that above 150 °C the deposition could happen and that crystalline $RuO_{2\,(s)}$ appeared, without strong bonding with steel surfaces which means that stainless steel surfaces do not play a role in decomposition of RuO_4. They believed that the decomposition of $RuO_{4(g)}$ can be described by *Equation 4.12* where no surface is involved in reaction.[50–52]

$$RuO_4(g) \rightarrow RuO_2(g) + O_2(g) \rightarrow RuO_2(s) + O_2(g) \qquad \text{Equation 4.12}$$

In this section, the decomposition of RuO_4 on different surfaces will be discussed in order to determine if the stainless steel surface plays an important role in the decomposition process. The interactions with the Cr_2O_3Cr (neutral chromium oxide surface), $Cr_2O_3Cr_2(OH)_3$ (hydrated chromium oxide surface) and Fe_2O_3Fe (neutral iron oxide surface) surfaces are discussed in this section, except for Chromyl (oxidized chromium oxide surface) surface, as RuO_4 cannot be adsorbed on this surface.

If surface plays a role in the reaction, the decomposition can be described by the following equation.

$$\text{Surface-}n\text{RuO}_4 \rightarrow \text{Surface-}n\text{RuO}_2 + n\text{O}_2(g) \qquad \text{Equation 4.14}$$
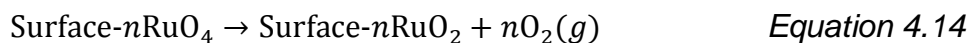
However, other reaction pathways may also exist for $RuO_{4(g)}$ decomposition without steam as propose by C. Mun[20]. They may be modelled according the following equations:

Low	$$\boldsymbol{RuO_4(g) \rightarrow RuO_3(g) + \frac{1}{2}O_2}$$	*Equation 4.4*
Low	$$RuO_3(g) \rightarrow \frac{1}{2}Ru_2O_5 + \frac{1}{4}O_2$$	*Equation 4.6*
Fast	$$RuO_3(g) + RuO_2(s) \rightarrow Ru_2O_5(s)$$	*Equation 4.8*
?	$$Ru_2O_5(s) \rightarrow 2RuO_2(s) + \frac{1}{2}O_2$$	*Equation 4.9*
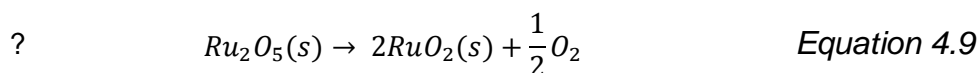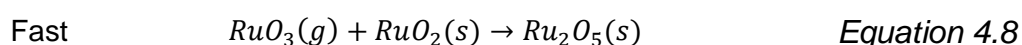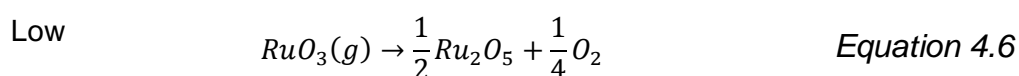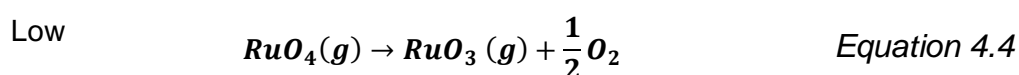
Firstly, $RuO_{4(g)}$ decompose to $RuO_{3(g)}$ where the kinetic of this step is low *(Equation 4.4)*. And then $RuO_{3(g)}$ will polymerize and former Ru_2O_5 by liberated oxygen with low kinetic coefficient *(Equation 4.6)*. And then Ru_2O_5 will be converted to RuO_2 by liberating oxygen *(Equation 4.9)*. It should be noticed that the formation of the first Ru_2O_5 is difficult. However, once RuO_2 formed, it could be a catalyser for the reaction *(Equation 4.8)*. RuO_4 on the stainless steel surface may also follow a similar reaction

pathway: first decomposed to RuO_3 and then to RuO_2. This process can be described by equations as follows:

$$\text{Surface-}n\text{RuO}_4 \rightarrow \text{Surface-}n\text{RuO}_3 + \frac{n}{2}\text{O}_2(g) \qquad \textit{Equation 4.15}$$

$$\text{Surface-}n\text{RuO}_3 \rightarrow \text{Surface-}n\text{RuO}_2 + \frac{n}{2}\text{O}_2(g) \qquad \textit{Equation 4.16}$$
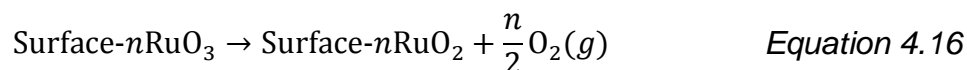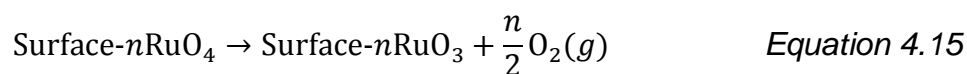
Additionally, we studied sublimation of $RuO_{4(g)}$ and $RuO_{3(g)}$ from the surfaces, in order to compare it with the decomposition processes. All the calculations are based on most stable structures with different coverages of ruthenium oxide species. All the energy for decomposition and sublimation of $RuO_{4(g)}$ from different surfaces with RuO_4 adsorbed are reported in **Table 4.11**.

By comparing decomposition energies on three different surfaces, it can be observed directly that, for $Cr_2O_3Cr_2(OH)_3$ surface, the sublimation of RuO_4 is more favourable than its decomposition. It should be noticed that the sublimation occurs almost spontaneously on this surface. On the other surfaces, the decomposition from RuO_4 directly into RuO_2 seems less favourable than RuO_3 formation. All the reactions are endothermic, it appears that the decomposition of RuO_4 on different surfaces is not favourable. To determine the possible reaction as a function of the temperature, we consider thermodynamic corrections on **$O_{2(g)}$** and **$RuO_{4(g)}$**. Gibbs free energy for decomposition and sublimation of $RuO_{4(g)}$ are calculated and traced in **Figure 4.22**, **Figure 4.23** and **Figure 4.24.**

Table 4.11. Energy for decomposition of $RuO_{4(g)}$ and sublimation of $RuO_{4(g)}$ from different surfaces with RuO_4 adsorbed at 0 K.

	N°	Reaction	Surface Model	ΔE (eV)
			Cr_2O_3Cr	3.09
	1	Surface-RuO_4 ➜ Surface-RuO_2 + O_2(g)	$Cr_2O_3Cr_2(OH)_3$	3.08
			Fe_2O_3Fe	2.53
			Cr_2O_3Cr	5.08
RuO_4 ➜ RuO_2	2	Surface-$2RuO_4$ ➜ Surface-$2RuO_2$ + $2O_2$(g)	$Cr_2O_3Cr_2(OH)_3$	5.28
			Fe_2O_3Fe	4.04
			Cr_2O_3Cr	10.03
	3	Surface-$4RuO_4$ ➜ Surface-$4RuO_2$ + O_2(g)	$Cr_2O_3Cr_2(OH)_3$	8.98
			Fe_2O_3Fe	9.62

Table 4.11 (suit) Energy for decomposition of $RuO_{4(g)}$ and sublimation of $RuO_{4(g)}$ from different surfaces with RuO_4 adsorbed at 0 K.

	N°	Reaction	Surface Model	ΔE (eV)
RuO_4➜ RuO_3	4	Surface-RuO_4 ➜ Surface-RuO_3 + ½ $O_{2(g)}$	Cr_2O_3Cr	0.78
			$Cr_2O_3Cr_2(OH)_3$	0.47
			Fe_2O_3Fe	0.40
	5	Surface-$2RuO_4$ ➜ Surface-$2RuO_3$ + $O_{2(g)}$	Cr_2O_3Cr	0.54
			$Cr_2O_3Cr_2(OH)_3$	0.96
			Fe_2O_3Fe	0.60
	6	Surface-$4RuO_4$ ➜ Surface-$4RuO_3$ + $2O_{2(g)}$	Cr_2O_3Cr	1.26
			$Cr_2O_3Cr_2(OH)_3$	1.91
			Fe_2O_3Fe	2.40
Sublimation $RuO_{4(g)}$	7	Surface-RuO_4 ➜ Surface + RuO_4(g)	Cr_2O_3Cr	1.89
			$Cr_2O_3Cr_2(OH)_3$	0.12
			Fe_2O_3Fe	1.86
	8	Surface-$2RuO_4$ ➜ Surface + $2RuO_4$(g)	Cr_2O_3Cr	2.60
			$Cr_2O_3Cr_2(OH)_3$	0.00
			Fe_2O_3Fe	2.41
	9	Surface-$4RuO_4$ ➜ Surface + $4RuO_4$(g)	Cr_2O_3Cr	4.42
			$Cr_2O_3Cr_2(OH)_3$	0.01
			Fe_2O_3Fe	2.84

By comparing decomposition energies on these three different surfaces, it can be observed directly that, for $Cr_2O_3Cr_2(OH)_3$ surface, the sublimation of RuO_4 is more favourable than its decomposition. The sublimation occurs almost spontaneously on this surface. On the other surfaces, the decomposition from RuO_4 directly into RuO_2 seems to be less favourable than RuO_3 formation. All the reactions are endothermic, it seems that the decomposition of RuO_4 on different surfaces is not favourable. To determine the possible reaction as a function of the temperature, we consider the thermodynamic corrections on **$O_{2(g)}$** and **$RuO_{4(g)}$**. Gibbs free energy for decomposition of RuO_4 and sublimation of $RuO_{4(g)}$ are then calculated and reported in **Figure 4.22**, **Figure 4.23** and **Figure 4.24.**
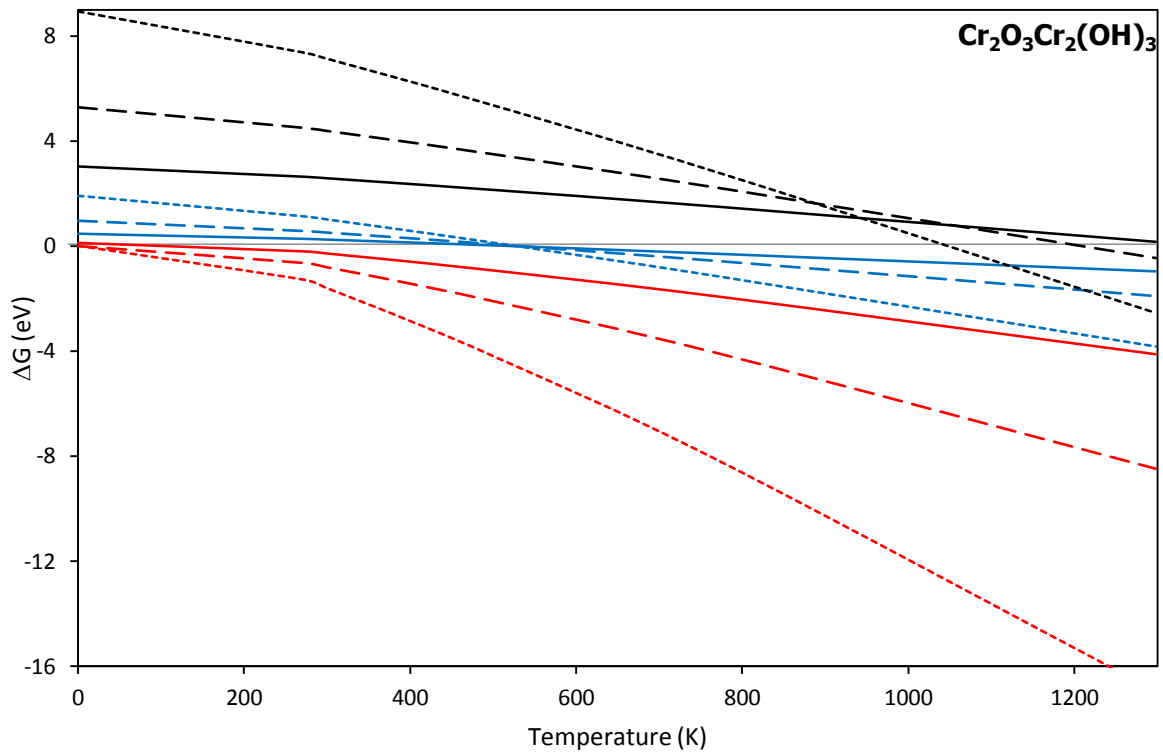
Figure 4.22. Gibbs free energy for (black) decomposition of RuO_4 into RuO_2, (blue) decomposition of RuO_4 into RuO_3 and (red) sublimation of $RuO_{4(g)}$ on $Cr_2O_3Cr_2(OH)_3$ with a coverage of RuO_4 equal to (line) 25%, (short line) 50% and (point) 100% from 0 K to 1300 K.
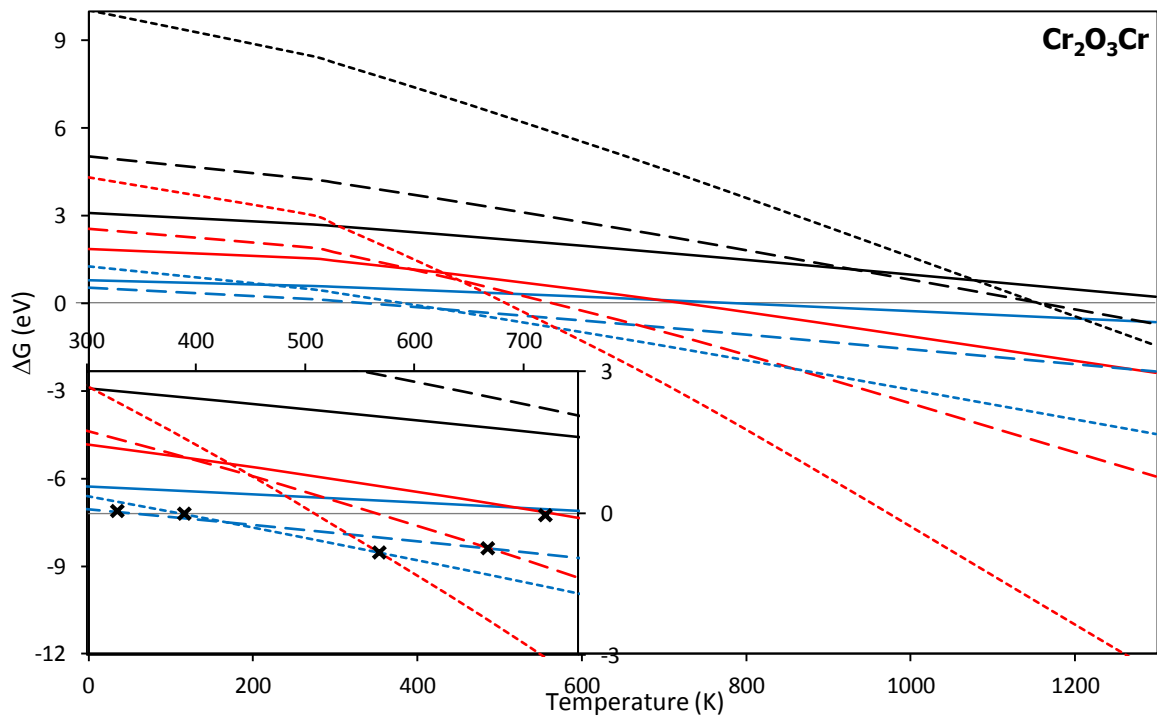
Figure 4.23. Gibbs free energy for (black) decomposition of RuO_4 into RuO_2, (blue) decompose

tion of RuO_4 into RuO_3 and (red) sublimation of $RuO_{4(g)}$ on Cr_2O_3Cr surfaces with a coverage of RuO_4 equal to (line) 25%, (short line) 50% and (point) 100% from 0 K to 1300 K.

On the **$Cr_2O_3Cr_2(OH)_3$** surface (**Figure 4.22**), the sublimation occurs almost spontaneously whatever the coverage of RuO_4 (except for 25% coverage sublimation occurs from 100 K). On the **Cr_2O_3Cr** surface (**Figure 4.23**), it can be observed that, the decomposition of RuO_4 into RuO_2 (black) is never favourable. At low temperature, the decomposition of RuO_4 into RuO_3 (blue) is more favourable than sublimation of RuO_4 (red). However, when the temperature increases, the latter becomes more favourable. For 25% coverage, only sublimation of $RuO_{4(g)}$ can occur spontaneously for temperature higher than 714 K. For 50 % coverage, as mentioned before, the decomposition of RuO_4 into RuO_3 occurs for temperature higher than 338 K. After 668 K the sublimation of RuO_4 takes advantage. Similar phenomena can be observed for a surface totally covered by RuO_4. The decomposition of RuO_4 into RuO_3 occurs from 383 K. And then above 568 K the sublimation of RuO_4 is favoured.
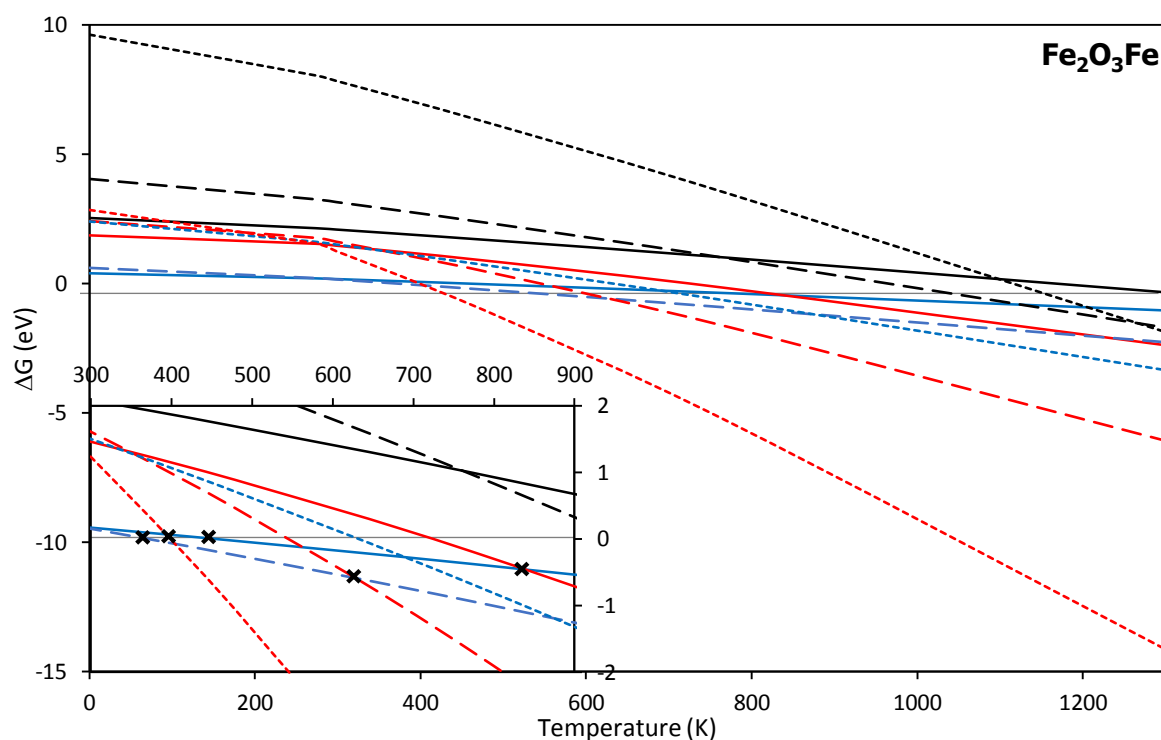
Figure 4.24. Gibbs free energy for (black) decomposition of RuO_4 into RuO_2, (blue) decomposition of RuO_4 into RuO_3 and (red) sublimation of $RuO_{4(g)}$ on surfaces Fe_2O_3Fe with a coverage of RuO_4 equal to (line) 25%, (short line) 50% and (point) 100% from 0 K to 1300 K.

Similar behaviour is observed on Fe_2O_3Fe surface (**Figure 4.24**), it can be observed that, decomposition of RuO_4 into RuO_2 (black) is never favourable. At low temperature,

the decomposition of RuO_4 into RuO_3 (blue) is also more favourable than sublimation (red). At high temperature, the latter becomes more favourable. For a Fe_2O_3Cr surface with 25% coverage, the decomposition of RuO_4 into RuO_3 occurs above 464 K. Above 821 K the sublimation of RuO_4 takes advantage. For 50 % coverage, the decomposition of RuO_4 into RuO_3 occurs above 379 K, and sublimation above 617 K. On the opposite, for a surface totally covered by RuO_4, the decomposition of RuO_4 to RuO_3 could not occur and sublimation of RuO_4 happens above 397 K.

In the following section, the reaction pathway and transition state for RuO_4 decomposition process on Cr_2O_3Cr and Fe_2O_3Fe surfaces will be studied. As mentioned before, the decomposition of RuO_4 occurs only on a surface with coverage equal to 50% and 100% by forming RuO_3.
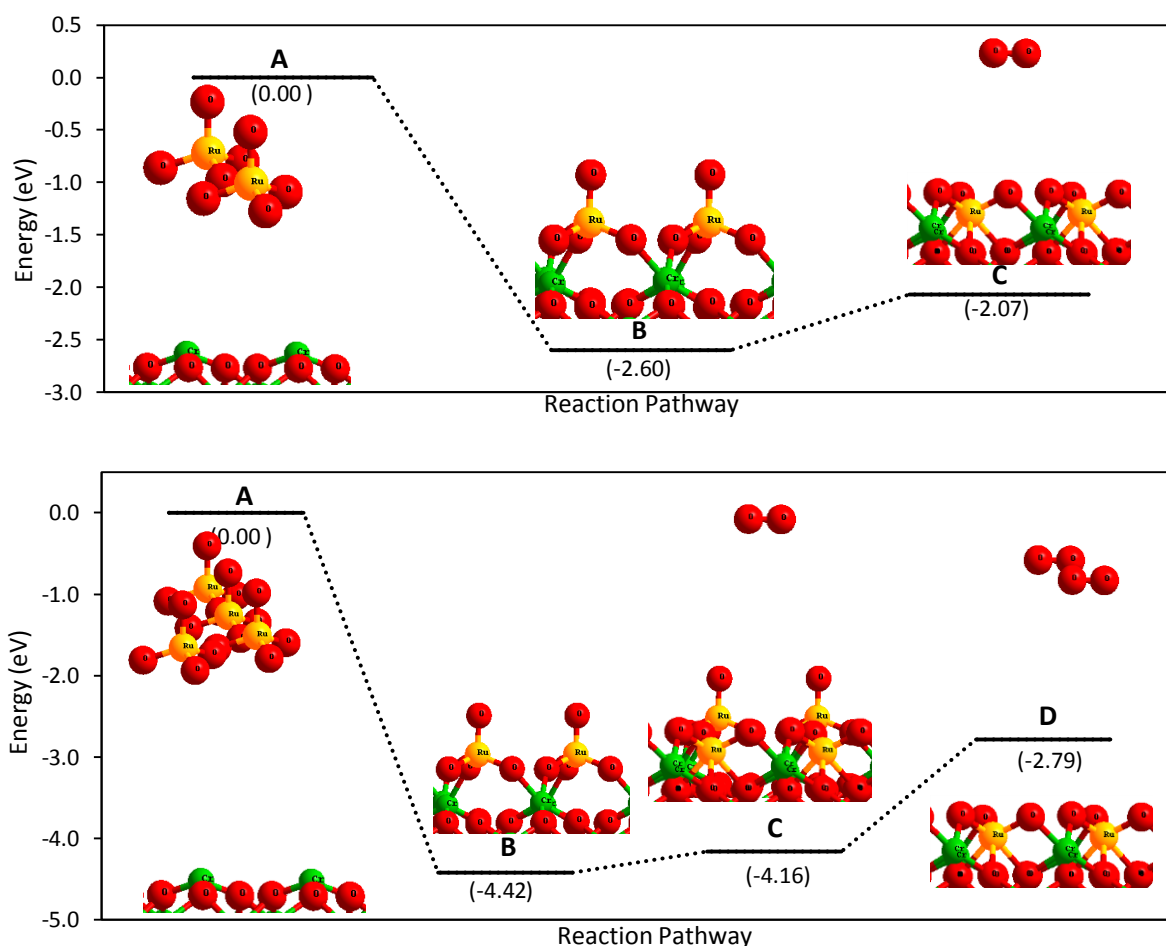
Figure 4.25 Energy diagram for decomposition of $RuO_{4(g)}$ on Cr_2O_3Cr surface adsorbed by RuO_4 with coverage equal to (Top) 50% and (Bottom) 100%. Chromium: green. Oxygen: red. Ruthenium: yellow.

For a Cr_2O_3Cr surface with RuO_4 coverage equal to 50%, a possible reaction pathway is shown in **Figure 4.25** (top). RuO_4 molecules are adsorbed on the surface (**A→B**)

and form three O-Cr bonds with the surface. Next two isolated oxygen atoms on the top of the RuO_4 molecules move closer until they formed $O_{2(g)}$ molecule. The reaction is slightly endothermic (0.53 eV) (**B→C**). During the O_2 formation, the two remaining RuO_3, move to the stable position on the surface (hollow site) (Ru-OOO, **Figure 4.10**). For a surface totally covered by RuO_4, the possible reaction pathway is shown in **Figure 4.25** (bottom). Four RuO_4 molecules are adsorbed on the Cr_2O_3Cr surface (**A→B**) and form three O-Cr bonds with surface. In a first step, two of the four isolated oxygen atoms on the top of the two RuO_4 molecules formed one $O_{2(g)}$ molecule (ΔE = 0.26 eV) (**B→C**). Similarly to the previous coverage(50%), ruthenium atoms move to a hollow site. And then, the last two isolated oxygen atoms on the top of other two RuO_4 molecules form a second $O_{2(g)}$ molecule. This step is more endothermic (ΔE = 1.37 eV) (**C→D**) and ruthenium will react as before.
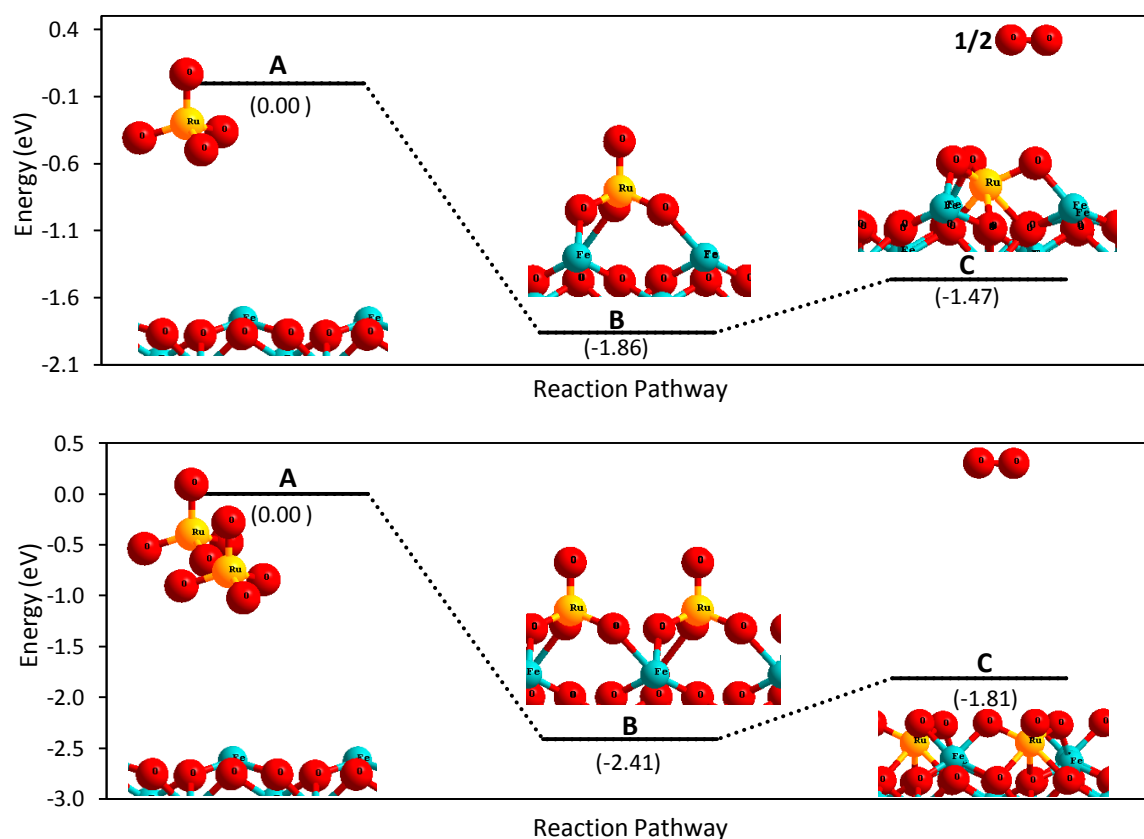
Figure 4.26. Energy diagram decomposition of $RuO_{4(g)}$ on Fe_2O_3Fe surface adsorbed by RuO_4 with a coverage equal to (top) 25% and (bottom) 50%. Iron: blue. Oxygen: red. Ruthenium: yellow.

 For a Fe_2O_3Fe surface with RuO_4 coverage equal to 25%, the possible reaction pathway is shown in **Figure 4.26** (top). Firstly, RuO_4 molecule is adsorbed on the surface (**A→B**) and form three O-Cr bonds. And then isolated oxygen atoms on the

top of the RuO_4 molecule and another isolated oxygen atoms from neighbour cell formed $O_{2(g)}$ ($\Delta E = 0.39$ eV (**B→C**)) and the RuO_3 move to the hollow site as mentioned before (Ru-OOO, **Figure 4.13**). For the 50% coverage, the possible reaction pathway is shown in **Figure 4.26** (bottom). The reaction path is similar to the previous ones. The formation of $O_{2(g)}$ is endothermic ($\Delta E = 0.60$ eV (**B→C**)).

The transition state for the decomposition of RuO_4 into RuO_3 on different adsorbed surfaces with different coverages have been calculated by using *Nudged elastic band method (NEB)* method[60–62] (Chapter II Section 2.3.1). Unfortunately, some spin problems have been encountered. Hence, until now, no coherent results have been found. After RuO_4 decomposed to RuO_3, two possible reaction pathways may occur on the surface: RuO_3 is decomposed into RuO_2 or the sublimation of $RuO_{3(g)}$. The competition between decomposition and sublimation of $RuO_{3(g)}$ on Cr_2O_3Cr and Fe_2O_3Fe surfaces have been already discussed in a previous section (Chapter IV 4.2.2.1). Furthermore, it has been concluded that the decomposition on $Cr_2O_3Cr_2(OH)_3$ surface is not possible as the sublimation of $RuO_{4(g)}$ occurs before. So, in conclusion, the decomposition of RuO_4 into RuO_2 could occur only via RuO_3 on Cr_2O_3Cr and Fe_2O_3Fe surfaces. The first step of this decomposition ($RuO_4 \rightarrow RuO_3$) occurs on the stainless steel surface and the second step of the decomposition ($RuO_3 \rightarrow RuO_2$) occurs in the gas phase ($RuO_{3(g)} \rightarrow RuO_{2(s)}$). This may explain why there is some discrepancies in literature.[39,42,50]. Surface does play an important role in the decomposition of RuO_4. Moreover, the decomposition of RuO_4 could not occur on a hydrated surface. This result is in agreement with U. Backman *et al.*[39,42] works as they showed that in an environment totally saturated by water, no RuO_4 decomposition can take place.

Compared to decomposition of $RuO_{4(g)}$ in air where the first reaction step is kinetically slow, the participation of stainless steel surface could help the decomposition of RuO_4 into RuO_3. Once $RuO_{3(g)}$ is formed (by sublimation), the decomposition of $RuO_{3(g)}$ into $RuO_{2(s)}$ will be rather fast and catalysed by RuO_2.

4.2.2.3 *RE-VAPORISATION OF GASEOUS RUTHENIUM OXIDES*

As mentioned in a previous section (Chapter IV section 4.1.2.1.2), U. Backman *et al.*[39,42] found that the re-vaporization of deposited RuO_2 particles is a very significant source of gaseous ruthenium oxides as confirmed by IRSN within the STEM/STEM2

OECD projects.[55] Hence, it is interesting to understand how adsorbed RuO_2 can form $RuO_{4(g)}$ or $RuO_{3(g)}$ on the stainless steel surfaces. Therefore, the re-vaporization of deposited RuO_2 over the three interested surfaces will be studied in this section. The sublimation of $RuO_{2(g)}$ from adsorbed surface has also been discussed. It will be compared to the re-vaporization processes. As mentioned in Chapter IV section 4.1.2.1.1, experimentally, B. Eichler *et al.*[3] observed that RuO_2 can form RuO_3 and RuO_4 by exposing to oxygen with following reaction[3,18]:

$$RuO_2 + \frac{1}{2}O_2 \rightleftharpoons RuO_3$$

<div align="right">*Equation 4.1*</div>

$$RuO_2 + O_2 \rightleftharpoons RuO_4$$

<div align="right">*Equation 4.2*</div>

Table 4.12. Energy for re-vaporization of $RuO_{3(g)}$ and $RuO_{4(g)}$ from different surfaces with RuO_2 adsorbed under presence of $O_2(g)$.

	N°	Reaction	Surface Model	ΔE (eV)
Re-vaporization RuO₃(g)	1	Surface-RuO₂ + ½ O₂(g) ➜ Surface + RuO₃(g)	Cr₂O₃Cr	0.84
			Chromyl	1.08
			Fe₂O₃Fe	1.38
	2	Surface-2RuO₂ + O₂(g) ➜ Surface + 2 RuO₃(g)	Cr₂O₃Cr	1.67
			Chromyl	1.77
			Fe₂O₃Fe	2.47
	3	Surface-4RuO₂ + 2O₂(g) ➜ Surface + 4 RuO₃(g)	Cr₂O₃Cr	2.58
			Chromyl	0.80
			Fe₂O₃Fe	1.42
Re-vaporization RuO₄(g)	4	Surface-RuO₂ + O₂(g) ➜ Surface + RuO₄(g)	Cr₂O₃Cr	-1.21
			Chromyl	-0.97
			Fe₂O₃Fe	-0.67
	5	Surface-2RuO₂ + 2O₂(g) ➜ Surface + 2 RuO₄(g)	Cr₂O₃Cr	-2.43
			Chromyl	-2.33
			Fe₂O₃Fe	-1.63
	6	Surface-4RuO₂ + 4O₂(g) ➜ Surface + 4 RuO₄(g)	Cr₂O₃Cr	-5.61
			Chromyl	-7.40
			Fe₂O₃Fe	-6.78

Hence, we suppose that the re-vaporization of gaseous ruthenium oxides may follow a similar mechanism. In **Table 4.12**, re-vaporization of $RuO_{4(g)}$ and $RuO_{3(g)}$ over the

three most interesting surface models with RuO_2 adsorbed under presence of $O_{2(g)}$ are displayed. All the calculations are based on the most stable structures with different coverages of RuO_2.

It is clearly shown that the re-vaporization of $RuO_{4(g)}$ is more favourable than re-vaporization of $RuO_{3(g)}$ from a surface. It can occur spontaneously in presence of oxygen (all the reactions are exothermic). Compared to the reaction directly in gas phase ($RuO_2 + O_2 \rightarrow RuO_3$ or RuO_4, mentioned in Chapter IV section 4.1.2.1.1 where equilibrium constant for direct sense of *Equation 4.2* is equal to 5×10^{-17} at 373 K[4]), the formation of $RuO_{4(g)}$ from ruthenium dioxide adsorbed on stainless steel surface with present of dioxygen is more favourable. Therefore, it can be concluded that the stainless steel surface can catalyse the $RuO_{2(s)}$ oxidation into $RuO_{4(g)}$.

The **Chromyl** surface is an oxidized chromium oxide surface, so the re-vaporization of $RuO_{4(g)}$ and $RuO_{3(g)}$ does not need the presence of oxygen. In **Table 4.13**, re-vaporization of $RuO_{4(g)}$ and $RuO_{3(g)}$ and sublimation energies for $RuO_{2(g)}$ over adsorbed Chromyl surface models without presence of $O_{2(g)}$ are reported. All the calculations are based on the most stable structures with various coverages of RuO_2.

Table 4.13. Energy for re-vaporization of $RuO_{3(g)}$ and $RuO_{4(g)}$ and sublimation of $RuO_{2(g)}$ from Chromyl surfaces with RuO_2 adsorbed without $O_{2(g)}$.

	N°	Reaction	ΔE (eV)
Re-vaporization RuO$_{3(g)}$	7	Chromyl-RuO$_2$ ➔ Cr$_2$O$_3$Cr-O$_3$ + RuO$_{3(g)}$	2.15
		Chromyl-2RuO$_2$ ➔ Cr$_2$O$_3$Cr-O$_2$ + 2RuO$_{3(g)}$	4.00
		Chromyl-4RuO$_2$ ➔ Cr$_2$O$_3$Cr + 4RuO$_{3(g)}$	5.80
Re-vaporization RuO$_{4(g)}$	8	Chromyl-RuO$_2$ ➔ Cr$_2$O$_3$Cr-O$_2$ + RuO$_{4(g)}$	1.26
		Chromyl-2RuO$_2$ ➔ Cr$_2$O$_3$Cr + 2RuO$_{4(g)}$	2.67
Sublimation RuO$_{2(g)}$	9	Chromyl-RuO$_2$ ➔ Chromyl + RuO$_{2(g)}$	3.48
		Chromyl -2RuO$_2$ ➔ Chromyl + 2RuO$_{2(g)}$	6.77
		Chromyl -4RuO$_2$ ➔ Chromyl + 4RuO$_{2(g)}$	10.49

By comparing formation energy on three different surfaces, it can be observed that, for a surface with 25% coverage, the re-vaporization of $RuO_{4(g)}$ (Reaction 8, **Table 4.13**) is the most favourable (ΔE = 1.26 eV) even if it is highly endothermic. For a surface

with 50% coverage, the same re-vaporization ($RuO_{4(g)}$) is the less unfavourable ($\Delta E = 2.67$ eV). For a surface totally covered by RuO_2, it is not possible to form $RuO_{4(g)}$ directly. However, the re-vaporization of $RuO_{3(g)}$ is more favourable than $RuO_{2(g)}$. The re-vaporization energy is equal to 5.80 eV. All these reactions are endothermic. Calculations of thermodynamic correction on **$RuO_{2(g)}$, $RuO_{3(g)}$** and **$RuO_{4(g)}$** have to be performed to take into account the temperature effects.

The thermodynamic stability and the possible reaction on the Chromyl surface are summarized in the next figure (**Figure 4.27**). It can be observed that, the re-vaporization of gaseous ruthenium oxide (red and green) are more favourable than the sublimation of $RuO_{2(g)}$ (black) whatever the coverages. The re-vaporization of $RuO_{4(g)}$ or $RuO_3(g)$ may occur ($\Delta G < 0$). At low coverages (25% and 50%) $RuO_{4(g)}$ will re-vaporization for temperature around 570 K (553 K and 580 K). At this temperature, the surface can oxidize the RuO_2 deposits. For 100% coverage, the re-vaporization of $RuO_{3(g)}$ is possible for temperature above 576 K. In the next section, the reaction path and corresponding transition state for re-vaporization process are discussed.
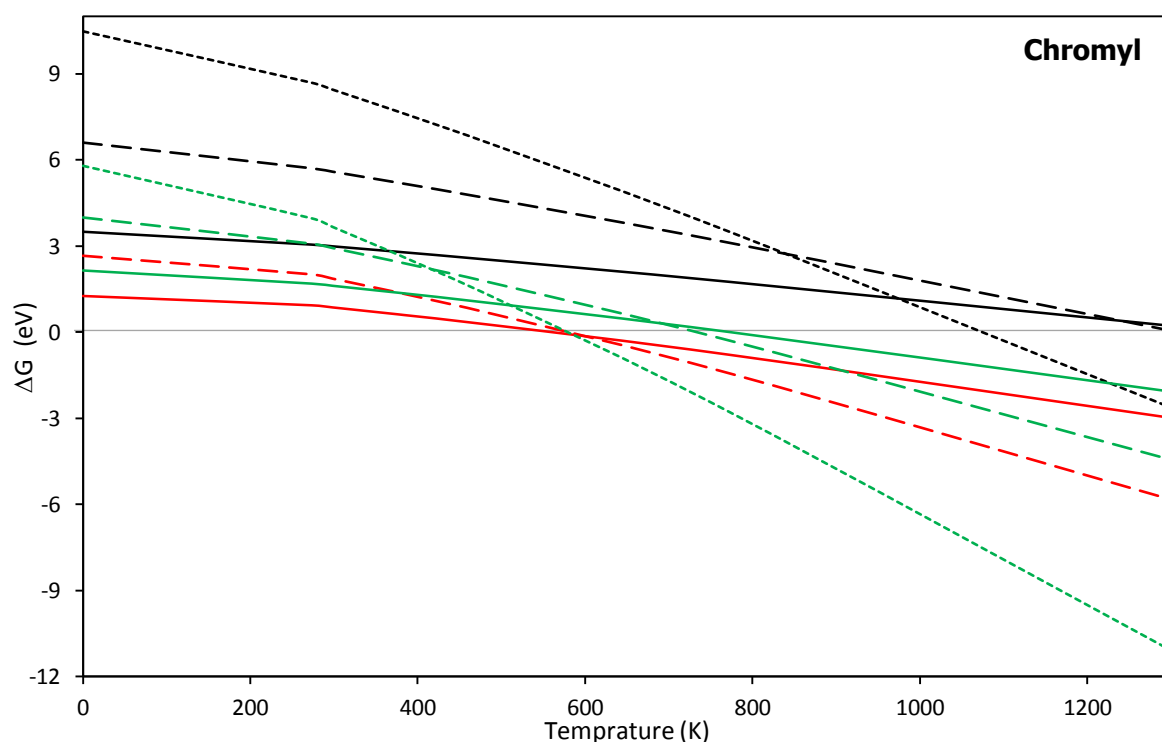
Figure 4.27. Gibbs free energy for (black) sublimation of $RuO_{2(g)}$, (red) re-vaporization of $RuO_{4(g)}$ and (green) re-vaporization of $RuO_{3(g)}$ on surfaces Chromyl with a coverage of RuO_2 equal to (line) 25%, (short line) 50% and (point) 100% from 0 K to 1300 K.

At 25% coverage, the possible reaction pathway is shown in **Figure 4.28**. Firstly, RuO_2 adsorbed on the surface. Only one bond is created between Ru atom and terminal oxygen on the surface. The form RuO_3 is planar (**A→B**). Then ruthenium can move towards the two terminal oxygen atoms and form a tetrahedral-like configuration with two terminal oxygen atoms. This step is exothermic (ΔE= -0.83 eV, **B→C**). The next step is desorption of RuO_4 from the reduced surface (**C→D**).
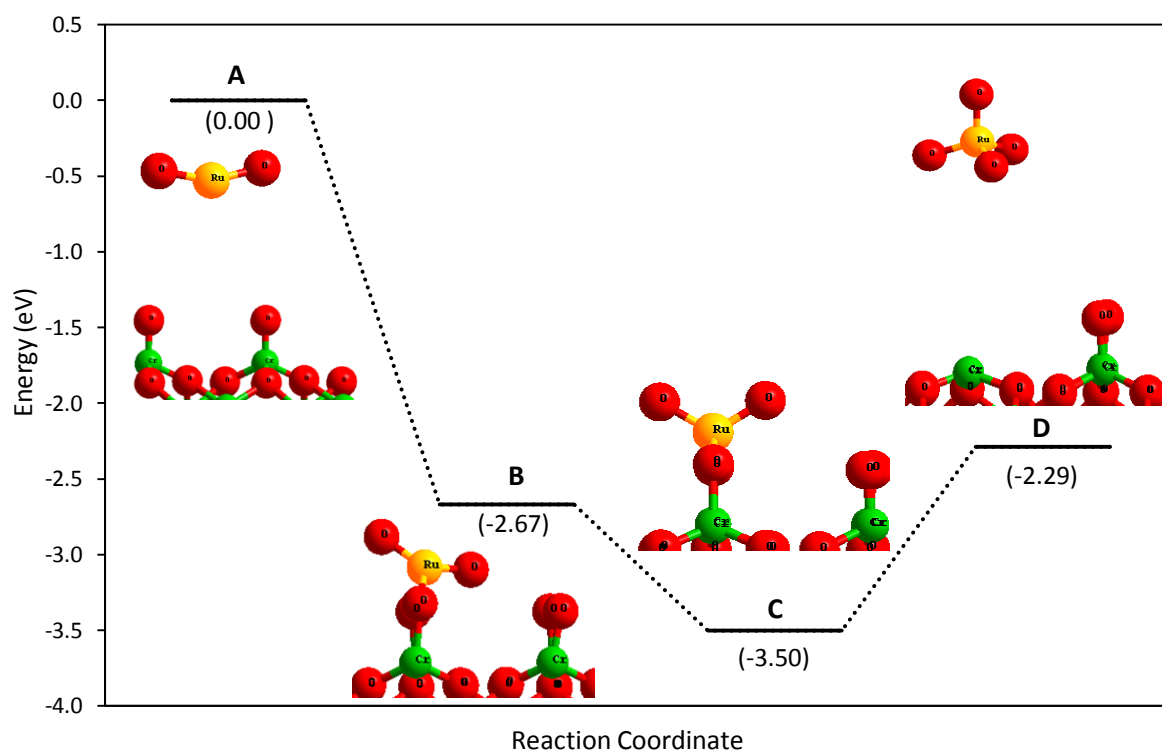
Figure 4.28. Energy diagram of the re-vaporization $RuO_{4(g)}$ from RuO_2 adsorbed on Chromyl surface with coverage equal to 25%. Chromium: green. Oxygen: red. Ruthenium: yellow.

The reaction from B to C (**Figure 4.29**, top) as a low activation energy (E_{act}= 0.36 eV). The RuO_2 molecule, adsorbed on the top of one terminal oxygen atom moves towards a second terminal atom and makes a bond. From **B** to **TS$_1$**, the distance between Ruthenium atom and one of the surface oxygen atom decreases (from 3.67 Å to 2.51 Å) and at the same time the distance between ruthenium atom and other oxygen atom increase (from 1.85 Å to 1.93 Å). From **TS$_1$** to **C**, there is a rearrangement of structure until the formation of a tetrahedral-like structure (**C**). From state C to D (**Figure 4.29**, bottom), the distance between tetrahedral-like structure and the adsorbed surface increase before desorption of $RuO_{4(g)}$ from the surface. The activation energy is equal to 1.27 eV.
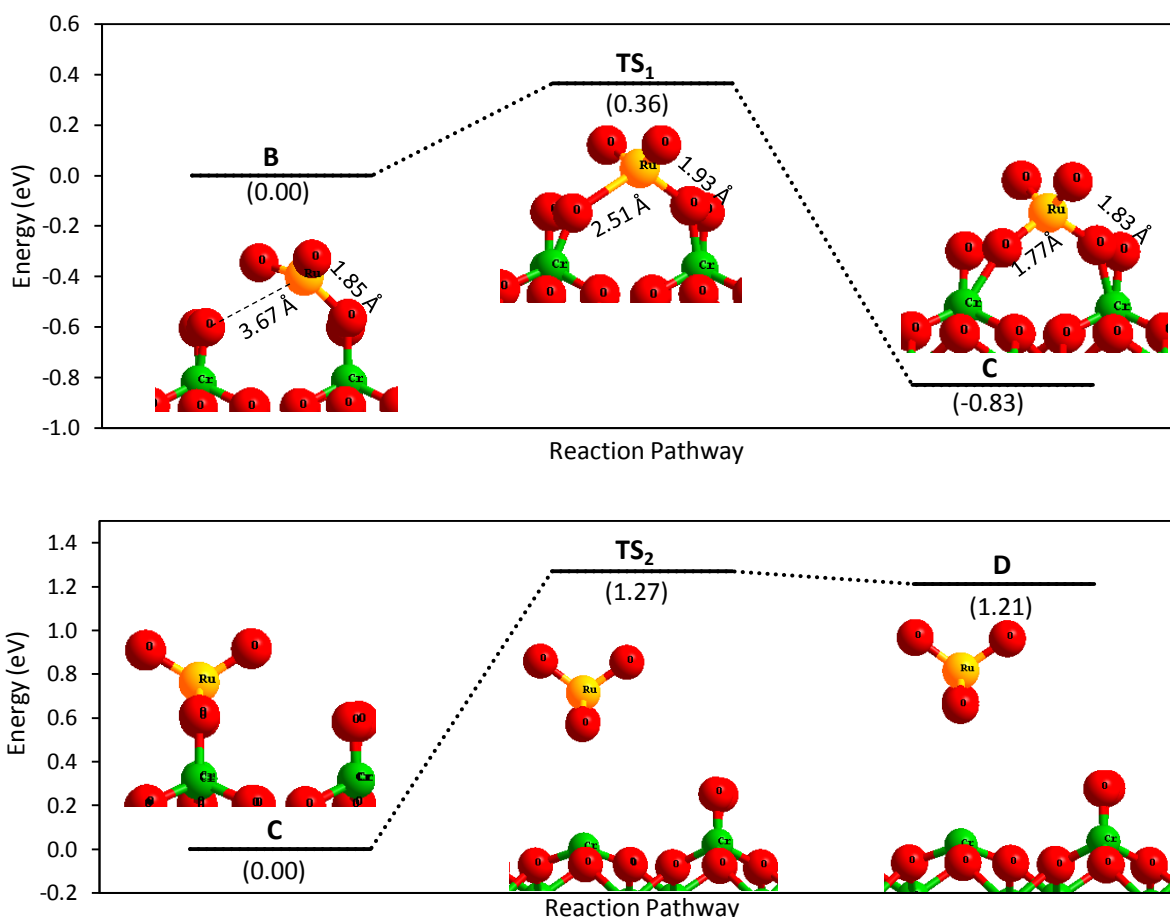
Figure 4.29. Energy diagram of the transition states for re-vaporization of $RuO_{4(g)}$ from RuO_2 adsorbed on a Chromyl surface with a coverage equal to 25%. (Top) transition state from state B to C (Bottom) transition state from state C to D. Chromium: green. Oxygen: red. Ruthenium: yellow.

At 50% coverage, a possible reaction pathway is shown in **Figure 4.30**. In a first step, two RuO_2 molecules are adsorbed on the surface. Each molecule forms one bond between Ru atom and terminal oxygen (**A→B**). The second step is the formation of a tetrahedral RuO_4 species on the surface. This step is exothermic (ΔE = -1.40 eV) (**B→C**). Then, one of the two tetrahedral-like structures can be liberated in air as RuO_4. Meanwhile, the other ruthenium species incline to the surface and a new bond is created between oxygen atom of ruthenium oxide species and chromium atom of the surface (which is similar to the configuration of RuO_4 on Cr_2O_3Cr surface **Figure 4.15**) (**C→D**). In the end, second $RuO_{4(g)}$ desorbs from the reduced Cr_2O_3Cr surface (**D→E**).
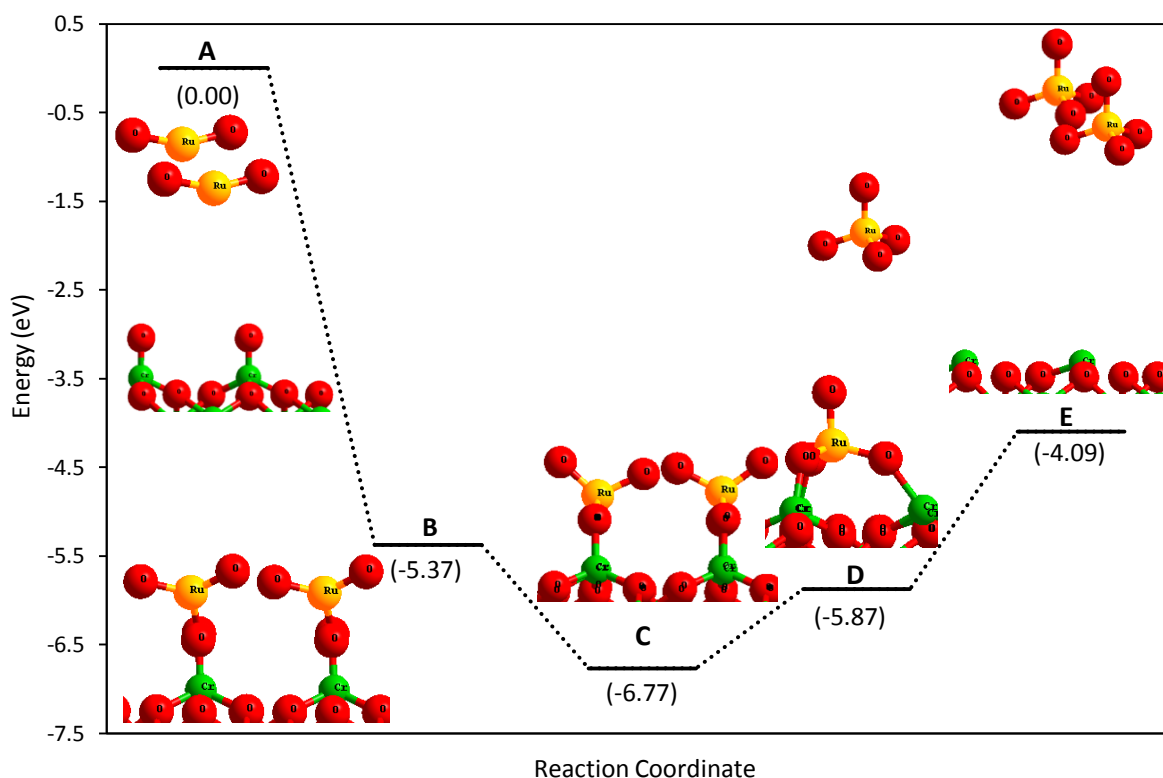
Figure 4.30. Energy diagram of the re-vaporization $RuO_{4(g)}$ on from RuO_2 adsorbed on Chromyl surface with coverage equal to 50%. Chromium: green. Oxygen: red. Ruthenium: yellow.

The geometries of the transition states are similar to the 25% coverage ones. This displacement of the Ru atom toward the second terminal oxygen atom (B to C (**Figure 4.31**, top)), has an activation energies of 0.49 eV. The presence of the second RuO_3 species on the surface has only a small effect on this step.

The reaction path between C to D (**Figure 4.31**, middle) is very simple. The two bonds between oxygen atoms and the surface are broken when the distance between the surface and the Ru increases. In the meantime, another tetrahedral-like structure is tilted towards the surface. The oxygen atoms in the second tetrahedral-like structure form three bonds with chromium atoms of the surface. The later geometry is equivalent to the one formed by adsorption of RuO_4 on Cr_2O_3Cr surface (**Figure 4.15**). The activation energy for this step is equal to 1.28 eV. The last step, from D to E (**Figure 4.31**, bottom), is the simple desorption of $RuO_{4(g)}$ with an activation energy equal to 1.92 eV.
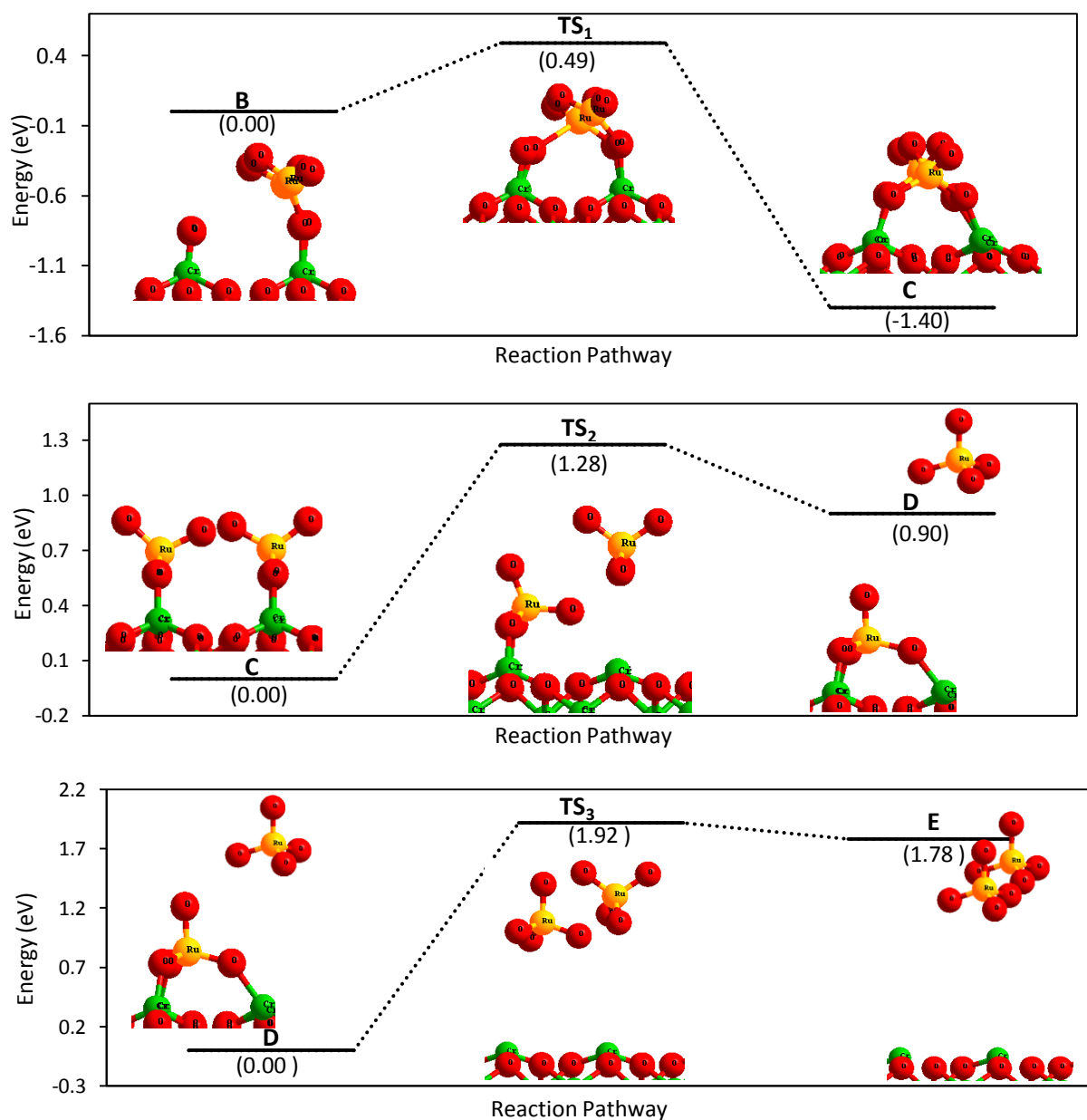
Figure 4.31. Energy diagram of transition states for re-vaporization of $RuO_{4(g)}$ from RuO_2 adsorbed on Chromyl surface with a coverage equal to 50%. (Top) transition state from state B to C (middle) transition state from state C to D (Bottom) transition state from state D to E. Chromium: green. Oxygen: red. Ruthenium: yellow.

For a surface totally covered by RuO_2, the RuO_3 desorption was studied. A possible reaction pathway is shown in **Figure 4.32**. Each RuO_2 molecule adsorbed on the surface creates a bond with the terminal oxygens of the surface and the ruthenium atom is in the centre of the triangle formed by the three oxygen atoms (similar to RuO_3) (**A→B**). Then a first RuO_3 molecule can desorb from the surface (**B→C**). The process is different for desorption of the second RuO_3 molecule (**C→D**). When RuO_3 desorbs, two other triangle structures are tilted towards to the surface and ruthenium are placed

in a threefold hollow site (Ru-OOO,**Figure 4.10**). Then, the last two Ru atoms are desorbed as RuO_3 (**D→E→F**). As a result, Chromyl surface is totally reduced.
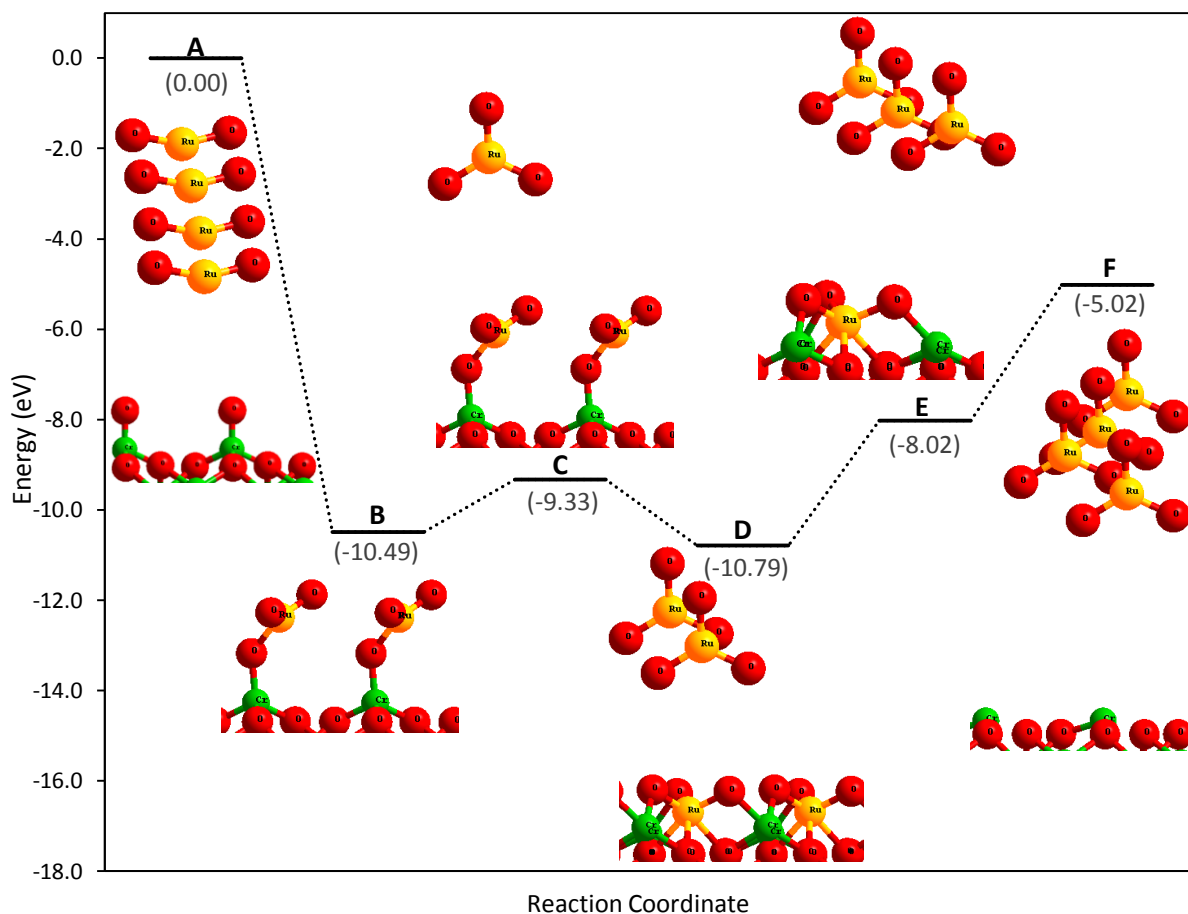
Figure 4.32. Energy diagram of the re-vaporization $RuO_{3(g)}$ from RuO_2 adsorbed on a Chromyl surface with coverage equal to 100 %. Chromium: green. Oxygen: red. Ruthenium: yellow.

The first two steps are similar. The distance between the surface and the RuO_3 increase till the complete desorption of the molecule. The activation energy of the first desorption is 1.24 eV (**Figure 4.33**, top). From the state C to D (**Figure 4.33**, middle top), one RuO_3 desorbs. The activation energy is equivalent to the previous one (E_{act}= 1.33 eV). In the meantime, two other ruthenium atoms move in the threefold hollow site on the surface (The geometry is similar to the geometry of RuO_3 adsorbed on the Cr_2-O_3-Cr surface Ru-OOO,**Figure 4.10**) which explains that this step is exothermic. The transition state for desorption of the third RuO_3 molecule is represented in **Figure 4.33**, middle down. The activation energy is quite important (2.93 eV) due to the formation of three bonds between the Ru and the oxygen atoms of the surface. From E to F (**Figure 4.33**, bottom), the last ruthenium atom is desorbed from the surface under $RuO_{3(g)}$ form. The activation energy is very high (to around 3.0 eV).
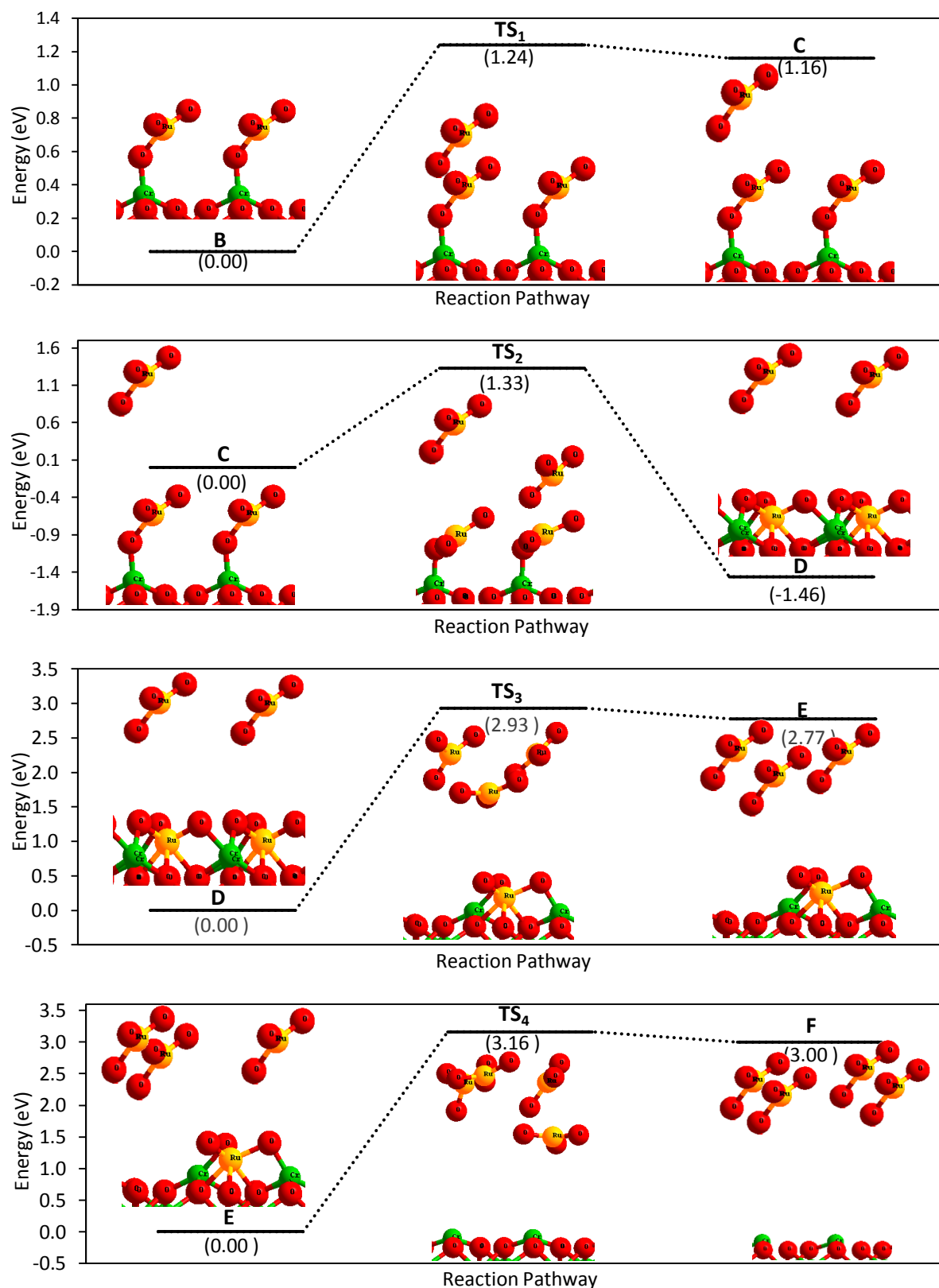
Figure 4.33. Energy diagram of the transition states for the re-vaporization of $RuO_{3(g)}$ from RuO_2 adsorbed on a Chromyl surface with a coverage equal to 100%. (Top) transition state from state B to C (middle, top) transition state from state C to D (middle, bottom) transition state from state D to E (Bottom) transition state from state E to F. Cr: green. O: red. Ru: yellow.

To sum up, the re-vaporization of RuO_2 from stainless steel surface is possible with or without oxygen. In presence of oxygen, ruthenium can be re-vaporized spontaneous (exothermic reaction) from all adsorbed surfaces as $RuO_{4(g)}$. Without oxygen, depending on coverage, ruthenium will desorb as $RuO_{3(g)}$ or $RuO_{4(g)}$ from the Chromyl surface. For a coverage in RuO_2 equal to 25% and 50%, ruthenium tetroxide will be released from the surface. The release of the first $RuO_{4(g)}$ molecule is not difficult with an activation energy lower than 1.30 eV. The sublimation of the second $RuO_{4(g)}$ is more difficile (activation energy close to 2.0 eV). On a totally covered surface, the re-vaporization of RuO_2 is possible but under $RuO_{3(g)}$ form. The desorption of the first two ruthenium oxide species is fast (activation energy around 1.3 eV). The desorption of the last ruthenium oxide will be very slow (activation energy around 3 eV).

4.2.3 CONCLUSION

In summary, ruthenium oxide species can be adsorbed on Cr_2O_3Cr and Fe_2O_3Fe surfaces and they stay isolated on the surface. On the Chromyl surface, only RuO_2 and RuO_3 can be adsorbed. On the hydrated surface ($Cr_2O_3Cr_2(OH)_3$), the adsorption in not favourable.

The decomposition of RuO_3 and RuO_4 on stainless steel have been studied. It has been shown that the decomposition of RuO_3 on different surfaces is not probable. The sublimation of RuO_3 is favoured.

Stainless steel surfaces play an important role in the decomposition of RuO_4. RuO_4 adsorbed first on the surface, and then it is reduced into RuO_3. The RuO_3 will desorb and its decomposition into RuO_2 might happen close to the surface due to the low stability of $RuO_{3(g)}$. This behaviour is in agreement with the experimental results published by P. Cains and S. Barnes[50]. They have deposited volatile ruthenium oxides on steel surface and found that above 150 °C the deposition could happen and lead to the formation crystalline $RuO_{2(s)}$. It should also be noticed that the participation of the surface of stainless steel may accelerate the decomposition of $RuO_{4(g)}$ as the first reaction step for the decomposition of $RuO_{4(g)}$ is kinetically slow. The decomposition of RuO_4 could not occur on a hydrated surface. On hydrate surface, the sublimation of RuO_4 take place before the formation of RuO_2. This result could explain that in an atmosphere saturated by water, no RuO_4 decomposition can take place[39,42].

The re-vaporization of deposited RuO_2 particles may be a significant source of gaseous ruthenium oxides[39,42]. In presence of oxygen, ruthenium dioxide can be re-vaporized spontaneously from all adsorbed surfaces as $RuO_{4(g)}$. On the opposite, without oxygen, ruthenium can be liberated as $RuO_{3(g)}$ or $RuO_{4(g)}$ only from Chromyl surface. The nature of the oxide formed will depend on the RuO_2 coverage.

4.3 ADSORPTION OF DIOXYGEN ON RUTHENIUM DIOXIDE AEROSOLS

As mentioned before (Chapter IV Section 4.1.1.2), $RuO_{2(g)}$ can exist only at very high temperature (> 2000 K)[9]. So, for the most of the time, ruthenium dioxide is in a solid state inside the reactor coolant system (RCS) and the nuclear containment. At high temperature, the main gaseous species present in the containment are $RuO_{4(g)}$ and $RuO_{3(g)}$. However, $RuO_{4(g)}$ is not stable at low temperature, it decomposes totally into $RuO_{2\ (s)}$ at temperature higher than ~110 °C. Hence, the formation of RuO_2 aerosols is expected when the temperature decreases. Furthermore, above 1500 K, the transported ruthenium species in the RCS are a mix between almost totally as aerosol particles $(RuO_{2\ (s)})$[39,42–44] and gaseous ruthenium oxides. In this section, first of all, the stability of different surfaces of RuO_2 will be studied. In a second part, oxygen will be adsorbed on this surface in order to investigate the re-vaporization of ruthenium species. Finally, we will study the re-vaporization of ruthenium gaseous species from our surface using *ab initio* dynamic molecular simulations.

4.3.1 STABILITY OF DIFFERENT RuO₂ SURFACES

Table 4.14. Surface energy for different surface RuO_2

Surface	$E_{surface}(J/m^2)$
[1 1 0]	1.22
[1 0 0]	1.53
[0 0 1]	1.92
[1 1 1]	2.98

First of all, the stability of different RuO_2 surfaces is studied in order to determine the surfaces exposed in RuO_2 aerosols. The bulk structure of RuO_2 is shown in **Figure 4.2** (b). It has a rutile structure (TiO_2 type). Several low miller index surfaces are shown in **Figure 4.34**. In this work, we have tested [1 1 0], [1 0 0], [0 0 1] and [1 1 1] surfaces. Surface energy for different surfaces are grouped in **Table 4.14.** The [1 1 0] surface is the most stable one, this result is consistent with literature data.[47–49]

On the first layer of the **[1 1 0]** surface, there are two kinds of ruthenium atoms and two kinds of oxygen atoms (**Figure 4.34**, right): Ru_{br} (ruthenium atoms construct the bridge structure), O_{br} (oxygen atoms construct the bridge structure), Ru_{cus} (ruthenium atoms expose on the surface), O_f (3-fold (bulk-coordinated) surface O atoms). Ru atoms can adsorb on Ru_{cus}, O_{br} and O_f. On the **[1 0 0]** surfaces (**Figure 4.34**, b), there is also a Ru-O-Ru bridge. The remaining surface is stepped. The oxygen can be adsorbed on the ruthenium site of the Ru-O-Ru bridge. On **[1 0 0]** surface (**Figure 4.34**, c), the oxygen is adsorbed on the defective Ru atoms. Finally, on **[1 1 1]** surface (**Figure 4.34**, d), Ru-O-Ru bridge formed on the surface and the oxygen can also adsorb on the low coordination Ru atom. In the following section, the adsorption of dioxygen on different RuO_2 surfaces will be discussed, in order to study the possible re-vaporization of gaseous ruthenium oxides from RuO_2 aerosols.
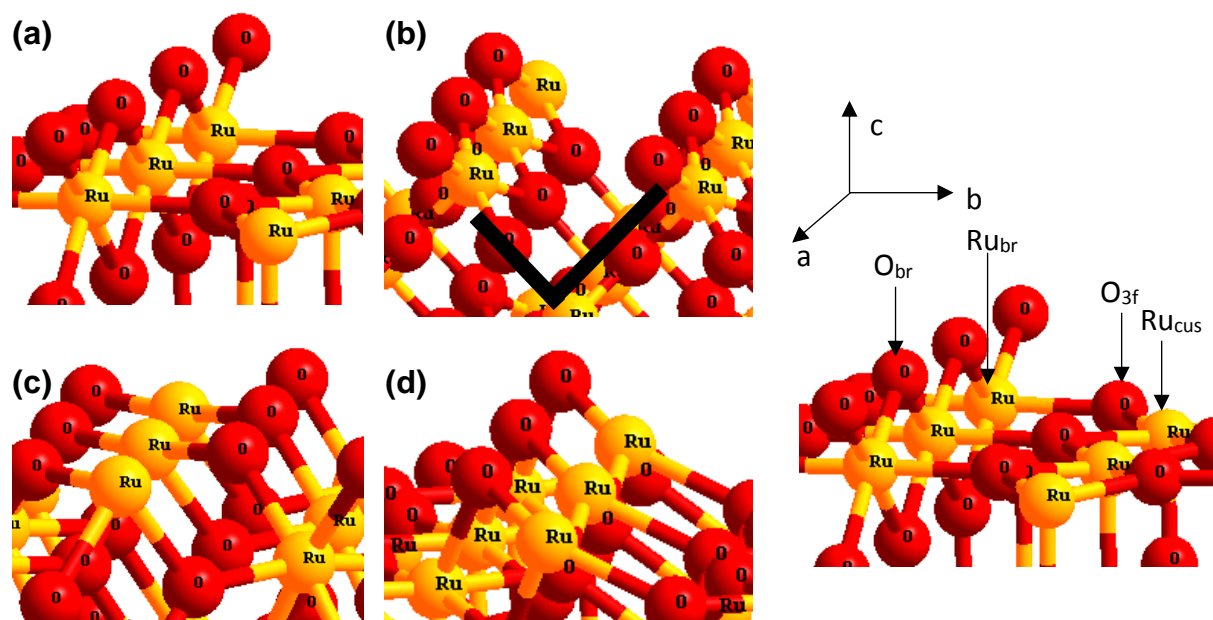
Figure 4.34. Theoretical model for RuO_2 surfaces. (Left)(a) [1 1 0] (b) [1 0 0] (c) [0 0 1] (d) [1 1 1]. (Right) The definitions of different special sites (Ru_{br}, Ru_{cus}, O_{br} and O_{3f}) for the most stable surface [1 1 0] are indicated in the figure. Ruthenium: yellow. Oxygen: red.
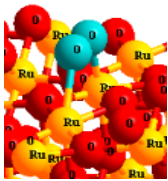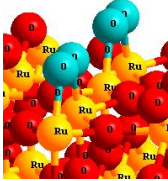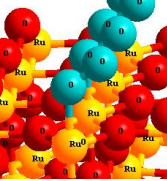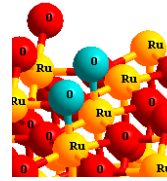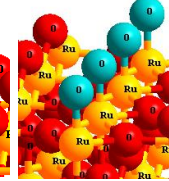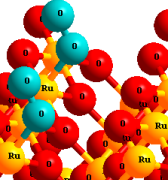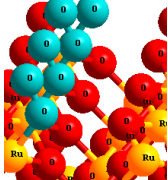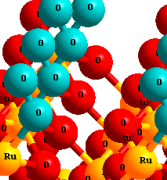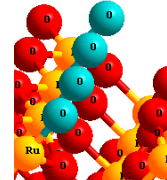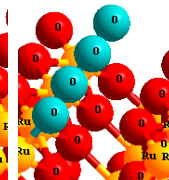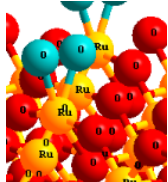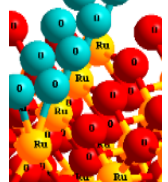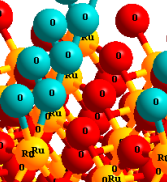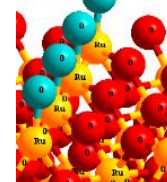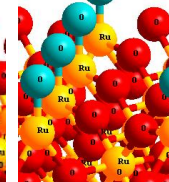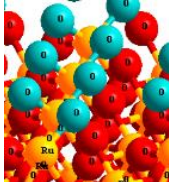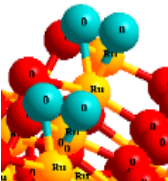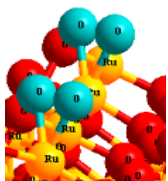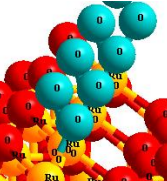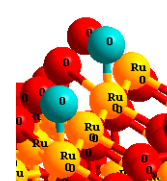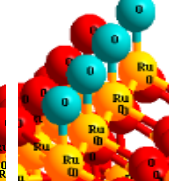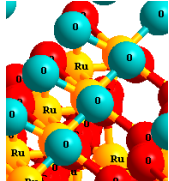
4.3.2 ADSORPTION $O_{2(g)}$ ON DIFFERENT RuO_2 SURFACES

The most stable structure for molecular and dissociative adsorption configurations are grouped in **Table 4.15**. The coverage is defined by equation below:

$$r = \frac{n_{O_2\ adsobed}}{n_{Ru\ sites}}$$

- $n_{O_2\ adsobed}$: Number of adsorbed dioxide molecules.

- $n_{Ru\ sites}$: Number of Ru sites available for O_2 adsorption.

Table 4.15. Most stable structures for molecular and dissociative adsorption of $O_{2(g)}$ on different RuO$_2$ surfaces and adsorption energy per O$_2$ adsorbed in electron volt. Ruthenium: yellow. Oxygen: red. Adsorbed oxygen atom: light blue.

Surface	Molecular Adsorption coverage (%)			Dissociative Adsorption coverage (%)		
	25	50	100	25	50	100
[1 1 0]						Does not exist
	-1.45	-1.38	-0.52	-2.24	-2.12	-
[1 0 0]						Does not exist
	-0.34	-0.37	-1.04	-1.68	-1.46	-
[0 0 1]						
	-1.42	-1.36	-2.69	-2.70	-2.65	-3.37
[1 1 1]						
	-1.53	-1.48	-1.41	-4.51	-4.34	-2.48

The adsorption energy per adsorbed molecule is calculated by equation in Chapter II Section 2.5.2 which can be written as below for adsorption of O$_2$.

$$E_{ads} = \frac{E_{total} - E_{surface} - \left(E_{O_2} \times n_{O_2}\right)}{n_{O_2}}$$

with $E_{ads} < 0$, corresponding to an exothermic reaction.
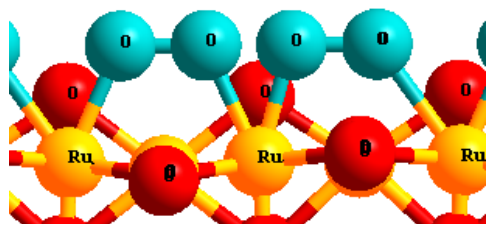
Figure 4.35. The Ru-O-O-Ru bridge structure in surface totally covered by O_2 who is found in literature[46]. Ru: yellow. O: red. Adsorbed O: light blue.

It can be easily noticed that adsorption of dioxygen molecules are favourable on all studied RuO_2 surfaces. On the **[1 1 0]** surface, the dissociative adsorption (25%: -2.24 eV; 50%: -2.12 eV) are more favourable than molecular ones for all the coverages (25%: -1.45 eV; 50%: -1.38 eV; 100%: -0.52 eV). These values are in agreement with values in the literature (molecular adsorption 25%: -1.27 eV; dissociative adsorption 25%: -1.83 eV)[46]. The oxygen atoms adsorb on Ru_{cus} site and form a -Ru-O-O-Ru- bridge in molecular adsorption. The only difference between our calculations and the literature results is on the surface totally covered by O_2, in literature, a -Ru-O-O-Ru-O-O-Ru- bridge (**Figure 4.35**) is formed which make ruthenium 7-fold coordinated. This configuration has been also tested in our calculation but this configuration is not stable and half of the adsorbed oxygen molecules desorbed during the geometry optimization. This desorption may be due to the 7-fold coordinated ruthenium atom. The difference between literature and our calculations may due to the functional used (PW91 in literature and PBE in our works) and different cut off value (400 eV in literature and 600 eV in our work). In our study, when the surface is totally covered by oxygen molecules, in the most stable configuration, only one of the two oxygen atoms makes a bond with ruthenium atom on the surface. The distance between two O atoms is equal to 1.28 Å which is close to distance between oxygen atoms in dioxygen gas form (d_{O-O} = 1.23 Å). The length of oxygen bridge in other molecular adsorptions is equal to about 1.37 Å. For dissociative adsorption, the distance between adsorbed oxygen atoms is close to 3.10 Å.

On the **[1 0 0]** surface, the molecular adsorption (25%: -0.34 eV; 50%: - 0.37 eV; 100%: -1.04 eV) are less favourable than dissociative ones (25%: -1.68 eV; 50%: -1.46 eV) for different coverages. The oxygen atoms adsorb on top of the ruthenium atoms situated au Ru-O-Ru bridge on the surface. In molecular adsorption, two oxygen atoms from the same oxygen molecule are adsorbed on the same ruthenium atom. The O-O distance ($d_{O-O} \approx 1.28$ Å) is close to the gas phase one indicating that the retro-donation is weak. For the dissociative adsorption, for a coverage lower or equal to 50%, the adsorption is exothermic ($\Delta E \sim -1.5$ eV) and the distance between two oxygen atoms is higher than 3.11 Å.

On the **[0 0 1]** surface, the dissociative adsorption (25%: -1.42 eV; 50%: -1.36 eV; 100%: -2.69 eV) are also more favourable than molecular one (25%: -2.70 eV; 50%: -2.65 eV; 100%: -3.37 eV). The oxygen atoms adsorb on top of the ruthenium atoms situated in the first atomic layer. In molecular adsorption, the distance between the two oxygen increases (d_{O-O} = 1.36 -1.40 Å). For the dissociative adsorption, there are two types of adsorption. For coverages lower or equal to 50%, two oxygen atoms coming from the same oxygen molecule are adsorbed on different ruthenium atoms with an adsorption energy equal to about -2.70 eV and the distance between two oxygen atoms is higher than 4.50 Å. For a surface totally covered by oxygen, two oxygen atoms from the same oxygen molecule are adsorbed on the same ruthenium atom. The adsorption energy is equal to -3.37 eV and the distance between two oxygen atoms corresponds to 2.76 Å.

For **[1 1 1]** surface, the dissociative adsorption (25%: - 4.51 eV; 50%: -4.34 eV; 100%: -2.48 eV) are more favourable than molecular ones (25%: -1.53 eV; 50%: -1.48 eV; 100%: -1.41 eV). The dissociative adsorption is very exothermic. The oxygen atoms adsorb on the defective ruthenium atoms situated in Ru-O-Ru bridge on the external of the surface. In molecular adsorption, distance between the two oxygens is $d_{O-O} \approx$ 1.40 Å). For the dissociative adsorption, at low coverage, two oxygen atoms from the same oxygen molecule are adsorbed on different ruthenium atoms. The reaction is very exothermic (more than -4 eV). For a surface totally covered by oxygen, two oxygen atoms from the same oxygen molecule are adsorbed on the same ruthenium atom. The reaction is less exothermic (-2.48 eV) and the distance between two oxygen atoms is equal to 2.82 Å.

We can conclude that the dissociative adsorption is more favourable than molecular one on all the surfaces. In the molecular adsorption, the oxygen-oxygen distance is slightly increased. On most stable surface [1 1 0], a peroxo-type (-Ru-O-O-Ru-) bridge is formed in molecular adsorption. As expected, the adsorption on the less stable surface i.e. the [1 1 1] one, gives the more exothermic reactions.

4.3.3 RE-VAPORIZATION OF RUTHENIUM GASEOUS SPECIES FROM DIFFERENT ADSORBED RuO$_2$ SURFACE

In this section, the pathway for re-vaporization of ruthenium gaseous species from different adsorbed RuO$_2$ surface will be studied. There are many possibilities to form

gaseous ruthenium species ($RuO_{3(g)}$ or $RuO_{4(g)}$) from these surface, so usual standard molecular simulation may not investigate all possibilities. Hence, Molecular Dynamic simulation is used, in order to understand the re-vaporization process. In our works, only one surface will be studied as the running time for a Molecular Dynamic simulation is quite long. The surface who has been chosen is **[0 0 1]** with a coverage of O_2 equal to 25% as it has a relatively short calculation time.

4.3.3.1 EXPERIMENTAL SECTION

Molecular dynamic calculations are performed with the Projector Augmented Waves (PAW) approach[63]. The functional of these potential are applied in the Vienna *Ab-initio* Simulation Package (VASP)[64,65]. In the initial configurations, a 2×2 cellule of [0 0 1] surface with one oxygen molecule adsorbed on the top of the surface (25% coverage) was utilized by molecular adsorption and dissociative adsorption (**Figure 4.36**).
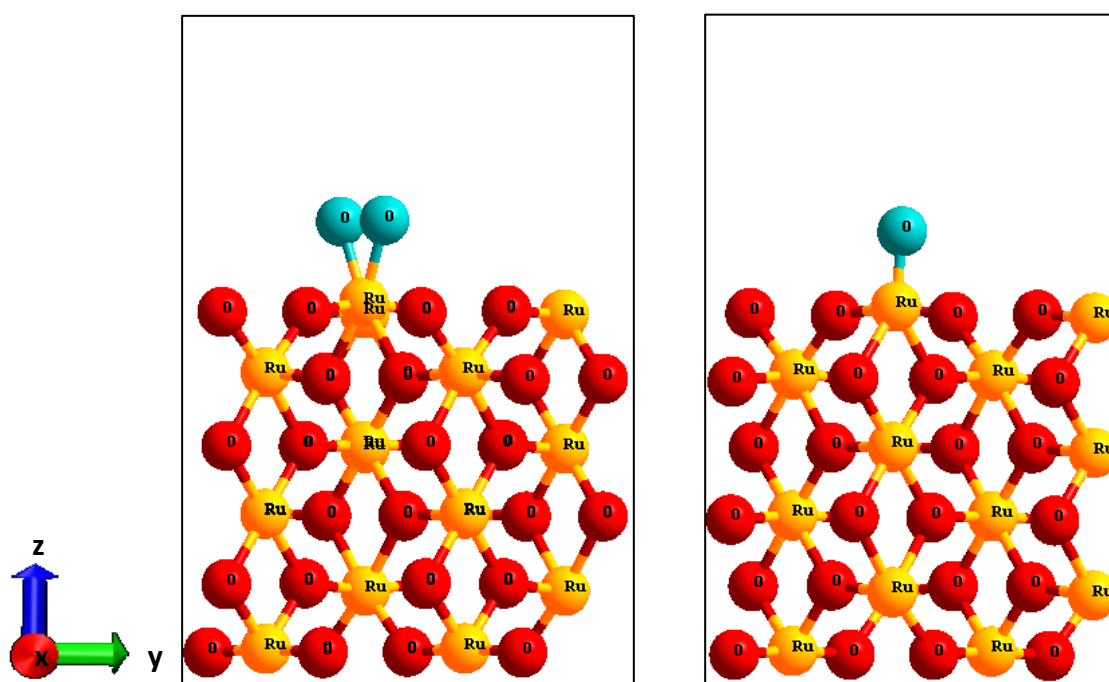
Figure 4.36. Systems used in Molecular Dynamics (left) molecular adsorption and (right) dissociative adsorption of dioxygen molecule on [0 0 1] ruthenium dioxide surface with a coverage of O_2 equal to 25%. $t = 0\ fs$. Ruthenium: yellow; Oxygen: red. Adsorbed oxygen atom: light blue.

Firstly a standard Molecular dynamic calculation was performed in order to stabilised the system, Born–Oppenheimer molecular dynamics simulations were carried out in the canonical NVT ensemble, the temperature was controlled by a Nosé–Hoover

thermostat[66,67] around 450 K. A time step of 1 fs was chosen for motion equation. Then a *Meta*-Molecule Dynamic simulation with Slow-growth approach was performed using Anderson thermostat[68] which also solves Newton's equation of motion using time step of 1 fs.

4.3.3.2 DYNAMICS EVOLUTION OF THE SYSTEM

The dynamics evolutions of the two systems with different modes of adsorption is divided in several parts: evolution of temperature, evolution of energy etc.

4.3.3.2.1 Molecular adsorption of dioxygen molecule on [0 0 1] RuO$_2$ surface
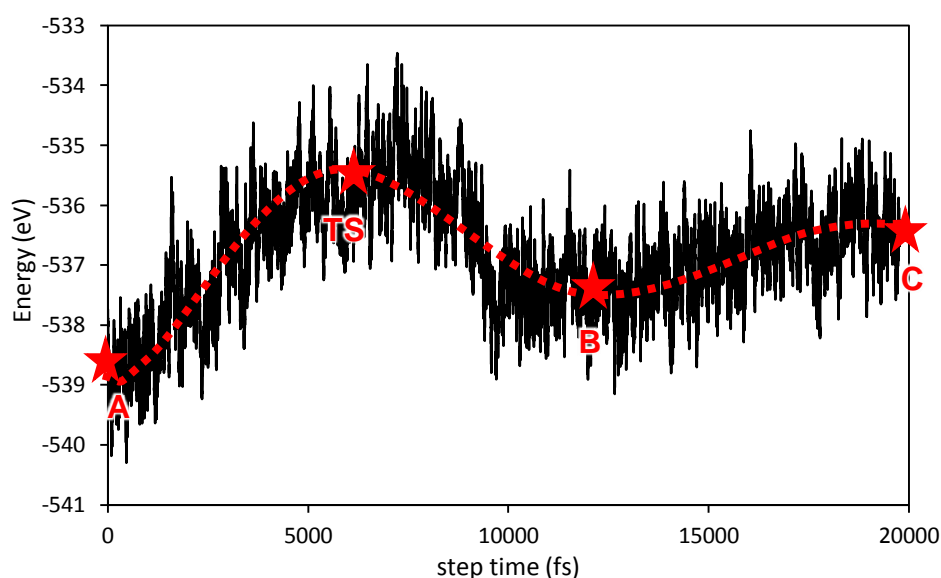
Figure 4.37. Variation of total energy during *Meta* Molecule Dynamic simulation with Slow-growth approach for ruthenium gaseous species from surface with dioxygen molecule adsorbed associative on [0 0 1] ruthenium dioxide surface from *t = 0 to 20 000 fs*.

The re-vaporization of ruthenium gaseous species from surface with associative adsorption of dioxygen molecule on [0 0 1] surface of RuO$_2$ will be discussed primary. The temperature profile of this simulation was shown in **Appendix** Figure A.9. It can be clearly observed that the temperature stays around the target temperature (450K). The variation of total energy for this system during the *Meta*-Molecule Dynamic simulation is presented in **Figure 4.37**.
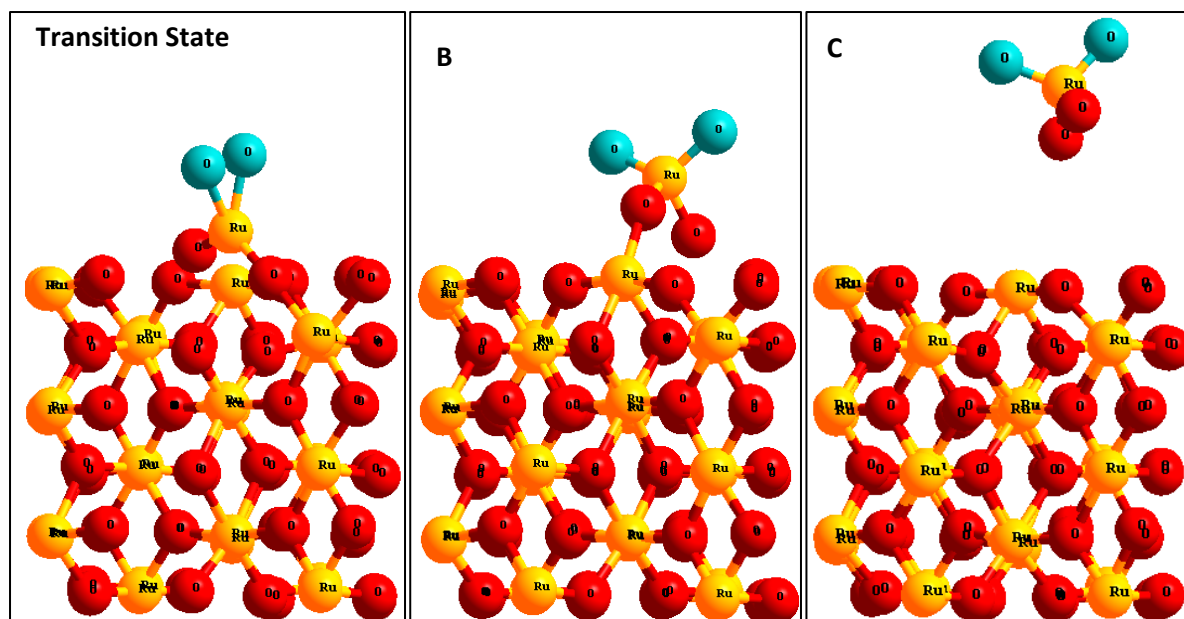
Figure 4.38. Configurations corresponding to stationary points for re-vaporization of ruthenium gaseous species from surface with dioxygen molecule adsorbed associative on [0 0 1] ruthenium dioxide surface. (Left) Transition state (**TS**): $t \approx 6\,000$ *fs.* (Middle) state **B**: $t \approx 12\,000$ *fs.* (Right) state **C**: $t \approx 20\,000$ *fs.* Ru: yellow; O: red. Adsorbed O: light blue.

It can be noticed that the re-vaporization path is composed of two steps: first step (A→ TS → B) and second step (B →C). The re-vaporization process began with an initial state **A** where two oxygen atoms are adsorbed on the same ruthenium atom (**Figure 4.36** left) with an energy of the system equal to about -538.8 eV. Next the system goes to state **B** by passing a transition state. During this pathway, the ruthenium atom where two oxygen atoms are adsorbed moves up to the vacuum by pulling one of the oxygen atom off the surface (around 6 000 fs. Transition state: **Figure 4.38** left). The energy for this configuration is around -535.5 eV. Afterward, some reorganisations happen on the surface. It can be observed that the ruthenium atom where two oxygen atoms adsorbed mobilises a little on the surface. The first detached oxygen atom of the surface makes a new bond with one of ruthenium atoms on the top of the surface. After some other rearrangements (around 12 000 fs), a second oxygen atom is pulled out of the surface (State B: **Figure 4.38** middle) with a total energy equal to about -537.5 eV. The activation energy for the first step of re-vaporization process is around 3 eV. In the second step, the distance between the formed ruthenium oxide and the RuO_2 cluster is increasing until being liberated from the RuO_2 surface. In this step, the ruthenium is released under RuO_4 form with no a transition state. Total energy for the final system

(around 20 000 fs) is about -536.5 eV with a different energy from the initial state (**A**) equal to 2.3 eV.

In conclusion, the re-vaporization of ruthenium gaseous species from surface with dioxygen molecule adsorbed associative on [0 0 1] surface ruthenium dioxygen can be simulated by Molecular Dynamic simulation. This process is occurring in two steps and ruthenium will be liberated in RuO_4 form with an activation energy equal to about 3 eV, meaning that it is not a very relevant way of formation.

4.3.3.2.2 Dissociative adsorption of dioxygen molecule on [0 0 1] RuO_2 surface

The re-vaporization of ruthenium gaseous species from surface with dioxygen molecule adsorbed according to a dissociative process on [0 0 1] surface of RuO_2 will be discussed in this section. The temperature profile of this simulation was shown in **Appendix** Figure A.10. It can be observed that the temperature of the system stays around the target temperature (450 K). The total energy variation for this system during the *Meta*-Molecule Dynamic simulation is presented in **Figure 4.39**.
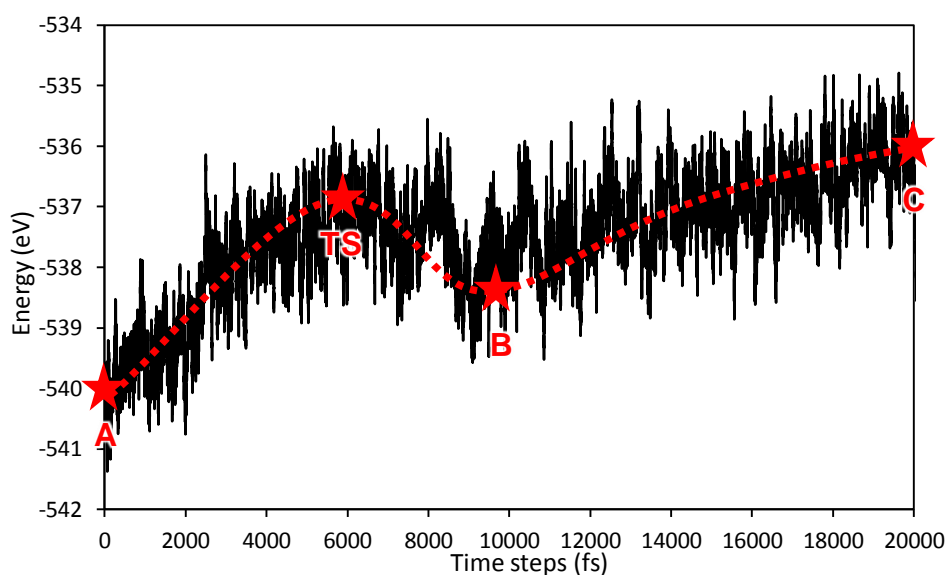
Figure 4.39. Variation of total energy during *Meta* Molecule Dynamic simulation with Slow-growth approach for ruthenium gaseous species from surface with dioxygen molecule adsorbed dissociative on [0 0 1] ruthenium dioxide surface from *t = 0 to 20 000 fs*.

The re-vaporization procedure began by a state **A** where two oxygen atoms adsorbed dissociative on two ruthenium atoms (**Figure 4.36** right) with an energy of the system equal to about -540.2 eV. Next the system goes to state **B** by passing a transition state (**TS**). During this pathway, one of the ruthenium atoms where oxygen atom adsorbed

moves up towards to vacuum by pulling one oxygen atom off the surface (around 6 000 fs. Transition State: **Figure 4.40** left) with an energy equal to -537 eV. Afterward, some reorganisations happen on the surface. It can be observed that formed ruthenium oxide will move toward another adsorbed oxygen atom by making a new Ru-O bond. Hence, the ruthenium oxide finishes by staying in RuO_4 configuration on the top of the surface. After some other rearrangements (around 10 000 fs), the gaseous ruthenium oxide will be pulled out of the surface (State B: **Figure 4.40** middle) with a total energy equal to about -538.5 eV. The activation energy for the first step of re-vaporization process is around 3 eV. Afterwards, the distance between the formed RuO_4 species and the RuO_2 cluster is increasing until release from RuO_2 surface. Total energy for the final system (around 20 000 fs. State C: **Figure 4.40** left) is about -536 eV with a difference energy from initial state (**A**) being equal to 4.2 eV.
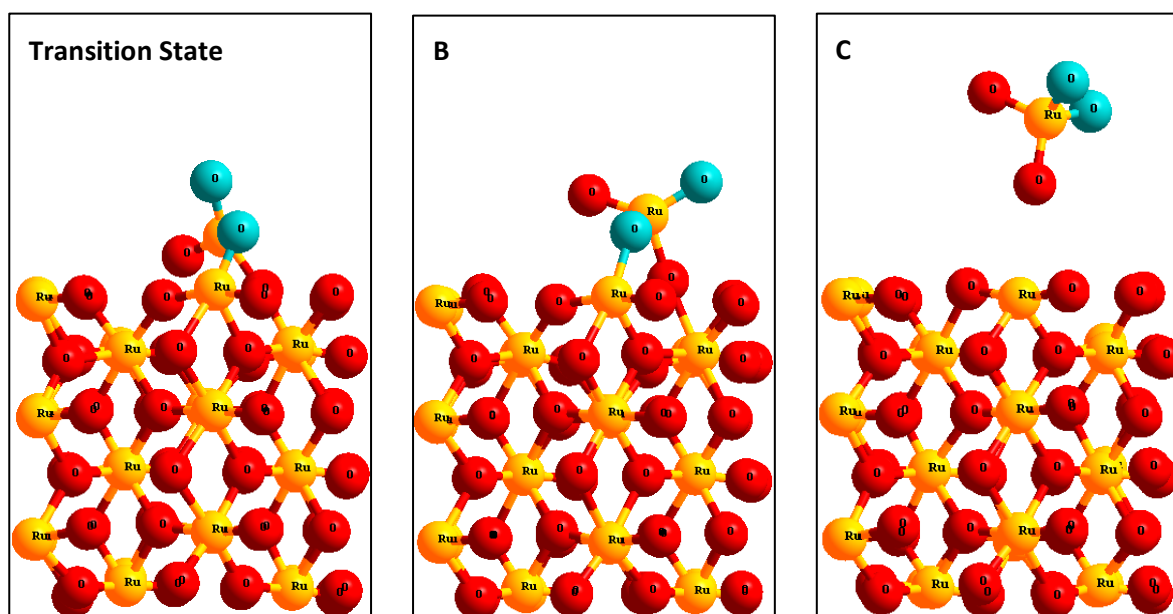
Figure 4.40. Configurations corresponding to stationary points for re-vaporization of ruthenium gaseous species from surface with dioxygen molecule adsorbed dissociative on [0 0 1] ruthenium dioxide surface. (Left) Transition State (**TS**): $t \approx$ *6 000 fs*. (Middle) state **B**: $t \approx$ *10 000 fs*. (Right) state **C**: $t \approx$ *20 000 fs*. Ru: yellow; O: red. Adsorbed O: light blue.

In conclusion, the re-vaporization of ruthenium gaseous species from surface with O_2 adsorbed dissociative on [0 0 1] surface ruthenium dioxygen can be simulated by Molecular Dynamic simulation. Ruthenium will be liberated in RuO_4 form with an energy over 4.2 eV which is very high and do not constitutes a relevant pathway of volatile ruthenium formation.

4.3.4 CONCLUSION AND PERSPECTIVE

In this section, the stability of different RuO_2 surfaces are discussed. In agreement with the literature data[47–49], the [1 1 0] surface appears to be the most stable. Then dioxygen molecule has been adsorbed on these surfaces by molecular and dissociative adsorptions. It can be shown that the dissociative adsorption is more favourable than the molecular adsorption for all the surfaces. The oxygen molecules adsorbed on the surface stay in this initial state (d_{O-O} close to the distance between oxygen atoms in dioxygen molecule) in the molecular adsorption process. Overall, the adsorption of O_2 on [1 1 1] surface is the most favourable one as it is the most unstable surface in our study. Then according to these results, re-vaporization of volatile ruthenium oxide from RuO_2 aerosol is studied by using Molecular Dynamic calculations. Unfortunately, due to excessive time of computation, only [0 0 1] surface has been explored as it has a relatively short calculation time. By this method, the reaction pathways have been identified in including the determination of the activation energy. Hence Molecular Dynamic calculation is a quite clear way to study a re-vaporization process. It can be observed that ruthenium is potentially released under RuO_4 from for these two adsorbed surfaces by creating a defect on RuO_2 aerosol surface. However, the activation energies in these two cases are very high (around 3.0 eV and 4.2 eV), thus the formation of $RuO_{4(g)}$ from low oxidized RuO_2 aerosol (25% coverage) will not be very relevant. In perspectives, other coverages and other adsorbed surfaces should be explored in the future to complete/achieve this study.

4.4 CONCLUSION

In this chapter, ruthenium oxides species are adsorbed on Cr_2O_3Cr surface, its modified surfaces and Fe_2O_3Fe surface. It can be noticed that the ruthenium oxides stay always isolated on the surfaces. The adsorption on a neutral surface is more favourable than on a modified surface. Based on these adsorbed surfaces, the decomposition of RuO_3 and RuO_4 and the re-vaporization of gaseous ruthenium oxides species on stainless steel have been investigated. The sublimation of RuO_3 is still more favourable than the decomposition of RuO_3 on different surfaces. Stainless steel surface plays an important role in the decomposition of RuO_4. The RuO_4 decomposed primarily on the surface to RuO_3 and then the decomposition of RuO_3 occurs in the gas phase after its sublimation. These reactive pathways can occur on Cr_2O_3Cr and

Fe_2O_3Fe surfaces but not on a hydrated surface. These results may explain several experimental observations[39,42,50]. It is also consistent with the fact that the stainless steel surface may accelerate the decomposition of $RuO_{4(g)}$. Furthermore, with or without presence of oxygen in the carrier gas, ruthenium can be re-vaporized spontaneous from adsorbed surfaces under $RuO_{3(g)}$ or $RuO_{4(g)}$ form depending on the coverage. This finding can explain that the re-vaporization of deposited RuO_2 particles is a source of gaseous ruthenium oxides as mentioned in litterature[39,42].

Then dioxygen molecule has been adsorbed on ruthenium dioxide surfaces (including the most stable one [1 1 0]) by molecular and dissociative adsorptions where the latter one is more advantageous. Afterward, based on these adsorbed surfaces, re-vaporization of gaseous ruthenium oxides species from RuO_2 aerosol is studied by using Molecular Dynamic simulation. By this method, the reaction pathways can be found including its activation energy. According to our calculations, on [0 0 1] surface, ruthenium species is released under $RuO_{4(g)}$ by generating defects on RuO_2 surface. However, the activation energy is quite important (over 3 eV), it means that this process will be very slow. In perspectives, using Molecular Dynamic simulations, the re-vaporization process involving other coverages and other adsorbed surfaces should be explored in the future to complete/achieve this study.

REFERENCE

(1) *Report on the IRSN's Investigations Following the Widespread Detection of 106 Ru in Europe Early October 2017*; IRSN, 2018.

(2) Holm, J.; Glänneskog, H.; Ekberg, C. Deposition of RuO4 on Various Surfaces in a Nuclear Reactor Containment. *J. Nucl. Mater.* **2009**, *392* (1), 55–62.

(3) Eichler, B.; Zude, F.; Fan, W.; Trautmann, N.; Herrmann, G. Volatilization and Deposition of Ruthenium Oxides in a Temperature Gradient Tube. *Radiochim. Acta* **1992**, *56* (3), 133–140.

(4) Mun, C.; Cantrel, L.; Madic, C.; Mun, C.; Institut, L. C.; Radioprotection, D.; Nucléaire, D. S. Review of Literature on Ruthenium Behavior in Nuclear Power Plant Severe Accidents. *Nucl. Technol.* **2006**, *156* (Decmber), 332.

(5) Caractéristiques Physiques et Toxicologiques de Radionucléides Significatifs. *clefs CEa* **2003**, *48*, 109–110.

(6) *The Merck Index: An Encyclopedia of Chemicals, Drugs, and Biologicals*, 14th ed.; O'Neil, M. J., Ed.; Merck and Co., Inc., 2006.

(7) Williams, M. L. CRC Handbook of Chemistry and Physics, 76th Edition. *Occup. Environ. Med.* **1996**, *53* (7), 504–504.

(8) Ashcroft, N.; Mermin, N. *Solid State Physics*; New York Holt, Rinehart and Winston, 1976.

(9) Garisto, F. Thermodynamic Behaviour of Ruthenium At High Temperatures Comportement Thermodynamique Du Ruthenium a Hautes Temperatures. *AECL-9552, Whiteshell Nucl. Res. Establ.* **1988**.

(10) Schäfer, H.; Schneidereit, G.; Gerhardt, W. Zur Chemie Der Platinmetalle. RuO2 Chemischer Transport, Eigenschaften, Thermischer Zerfall. *Zeitschrift für Anorg. und Allg. Chemie* **1963**, *319* (5–6), 327–336.

(11) Bell, W. E.; Tagami, M. High-Temperature Chemistry of the Ruthenium Oxygen System 1. *J. Phys. Chem.* **1963**, *67* (11), 2432–2436.

(12) Kay, J. G.; Green, D. W.; Duca, K.; Zimmerman, G. L. Identification and Structures of Matrix-Isolated Ruthenium Oxide Molecules from Infrared Spectra.

J. Mol. Spectrosc. **1989**, *138* (1), 49–61.

(13) Seiler, H. G.; Sigel, H.; Sigel, A. Handbook on Toxicity of Inorganic Compounds. **1988**.

(14) *Patty's Industrial Hygiene and Toxicology: Volume 2A, 2B, 2C*, 3rd ed.; Clayton, G. D., Clayton, F. E., Eds.; John Wiley Sons: New York, 1981.

(15) Pascal, P.; Charonnat, R.; Ciepka, G.; Delépine, M.; Poulenc, P.; Duval, C. *Nouveau Traité de Chimie Minérale—Tome XIX, Ruthénium, Osmium, Rhodium, Iridium, Palladium, Platine*; Masson & Cie, E., Ed.; Paris, 1958.

(16) Tojo, G.; Fernández, M. Ruthenium Tetroxide and Other Ruthenium Compounds. In *Oxidation of Primary Alcohols to Carboxylic Acids*; Springer New York: New York, NY, 2007; pp 61–78.

(17) Norman, J. H.; Staley, H. G.; Bell, W. E. Mass Spectrometric Study of the Noble Metal Oxides. In *Mass Spectrometry in Inorganic Chemistry*; 1968; pp 101–114.

(18) Schäfer, H.; Gerhardt, W.; Tebben, A. Gasförmige Rutheniumoxyde Bei Hoher Temperatur. *Angew. Chemie* **1961**, *73* (1), 27–27.

(19) Leudet, A. *Comportement Du Ruthénium à La Dissolution -Entraînement Dans Les Effluents Gazeux*; 1981.

(20) Mun, C.; Cantrel, L.; Madic, C. Study of RuO4decomposition in Dry and Moist Air. *Radiochim. Acta* **2007**, *95* (11), 643–656.

(21) Cordfunke, E. H. P.; Konings, R. J. M. Thermochemical Data for Reactor Materials and Fission Products: The ECN Database. *J. Phase Equilibria* **1993**, *14* (4), 457–464.

(22) Barin, I.; Knacke, O.; Kubaschewski, O. *Thermochemical Properties of Inorganic Substances*; Springer Berlin Heidelberg: Berlin, Heidelberg, 1977.

(23) Zimmerman, G. L.; Riviello, S. J.; Glauser, T. A.; Kay, J. G. Photochemical Decomposition of Ruthenium Tetroxide. *J. Phys. Chem.* **1990**, *94* (6), 2399–2404.

(24) Miradji, F.; Souvi, S.; Cantrel, L.; Louis, F.; Vallet, V. Thermodynamic Properties of Gaseous Ruthenium Species. *J. Phys. Chem. A* **2015**, *119* (20), 4961–4971.

(25) Cordfunke, E. H. P.; Konings, R. J. M.; Westrum, E. F. Recent Thermochemical

Research on Reactor Materials and Fission Products. *J. Nucl. Mater.* **1989**, *167* (C), 205–212.

(26) Rard, J. A. Chemistry and Thermodynamics of Ruthenium and Some of Its Inorganic Compounds and Aqueous Species. *Chem. Rev.* **1985**, *85* (1), 1–39.

(27) Pedley, J. B.; Marshall, E. M. Thermochemical Data for Gaseous Monoxides. *J. Phys. Chem. Ref. Data* **1983**, *12* (4), 967–1031.

(28) Ronchi, C.; Turrini, F. *Thermochemical Data for Reactor Materials*; North-Holland: Amsterdam ;1990.

(29) Cordfunke, E. H. P.; Konings, R. J. M. The Enthalpy of Formation of RuO2. *Thermochim. Acta* **1988**, *129* (1), 63–69.

(30) Schäfer, L.; Seip, H. M.; Santesson, J.; Holmberg, P.; Eriksson, G.; Blinc, R.; Paušak, S.; Ehrenberg, L.; Dumanović, J. Studies on the Failure of the First Born Approximation in Electron Diffraction. VI. Ruthenium Tetraoxide. *Acta Chem. Scand.* **1967**, *21*, 737–744.

(31) Panish, M. B.; Reif, L. Vaporization of Ruthenium and Osmium. *J. Chem. Phys.* **1962**, *37* (1), 128–131.

(32) Paule, R. C.; Margrave, J. L. Vapor pressures of platinum metals. III. Iridium and ruthenium 1. *J. Phys. Chem.* **1963**, *67* (9), 1896–1897.

(33) Krikorian, O. H.; Carpenter, J. H.; Newbury, R. S. *A Mass Spectrometric Study Of The Enthalpy Of Sublimation Of Technetium.*; Univ. of California, Livermore, 1969.

(34) Carrera, N. J.; Walker, R. F.; Plante, E. R. Vapor Pressures of Ruthenium and Osmium. *J. Res. Natl. Bur. Stand. Sect. A Phys. Chem.* **1964**, *68A* (3), 325.

(35) Penman, B. D.; Hammer., R. R. *The Ruthenium Dioxide-Oxygen- Ruthenium Tetroxide Equilibrium*; 1968.

(36) Green, D. W.; Kay, J. G.; Zimmerman, G. L.; Balko, B. A. Infrared Spectrum of Ruthenium Tetroxide Isotopomers in an Argon Matrix. *J. Mol. Spectrosc.* **1989**, *138* (1), 62–68.

(37) Werner, H.; Knowles, P. J.; Knizia, G.; Manby, F. R.; Sch, M.; Wiley, J. Molpro : A General-Purpose Quantum Chemistry Program Package. **2012**, *2* (April), 242–

253.

(38) Nerisson, P.; Hu, H.; Paul, J. F.; Cantrel, L.; Vesin, C. Filtration Tests of Gaseous Ruthenium Tetroxide by Sand Bed and Metallic Filters. *J. Radioanal. Nucl. Chem.*(Submitted)

(39) Backman, U.; Lipponen, M.; Auvinen, A.; Jokiniemi, J.; Zilliacus, R. Ruthenium Behaviour in Severe Nuclear Accident Conditions Final Report. **2004**, No. August, 26.

(40) Miradji, F.; Virot, F.; Souvi, S.; Cantrel, L.; Louis, F.; Vallet, V. Thermochemistry of Ruthenium Oxyhydroxide Species and Their Impact on Volatile Speciations in Severe Nuclear Accident Conditions. *J. Phys. Chem. A* **2016**, *120* (4), 606–614.

(41) Froment, P.; Cara, J.; Vanbegin, J.; Ronneau, C. Study of Ru Released under Accidental Conditions by Overheated Nuclear Fuel: The Emission of Ru and U. *Radiochim. Acta* **2001**, *89* (3), 155–159.

(42) Backman, U.; Lipponen, M.; Auvinen, A.; Tapper, U.; Zilliacus, R.; Jokiniemi, J. K. On the Transport and Speciation of Ruthenium in High Temperature Oxidising Conditions. *Radiochim. Acta* **2005**, *93* (5), 297–304.

(43) Kärkelä, T.; Backman, U.; Auvinen, A.; Zilliacus, R.; Lipponen, M.; Kekki, T.; Tapper, U.; Jokiniemi, J. Experiments on the Behaviour of Ruthenium in Air Ingress Accidents. *VTT Tied. - Valt. Tek. Tutkimusk.* **2006**, No. 2363, 253–262.

(44) Kärkelä, T.; Vér, N.; Haste, T.; Davidovich, N.; Pyykönen, J.; Cantrel, L. Annals of Nuclear Energy Transport of Ruthenium in Primary Circuit Conditions during a Severe NPP Accident. **2014**, *74*, 173–183.

(45) Berlijn, T.; Snijders, P. C.; Delaire, O.; Zhou, H. D.; Maier, T. A.; Cao, H. B.; Chi, S. X.; Matsuda, M.; Wang, Y.; Koehler, M. R.; et al. Itinerant Antiferromagnetism in RuO_2. *Phys. Rev. Lett.* **2017**, *118* (7), 1–12.

(46) Wang, H.; Schneider, W. F. Effects of Coverage on the Structures, Energetics, and Electronics of Oxygen Adsorption on RuO_2 (110). *J. Chem. Phys.* **2007**, *127* (6).

(47) Hess, F.; Krause, P. P. T.; Rohrlack, S. F.; Hofmann, J. P.; Farkas, A.; Over, H. One-Dimensional Confinement in Heterogeneous Catalysis: Trapped Oxygen on RuO_2(110) Model Catalysts. *Surf. Sci.* **2012**, *606* (17–18).

(48) Reuter, K.; Scheffler, M. Composition, Structure, and Stability of (Formula Presented) as a Function of Oxygen Pressure. *Phys. Rev. B - Condens. Matter Mater. Phys.* **2002**, *65* (3), 1–11.

(49) Wang, H.; Schneider, W. F.; Schmidt, D. Intermediates and Spectators in O_2 Dissociation at the RuO_2(110) Surface. *J. Phys. Chem. C* **2009**, *113* (34), 15266–15273.

(50) Cains, P. W.; Barnes, S. J. Deposition of Volatilized Ruthenium on Stainless Steels. *J. Nucl. Mater.* **1991**, *186* (1), 83–86.

(51) Holdoway, M. J. *The Volatilisation and Deposition of Ruthenium Dioxide in Relation to the FINGAL Process*; 1971.

(52) Maas, E. T.; Longo, J. M. Confinement of Ruthenium Oxides Volatilized during Nuclear Fuels Reprocessing. *Nucl. Technol.* **1980**, *47* (3), 451–456.

(53) Sakurai, T.; Hinatsu, Y.; Takahashi, A.; Fujisawa, G. Adsorption of Ruthenium Tetroxide on Metal Surfaces. *J. Phys. Chem.* **1985**, *89* (10), 1892–1896.

(54) Mun, C.; Ehrhardt, J. J.; Lambert, J.; Madic, C. XPS Investigations of Ruthenium Deposited onto Representative Inner Surfaces of Nuclear Reactor Containment Buildings. *Appl. Surf. Sci.* **2007**, *253* (18), 7613–7621.

(55) Ohnet, M. N.; Leroy, O.; Mamede, A. S. Ruthenium Behavior in the Reactor Cooling System in Case of a PWR Severe Accident. *J. Radioanal. Nucl. Chem.* **2018**, *316* (1), 161–177.

(56) Souvi, S. M. O.; Badawi, M.; Paul, J.-F.; Cristol, S.; Cantrel, L. A DFT Study of the Hematite Surface State in the Presence of H_2, H_2O and O_2. *Surf. Sci.* **2013**, *610*, 7–15.

(57) Souvi, S. M. O.; Badawi, M.; Virot, F.; Cristol, S.; Cantrel, L.; Paul, J.-F. Influence of Water, Dihydrogen and Dioxygen on the Stability of the Cr_2O_3 Surface: A First-Principles Investigation. *Surf. Sci.* **2017**, *666*, 44–52.

(58) Bader, R. F. W. A Quantum Theory of Molecular Structure and Its Applications. *Chem. Rev.* **1991**, *91* (5), 893–928.

(59) Backman, U.; Lipponen, M.; Auvinen, A.; Jokiniemi, J.; Zilliacus, R. Ruthenium Behaviour in Severe Nuclear Accident Conditions Final Report. **2004**.

(60) Sheppard, D.; Terrell, R.; Henkelman, G. Optimization Methods for Finding Minimum Energy Paths. *J. Chem. Phys.* **2008**, *128* (13).

(61) Henkelman, G.; Uberuaga, B. P.; Jónsson, H. Climbing Image Nudged Elastic Band Method for Finding Saddle Points and Minimum Energy Paths. *J. Chem. Phys.* **2000**, *113* (22), 9901–9904.

(62) Henkelman, G.; Jónsson, H. Improved Tangent Estimate in the Nudged Elastic Band Method for Finding Minimum Energy Paths and Saddle Points. *J. Chem. Phys.* **2000**, *113* (22), 9978–9985.

(63) Kresse, G.; Joubert, D. From Ultrasoft Pseudopotentials to the Projector Augmented-Wave Method. *Phys. Rev. B* **1999**, *59* (3), 1758–1775.

(64) Kresse, G.; Furthmüller, J. Efficiency of Ab-Initio Total Energy Calculations for Metals and Semiconductors Using a Plane-Wave Basis Set. *Comput. Mater. Sci.* **1996**, *6* (1), 15–50.

(65) Kresse, G.; Hafner, J. *Ab Initio* Molecular-Dynamics Simulation of the Liquid-Metal–amorphous-Semiconductor Transition in Germanium. *Phys. Rev. B* **1994**, *49* (20), 14251–14269.

(66) Nosé, S. A Unified Formulation of the Constant Temperature Molecular Dynamics Methods. *J. Chem. Phys.* **1984**, *81* (1), 511–519.

(67) Hoover, W. G. Canonical Dynamics: Equilibrium Phase-Space Distributions. *Phys. Rev. A* **1985**, *31* (3), 1695–1697.

(68) Andersen, H. C. Molecular Dynamics Simulations at Constant Pressure and/or Temperature Hydrophobic Interactions in Presence of Osmolytes Urea and Trimethylamine-N-Oxide Molecular Dynamics Simulations at Constant Pressure and/or Temperature A). *J. Chem. Phys. J. Chem. Phys. J. Chem. Phys. Addit. Inf. J. Chem. Phys. J. Homepage* **1980**, *72* (154508), 2384–174501.

CHAPTER 5   GENERAL CONCLUSION AND PERSPECTIVES

During a nuclear accident, radionuclides can be released into the environment under different forms from the reactor containment building and these outside releases have important radiological consequences on human health and on the nature. The good prediction of the contamination, based on simulations of the outside radioactive releases for different types of accident, for realistic dose assessment and be able to make a suitable crisis management to better protect the public. The gas phase chemical reactivity of the fission products is relatively well-known but effect of the contribution of revaporisation processes from deposits on surfaces, typically the reactor coolant system surfaces (RCS), is not understood. To simulate the potential remobilisation of radionuclides species deposits during a severe nuclear accident, we focus our works on iodine and ruthenium fission products and more precisely on deposits on stainless steel surfaces. These two elements are chosen due to their important consequences on environment and human's health. Iodine produced by nuclear fission reactions can react at high temperature, in the RCS with control rod materials (forming, for example: AgI and CdI_2). These metallic iodide species may reach the containment building and can be oxidized to gaseous molecular iodine $I_{2(g)}$.[1] Some oxidative reactions can form ruthenium oxides and more particularly the volatile $RuO_{4(g)}$ form that can, be deposited on the surface of the reactor coolant system and of the nuclear containment building made with stainless steel for a part of them.[2,3] For these reasons, we study theoretically, the adsorption of metal iodides (AgI and CdI_2) and of ruthenium oxides (RuO_2, RuO_3 and RuO_4) on stainless steel surfaces (chromium oxide and iron oxide) as well as the formation volatile species ($I_{2(g)}$, $RuO_{3(g)}$ and $RuO_{4(g)}$).

The adsorption of control rod metal iodides (AgI and CdI_2) on stainless steel surface (Fe_2O_3Fe[4], Cr_2O_3Cr and its oxidized surfaces[5]) were studied. For iodine, the associative adsorption is more favourable than the dissociative adsorption on most of

the surfaces and the adsorption on a neutral surface is more advantageous than on a modified surface. The adsorbed molecules form a threefold hollow site on surfaces (Ag-OOO or Cd-OOO) except on the chromyl surface (which is the oxidized chromium oxide surface) where they form a tetrahedral structure with terminal oxygen atoms of the surface. At high coverage, adsorbed AgI molecules form a chain or a ring structure on the surface, keeping bonds between silver atoms and the surface. On the opposite, adsorbed CdI_2 molecules do not form any covalent bond with the surface at high coverage. From a reactivity point of view, the formation of $I_{2\,(g)}$ is possible on a Chromyl surface when AgI or CdI_2 have been adsorbed. However, the temperature that allows this reaction depends both on the coverage and on the adsorbed species. From a Chromyl surface with AgI adsorbed, the formation of $I_{2(g)}$ is possible at low temperature. At 25% coverage, the formation occurs almost spontaneously (at 75 K) until above 930 K. When the coverage increases to 50%, the formation of $I_{2\,(g)}$ can happen between 305 K and 780 K. The formation for a surface totally covered by AgI is very restricted to a very small temperature ranges (from 593 K to 637 K). From a Chromyl surface with CdI_2 adsorbed, only with low coverage (25%) the formation of $I_{2(g)}$ is possible (up to 700 K). This reaction can explain the partial re-vaporization of AgI as $I_{2(g)}$ on stainless steel[6] and the limitation in formation of CdI_2[7] in certain conditions. Additionally, formation of $I_{2(g)}$ is possible in presence of an oxidant such as $OH^\bullet$ from neutral surfaces (Cr_2O_3Cr and Fe_2O_3Fe).

Ru exists in several oxidation states (0 to +8). In this study, we focus on the more stable oxides (RuO_2, RuO_3 and RuO_4). As $RuO_{2(g)}$ can only exist at very high temperature, ruthenium dioxide is supposed to be in solid state inside the reactor coolant system (RCS) and in the nuclear containment building. RuO_3 and RuO_4 are the two main ruthenium gaseous species at high temperature.[8] To simulate the behaviours of ruthenium oxides on stainless steel surface, RuO_2, RuO_3 and RuO_4 have been adsorbed on Fe_2O_3Fe, Cr_2O_3Cr and its modified surfaces. This work shows that these ruthenium oxides are often isolated on these surfaces. The adsorption is more exothermic on the neutral surface than on the modified ones. Furthermore, by combining Density of State (DOS) and *bader*[9] calculation for adsorbed ruthenium species, it was evidenced that the adsorption RuO_2 and RuO_3 on Chromyl surface (25% coverage) leads to the RuO_4 formation, the charge on the Ru atoms being similar to the charge on the gaseous ruthenium tetroxide. So it is possible that adsorbed

species can be released from the Ru deposits on the surface under $RuO_{4(g)}$ or $RuO_{3(g)}$ form. According to our modelling works, with or without the presence of oxygen in the gas phase, ruthenium can be re-vaporized from adsorbed surfaces as $RuO_{3(g)}$ or $RuO_{4(g)}$ depending on the coverage. With presence of oxygen in the gas phase, the re-vaporization of $RuO_{4(g)}$ occurs spontaneously on different surfaces. Without presence of oxygen, from a chromyl surface with 25% and 50% coverage of RuO_2, $RuO_{4(g)}$ will be re-vaporization for temperature higher than around 570 K. When the chromyl surface is totally covered by RuO_2, $RuO_{3(g)}$ will be re-vaporized for a temperature higher than 576 K without presence of oxygen. These results tend to show that re-vaporization of RuO_2 deposits is a source of gaseous ruthenium oxides, at high temperature, as mentioned in litterature[8,10]. The decomposition of RuO_3 and RuO_4 and the re-vaporization of gaseous ruthenium oxides on stainless steel have also been studied. Stainless steel surfaces play an important role in decomposition of RuO_4 and it may accelerate its decomposition. In a first step, it decomposes into RuO_3 on Cr_2O_3Cr and Fe_2O_3Fe surfaces and in a second step, the released gaseous RuO_3 will be reduced to $RuO_{2(g)}$. The studies performed on the RuO_2 surfaces, modelling RuO_2 aerosols, have shown that the dissociative adsorption of O_2 molecule is more favourable than the molecular adsorption on all the surfaces investigated. The re-vaporization of RuO_3 and RuO_4 from RuO_2 aerosols was studied by Molecular Dynamic simulations. This calculation method allows characterising each step in a reaction pathway and also to determine the activation energy. Ruthenium could be liberated under $RuO_{4(g)}$ by creating a defect on RuO_2 [0 0 1] surface, even if, due to the high energetic barrier, this process should not be relevant.

In order to complete the work presented in this thesis, the adsorption of control rod metal iodides and ruthenium oxide species on other possible components of stainless steel surface (for example: manganese oxide (MnO) and manganese chromite ($MnCr_2O_4$)) could be performed in order to get a more global point of view on these adsorptions during severe nuclear accident. Furthermore, using Molecular Dynamic simulations, the re-vaporization process of gaseous ruthenium oxide species with other O_2 coverage and on other RuO_2 surfaces can also be investigated in order to determine the role of all the surfaces in the re-vaporization process of gaseous ruthenium oxides species.

REFERENCE

(1) Kress, T. S.; Beahm, E. C.; Weber, C. F.; Parker, G. W. Fission Product Transport Behavior. *Nucl. Technol.* **1993**, *101* (3), 262–269.

(2) Holm, J.; Glänneskog, H.; Ekberg, C. Deposition of RuO4 on Various Surfaces in a Nuclear Reactor Containment. *J. Nucl. Mater.* **2009**, *392* (1), 55–62.

(3) Eichler, B.; Zude, F.; Fan, W.; Trautmann, N.; Herrmann, G. Volatilization and Deposition of Ruthenium Oxides in a Temperature Gradient Tube. *Radiochim. Acta* **1992**, *56* (3), 133–140.

(4) Souvi, S. M. O.; Badawi, M.; Paul, J.-F.; Cristol, S.; Cantrel, L. A DFT Study of the Hematite Surface State in the Presence of H_2, H_2O and O_2. *Surf. Sci.* **2013**, *610*, 7–15.

(5) Souvi, S. M. O.; Badawi, M.; Virot, F.; Cristol, S.; Cantrel, L.; Paul, J.-F. Influence of Water, Dihydrogen and Dioxygen on the Stability of the Cr_2O_3 Surface: A First-Principles Investigation. *Surf. Sci.* **2017**, *666*, 44–52.

(6) Obada, D. Evaluation de Rejets Moyen-Terme En Situation Accidentelle Grave d'un Réacteur à Eau Pressurisée : Étude Expérimentale de La Re-Vaporisation de Dépôts de Produits de Fission (Cs, I),Thesis, Université de Lille 1, 2017.

(7) Bosland, L.; Cantrel, L. Iodine Behaviour in the Circuit and Containment: Modeling Improvements in the Last Decade and Remaining Uncertainties. In *Proceedings of the International OECD-NEA/NUGENIA-SARNET*; Marseille, France, 2015.

(8) Backman, U.; Lipponen, M.; Auvinen, A.; Jokiniemi, J.; Zilliacus, R. Ruthenium Behaviour in Severe Nuclear Accident Conditions Final Report. **2004**, No. August, 26.

(9) Bader, R. F. W. A Quantum Theory of Molecular Structure and Its Applications. *Chem. Rev.* **1991**, *91* (5), 893–928.

(10) Backman, U.; Lipponen, M.; Auvinen, A.; Tapper, U.; Zilliacus, R.; Jokiniemi, J. K. On the Transport and Speciation of Ruthenium in High Temperature Oxidising Conditions. *Radiochim. Acta* **2005**, *93* (5), 297–304.
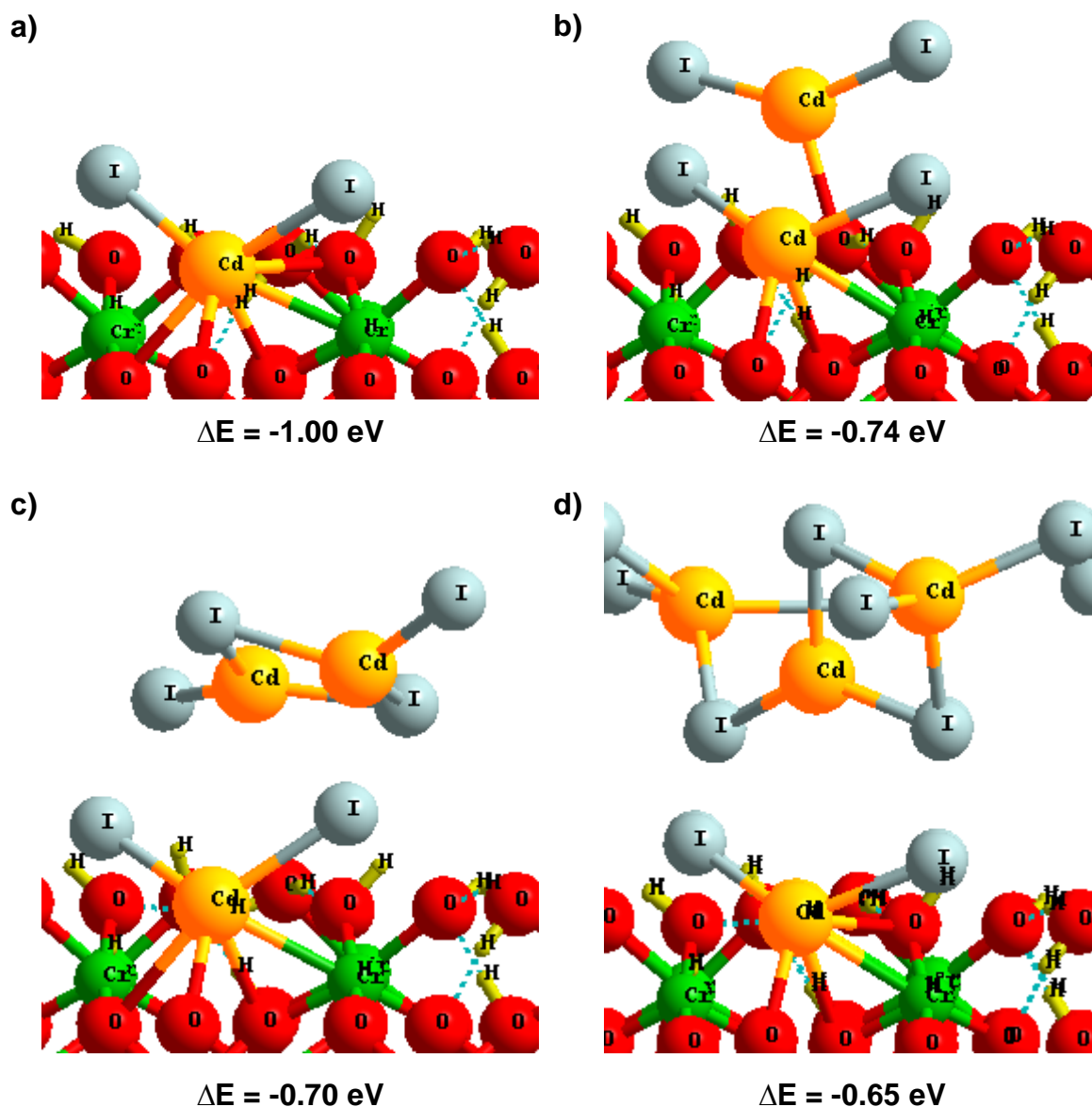
A.1 SATURATED HYDRATE CHROMIUM OXIDE SURFACE

a)

ΔE = -1.61 eV

b)

ΔE = -1.64 eV

c)

ΔE = -1.35 eV

d)

ΔE = -1.42 eV
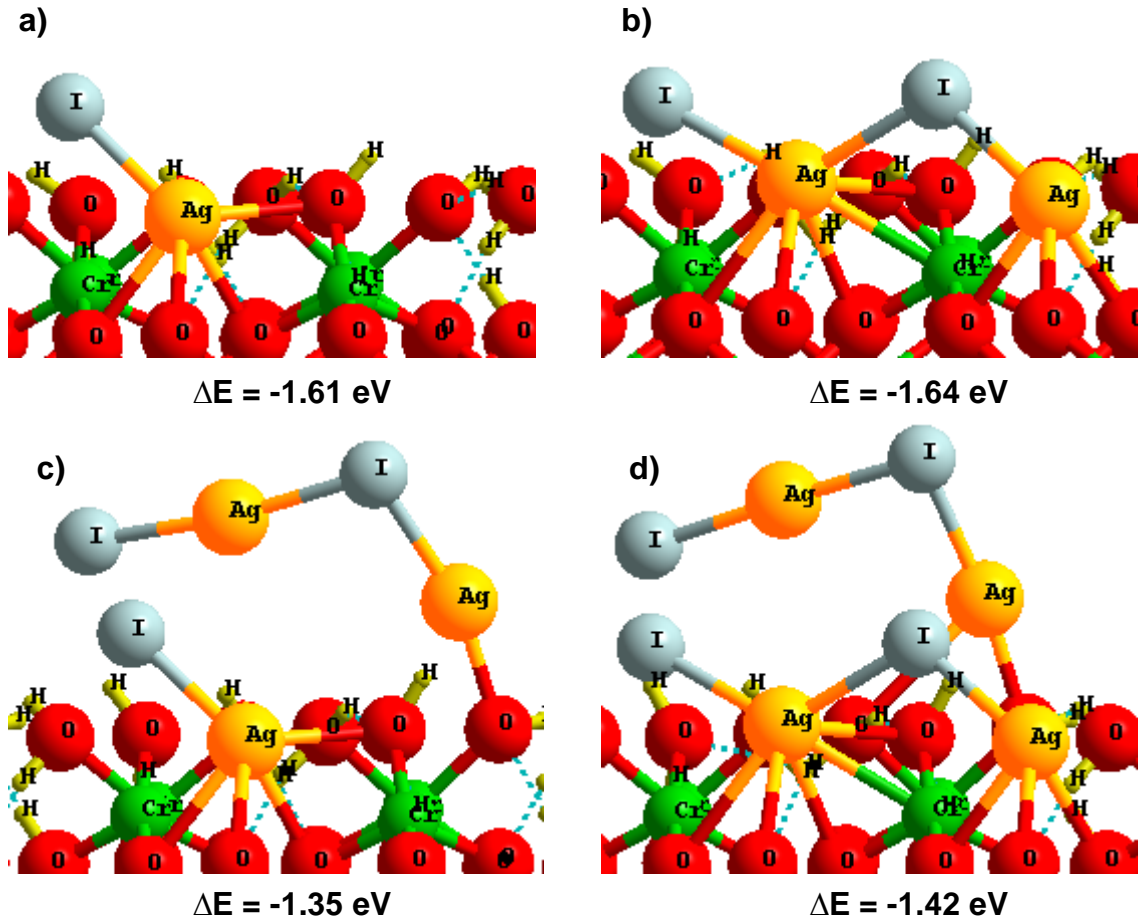
Figure A.1. Adsorption of AgI with (a) 25% (b) 50% (c) 75% and (d)100% coverage adsorbed on totally saturated hydrated chromium oxide surface (with six water molecules). ΔE is the adsorption energy per AgI molecule adsorbed with equation shown as below. Chromium: green. Oxygen: red. Cadmium: yellow. Iodine: grey. Hydrogen: light yellow.

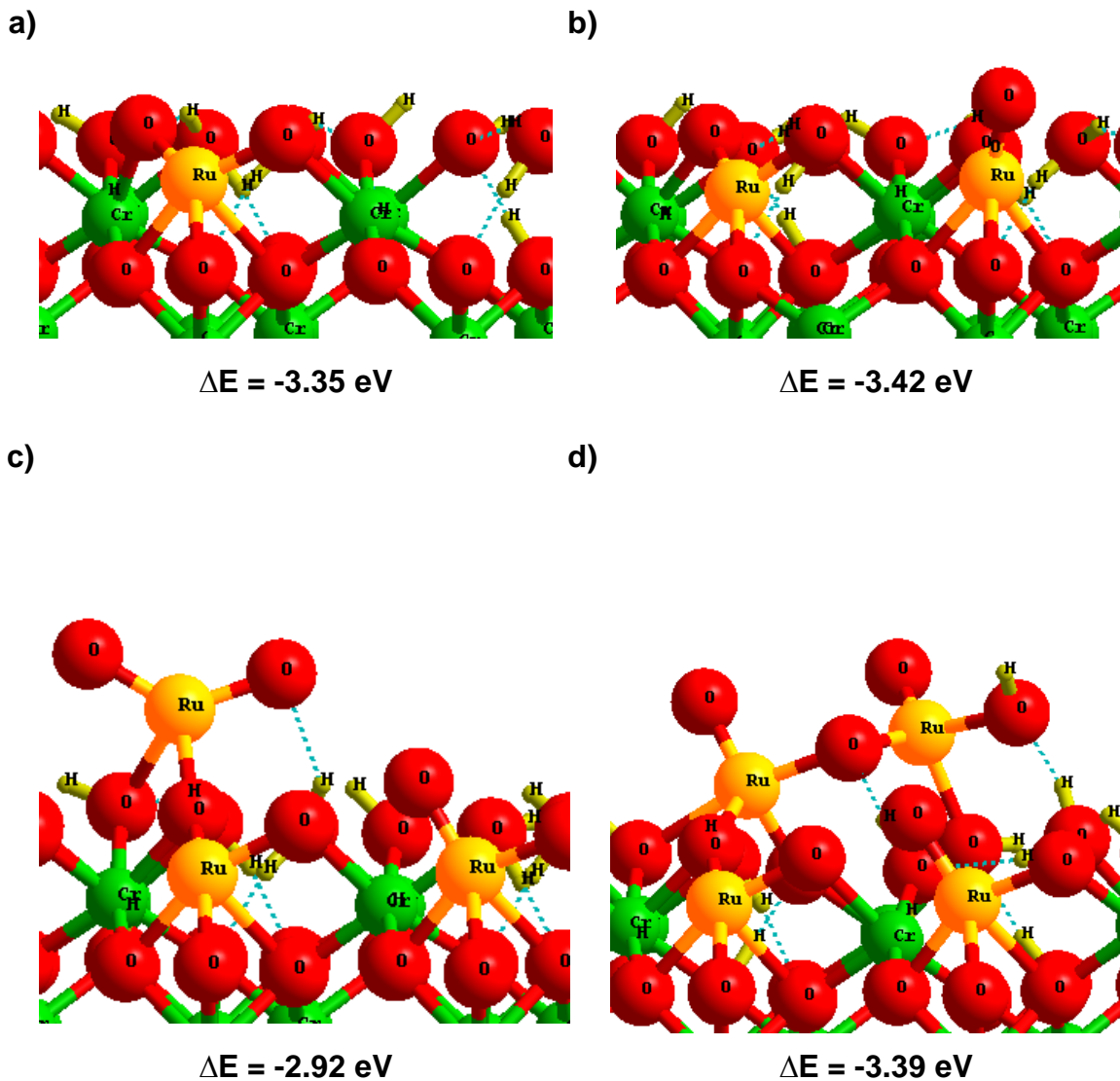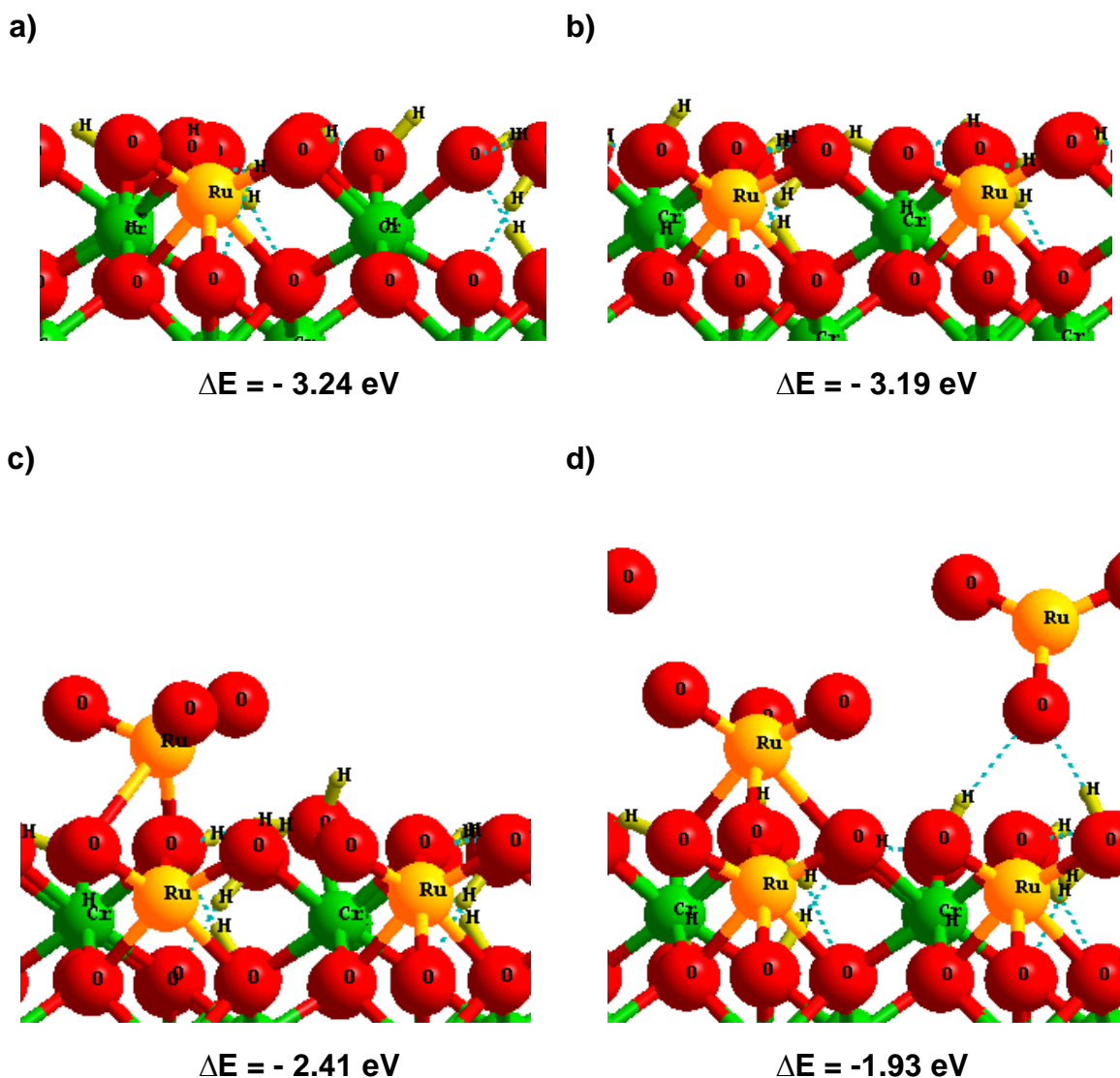$$\Delta E_{ads} = \frac{E_{total} - E_{surface} - \left(E_{AgI} \times n_{AgI}\right)}{n_{AgI}}$$

with $E_{ads} < 0$, corresponding to an exothermic reaction.

Figure A.2. Adsorption of CdI$_2$ with (a) 25% (b) 50% (c) 75% and (d)100% coverage adsorbed on totally saturated hydrated chromium oxide surface (with six water molecules). ΔE is the adsorption energy per CdI$_2$ molecule adsorbed with equation shown as below. Chromium: green. Oxygen: red. Cadmium: yellow. Iodine: grey. Hydrogen: light yellow.

$$\Delta E_{ads} = \frac{E_{total} - E_{surface} - \left(E_{CdI_2} \times n_{CdI_2}\right)}{n_{CdI_2}}$$

with $E_{ads} < 0$, corresponding to an exothermic reaction.

a)

ΔE = -3.35 eV

b)

ΔE = -3.42 eV

c)

ΔE = -2.92 eV

d)

ΔE = -3.39 eV

Figure A.3. Adsorption of RuO$_2$ with (a) 25% (b) 50% (c) 75% and (d)100% coverage adsorbed on totally saturated hydrated chromium oxide surface (with six water molecules). ΔE is the adsorption energy per RuO$_2$ molecule adsorbed with equation shown as below. Chromium: green. Oxygen: red. Ruthenium: yellow. Hydrogen: light yellow.

$$\Delta E_{ads} = \frac{E_{total} - E_{surface} - \left(E_{RuO_2} \times n_{RuO_2}\right)}{n_{RuO_2}}$$

with $E_{ads} < 0$, corresponding to an exothermic reaction.

a)

b)

ΔE = - 3.24 eV

ΔE = - 3.19 eV

c)

d)

ΔE = - 2.41 eV

ΔE = -1.93 eV

Figure A.4. Adsorption of RuO$_3$ with (a) 25% (b) 50% (c) 75% and (d)100% coverage adsorbed on totally saturated hydrated chromium oxide surface (with six water molecules). ΔE is the adsorption energy per RuO$_3$ molecule adsorbed with equation shown as below. Chromium: green. Oxygen: red. Ruthenium: yellow. Hydrogen: light yellow.

$$\Delta E_{ads} = \frac{E_{total} - E_{surface} - \left(E_{RuO_3} \times n_{RuO_3}\right)}{n_{RuO_3}}$$

with $E_{ads} < 0$, corresponding to an exothermic reaction.

a)

ΔE = - 1.37 eV

b)

ΔE = - 0.94 eV

c)

ΔE = - 0.64 eV

d)

ΔE = - 0.51 eV
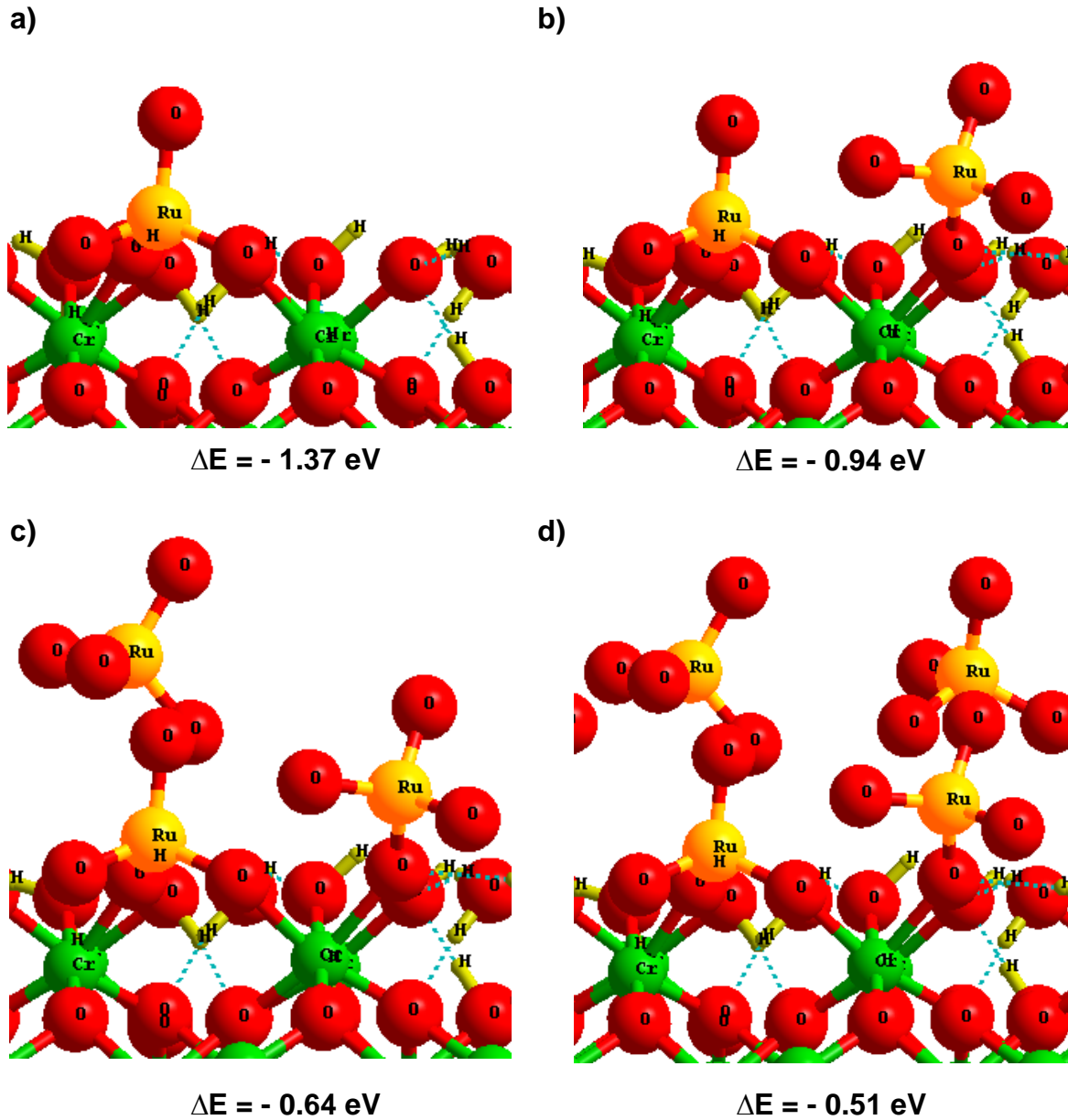
Figure A.5. Adsorption of RuO_4 with (a) 25% (b) 50% (c) 75% and (d)100% coverage adsorbed on totally saturated hydrated chromium oxide surface (with six water molecules). ΔE is the adsorption energy per RuO_4 molecule adsorbed with equation shown as below. Chromium: green. Oxygen: red. Ruthenium: yellow. Hydrogen: light yellow.

$$\Delta E_{ads} = \frac{E_{total} - E_{surface} - \left(E_{RuO_4} \times n_{RuO_4}\right)}{n_{RuO_4}}$$

with $E_{ads} < 0$, corresponding to an exothermic reaction.
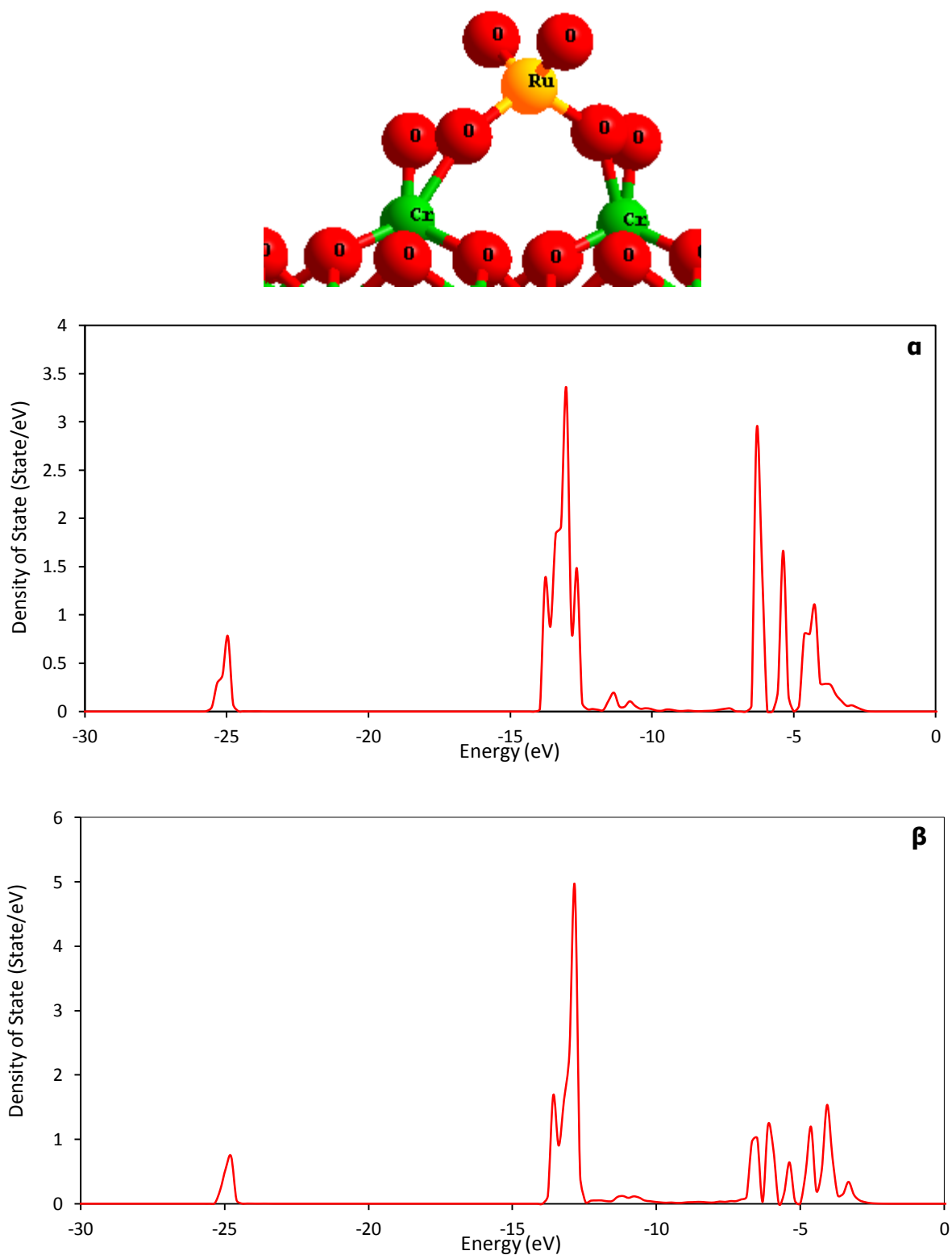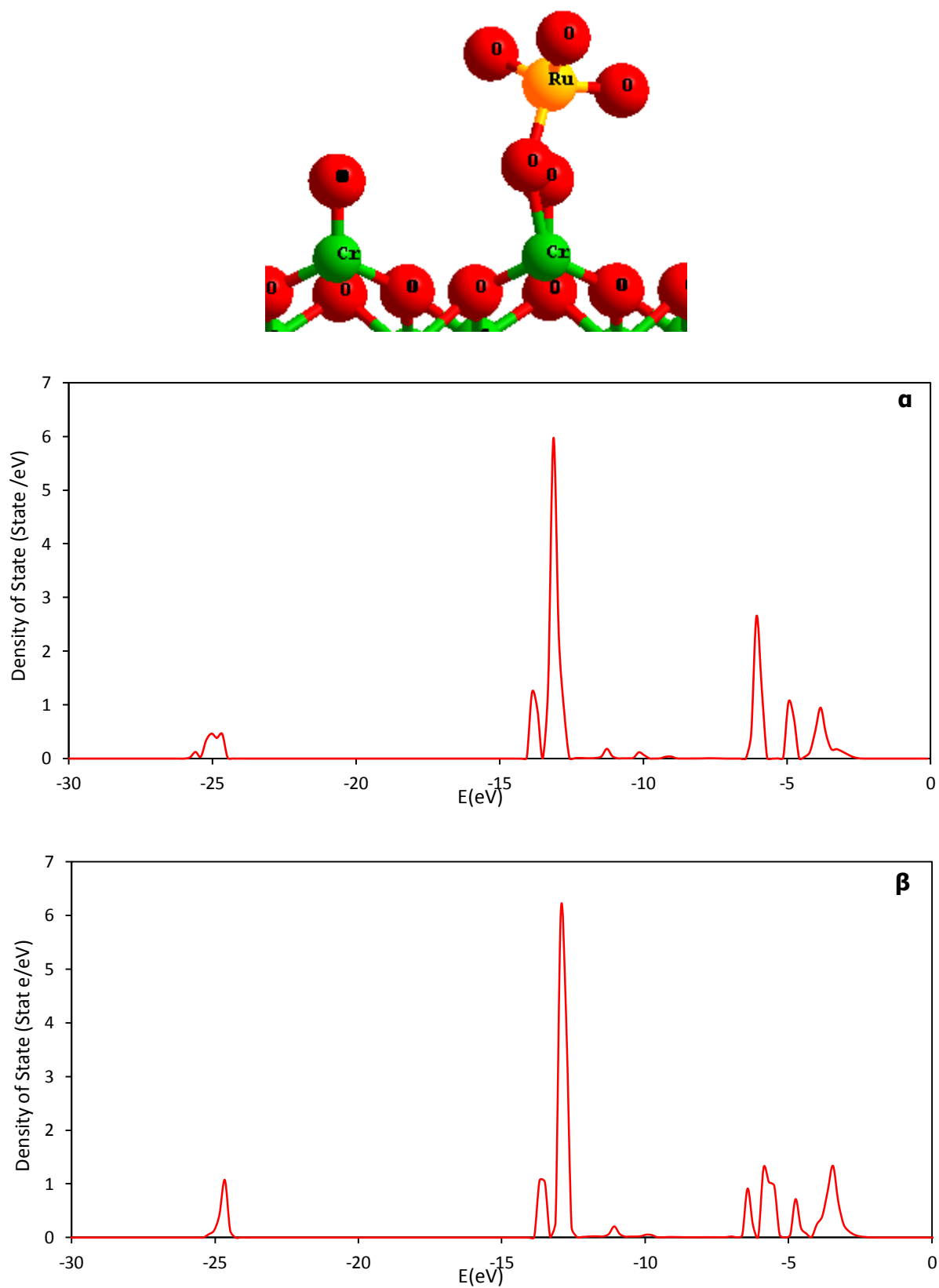
A.2   DENSITY OF STATE FOR DIFFERENT ADSORBED RUTHENIUM SPECIES
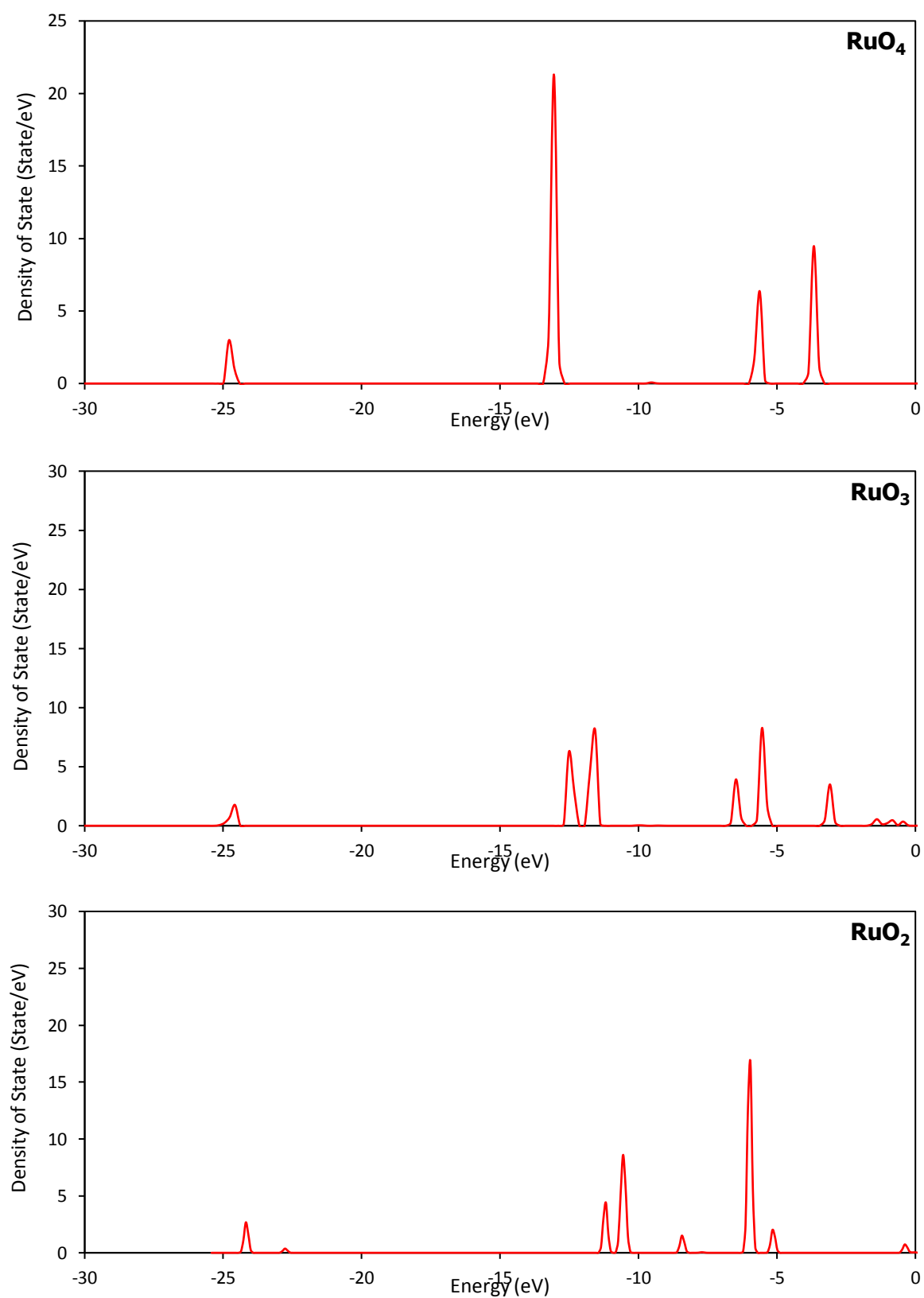
Figure A.6. Density of states for d orbitals (Ru) of reference molecules (top) RuO_4 (middle) RuO_3 (bottom) RuO_2.

Figure A.7. Density of states for d orbitals for most stable structure of RuO_2 adsorbed on Chromyl surface with 25% of coverage (top) alpha (bottom) beta.

Figure A.8. Density of states for d orbitals for most stable structure of RuO_3 adsorbed on Chromyl surface with 25% of coverage (top) alpha (bottom) beta.

A.3 Molecular Dynamic Simulation for Re-vaporization of RuO₃ or RuO₄ from Adsorbed Ruo₂ Surface
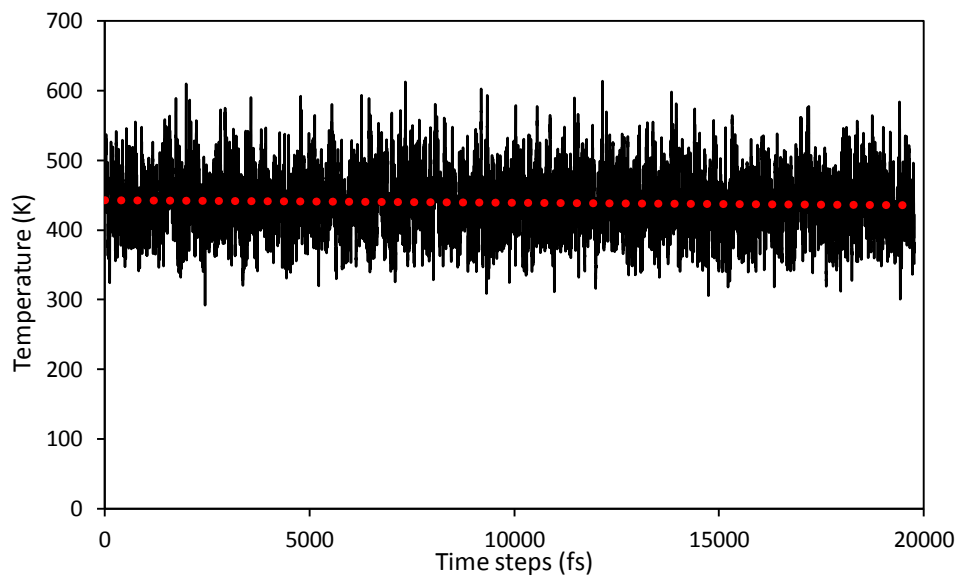
Figure A.9. Variation of temperature during Meta Molecule Dynamic simulation with Slow-growth approach for associative adsorption of dioxygen molecule on [0 0 1] surface of ruthenium dioxygen. *t = 0 to 20 000 fs.*
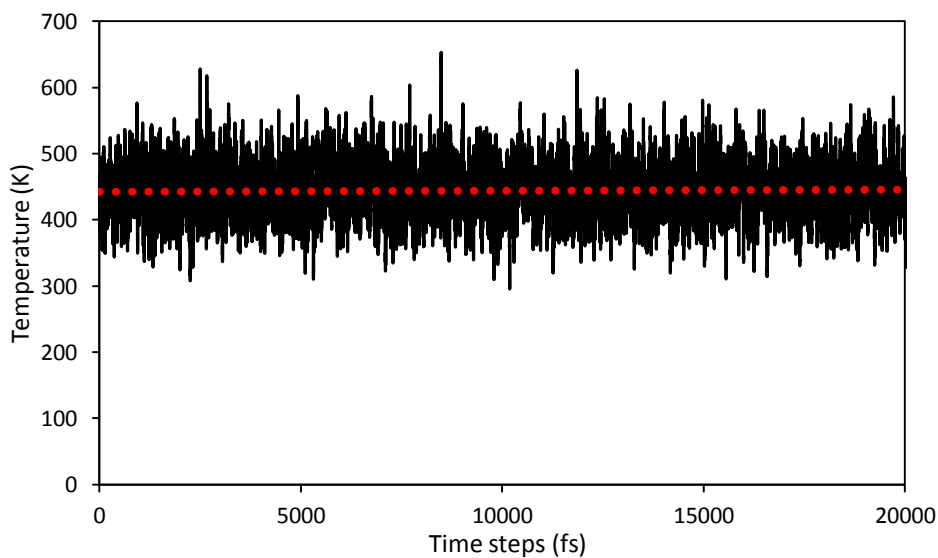
Figure 4.10. Variation of temperature during Meta Molecule Dynamic simulation with Slow-growth approach for associative adsorption of dioxygen molecule on [0 0 1] surface of ruthenium dioxygen. *t = 0 to 20 000 fs.*